Title

Investigation of the Isotopic Composition of Atmospheric Trace Gases Through Observations, Experiments, and Modeling

Author

Carlstad, Julia Marianne

Publication Date

2021

Peer reviewed|Thesis/dissertation

Investigation of the Isotopic Composition of Atmospheric Trace Gases Through Observations, Experiments, and Modeling

By

Julia M. Carlstad

A dissertation submitted in partial satisfaction of the

requirements for the degree of

Doctor of Philosophy

in

Chemistry

in the

Graduate Division

of the

University of California, Berkeley

Committee in charge:

Professor Kristie A. Boering, Chair
Professor Ronald C. Cohen
Professor Ronald Amundson

Summer 2021

Investigation of the Isotopic Composition of Atmospheric Trace Gases

Through Observations, Experiments, and Modeling

by

Julia M. Carlstad

Abstract

Investigation of the Isotopic Composition of Atmospheric Trace Gases

Through Observations, Experiments, and Modeling

by

Julia M. Carlstad

Doctor of Philosophy in Chemistry

University of California, Berkeley

Professor Kristie A. Boering, Chair

This dissertation presents a series of experiments and observations using the isotopic composition of trace gases to inform atmospheric chemistry and transport ranging from Earth's troposphere to the mesosphere. These include (1) the investigation of the isotopic composition of nitrous oxide (N_2O) produced in plasma discharges relevant to atmospheric processes, (2) analysis of radiocarbon in carbon dioxide (CO_2) sampled in the upper troposphere and lower stratosphere at high latitudes in the northern and southern hemispheres, and (3) a review of the chemical physics of isotope effects relevant for atmospheric chemistry.

First, because N_2O is both a long-lived greenhouse gas and an ozone depleting substance, the processes responsible for the dramatic rise in atmospheric N_2O concentrations continues to warrant investigation. Recent observations from aircraft and satellites suggest that there are potential *in-situ* atmospheric sources from lightning in the troposphere and high-energy events in the upper atmosphere that are not well constrained; although the global source strengths are likely small, their transient nature may confound analyses of atmospheric observations of N_2O unless they are quantified and understood. In principle, the source of N_2O can be inferred by measuring its isotopic composition, but that of N_2O produced by these non-equilibrium plasmas is not known. In this study, N_2O produced in four different types of plasma discharges (e.g., corona, pin-to-plane, plasma flashlight, and surface microdischarge) and under different conditions was analyzed by isotope ratio mass spectrometry, yielding distinctly different isotopic compositions. Kinetics modeling was performed to understand the importance of different reactions to the production of N_2O and its isotopic composition. This work provides new constraints on the kinetics and chemical mechanisms of N_2O production and destruction pathways in low-temperature, non-equilibrium plasmas, to which isotope compositions have not been applied before, as well as the 'isotopic

fingerprints' of plasma-generated N_2O – distinct from the microbial and combustion sources of N_2O to the atmosphere – to compare with aircraft and satellite observations.

Second, vertical profiles are presented of $\Delta^{14}C\text{-}CO_2$ measured on whole air samples collected across the tropopause at high latitudes in the northern and southern hemispheres by the NASA DC-8 aircraft during the fourth Atmospheric Tomography Mission (ATom-4) deployment in May 2018. These profiles not only provide important new constraints for inverse models of the carbon cycle but also show interesting differences between the hemispheres. These differences could result from differences in the amounts of isentropic transport from the subtropical troposphere into the lowermost stratosphere, the magnitudes of downwelling from the stratospheric overworld, tropospheric radiocarbon levels, or some combination of these factors. These data will be used to provide guidance for selecting the timing and location of future aircraft sampling missions needed to deconvolve the influence of these dynamical factors on the composition of the lowermost stratosphere. In addition, inferred cosmogenic ^{14}C production rates are calculated and compared with past aircraft and ballooning missions from 1997 to 2013. The ATom-4 production rates are skewed high likely due to substantial isentropic mixing in of new air from the troposphere into the lowermost stratosphere; these results indicate the importance of sampling in the stratosphere above 15 km for studies using $^{14}CO_2$ levels as a tracer of stratospheric residence times.

Third, a review of the chemical physics of isotope effects relevant for atmospheric chemistry is included that focuses on recent developments in the field and their historical context. The discussion includes non-mass dependent isotope effects in oxygen-containing species and an overview of the recent growth of "clumped isotope" measurements at natural isotopic abundances – i.e., of doubly-isotopically substituted species. This review lays the groundwork for introducing chemistry researchers to the field and summarizing the outstanding research questions to which experimental and theoretical physical chemists can contribute.

For my family

Table of Contents

List of Figures iv

List of Tables vii

Chapter 1. Introduction and Overview

1.1 Investigation of the isotopic composition of nitrous oxide produced in plasma discharges through experiments and modeling (Chapter 2) 1

1.2 Vertical profiles of $\Delta^{14}C\text{-}CO_2$ from the NASA ATom mission (Chapter 3) 5

1.3 Review of isotope effects and the atmosphere (Chapter 4) 6

References 9

Chapter 2. Analysis of the Isotopic Composition of N_2O Generated in Plasma Discharges

2.1 Introduction 17

2.2 Methods

2.2.1 Corona Discharge Sample Generation 18

2.2.2 Corona Discharge Sample Preparation and Analysis by IRMS 20

2.2.3 Atmospheric Plasma Sample Generation and Analysis 22

2.2.4 FTIR measurements of gases generated by the atmospheric pressure plasmas 23

2.2.5 Optical Emission Spectra (OES) Measurements 24

2.2.6 Kinetics modeling details: Sensitivity runs including hypothetical KIEs 24

2.3 Results and Discussion

2.3.1 Corona Discharge Results 29

2.3.2 Results of Atmospheric Pressure Discharges 33

2.3.3 Insights into Chemical Mechanisms 36

2.3.4 Atmospheric Applications 40

2.4 Conclusions and Future Work 41

References 43

Appendix: Supplementary Information 48

Chapter 3. High Latitude Vertical Profiles of $^{14}CO_2$ across the Tropopause from the Atmospheric Tomography (ATom) Mission

Abstract 53

3.1 Introduction 53

3.2 Methods 55

3.3 Results and Discussion 57
3.4 Conclusions 65
References 66
Appendix: Supplementary Information 71
Chapter 4. Isotope Effects and the Atmosphere
4.1. Introduction 76
4.2. Background 77
4.2.1 Conventions when discussing isotopes at natural abundances 77
4.2.2 Mass Dependent vs. Non-mass Dependent Isotope Effects 78
4.2.3 Instrumentation 81
4.3 Oxygen NMD Isotope Effects and Isotope Compositions
4.3.1 Ozone 82
4.3.2 Species with O-MIF derived from ozone
4.3.2.1 Stratospheric CO_2 86
4.3.2.2 Tropospheric CO_2 88
4.3.2.3 O_2 89
4.3.2.4 Minerals 89
4.3.2.5 Atmospheric Nitrates 90
4.3.2.6 Atmospheric Sulfates 90
4.3.3 O-MIF in other species including CO and SiO 91
4.4. Normal and Inverse Kinetic Isotope Effects 92
4.4.1 Methane (CH_4) 93
4.4.2 Molecular hydrogen (H_2) 94
4.4.3 Nitrous oxide (N_2O) 95
4.4.4 Reactive nitrogen species (NO_x, NH_3, HNO_3, HONO) 96
4.5. Multiply Substituted Isotopologue Abundances 96
4.5.1 CO_2 ($^{13}C^{18}O^{16}O$) 97
4.5.2 O_2 ($^{18}O^{18}O$ and $^{17}O^{18}O$) 97
4.5.3 CH_4 ($^{13}CH_3D$, CH_2D_2) 98
4.5.4 H_2 (D_2) 98
4.5.5 N_2O ($^{14}N^{15}N^{18}O$ and $^{15}N^{14}N^{18}O$) 98
4.5.6 N_2 ($^{15}N^{15}N$) 99
4.5.7 Ethane ($^{13}C_2H_6$) 99
4.6 Conclusions 99
References 100

List of Figures

1.1 Schematic of the sources and sinks of atmospheric N_2O. Emissions estimates are from Bouwman *et al., (*2013). 2

2.1 Diagram of the corona discharge line used for sample generation, with the discharge cell shown with purple coloration. (PA=picoammeter, NV= needle valve, CG=convection gauge, BG=Baratron capicitance manometer.) 19

2.2 Measurements of the isotopic composition of N_2O generated in the corona discharge apparatus isotopic composition, for which $\delta^{15}N$ is the "bulk" nitrogen isotopic composition averaged over the two nitrogen atom positions and $\delta^{15}N^{\alpha}$ is the isotopic composition at the central (or α) nitrogen atom position in NNO, both on the air N_2 scale. 31

2.3 Measurements of the isotopic composition of N_2O generated in the corona discharge apparatus isotopic composition, for which $\delta^{15}N$ is the "bulk" nitrogen isotopic composition averaged over the two nitrogen atom positions on the air N_2 scale and $\delta^{18}O$ is the oxygen isotopic composition on the air O_2 scale. 31

2.4 Relationship between $\delta^{18}O$ and $\delta^{15}N^{\alpha}$ (circles) or $\delta^{15}N^{\beta}$ (squares) for all the corona discharge data (cool colors) and for the 3 types of atmospheric pressure plasmas studied (plasma flashlight, surface microdischarge, and pin-to-plane). There is an anti-correlation between $\delta^{15}N^{\alpha}$ and $\delta^{18}O$ and only a weak correlation between $\delta^{15}N^{\beta}$ and $\delta^{18}O$ for the corona discharge data indicating that there is an isotope effect in a reaction that creates or destroys the N—O bond of N_2O. 32

2.5 Same as Figure 2.3 with measurements of the atmospheric pressure NEPs added. Corona discharge data from Smith *et al.* (2021) are shown as purple circles, that of this work are shown in dark and light blue circles, surface microdischarge is shown as a red square, plasma flashlight is shown as an orange star, and pin-to-plane is shown as a yellow triangle. 34

2.6 Same as Figure 2.4 measurements of the three atmospheric pressure NEPs added. Corona discharge data from Smith *et al.* (2021) are shown as purple circles, that of this work are shown in dark and light blue circles, surface microdischarge is shown as a red square, plasma flashlight is shown as an orange star, and pin-to-plane is shown as a yellow triangle. 35

2.7 FTIR spectra of the gases produced in the atmospheric pressure NEPs. Peaks are labeled based on the molecule(s) that are inferred at particular wavenumbers. 36

2.S1 Diagram of the gas transfer line used for sample aliquot preparation before analysis on the IRMS. 48

2.S2 Schematic of the preconcentrator, GC, and open split interface for N_2O as part of the online continous-flow IRMS apparatus for analysis of the isotope composition of N_2O. 48

2.S3 Diagram of the IRMS used for isotopic analysis. 49

2.S4 Diagram of setup for plasma sample generation and collection. 49

2.S5 Yield of (a) condensable gas (largely NO and N_2O) from the manometric calibration on the corona discharge line and (b) N_2O from the IRMS peak area, both as a function of measured pressure in the corona discharge cell. Note that the Smith *et al.* (2021) pressures at 5 and 10 Torr are likely much higher (40 to 60 Torr); see text. 50

2.S6 Plot of $\delta^{15}N$ bulk versus pressure in the corona discharge cell. 50

2.S7 Plot of $\delta^{18}O$ versus pressure in the corona discharge cell for the corona discharge experiments. 51

2.S8 Plots of (a) $\delta^{15}N$ and (b) $\delta^{18}O$ of N_2O generated in the corona discharge versus residence time measured with the flow meter. 51

2.S9 Reaction rates from the Kintecus-based NEP simulations for the corona discharge over 30 minutes. R1a is plotted in dark blue, R2 is plotted in light blue, and R3 is plotted in yellow. 52

3.1 Schematic of the troposphere, different regions of the stratosphere, and the mass fluxes between them: Air enters the stratospheric "overworld" in the tropics across the tropical tropopause (θ~380K) and follows the global-scale meridional stratospheric circulation (open arrows), also known as the Brewer-Dobson circulation (BDC). Air descends from the overworld across the 380K surface that separates the "stratospheric overworld" from the "lowermost stratosphere" (shown as the top solid curve) with flux F_{in}. The magnitude of F_{in} varies seasonally and, thus, the mass of the lowermost stratosphere varies seasonally as well. Air leaves the lowermost stratosphere across the extratropical tropopause (denoted by the lower solid line) via the flux indicated by F_{out}. Air can also be transported isentropically (or "quasi-horizontally") into and out of the lowermost stratosphere without ever having entered the stratospheric overworld, with a flux indicated by F_h, in effect "short-circuiting" the BDC. [Adapted from Figure 1 of Appenzeller (1996).] 55

3.2 Map of the NASA DC-8 flight tracks for which samples were collected and analyzed for $\Delta^{14}C\text{-}CO_2$: Flight 7 (20180509), Flight 10 (20180517), and Flight 12 (20180519). 57

3.3 Vertical profiles of $\Delta^{14}C\text{-}CO_2$ (N=41) measured on samples collected below (squares) and above (circles) the regional tropopause (black dotted lines) for (a) Flight 10=20180517, (b) Flight 12=20180519, and (c, d) Flight 7=20180509. The latitude range of the observations are given in the lower right of each figure. The tropopauses indicated by thin solid lines were determined by (a) a radiosonde launch at BGEM within 6 hours, (b) radiosondes at PANC (Anchorage) and PABR (Barrow) as well as a mid-flight temperature profile, and (c, d) by a radiosonde launch at Rothera and an ozonesonde launch at the Amundsen-Scott South Pole station. Profiles as a 58

function of potential temperature are shown in Figure 3.S1, and additional tropospheric samples not plotted here are shown in Figure 3.S3 of Supplementary Materials.

3.4 Measurements of $\Delta^{14}C\text{-}CO_2$ versus N_2O mixing ratio for samples collected in the lowermost stratosphere in the northern and southern hemispheres. The Williamson-York regressions are: for the NH (N=16): $\Delta^{14}C\text{-}CO_2 = (-1.15 \pm 0.14)[N_2O] + (384 \pm 42)$; for the SH (N=9): $\Delta^{14}C\text{-}CO_2 = (-1.06 \pm 0.13)\,[N_2O] + (366 \pm 41)$; for the combined stratospheric dataset (N=25): $\Delta^{14}C\text{-}CO_2 = (-0.74 \pm 0.04)\,[N_2O] + (263 \pm 13)$. The regressions yield an offset of -8 ± 1‰ for the NH compared to the SH. (Samples collected above the tropopause and with low water vapor (NH with $H_2O(v) < 9$ ppmv and in SH with $H_2O(v) < 10$ ppmv) were included in the fits; see text.) All uncertainties given are 1σ. 60

3.5 Back trajectories calculated using NOAA HYSPLIT for the $\Delta^{14}C\text{-}CO_2$ outliers in Figure 3.4 as a function of (a) latitude and longitude and (b) altitude: Asterisks denote the sampling location, triangles the location at 30 hours back in time, black indicates the back trajectory for the high outlier with $\Delta^{14}C\text{-}CO_2$ of 56‰, and blue indicates the back trajectory for the low outlier with $\Delta^{14}C\text{-}CO_2$ of 30‰. 62

3.S1 Vertical profiles of $\Delta^{14}C\text{-}CO_2$ (N=41) as a function of potential temperature measured on samples collected below (squares) and above (circles) the regional tropopause (black dotted lines) for (a) Flight 10, (b) Flight 12, and (c, d) Flight 7. The tropopauses were determined by (a) a radiosonde launch at BGEM within 6 hours, (b) radiosondes at PANC and PABR as well as a mid-flight temperature profile, and (c, d) by a radiosonde launch at Rothera and an ozonesonde launch at the Amundsen-Scott South Pole station. 71

3.S2 NOAA HYSPLIT back trajectory for the biomass burning outlier with $\Delta^{14}C\text{-}CO_2$ of 30‰ sampled on 19 May 2018 (asterisk) at 72.25°N, -138.67°W at an altitude of 5661 and θ=300 K (the tropopause was at ~9.3 km and θ=316 K). 72

3.S3 All tropospheric samples collected on Flight 12 (purple) and Flight 7 (green). The tropopauses are the same as in Figure 3.2(b) and (c) and are colorized by flight. 73

4.1 Triple isotope plot ($\delta^{17}O$ vs $\delta^{18}O$) for selected species including laboratory (Thiemens & Heidenreich, 1983), stratospheric (Krankowsky et al., 2007), and tropospheric ozone (Vicars & Savarino, 2014); atmospheric H_2O_2 (Savarino & Thiemens, 1999); atmospheric O_2 (Barkan & Luz, 2005); sulfates (Dominguez et al., 2008; Lee & Thiemens, 2001); nitrates (Michalski et al., 2004); stratospheric CO_2 (Garofalo et al.; Lämmerzahl et al., 2002; Thiemens, Jackson, Zipf, et al., 1995), and calcium aluminum inclusions (CAI) in carbonaceous chondrite meteorites (Clayton et al., 1973). The dashed line with slope of ½ corresponds to mass-dependent fractionation. 80

List of Tables

2.1	Selected reactions of interest in plasma discharges	26
2.2	Summary of modeled sensitivity tests	28
2.3	Summary of results from the corona discharge experiments	30
2.4	Summary of atmospheric plasma discharge yields and isotope composition for N_2O	34
3.1	Global annual mean ^{14}C production rates calculated for ATom-4 compared with previous missions.	64
3.S1	Measurements (N=46) of $\Delta^{14}C$-CO_2 on whole air samples collected during ATom-4	74

Acknowledgements

First, I have so much gratitude for my adviser, Kristie Boering, who was an amazing mentor throughout the trials of graduate school. I am so grateful for your guidance as I continue to develop as a scientist. I also want to express my thanks to my dissertation committee Ron Cohen and Ron Amundson for your support and advice throughout my PhD, and to my additional qualifying exam committee members, Rich Saykally and Evan Williams for conversations around my early research.

Thank you to my graduate school friends Scott Stonemeyer, Bethany De'Roulet, and Naomi Biggins who often made time to eat lunch together on the chemistry plaza and helped me to make first semester classes and adjustment to Berkeley more fun. Thank you to Kaitlyn Liescke for showing me the ropes of rock climbing and Nofel Naoman for always being up for an evening climbing session or a weekend hiking trip.

Boering group members of the past have laid the groundwork for the research done here, especially John Randazzo, Mica Smith, Lauren Garofalo, and Aaron Wiegel. Thank you for the times you have answered my questions even as you have moved on to other positions. I am also grateful to be included by the Cohen group members for literature club and birthday celebrations especially when our group was so small, you helped to bring levity to my weeks. And of course, thank you to Arianna Kazez, who taught me so much in the early days of working in lab, helped me overcome each hurdle of graduate school, and through it all, became my friend.

Research discussed in this dissertation would not have been possible without collaborators at Lawrence Livermore National Lab Center for Accelerator Mass Spectrometry, the ATom sampling team, and the NOAA Air Resources Laboratory (ARL) for the provision of the HYSPLIT transport and dispersion model. I am also grateful for our plasma discharge collaborators, Professor David Graves, Professor Ali Mesbah, and Dr. Xuekai Pei. Thank you to the National Science Foundation Graduate Research Fellowship for the financial support of my degree. My time within the College of Chemistry would have been immeasurably more difficult without the administrative staff especially Leslie Dietterick and Joel Adlen and glass, machine, and electrical shop staff Jim Breen, Doug Scudder, Yi Min Li, and Manny Druga who have supported my research projects and helped me learn about glass blowing, electronics, and machining. Thank you also to the SLAM committees of 2020 and 2021 and our advisers, Professor Anne Baranger and Rosanne Lurie. I so appreciated and enjoyed working with you all.

And finally, I am so thankful for my family, more than I can ever fully express here. My parents, Bret and Cynthia always supported me and encouraged me to take a break to join them to ski and camp. I especially am grateful for my mom, who was my first picture of a scientist and who pushed me away from my grade school hatred of math, without which I wouldn't be here today. Thank you to my uncle and aunt, Rich and Margarite who came to visit us regularly in Berkeley and always take an interest in my pursuits, and to Catara for all our time together during the pandemic. To my biggest day-to-day supporter, Ahmed Qureshi, I am so thankful that you are unwaveringly with me on these journeys, always believing in me, and of course, bringing humor and fun to our lives.

Chapter 1

Introduction and Overview

Climate change is one of the most pressing problems facing humanity today, with increasing focus from the public, media, and politicians, and where Earth and physical scientists can contribute to our understanding of the atmosphere. In past crises related to the atmosphere, such as choking air quality in major cities and the Antarctic ozone hole (National Academies of Sciences & Medicine, 2016), scientists have provided the quantitative foundation from which effective mitigation polices could be developed such as the Clean Air Act of 1970 (*Summary of the Clean Air Act*) and the Montreal Protocol of 1987 (*The Montreal Protocol*). With climate change, the atmospheric composition and chemistry is also changing, and there are new questions for atmospheric chemists to address.

Isotopic analysis has proven to be a powerful tool for understanding the atmosphere, including deciphering atmospheric chemical reactions, atmospheric dynamics, and the sources and sinks of trace gases. The three most important anthropogenic greenhouse gases – CO_2, CH_4, and N_2O – are examples of trace gases for which isotopic composition measurements can be used to target reductions in emissions through "top-down" efforts such as inverse modeling to understand the magnitudes and geographic distributions of emissions and quantify the atmospheric circulation and stratosphere-troposphere exchange. In addition to these valuable atmospheric applications, chemists have long used stable isotope analysis to provide insights into chemical rates and mechanisms, as the substitution of a heavy isotope leads to equilibrium and kinetic isotope effects, primarily caused by differences in the vibrational energies of the different isotopologs. Atmospheric chemists can combine these applications to provide insights and seek answers to fundamental and global scale questions, such as those addressed in this dissertation about atmospheric composition, circulation, and chemistry.

In each section below, I present the background and an overview of the content and scientific advances described in subsequent chapters and their importance in the fields of physical and atmospheric chemistry. These include (1) the isotopic analysis of nitrous oxide (N_2O) produced in low-temperature non-equilibrium plasma discharges relevant to lightning and other high energy charged particle phenomena in the atmosphere, (2) vertical profiles of the radiocarbon content of atmospheric CO_2 ($\Delta^{14}C$-CO_2) collected during the NASA ATom-4 mission that are important for constraining fossil fuel emissions, biosphere-atmosphere exchange, and the stratospheric circulation, and (3) an overview of the unanswered questions in the study of isotopes relevant to atmospheric chemistry to which experimental and theoretical physical chemists can contribute.

1.1 Investigation of the isotopic composition of nitrous oxide produced in plasma discharges through experiments and modeling (Chapter 2)

Nitrous oxide is a potent greenhouse gas and ozone depleting substance (ODS), with rising concentrations in the atmosphere (Intergovernmental Panel on Climate, 2014) and a long atmospheric lifetime of ~120 years (Bouwman et al., 2013). The dominant source of N_2O is from microbial activity in the soils and oceans; soil emissions of N_2O have been increasing dramatically due to increased fertilizer use (Bouwman et al., 2013; Davidson, 2009; Stein & Yung, 2003) especially since the Green Revolution in the 1960s in order to feed a growing world population

(Davidson, 2009; Intergovernmental Panel on Climate, 2014; Miller et al., 2012; Park et al., 2012; Röckmann et al., 2003). The minor sources of N_2O to the atmosphere include biomass burning, human and animal waste, industrial processes, and atmospheric sources (Schumann & Huntrieser, 2007; Stein & Yung, 2003), and the two destruction processes, photolysis and photo-oxidation, occur in the stratosphere (Bouwman et al., 2013). Photo-oxidation produces NO in the stratosphere and leads to the catalytic destruction of ozone, making N_2O an ODS, and it is the only ODS that is still unregulated (Bouwman et al., 2013). Figure 1.1 shows a schematic of the sources and sinks of N_2O. Understanding the relative quantities of each of these sources and sinks is crucial for targeted emissions reductions.

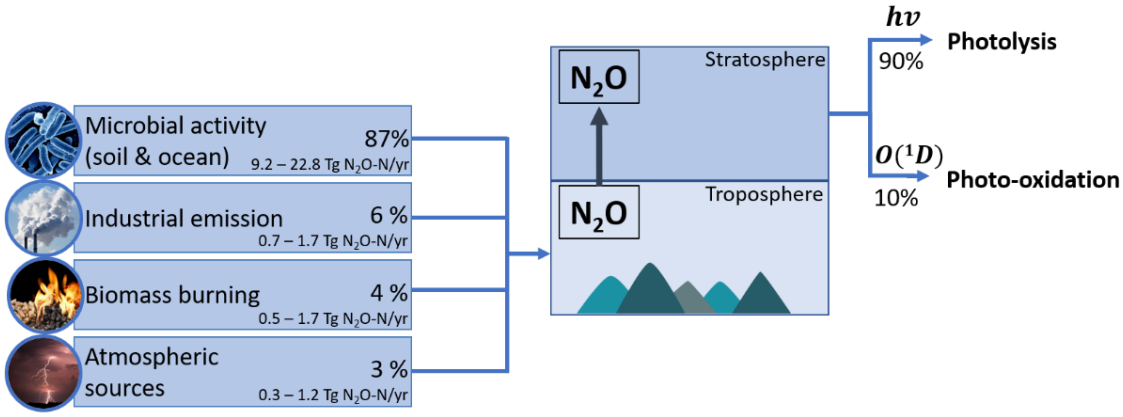

Figure 1.1: Schematic of the sources and sinks of atmospheric N_2O. Emissions estimates are from Bouwman *et al.* (2013).

The isotopic composition of nitrous oxide can be used as an integrated tracer of the different sources and chemical processes that have brought N_2O into and out of the atmosphere (e.g., Kim & Craig, 1993; Park et al., 2011; Rahn & Wahlen, 1997). For example, the global average isotopic composition of nitrous oxide is becoming increasingly depleted in ^{15}N due to the increases in the isotopically depleted sources from fertilizer use. Indeed, the 'isotopic fingerprint' of terrestrial microbial sources stimulated by increasing fertilizer was conclusively identified through measurements of the isotopic composition of N_2O in archived air samples over the time period 1978-2005 (Park et al., 2012). Another example of source attribution using the isotopic fingerprint of N_2O was derived from samples collected during the NASA TC4 mission in which a plume of air influenced by biomass burning was encountered in the upper tropical troposphere; this source was identified based on only a 2‰ change in $\delta^{15}N^{\alpha}$ (the ^{15}N enrichment at the central nitrogen atom position in NNO) and a roughly 5‰ change in ^{18}O, even while the mixing ratio of N_2O increased by only ~1 ppb (Croteau et al., 2010). This study demonstrated that measuring the isotopic composition of atmospheric N_2O can be used as a fingerprint to identify the source of a parcel of air, even when the enhancement in N_2O is relatively small.

Enhancements in N_2O mixing ratios were measured during the HIAPER Pole-to-Pole (HIPPO) flight campaign in January and November 2009 aloft above a wide swath of the tropical and subtropical Pacific Ocean, the source of which could not be conclusively identified (Wofsy, 2011). The possible source of the N_2O enhancements could be biomass burning, microbial emissions that were lofted from the surface, or an *in situ* atmospheric source such as from lightning

production. It was found in a previous flight campaign flown into a thunderstorm that there were N_2O mixing ratio enhancements of at least 10% after lightning discharged (Levine & Shaw, 1983), although some have questioned whether the N_2O was generated in the atmosphere or by some unknown surface reactions occurring after sample collection (Muzio & Kramlich, 1988). Additionally, ground-based lightning studies have also shown N_2O enhancements after lightning discharges (Brandvold et al., 1996). While samples from the HIPPO mission are no longer available and were not measured for isotope compositions, measurements of the N_2O isotope composition would likely have conclusively identified the source of the widespread N_2O enhancements in the upper troposphere. Stratospheric N_2O is enriched in ^{15}N and ^{18}O (Bernath et al., 2017; Kaiser et al., 2006; Park, 2004; Toyoda, 2004; 2018), while emissions from microbial sources are depleted in ^{15}N and ^{18}O (Gil et al., 2017; Ostrom et al., 2007; Park et al., 2011; Pérez et al., 2000; 2001; 2006; Sutka et al., 2003; 2004; 2006; Zhang et al., 2016), and combustion sources like biomass burning emissions are neutral in ^{15}N and slightly enriched in ^{18}O (Ogawa & Yoshida, 2004, 2005). However, the isotopic composition of N_2O generated by lightning in the atmosphere is not known, and only one previous study from our lab has quantified the nitrogen and oxygen isotopic composition of N_2O produced in a corona discharge, simulating atmospheric inter- and intra-cloud lightning (Smith et al., 2021). Chapter 2 builds on this one previous study, with continued measurements of N_2O produced in laboratory simulated lightning using a corona discharge.

The corona discharge has been used previously to investigate chemical production of NO, NO_2, N_2O, and O_3 in lightning in the atmosphere (Bhetanabhotla et al., 1985; Hill et al., 1984; 1988; Sisterson & Liaw, 1990; Smith et al., 2021), and N_2O has previously been measured from corona discharges (Kline et al., 1991; Kossyi et al., 1992; Pavlovich et al., 2013; 2014) and atmospheric lightning (Brandvold et al., 1996; Levine & Shaw, 1983). Even while there is indeed evidence that plasma discharges can lead to enrichments in ^{15}N in N atoms, nitrogen oxides, and N_2O produced in corona discharges (Gorshunov & Gudenko, 2003; Manuccia & Clark, 1976; Nguyen et al., 2011; Smith et al., 2021), only Smith *et al.* (2021) has measured the oxygen isotopic composition. Furthermore, the underlying chemical mechanisms and kinetic isotope effects responsible for the ^{15}N (and ^{18}O) compositions of NO_x, N atoms, and N_2O generated by plasmas in the laboratory and the atmosphere are yet unknown.

Another important gap in the understanding of atmospheric processes that generate N_2O is in in the upper stratosphere and mesosphere, where recent satellite measurements from ACE and MIPAS have found enhancements of N_2O likely due to high energy auroral electron precipitation events (Bernath et al., 2017; B. Funke et al., 2008a; 2008b; Semeniuk et al., 2008) or potentially due to transient luminous events such as sprites or blue jets (Pérez-Invernón et al., 2020). These involve high energy electrons colliding with gases in the mesosphere, leading to electron impact dissociation and excitation, and likely have similar formation processes as the N_2O produced in low-temperature plasma discharges in the laboratory. Thus, insights into the plasma chemistry through the study of low-temperature non-equilibrium discharges, such as those presented in Chapter 2, are also relevant to formation processes and isotope compositions of N_2O in the mesosphere and upper stratosphere. Furthermore, an unexpected source of N_2O through these electron precipitation events in the mesosphere (and transported to the stratosphere) with an unusual isotope composition compared to that induced by photo-destruction processes in the stratosphere would need to be accounted for when using the isotopic composition of N_2O to deduce stratospheric processes (e.g., Garofalo et al.; Park, 2004).

In addition to the atmospheric applications of measurements of the isotopic composition of N_2O generated in plasma discharges, a thorough understanding of the underlying chemistry is important for the design of plasma discharge devices for industrial applications. These non-equilibrium, low-temperature plasmas are not well understood, particularly the chemical mechanisms, which involve electrons, ions, and molecules, and surface-gas interactions. Low temperature plasmas have traditionally been used in semiconductor applications such as etching in microelectronics (e.g., Davydova et al., 2015), and new applications have arisen in the biotechnology sectors. They are now used in treatment of organic waste to reduce nitrogen loss and ammonia emissions (Graves et al., 2019), and in medicine for the disinfection of equipment and wounds (Pei et al., 2014), for reducing head and neck cancer (Metelmann et al., 2018), and for accelerated healing of abrasions (Isbary et al., 2013). These applications are in their infancy, however, and it is critical to understand how the configuration, voltage, and current density, impact the chemical mechanisms, as well as to be able to distinguish gas-phase reactions from reactions at the interfaces, including aqueous chemistry in waste treatment and biological surfaces for medical applications. Coupled with the recent development of machine learning techniques to understand and optimize the parameters and chemical concentration data (e.g., for NO_x, O_3, and N_2O) (Gidon et al., 2019), new measurements of the isotopic composition of these gaseous products in low-temperature plasmas could potentially be a transformative breakthrough in plasma diagnostics.

In Chapter 2, I present new measurements of the nitrogen and oxygen isotopic composition of four different types of plasma discharges with markedly different energies and configurations. These include 28 new samples of corona discharge-generated N_2O at higher pressures than in the previous experiments of Smith *et al.* (2021) and with measured residence times in the corona discharge cell. The samples were generated at pressures from <1 Torr up to 50 Torr and include samples under static flow and under flowing conditions, with measured flow rates up to 124 sccm and residence times spanning 1 to 6 seconds. The values for $\delta^{15}N$-N_2O ranged from ~5‰ to 35‰ versus air N_2, $\delta^{18}O$ from ~9‰ to –67‰ versus air O_2, and $\delta^{15}N^{\alpha}$ from ~6‰ to 83‰ versus air N_2. The highest $\delta^{15}N$ values and lowest $\delta^{18}O$ values are generally observed at higher pressures and shorter residence times. These data are compared to the isotopic composition of N_2O generated in three different types of atmospheric pressure discharges: the surface microdischarge (SMD), plasma flashlight, and pin-to-plane discharge. Each of these plasmas exhibit distinct N_2O isotope compositions, with the atmospheric discharge-generated N_2O enriched in ^{15}N and ^{18}O, but to different amounts, indicating that there are major differences in the chemical mechanisms and kinetics occurring in each of these different plasmas and in the corona discharge. While differences in chemical kinetics and mechanisms are of course expected, based on measurements of the concentrations of various gas phase products (e.g., O_3, NO_x, N_2O) and kinetics modeling using the measured concentrations as constraints, these are the first isotope data comparing plasmas. The large differences in isotope composition promise to provide new diagnostics for plasma chemistry that is complementary and unique to those from concentration measurements.

In addition to the measured N_2O isotope compositions, N_2O concentrations generated in the plasmas were determined, and the rotational and vibrational temperatures were quantified by Optical Emission Spectroscopy (OES). Chemical kinetics models were also created for each type of plasma discharge, with isotopes included, which allowed for sensitivity studies of hypothetical isotope effects and mechanistic differences that may lead to the different N_2O isotope compositions measured. The simulations provide some insights into the operative chemical mechanisms

occurring in each plasma. This study demonstrates that isotope ratio mass spectrometry (IRMS) analysis of plasma-generated species can serve as a powerful diagnostic tool to investigate the underlying chemical mechanisms.

Through our ongoing and planned collaborations to study these low-temperature plasma discharges, there are additional opportunities to provide insights into the chemical mechanisms operative in the different types of plasmas. In the Boering laboratory, continued systematic experiments are ongoing, including studies at higher discharge pressures and at various cell residence times. The continuing optical emission spectroscopy, isotopic analysis, and concentration measurements will provide insights into the chemical mechanisms. The modeling efforts for each discharge will also be expanded to include additional reactions such as ion-molecule reactions and additional sensitivity tests will be performed, particularly to investigate the oxygen isotopic composition of N_2O. The atmospheric pressure plasma discharges will continue to be analyzed over different operation times and current densities. The ongoing collaboration across the UC Berkeley College of Chemistry will allow for the measurement of two additional discharges, the plasma jet and pin-to-pin plasma. In the longer term, measurements of the isotopic composition of NO_x can be analyzed (e.g., Fibiger et al., 2014) and will be useful for this analysis and numerous additional plasma applications related to nitrogen fixation in fertilizers and with plasma-catalyst interactions. These can be combined with high fidelity physics models (e.g., Gidon et al., 2019) to optimize experiments and thus continuing to provide insights into chemical kinetics to allow for better plasma design and control of the chemistry for each application.

1.2 Vertical profiles of $\Delta^{14}C$-CO_2 from the NASA ATom mission (Chapter 3)

Radiocarbon is produced in the lower stratosphere and extratropical upper troposphere by cosmic rays and has served as an important tracer of a number of processes in the Earth system. For example, it has been used to understand the carbon cycle including partitioning between the atmosphere, biosphere, and oceans (e.g., Graven, 2015; Levin et al., 2003; 2010; Randerson et al., 2002; Turnbull et al., 2011). Inverse models of $\Delta^{14}C$-CO_2 in the troposphere are used to constrain the sources and sinks of CO_2, including empirical estimates of regional and global fossil fuel emissions (Basu et al., 2016; 2020; Suess, 1955). Recent work from the Boering group showed that precise measurements of $\Delta^{14}C$-CO_2 on small atmospheric samples using accelerator mass spectrometry (AMS) provide important constraints on stratospheric transport and stratosphere-troposphere (S-T) exchange (Garofalo et al.; Kanu et al., 2016). Current interest in quantifying the stratospheric circulation comes from General Circulation Models (GCMs) simulating the stratospheric circulation under future climate change scenarios and predicting an acceleration of the Brewer-Dobson Circulation (reviewed in Butchart, 2014; e.g., Rind et al., 1990; Wang & Huang, 2020). Such an acceleration would increase the transport of water vapor into the stratosphere, further accelerating climate change (Dessler et al., 2013; Solomon et al., 2010), and potentially having significant impacts on the recovery of the Antarctic ozone hole (Shepherd, 2008). An acceleration of the Brewer-Dobson Circulation also has the potential to increase the transport of ozone from the stratosphere to the troposphere, impacting air quality (Rind et al., 1990). These predictions have not been confirmed due to lack of regular sampling of tracers in the stratosphere that can inform changes in the transport timescales (e.g., CO_2 and SF_6), so adding radiocarbon measurements to future tracer measurement campaigns may add additional information on the rates and characteristics of any changes in the Brewer-Dobson circulation (e.g., Hall & Waugh, 2000; Kanu et al., 2016).

In addition to informing stratospheric transport and strat-trop exchange, measurements of radiocarbon in the stratosphere can be used to estimate the cosmogenic ^{14}C production rate (Kanu et al., 2016). This can be calculated entirely empirically from the measured $\Delta^{14}C\text{-}CO_2$:N_2O relationship (Plumb & Ko, 1992), which is twice the global annual mean net $\Delta^{14}CO_2$ flux from the stratosphere to the troposphere (Kanu et al., 2016). Radiocarbon production in the stratosphere is influenced by solar activity which modulates the cosmic ray flux over the 11-year solar cycle (e.g., Jöckel et al., 1999), and is challenging to calculate through other methods, such as analysis of carbon reservoirs and exchange rates (Levin et al., 2010) or physics calculations (e.g., Kovaltsov et al., 2012). The cosmogenic radiocarbon production rate, and the modulation by the solar cycle, is needed for carbon cycle studies, that seek to understand global carbon reservoirs and the transfer rates between them as well as to infer regional fossil fuel emissions (e.g., Graven, 2015; LaFranchi et al., 2016; Levin et al., 2003; 2010; Randerson et al., 2002; Riley et al., 2008).

In Chapter 3, I present measurements of $\Delta^{14}C\text{-}CO_2$ from 46 whole air samples collected aboard the NASA DC-8 aircraft during the fourth Atmospheric Tomography (ATom-4) mission. This deployment occurred in May 2018 and spanned latitudes of 62 to 69°N and altitudes of 183 to 12,079 m, with a maximum potential temperature of 366K in the northern hemisphere, and 57 to 81°S and 186 to 11,485 m, with a maximum 350K in the southern hemisphere. This dataset provides the first near-simultaneous high latitude vertical profiles of $\Delta^{14}C\text{-}CO_2$ across the tropopause in both hemispheres, allowing for new insights into the dynamics and mixing of the upper troposphere and lower stratosphere, and providing new information for inverse models that constrain sources and sinks of CO_2. Notably, an offset in lowermost stratospheric $\Delta^{14}C\text{-}CO_2$ values -8 ± 1‰ is observed between the northern and southern hemispheres, and proposed reasons for this offset are discussed. These include differences in the amounts of isentropic transport into the lowermost stratosphere from the subtropical troposphere, the magnitudes of downwelling from the overworld (θ>380K), the northern and southern hemispheric $\Delta^{14}C\text{-}CO_2$ values in the upper troposphere, or some combination of these factors. These new measurements are also used to calculate global annual mean ^{14}C production rates, and these are compared to past missions, including SEAC^{4}RS (2013), DC-3 (2012), Pre-AVE (2004), SOLVE (2000), POLARIS (1997), and balloon flights in 2003, 2004, and 2005 (Garofalo et al.). The ^{14}C production rates calculated from ATom-4 data demonstrate that those from measurements of $\Delta^{14}C\text{-}CO_2$:N_2O in the lowermost stratosphere are not robust due to substantial mixing in of new air from the troposphere. Future sampling missions seeking to calculate ^{14}C production rates and global net vertical fluxes using the Plumb (2007) approach must use stratospheric balloons or high-altitude aircraft campaigns to collect samples above θ=380K, and these are needed to conclusively address if there are changes to the Brewer Dobson circulation due to climate change and how those will impact the recovery of the ozone hole.

1.3 Isotope effects and the atmosphere (Chapter 4)

Early investigations using stable isotopes date back to the late 1930s and 1940s (Bigeleisen & Mayer, 1947; Urey, 1947), and have since enabled and inspired inquiry across a wide range of Earth and planetary science and in the use of isotopes to understand the underlying physical and chemical mechanisms of processes in the Earth System, including those presented in Chapters 2 and 3. In Chapter 4, I present a review of isotope effects relevant to our understanding of the atmosphere from a physical chemistry point of view. Isotope composition measurements have proven useful due to the fact that reaction rates change upon the substitution of a heavy, rare

isotope for a light, common isotope in a molecule, and therefore, measurements of how isotope distributions change between reactants and products can be used to elucidate reaction mechanisms and chemical reaction histories. In Earth and planetary sciences, measurement of the isotopic composition allows for understanding of the reactants and transformations that have occurred where only products remain, and there would otherwise be too little information. These measurements, for example, of tree rings, corals, ice cores, and sedimentary rocks, combined with modeling, provide insights and constraints. Over the past decades, the use of isotope composition measurements to understand atmospheric processes has advanced the understanding of climate change, air pollution, and paleoclimates. While many equilibrium and kinetic isotope effects relevant to the Earth system can be estimated using statistical mechanics, in a few cases the reactions are more complicated, discussed further below.

In Chapter 4, I present an overview of interesting isotope effects relevant to the atmosphere and the remaining outstanding questions for which physical chemists can contribute their expertise through needed experiments and theory. I begin by outlining the instrumentation used to analyze isotope compositions at natural abundances, the terminology used to describe mass-dependent, mass-independent, and non-mass dependent isotope effects, and the notation used to quantify isotope compositions. I then discuss three main topical areas of isotope effects relevant to atmospheric chemistry and climate including: non-mass dependent oxygen isotope effects, more traditional (but still "under-determined") normal and inverse kinetic isotope effects in atmospheric trace gases such as CH_4, H_2, and N_2O, and new questions raised by the recent advances in measuring multiply isotopically-substituted species – so-called "clumped isotope" measurements. A brief summary of each topic area is included below.

The section on mass-independent (or 'non-mass-dependent') oxygen isotope effects, abbreviated as "O-MIF", includes a discussion of the mass-independent ozone formation reaction that occurs in the atmosphere and in the laboratory, leading to ozone that is equally enriched in ^{17}O and ^{18}O relative to the common isotope ^{16}O, discovered nearly 40 years ago by Thiemens and Heidenreich (Thiemens & Heidenreich, 1983). Even after decades of study, the chemical physics of the underlying "O-MIF" mechanism in ozone formation is still unknown but remains crucial for our understanding of the current and past atmosphere because the O-MIF signal in ozone is photochemically transferred to a number of other oxygen-containing species that serve as interesting tracers of atmospheric chemistry and climate on annual to decadal to millennial and even billion-year time scales. I first provide some brief insights into the relevant experimental and theoretical studies that have been performed to date, and that remain important. Then I discuss promising current areas of investigation for the ozone formation reaction and transfer of the ^{17}O MIF anomaly to other species, including stratospheric and tropospheric CO_2, O_2 in the current and past atmosphere, nitrates, and sulfates, and the applications of these measurements in Earth science. The one other "robustly non-mass-dependent" species – carbon monoxide (CO) produced from the reaction of CO with the hydroxyl radical (OH) is also briefly summarized.

The section on normal and inverse kinetic isotopes highlights measurements of the isotopic composition of trace gases CH_4, H_2, N_2O, and reactive nitrogen species in the atmosphere, and the current understanding of kinetic and photolysis isotope effects resulting in their observed isotopic compositions. Methane sources and sinks can be studied using isotopic composition (e.g., Quay et al., 1999), but more interesting to physical chemists are the isotope effects that exist in the sink reactions in the stratosphere through reactions with Cl, OH, and $O(^1D)$. Isotope effects involving

molecular hydrogen occur in the formation and destruction reactions. Hydrogen in the atmosphere is produced when CH_4 is oxidized and is destroyed through reactions with OH, both of which have distinct isotope effects. Other sources of H_2 include biomass burning and fossil fuel combustion, and it is also removed from the atmosphere through uptake by soils (e.g., Gerst & Quay, 2001). In many cases noted, additional experimental and theoretical work is needed to for a more robust understanding of various KIEs or photolysis isotope effects over a range of atmospheric conditions. Some examples – particularly those relevant for other chapters of this dissertation – include isotope effects in plasmas relevant for the isotopic composition of atmospheric N_2O, NO_x, NH_3, and HNO_3. In short, while quantification of N_2O sources and sinks for emissions reductions has benefited from isotope analysis, new questions have arisen, such as the quantification of a newly confirmed in situ source of N_2O in the mesosphere (e.g., Bernath et al., 2017; Semeniuk et al., 2008). Further, recent advances in the measurement of the isotopic composition of reactive nitrogen species such as NO_x, NH_3, HNO_3, and HONO will allow further investigation of the chemical mechanisms of the reactions that involve these species and quantify the sources – both in the troposphere and in low temperature non-equilibrium plasmas. While extensive progress has been made in understanding atmospheric processes involving these trace gases over the past three decades, there are still questions to be answered, particularly in the underlying physical chemistry over a range of atmospheric conditions.

The section on clumped isotopes – that is, multiply isotopically substituted species, such as $^{13}C^{18}O^{16}O$ or $^{13}CH_3D$ – highlights the recent development of high resolution gas source isotope ratio mass spectrometry (e.g., Eiler et al., 2013; Young et al., 2016) that enable measurements of these species at natural abundances for the first time. These new measurement capabilities are, for example, a new means of differentiating sources and sinks that may be similar in their singly-substituted isotopic composition but show a different isotopic fingerprint for the clumped isotopes. Measurements of the clumped isotopes of CO_2, O_2, CH_4, H_2, N_2O, N_2, and ethane can inform atmospheric sources and sinks. To make progress in their application to the atmosphere and climate, the new measurements will need to be accompanied by laboratory kinetics and photochemical experiments and theoretical studies to elucidate the underlying fundamental isotope effects. Finally, I note that, while synthetic chemists have used isotope enrichment to elucidate chemical mechanisms through primary and secondary isotope effects, the ability to measure multiply-substituted isotope species at natural abundances opens up this capability to the Earth and planetary sciences and, indeed, makes it easier for chemists to measure isotope effects as well and to compare with theoretical predictions.

Overall, the goal of Chapter 4 is to provide updates to past reviews on this topic (e.g., Brenninkmeijer et al., 2003; Brinjikji & Lyons, 2021; Johnson et al., 2002; Kaye, 1987; Mauersberger et al., 2005; Ono, 2017; Thiemens, 2006; Thiemens et al., 2012; Thiemens & Lin, 2019; Weston, 2006; Zhao et al., 2021) and present information clearly and concisely such that it can serve as an introduction to the field for new researchers. It also highlights the areas in which theoretical and experimental physical chemists can contribute to our understanding of the underlying physics and chemistry that occurs in the atmosphere.

References

Basu, S., Lehman, S. J., Miller, J. B., Andrews, A. E., Sweeney, C., Gurney, K. R., Xu, X., Southon, J., & Tans, P. P. (2020). Estimating US fossil fuel CO_2 emissions from measurements of ^{14}C in atmospheric CO_2. *Proceedings of the National Academy of Sciences*, *117*(24), 13300-13307. https://doi.org/10.1073/pnas.1919032117

Basu, S., Miller, J. B., & Lehman, S. (2016). Separation of biospheric and fossil fuel fluxes of CO_2 by atmospheric inversion of CO_2 and $^{14}CO_2$ measurements: Observation System Simulations. *Atmos. Chem. Phys.*, *16*(9), 5665-5683. https://doi.org/10.5194/acp-16-5665-2016

Bernath, P. F., Yousefi, M., Buzan, E., & Boone, C. D. (2017). A Near-Global Atmospheric Distribution of N_2O Isotopologues. *Geophysical Research Letters*, *44*(20), 10,735-710,743. https://doi.org/10.1002/2017gl075122

Bhetanabhotla, M. N., Crowell, B. A., Coucouvinos, A., Hill, R. D., & Rinker, R. G. (1985). Simulation of trace species production by lightning and corona discharge in moist air. *Atmospheric Environment (1967)*, *19*(9), 1391-1397. https://doi.org/https://doi.org/10.1016/0004-6981(85)90276-8

Bigeleisen, J., & Mayer, M. G. (1947). Calculation of Equilibrium Constants for Isotopic Exchange Reactions. *The Journal of Chemical Physics*, *15*(5), 261-267. https://doi.org/10.1063/1.1746492

Bouwman, L., Daniel, J. S., Davidson, E. A., de Klein, C., Holland, E., Ju, X., Kanter, D., Oenema, O., Ravishankara, A., & Skiba, U. M. (2013). *Drawing down N_2O to protect climate and the ozone layer. A UNEP Synthesis Report*. United Nations Environment Programme (UNEP).

Brandvold, D. K., Martinez, P., & Hipsh, R. (1996). Field measurements of O_3 and N_2O produced from corona discharge. *Atmospheric Environment*, *30*(6), 973-976. https://doi.org/https://doi.org/10.1016/1352-2310(95)00234-0

Brenninkmeijer, C. A. M., Janssen, C., Kaiser, J., Röckmann, T., Rhee, T. S., & Assonov, S. S. (2003). Isotope Effects in the Chemistry of Atmospheric Trace Compounds. *Chemical Reviews*, *103*(12), 5125-5162. https://doi.org/10.1021/cr020644k

Brinjikji, M., & Lyons, J. R. (2021). Mass-Independent Fractionation of Oxygen Isotopes in the Atmosphere. *Reviews in Mineralogy and Geochemistry*, *86*(1), 197-216. https://doi.org/10.2138/rmg.2021.86.06

Butchart, N. (2014). The Brewer-Dobson circulation. *Reviews of Geophysics*, *52*(2), 157-184. https://doi.org/https://doi.org/10.1002/2013RG000448

Croteau, P., Atlas, E. L., Schauffler, S. M., Blake, D. R., Diskin, G. S., & Boering, K. A. (2010). Effect of local and regional sources on the isotopic composition of nitrous oxide in the tropical free troposphere and tropopause layer. *Journal of Geophysical Research: Atmospheres*, *115*(D10). https://doi.org/https://doi.org/10.1029/2009JD013117

Davidson, E. A. (2009). The contribution of manure and fertilizer nitrogen to atmospheric nitrous oxide since 1860. *Nature Geoscience*, *2*(9), 659-662. https://doi.org/10.1038/ngeo608

Davydova, A., Despiau-Pujo, E., Cunge, G., & Graves, D. B. (2015). Etching mechanisms of graphene nanoribbons in downstream H_2 plasmas: insights from molecular dynamics simulations. *Journal of Physics D: Applied Physics*, *48*(19), 195202. https://doi.org/10.1088/0022-3727/48/19/195202

Dessler, A. E., Schoeberl, M. R., Wang, T., Davis, S. M., & Rosenlof, K. H. (2013). Stratospheric water vapor feedback. *Proceedings of the National Academy of Sciences*, *110*(45), 18087-18091. https://doi.org/10.1073/pnas.1310344110

Eiler, J. M., Clog, M., Magyar, P., Piasecki, A., Sessions, A., Stolper, D., Deerberg, M., Schlueter, H.-J., & Schwieters, J. (2013). A high-resolution gas-source isotope ratio mass spectrometer. *International Journal of Mass Spectrometry*, *335*, 45-56. https://doi.org/10.1016/j.ijms.2012.10.014

Fibiger, D. L., Hastings, M. G., Lew, A. F., & Peltier, R. E. (2014). Collection of NO and NO_2 for Isotopic Analysis of NO_x Emissions. *Analytical Chemistry*, *86*(24), 12115-12121. https://doi.org/10.1021/ac502968e

Funke, B., García-Comas, M., López-Puertas, M., Glatthor, N., Stiller, G. P., Von Clarmann, T., Semeniuk, K., & McConnell, J. C. (2008a). Enhancement of N_2O during the October–November 2003 solar proton events. *Atmospheric Chemistry and Physics*, *8*(14), 3805-3815. https://doi.org/10.5194/acp-8-3805-2008

Funke, B., López-Puertas, M., Garcia-Comas, M., Stiller, G., Clarmann, T. v., & Glatthor, N. (2008b). Mesospheric N_2O enhancements as observed by MIPAS on Envisat during the polar winters in 2002–2004. *Atmospheric Chemistry and Physics*, *8*(19), 5787-5800.

Garofalo, L., Kanu, A., Hoag, K. J., & Boering, K. A. The Effects of Stratospheric Chemistry and Transport on the Isotopic Compositions of Long-Lived Gases Measured at Earth's Surface. In *Advances in Atmospheric Chemistry* (pp. 529-587). https://doi.org/10.1142/9789813271838_0007

Gerst, S., & Quay, P. (2001). Deuterium component of the global molecular hydrogen cycle. *Journal of Geophysical Research: Atmospheres*, *106*(D5), 5021-5031. https://doi.org/10.1029/2000jd900593

Gidon, D., Pei, X., Bonzanini, A. D., Graves, D. B., & Mesbah, A. (2019). Machine Learning for Real-Time Diagnostics of Cold Atmospheric Plasma Sources. *IEEE Transactions on Radiation and Plasma Medical Sciences*, *3*(5), 597-605. https://doi.org/10.1109/TRPMS.2019.2910220

Gil, J., Pérez, T., Boering, K., Martikainen, P. J., & Biasi, C. (2017). Mechanisms responsible for high N2O emissions from subarctic permafrost peatlands studied via stable isotope techniques. *Global Biogeochemical Cycles*, *31*(1), 172-189. https://doi.org/https://doi.org/10.1002/2015GB005370

Gorshunov, N. M., & Gudenko, S. V. (2003). Enrichment of the nitrogen atomic component with the ^{15}N isotope in a post-discharge zone. *Journal of Experimental and Theoretical Physics Letters*, *77*(4), 162-166. https://doi.org/10.1134/1.1571874

Graven, H. D. (2015). Impact of fossil fuel emissions on atmospheric radiocarbon and various applications of radiocarbon over this century. *Proceedings of the National Academy of Sciences*, *112*(31), 9542-9545. https://doi.org/10.1073/pnas.1504467112

Graves, D. B., Bakken, L. B., Jensen, M. B., & Ingels, R. (2019). Plasma Activated Organic Fertilizer. *Plasma Chemistry and Plasma Processing*, *39*(1), 1-19. https://doi.org/10.1007/s11090-018-9944-9

Hall, T. M., & Waugh, D. W. (2000). Stratospheric residence time and its relationship to mean age. *Journal of Geophysical Research: Atmospheres*, *105*(D5), 6773-6782. https://doi.org/https://doi.org/10.1029/1999JD901096

Hill, R. D., Rahmim, I., & Rinker, R. G. (1988). Experimental study of the production of nitric oxide, nitrous oxide, and ozone in a simulated atmospheric corona. *Industrial & Engineering Chemistry Research*, *27*(7), 1264-1269. https://doi.org/10.1021/ie00079a029

Hill, R. D., Rinker, R. G., & Coucouvinos, A. (1984). Nitrous oxide production by lightning. *Journal of Geophysical Research: Atmospheres*, *89*(D1), 1411-1421. https://doi.org/https://doi.org/10.1029/JD089iD01p01411

Intergovernmental Panel on Climate, C. (2014). *Climate Change 2013 – The Physical Science Basis: Working Group I Contribution to the Fifth Assessment Report of the Intergovernmental Panel on Climate Change*. Cambridge University Press. https://doi.org/DOI: 10.1017/CBO9781107415324

Isbary, G., Zimmermann, J. L., Shimizu, T., Li, Y. F., Morfill, G. E., Thomas, H. M., Steffes, B., Heinlin, J., Karrer, S., & Stolz, W. (2013). Non-thermal plasma—More than five years of clinical experience. *Clinical Plasma Medicine*, *1*(1), 19-23. https://doi.org/https://doi.org/10.1016/j.cpme.2012.11.001

Jöckel, P., Lawrence, M. G., & Brenninkmeijer, C. A. M. (1999). Simulations of cosmogenic^{14}CO using the three-dimensional atmospheric model MATCH: Effects of ^{14}C production distribution and the solar cycle. *Journal of Geophysical Research: Atmospheres*, *104*(D9), 11733-11743. https://doi.org/10.1029/1999jd900061

Johnson, M. S., Feilberg, K. L., Hessberg, P. V., & Nielsen, O. J. (2002). Isotopic processes in atmospheric chemistry. *Chemical Society Reviews*, *31*(6), 313-323. https://doi.org/10.1039/b108011n

Kaiser, J., Engel, A., Borchers, R., & Röckmann, T. (2006). Probing stratospheric transport and chemistry with new balloon and aircraft observations of the meridional and vertical N_2O isotope distribution. *Atmos. Chem. Phys.*, *6*(11), 3535-3556. https://doi.org/10.5194/acp-6-3535-2006

Kanu, A. M., Comfort, L. L., Guilderson, T. P., Cameron-Smith, P. J., Bergmann, D. J., Atlas, E. L., Schauffler, S., & Boering, K. A. (2016). Measurements and modeling of contemporary radiocarbon in the stratosphere. *Geophysical Research Letters*, *43*(3), 1399-1406. https://doi.org/https://doi.org/10.1002/2015GL066921

Kaye, J. A. (1987). Mechanisms and observations for isotope fractionation of molecular species in planetary atmospheres. *Reviews of Geophysics*, *25*(8), 1609. https://doi.org/10.1029/rg025i008p01609

Kim, K.-R., & Craig, H. (1993). Nitrogen-15 and Oxygen-18 Characteristics of Nitrous Oxide: A Global Perspective. *Science*, *262*(5141), 1855-1857. https://doi.org/10.1126/science.262.5141.1855

Kline, L. E., Partlow, W. D., Young, R. M., Mitchell, R. R., & Congedo, T. V. (1991). Diagnostics and modeling of RF discharge dissociation in N_2O. *IEEE Transactions on Plasma Science*, *19*(2), 278-285. https://doi.org/10.1109/27.106825

Kossyi, I. A., Kostinsky, A. Y., Matveyev, A. A., & Silakov, V. P. (1992). Kinetic scheme of the non-equilibrium discharge in nitrogen-oxygen mixtures. *Plasma Sources Science and Technology*, *1*(3), 207-220. https://doi.org/10.1088/0963-0252/1/3/011

Kovaltsov, G. A., Mishev, A., & Usoskin, I. G. (2012). A new model of cosmogenic production of radiocarbon ^{14}C in the atmosphere. *Earth and Planetary Science Letters*, *337-338*, 114-120. https://doi.org/https://doi.org/10.1016/j.epsl.2012.05.036

LaFranchi, B. W., McFarlane, K. J., Miller, J. B., Lehman, S. J., Phillips, C. L., Andrews, A. E., Tans, P. P., Chen, H., Liu, Z., Turnbull, J. C., Xu, X., & Guilderson, T. P. (2016). Strong

regional atmospheric ^{14}C signature of respired CO_2 observed from a tall tower over the midwestern United States. *Journal of Geophysical Research: Biogeosciences*, *121*(8), 2275-2295. https://doi.org/https://doi.org/10.1002/2015JG003271

Levin, I., Kromer, B., Schmidt, M., & Sartorius, H. (2003). A novel approach for independent budgeting of fossil fuel CO_2 over Europe by $^{14}CO_2$ observations. *Geophysical Research Letters*, *30*(23). https://doi.org/https://doi.org/10.1029/2003GL018477

Levin, I., Naegler, T., Kromer, B., Diehl, M., Francey, R., Gomez-Pelaez, A., Steele, P., Wagenbach, D., Weller, R., & Worthy, D. (2010). Observations and modelling of the global distribution and long-term trend of atmospheric $^{14}CO_2$. *Tellus B: Chemical and Physical Meteorology*, *62*(1), 26-46. https://doi.org/10.1111/j.1600-0889.2009.00446.x

Levine, J. S., & Shaw, E. F. (1983). In situ aircraft measurements of enhanced levels of N_2O associated with thunderstorm lightning. *Nature*, *303*(5915), 312-314. https://doi.org/10.1038/303312a0

Manuccia, T. J., & Clark, M. D. (1976). Enrichment of N^{15} by chemical reactions in a glow discharge at 77 °K. *Applied Physics Letters*, *28*(7), 372-374. https://doi.org/10.1063/1.88785

Mauersberger, K., Krankowsky, D., Janssen, C., & Schinke, R. (2005). Assessment of the ozone isotope effect. In *Advances in Atomic, Molecular, and Optical Physics* (Vol. 50, pp. 1-54). Elsevier. https://doi.org/10.1016/s1049-250x(05)80006-0

Metelmann, H.-R., Seebauer, C., Rutkowski, R., Schuster, M., Bekeschus, S., & Metelmann, P. (2018). Treating cancer with cold physical plasma: On the way to evidence-based medicine. *Contributions to Plasma Physics*, *58*(5), 415-419. https://doi.org/https://doi.org/10.1002/ctpp.201700085

Miller, S. M., Kort, E. A., Hirsch, A. I., Dlugokencky, E. J., Andrews, A. E., Xu, X., Tian, H., Nehrkorn, T., Eluszkiewicz, J., Michalak, A. M., & Wofsy, S. C. (2012). Regional sources of nitrous oxide over the United States: Seasonal variation and spatial distribution. *Journal of Geophysical Research: Atmospheres*, *117*(D6). https://doi.org/https://doi.org/10.1029/2011JD016951

The Montreal Protocol. United Nations Environment Programme. Retrieved 7/28/2021 from https://www.unep.org/ozonaction/who-we-are/about-montreal-protocol

Muzio, L. J., & Kramlich, J. C. (1988). An artifact in the measurement of N_2O from combustion sources. *Geophysical Research Letters*, *15*(12), 1369-1372. https://doi.org/https://doi.org/10.1029/GL015i012p01369

National Academies of Sciences, E., & Medicine. (2016). *The Future of Atmospheric Chemistry Research: Remembering Yesterday, Understanding Today, Anticipating Tomorrow*. The National Academies Press. https://doi.org/doi:10.17226/23573

Nguyen, N. T. A., Ichikawa, M., Mori, S., & Suzuki, M. (2011). Nitrogen Isotope Separation by Plasma Chemical Reaction in N_2-O_2 DC Glow Discharge. Journal of Chemical Engineering of Japan, *44*(8), 572-576. https://doi.org/10.1252/jcej.10we225

Ogawa, M., & Yoshida, N. (2004). Stable isotope fractionation of nitrous oxide during thermal decomposition and reduction processes. *Journal of Geophysical Research: Atmospheres*, *109*(D19). https://doi.org/https://doi.org/10.1029/2004JD004652

Ogawa, M., & Yoshida, N. (2005). Nitrous oxide emission from the burning of agricultural residue. *Atmospheric Environment*, *39*(19), 3421-3429. https://doi.org/https://doi.org/10.1016/j.atmosenv.2005.01.059

Ono, S. (2017). Photochemistry of Sulfur Dioxide and the Origin of Mass-Independent Isotope Fractionation in Earth's Atmosphere. *Annual Review of Earth and Planetary Sciences*, *45*(1), 301-329. https://doi.org/10.1146/annurev-earth-060115-012324

Ostrom, N. E., Pitt, A., Sutka, R., Ostrom, P. H., Grandy, A. S., Huizinga, K. M., & Robertson, G. P. (2007). Isotopologue effects during N_2O reduction in soils and in pure cultures of denitrifiers. *Journal of Geophysical Research: Biogeosciences*, *112*(G2). https://doi.org/https://doi.org/10.1029/2006JG000287

Park, S. (2004). Measurements of N_2O isotopologues in the stratosphere: Influence of transport on the apparent enrichment factors and the isotopologue fluxes to the troposphere. *Journal of Geophysical Research*, *109*(D1). https://doi.org/10.1029/2003jd003731

Park, S., Croteau, P., Boering, K. A., Etheridge, D. M., Ferretti, D., Fraser, P. J., Kim, K. R., Krummel, P. B., Langenfelds, R. L., Van Ommen, T. D., Steele, L. P., & Trudinger, C. M. (2012). Trends and seasonal cycles in the isotopic composition of nitrous oxide since 1940. *Nature Geoscience*, *5*(4), 261-265. https://doi.org/10.1038/ngeo1421

Park, S., Pérez, T., Boering, K. A., Trumbore, S. E., Gil, J., Marquina, S., & Tyler, S. C. (2011). Can N_2O stable isotopes and isotopomers be useful tools to characterize sources and microbial pathways of N_2O production and consumption in tropical soils? *Global Biogeochemical Cycles*, *25*(1). https://doi.org/https://doi.org/10.1029/2009GB003615

Pavlovich, M. J., Clark, D. S., & Graves, D. B. (2014). Quantification of air plasma chemistry for surface disinfection. *Plasma Sources Science and Technology*, *23*(6), 065036. https://doi.org/10.1088/0963-0252/23/6/065036

Pavlovich, M. J., Sakiyama, Y., Clark, D. S., & Graves, D. B. (2013). Antimicrobial Synergy Between Ambient-Gas Plasma and UVA Treatment of Aqueous Solution. *Plasma Processes and Polymers*, *10*(12), 1051-1060. https://doi.org/https://doi.org/10.1002/ppap.201300065

Pei, X., Liu, J., Xian, Y., & Lu, X. (2014). A battery-operated atmospheric-pressure plasma wand for biomedical applications. *Journal of Physics D: Applied Physics*, *47*(14), 145204. https://doi.org/10.1088/0022-3727/47/14/145204

Pérez-Invernón, F. J., Malagón-Romero, A., Gordillo-Vázquez, F. J., & Luque, A. (2020). The Contribution of Sprite Streamers to the Chemical Composition of the Mesosphere-Lower Thermosphere. *Geophysical Research Letters*, *47*(14), e2020GL088578. https://doi.org/https://doi.org/10.1029/2020GL088578

Pérez, T., Garcia-Montiel, D., Trumbore, S., Tyler, S., Camargo, P. d., Moreira, M., Piccolo, M., & Cerri, C. (2006). Nitrous Oxide Nitrification and Denitrification ^{15}N Enrichment Factors from Amazon Forest Soils. *Ecological Applications*, *16*(6), 2153-2167. https://doi.org/https://doi.org/10.1890/1051-0761(2006)016[2153:NONADN]2.0.CO;2

Pérez, T., Trumbore, S. E., Tyler, S. C., Davidson, E. A., Keller, M., & de Camargo, P. B. (2000). Isotopic variability of N_2O emissions from tropical forest soils. *Global Biogeochemical Cycles*, *14*(2), 525-535. https://doi.org/https://doi.org/10.1029/1999GB001181

Pérez, T., Trumbore, S. E., Tyler, S. C., Matson, P. A., Ortiz-Monasterio, I., Rahn, T., & Griffith, D. W. T. (2001). Identifying the agricultural imprint on the global N_2O budget using stable isotopes. *Journal of Geophysical Research: Atmospheres*, *106*(D9), 9869-9878. https://doi.org/https://doi.org/10.1029/2000JD900809

Plumb, R. A. (2007). Tracer interrelationships in the stratosphere. *Reviews of Geophysics*, *45*(4). https://doi.org/https://doi.org/10.1029/2005RG000179

Plumb, R. A., & Ko, M. K. W. (1992). Interrelationships between mixing ratios of long-lived stratospheric constituents. *Journal of Geophysical Research: Atmospheres*, *97*(D9), 10145-10156. https://doi.org/https://doi.org/10.1029/92JD00450

Quay, P., Stutsman, J., Wilbur, D., Snover, A., Dlugokencky, E., & Brown, T. (1999). The isotopic composition of atmospheric methane [https://doi.org/10.1029/1998GB900006]. *Global Biogeochemical Cycles*, *13*(2), 445-461. https://doi.org/https://doi.org/10.1029/1998GB900006

Rahn, T., & Wahlen, M. (1997). Stable Isotope Enrichment in Stratospheric Nitrous Oxide. *Science*, *278*(5344), 1776-1778. https://doi.org/10.1126/science.278.5344.1776

Randerson, J. T., Enting, I. G., Schuur, E. A. G., Caldeira, K., & Fung, I. Y. (2002). Seasonal and latitudinal variability of troposphere $\Delta^{14}CO_2$: Post bomb contributions from fossil fuels, oceans, the stratosphere, and the terrestrial biosphere. *Global Biogeochemical Cycles*, *16*(4), 59-51-59-19. https://doi.org/https://doi.org/10.1029/2002GB001876

Riley, W. J., Hsueh, D. Y., Randerson, J. T., Fischer, M. L., Hatch, J. G., Pataki, D. E., Wang, W., & Goulden, M. L. (2008). Where do fossil fuel carbon dioxide emissions from California go? An analysis based on radiocarbon observations and an atmospheric transport model. *Journal of Geophysical Research: Biogeosciences*, *113*(G4). https://doi.org/https://doi.org/10.1029/2007JG000625

Rind, D., Suozzo, R., Balachandran, N. K., & Prather, M. J. (1990). Climate Change and the Middle Atmosphere. Part I: The Doubled CO_2 Climate. *Journal of the Atmospheric Sciences*, *47*(4), 475-494. https://doi.org/10.1175/1520-0469(1990)047

Röckmann, T., Kaiser, J., Brenninkmeijer, C. A. M., & Brand, W. A. (2003). Gas chromatography/isotope-ratio mass spectrometry method for high-precision position-dependent ^{15}N and ^{18}O measurements of atmospheric nitrous oxide. *Rapid Communications in Mass Spectrometry*, *17*(16), 1897-1908. https://doi.org/https://doi.org/10.1002/rcm.1132

Schumann, U., & Huntrieser, H. (2007). The global lightning-induced nitrogen oxides source. *Atmos. Chem. Phys.*, *7*(14), 3823-3907. https://doi.org/10.5194/acp-7-3823-2007

Semeniuk, K., McConnell, J. C., Jin, J. J., Jarosz, J. R., Boone, C. D., & Bernath, P. F. (2008). N_2O production by high energy auroral electron precipitation. *Journal of Geophysical Research*, *113*(D16). https://doi.org/10.1029/2007jd009690

Shepherd, T. G. (2008). Dynamics, stratospheric ozone, and climate change. *Atmosphere-Ocean*, *46*(1), 117-138. https://doi.org/10.3137/ao.460106

Sisterson, D. L., & Liaw, Y. P. (1990). An evaluation of lightning and corona discharge on thunderstorm air and precipitation chemistry. *Journal of Atmospheric Chemistry*, *10*(1), 83-96. https://doi.org/10.1007/BF01980039

Smith, M. C., Carlstad, J. M., Hunter, P. Q., Randazzo, J., & Boering, K. A. (2021). Nitrous Oxide Formation by Corona Discharge: Isotopic Composition Measurements and Atmospheric Applications. *Journal of Geophysical Research: Atmospheres*, *126*(8). https://doi.org/10.1029/2020jd033927

Solomon, S., Rosenlof, K. H., Portmann, R. W., Daniel, J. S., Davis, S. M., Sanford, T. J., & Plattner, G.-K. (2010). Contributions of Stratospheric Water Vapor to Decadal Changes in the Rate of Global Warming. *Science*, *327*(5970), 1219-1223. https://doi.org/10.1126/science.1182488

Stein, L. Y., & Yung, Y. L. (2003). Production, Isotopic Composition, and Atmospheric Fate of Biologically Produced Nitrous Oxide. *Annual Review of Earth and Planetary Sciences*, *31*(1), 329-356. https://doi.org/10.1146/annurev.earth.31.110502.080901

Suess, H. E. (1955). Radiocarbon Concentration in Modern Wood. *Science*, *122*(3166), 415-417. https://doi.org/10.1126/science.122.3166.415-a

Summary of the Clean Air Act. United States Environmental Protection Agency. Retrieved 7/28/2021 from https://www.epa.gov/laws-regulations/summary-clean-air-act

Sutka, R. L., Ostrom, N. E., Ostrom, P. H., Breznak, J. A., Gandhi, H., Pitt, A. J., & Li, F. (2006). Distinguishing Nitrous Oxide Production from Nitrification and Denitrification on the Basis of Isotopomer Abundances. *Applied and Environmental Microbiology*, *72*(1), 638-644. https://doi.org/doi:10.1128/AEM.72.1.638-644.2006

Sutka, R. L., Ostrom, N. E., Ostrom, P. H., Gandhi, H., & Breznak, J. A. (2003). Nitrogen isotopomer site preference of N_2O produced by Nitrosomonas europaea and Methylococcus capsulatus Bath. *Rapid Communications in Mass Spectrometry*, *17*(7), 738-745. https://doi.org/https://doi.org/10.1002/rcm.968

Sutka, R. L., Ostrom, N. E., Ostrom, P. H., Gandhi, H., & Breznak, J. A. (2004). Nitrogen isotopomer site preference of N_2O produced by Nitrosomonas europaea and Methylococcus capsulatus Bath. *Rapid Communications in Mass Spectrometry*, *18*(12), 1411-1412. https://doi.org/https://doi.org/10.1002/rcm.1482

Thiemens, M. H. (2006). History and Applications of Mass-Independent Isotope Effects. *Annual Review of Earth and Planetary Sciences*, *34*(1), 217-262. https://doi.org/10.1146/annurev.earth.34.031405.125026

Thiemens, M. H., Chakraborty, S., & Dominguez, G. (2012). The Physical Chemistry of Mass-Independent Isotope Effects and Their Observation in Nature. *Annual Review of Physical Chemistry*, *63*(1), 155-177. https://doi.org/10.1146/annurev-physchem-032511-143657

Thiemens, M. H., & Heidenreich, J. E. (1983). The Mass-Independent Fractionation of Oxygen: A Novel Isotope Effect and Its Possible Cosmochemical Implications. *Science*, *219*(4588), 1073-1075. https://doi.org/10.1126/science.219.4588.1073

Thiemens, M. H., & Lin, M. (2019). Use of Isotope Effects To Understand the Present and Past of the Atmosphere and Climate and Track the Origin of Life. *Angewandte Chemie International Edition*, *58*(21), 6826-6844. https://doi.org/https://doi.org/10.1002/anie.201812322

Toyoda, S. (2004). Temporal and latitudinal distributions of stratospheric N_2O isotopomers. *Journal of Geophysical Research*, *109*(D8). https://doi.org/10.1029/2003jd004316

Toyoda, S., Yoshida, N., Morimoto, S., Aoki, S., Nakazawa, T., Sugawara, S., Ishidoya, S., Uematsu, M., Inai, Y., Hasebe, F., Ikeda, C., Honda, H., & Ishijima, K. (2018). Vertical distributions of N_2O isotopocules in the equatorial stratosphere. *Atmos. Chem. Phys.*, *18*(2), 833-844. https://doi.org/10.5194/acp-18-833-2018

Turnbull, J. C., Karion, A., Fischer, M. L., Faloona, I., Guilderson, T., Lehman, S. J., Miller, B. R., Miller, J. B., Montzka, S., Sherwood, T., Saripalli, S., Sweeney, C., & Tans, P. P. (2011). Assessment of fossil fuel carbon dioxide and other anthropogenic trace gas emissions from airborne measurements over Sacramento, California in spring 2009. *Atmos. Chem. Phys.*, *11*(2), 705-721. https://doi.org/10.5194/acp-11-705-2011

Urey, H. C. (1947). The thermodynamic properties of isotopic substances. *Journal of the Chemical Society (Resumed)*, 562. https://doi.org/10.1039/jr9470000562

Wang, Y., & Huang, Y. (2020). Understanding the Atmospheric Temperature Adjustment to CO_2 Perturbation at the Process Level. *Journal of Climate*, *33*(3), 787-803. https://doi.org/10.1175/jcli-d-19-0032.1

Weston, R. E. (2006). When Is an Isotope Effect Non-Mass Dependent? *Journal of Nuclear Science and Technology*, *43*(4), 295-299. https://doi.org/10.1080/18811248.2006.9711092

Wofsy, S. C. (2011). HIAPER Pole-to-Pole Observations (HIPPO): fine-grained, global-scale measurements of climatically important atmospheric gases and aerosols. *Philosophical Transactions of the Royal Society A: Mathematical, Physical and Engineering Sciences*, *369*(1943), 2073-2086. https://doi.org/doi:10.1098/rsta.2010.0313

Young, E. D., Rumble, D., Freedman, P., & Mills, M. (2016). A large-radius high-mass-resolution multiple-collector isotope ratio mass spectrometer for analysis of rare isotopologues of O_2, N_2, CH_4 and other gases. *International Journal of Mass Spectrometry*, *401*, 1-10. https://doi.org/10.1016/j.ijms.2016.01.006

Zhang, W., Li, Y., Xu, C., Li, Q., & Lin, W. (2016). Isotope signatures of N_2O emitted from vegetable soil: Ammonia oxidation drives N_2O production in NH_4^+-fertilized soil of North China. *Scientific Reports*, *6*(1), 29257. https://doi.org/10.1038/srep29257

Zhao, Y., Zhang, Y.-L., & Sun, R. (2021). The mass-independent oxygen isotopic composition in sulfate aerosol-a useful tool to identify sulfate formation: a review. *Atmospheric Research*, *253*, 105447. https://doi.org/https://doi.org/10.1016/j.atmosres.2020.105447

Chapter 2

Analysis of the Isotopic Composition of Nitrous Oxide Generated in Low-temperature Non-Equilibrium Plasmas

2.1 Introduction

Low-temperature non-equilibrium plasmas (NEPs) are systems in which hot electrons and relatively cold neutrals and ions interact to create non-equilibrium distributions of species in excited electronic, vibrational, rotational, and translational states (Fridman, 2008). These species can dissociate and react, generating numerous products. The underlying kinetics and chemical pathways in such plasmas must be understood in order to design effective plasma instrumentation for applications such as semiconductor etching, medicine, and waste treatment. For example, new and potentially transformative applications of NEPs – especially plasma discharges in air – have arisen for nitrogen fixation through the treatment of organic waste to reduce ammonia emissions (Graves et al., 2019), and medical purposes such as disinfection (Pei et al., 2014), reducing head and neck cancer (Metelmann et al., 2018), and healing wounds (Isbary et al., 2013). In addition, these systems are relevant in atmospheric chemistry and space weather, as the reactions occurring are similar to those of low-temperature intra- and inter-cloud lightning discharges in the troposphere and to high energy particle events in the upper stratosphere and lower mesosphere where in-situ generation of N_2O has been detected by the MIPAS and ACE satellites (Bernath et al., 2017; Funke, García-Comas, et al., 2008; Semeniuk et al., 2008).

Previously, experimental investigations of plasma discharges have been largely limited to mass spectrometric and spectroscopic studies of the concentrations of species, combined with chemical kinetics computer simulations. In spite of decades of continuing study, the chemical kinetics of NEPs are arguably still neither well understood nor validated, so novel diagnostics are being sought (National Academies of Sciences & Medicine, 2021). The substitution of a rare, heavy isotope for a common, light isotope – such as ^{15}N for ^{14}N or ^{18}O for ^{16}O – often results in a change in the rate coefficient for a particular reaction. Furthermore, whether a reaction product contains a heavy isotope or not and at which position in the molecule can also be determined, and so the distribution of isotopes in reactants and products can provide additional information on kinetics and reaction pathways than concentrations alone. Before our recent measurements of the nitrogen and oxygen isotopic composition of nitrous oxide (N_2O) produced in a corona discharge (Smith et al., 2021), only four previous studies had investigated the isotopic composition of nitrogen-containing species produced in plasma discharges. Using a magnetic sector mass spectrometer Basov *et al.*, 1974 measured the fractionation of nitrogen in NO formed in a pulsed discharge in N_2 and O_2 and found enrichments of 20,000‰ relative to reactant N_2 (Basov et al., 1974) but follow up studies by Manuccia and Clark, (1976) determined this was likely an artifact due to protonation of NO^+ to HNO by water in the ion source of the mass spectrometer (Manuccia & Clark, 1976). Mannucia and Clark (1976) showed enrichments in ^{15}N of 13% in the sum of nitrogen oxides relative to the reactant N_2 in a pulsed glow discharge in air using traditional mass spectrometry. Gorshunov and Gudenko (2003) showed 30-fold enrichments in ^{15}N atoms in a pulsed discharge in N_2 by electron paramagnetic resonance. Nguyen *et al.,* (2011) used a pulsed discharge in mixtures of N_2 and O_2 to with the goal of enriching ^{15}N through the production of

nitrogen oxides, which were then reduced back to N_2 and measured on a mass spectrometer (Nguyen et al., 2011). While promising in that these earlier studies showed that significant isotope effects exist in NEP chemistry, none of these studies used the tools of modern Isotope Ratio Mass Spectrometry (IRMS) to look systematically and precisely at the isotopic composition of specific reaction products, and no studies we are aware of have considered oxygen isotope effects. Building on our earlier work in Smith *et al.*, (2021), in which we measured by IRMS both large ^{15}N enrichments and large ^{18}O depletions in the N_2O produced in a corona discharge, here we present results for the nitrogen and oxygen isotopic compositions of N_2O generated in 4 types of NEPs in air: corona discharge (CD), plasma flashlight (PF), surface microdischarge (SMD), and pin-to-plane (PP). The isotopic results provide new insights into the chemical mechanisms in the different plasmas under different conditions and demonstrate that performing IRMS measurements at natural abundances on discharge reaction products can serve as a new diagnostic for NEP chemistry.

2.2 Methods

2.2.1 Corona Discharge Sample Generation

The methodology used in this study is discussed in Smith *et al.* (2021), and only a brief summary along with modifications to the apparatus are included here. To generate N_2O, a corona discharge experimental setup is contained within a vacuum manifold, laid out as in Figure 2.1, which is pumped by a turbomolecular pump (CFV100, Alcatel Vacuum Technology) backed by a rotary vane roughing pump (Edwards rotary vacuum pump EM1.5, West Sussex, UK). Highly purified air (Ultra Zero grade, Praxair, Danbury, CT; delivery pressure of 15 psig) is introduced into the vacuum line through a needle valve (Nupro valve M series, Kurt J. Lesker Company) to control the pressure and flow rate of air through the corona discharge region.

The corona discharge is created with a positive electrode of tungsten wire (Saturn industries, Hudson, NY) 100 micrometers in diameter inside a 20 cm long grounded stainless-steel tube, with a volume of 38 cm^3. The corona discharge is powered by a high voltage power supply (MJ10P1550, Glassman High Voltage, High Bridge, NJ) which is controlled by a low voltage power supply (1651A, B&K Precision, Yorba Linda, CA). The low voltage power supply has two 0-10 V outputs that proportionally control the current from 0-1,500 μA and voltage from 0-10 kV of the high voltage power supply. Experiments in this work were conducted at 5 kV and 1,500 μA. The system is grounded and monitored through a picoammeter (6485, Keithley Instruments, Cleveland, OH). The pressure in the plasma region is measured just downstream on a convection gauge (317, MKS Instruments, Andover, MA, calibrated for air) and is monitored throughout the typical 15-minute discharge run.

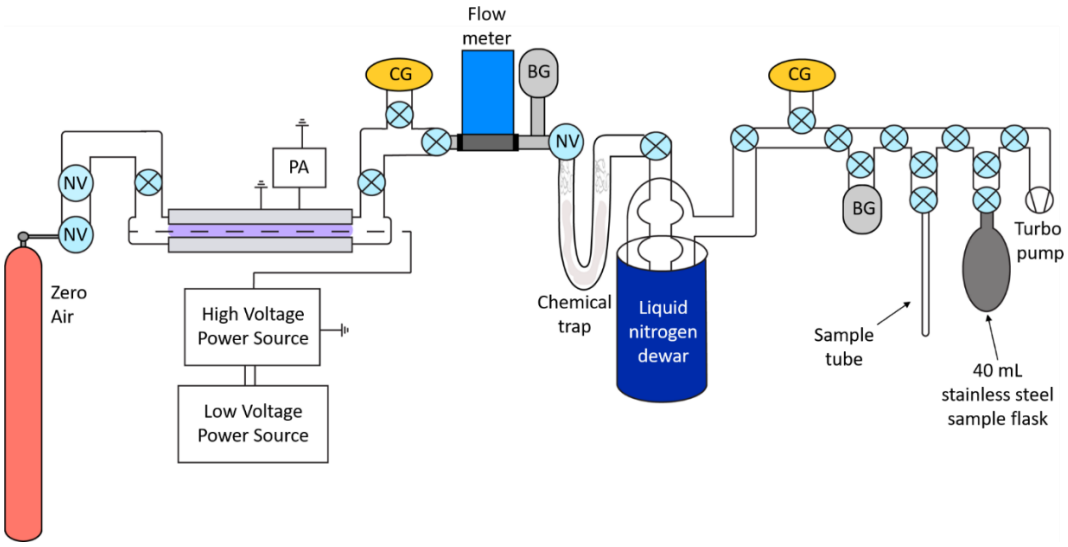

Figure 2.1: Diagram of the corona discharge line used for sample generation, with the discharge cell shown with purple coloration. (PA=picoammeter, NV= needle valve, CG=convection gauge, BG=Baratron capicitance manometer.)

After February 2019, a 200 sccm mass flow meter calibrated for air (MKS Andover, MA) was installed downstream of the convection gauge to allow for measurement of the flow rate in the discharge cell. After installation, it was found that the metering controls currently installed were not sufficient to independently vary the pressure and the flow rate; rather, there remained a strong correlation between higher flows at higher pressures. To monitor and control these variables independently in the future, a capacitance manometer (Baratron, 1000 Torr range, MKS Instruments, Andover, MA; calibrated for air) and a high flow metering valve (Swagelok stainless steel high flow metering valve; Sunnyvale Fluid Systems Technologies, Inc., Fremont, CA) were installed directly after the flow meter in August 2019, although results for these later studies are not included here.

With zero air flowing through the discharge region, the effluent out of the discharge cell is then sent through a chemical trap of silver wool (Sigma-Aldrich, St. Louis, MO) to remove ozone created in the discharge and NaOH-coated silica (Ascarite, Sigma-Aldrich, St. Louis, MO) to remove any NO_2 produced in the discharge or CO_2 impurities. Then, a Russian doll trap (Brenninkmeijer & Röckmann, 1996) immersed in a dewar containing liquid nitrogen is used to cryogenically trap the N_2O (and any other gases condensable at 77K) while the unreacted N_2 and O_2 gases are pumped away. After the discharge is turned off, the valve to the zero-air supply is closed, while the Russian doll trap is kept open to the upstream until the pressure in the corona discharge region returns to background in order to ensure complete collection of the condensable gases generated in the discharge. After this period, the upstream valve of the Russian doll trap is closed, and the sample region of the vacuum line was fully pumped to background level while the condensable gases produced in the discharge remain cryogenically trapped. The line is then isolated from the vacuum pump, liquid nitrogen is placed on the evacuated sample tube, and an ethanol/LN_2 slush at −75 °C is placed on the Russian doll trap to transfer the condensable gases (N_2O and NO, and, if not fully removed by the chemical trap, O_3) to the sample tube while leaving

behind any other gases that condense −75 °C (e.g., water and NO_2) in the Russian doll trap; see Smith *et al.*,(2021)for more details. The successful transfer can be observed on the capacitance manometer (Baratron, 10 Torr range, MKS Instruments, Andover, MA, calibrated for air) and a convection gauge (317, MKS Instruments, Andover, MA, calibrated for air). Once all the sample is transferred to the sample tube, the valve downstream of the Russian doll trap is closed, the valve to the pump is opened, and the line is pumped to background. The sample section of the vacuum line is then isolated and the liquid nitrogen is removed from the sample tube to allow the sample to warm to room temperature. A pressure reading is taken on the capacitance manometer in a calibrated volume and used to determine the amount of condensable gases produced in the corona discharge (typically N_2O with some residual O_3 and NO in some experiments). The sample is then refrozen into the sample tube, the line is pumped, and the sample is allowed to expand into the isolated calibrated volume and warm again to room temperature. This freeze-pump-thaw cycle was repeated until the sample pressure remained consistent. Specifically, any excess NO and O_3 produced in the discharge that is not otherwise removed by the steel wool or by pumping at LN2 temperatures can be transferred to the sample region with the −75 °C LN2/Ethanol slush, and in some experiments a blue ring is observed due to the presence of these gases. These freeze-pump-thaw cycles reduced some of the NO and O_3 trapped in the sample region. After the freeze-pump-thaw cycles, the sample is then expanded into a 40 mL stainless steel sample flask (Swagelok) and isolated for sample storage and subsequent analysis by IRMS.

2.2.2 Corona Discharge Sample Preparation and Analysis by IRMS

To measure the isotopic composition of the N_2O generated by the corona discharge by IRMS, aliquots of 2 to 7 nmol are needed, which requires sample aliquot expansions on a separate gas transfer line (shown in Figure S2.1). This glass line is pumped by a diffusion pump (Edwards B30207110) backed by a rotary vane roughing pump (Edwards RV3). The 40 mL stainless steel sample flask containing the sample from the corona discharge run is attached below a 20 mL double-valved flask designed to fit on the preconcentrator section of the IRMS (see below) on the gas transfer line that also included additional 100 mL and/or 20 mL IRMS flasks (depending on the sample size) that serve as ballast to cut the sample to the appropriate sample size. An aliquot of the sample is taken in the space between the 40 mL stainless steel flask containing the N_2O sample from the discharge line and the IRMS flask used for IRMS analysis. This aliquot is then expanded into the gas transfer line and the ballast volume(s), and a pressure reading is taken on two convection gauges (317, MKS Instruments, Andover, MA, calibrated for air) and a capacitance manometer (Baratron, 10 Torr range, MKS Instruments, Andover, MA, calibrated for air). The 20 mL IRMS flask is then isolated and removed from the line to be analyzed for its isotopic composition. Three aliquots were taken in this method for analysis for $\delta^{15}N$ and $\delta^{18}O$ and another three were taken for analysis for the "site-specific" $\delta^{15}N$ measurements.

Isotopic composition analyses follow our laboratory's standard protocol for isotopic analysis by continuous-flow IRMS that includes online preconcentration and purification by gas chromatography prior to injection into a Finnigan MAT 252 Isotope Ratio Mass Spectrometer (Croteau et al., 2010; Park et al., 2012). The double-valved IRMS flask containing the corona discharge sample gas is mounted on the preconcentrator (shown in Figure S2.2), and helium carrier

gas is introduced into the sample flask with the downstream valve closed for 50 seconds at a flow rate of ~25 mL/min in order to pressurize the sample to atmospheric pressure or slightly above (in order to avoid back flow of lab air into the system). Then the downstream valve is opened, and the sample is carried in the helium flow through a chemical trap of ascarite to remove CO_2 and magnesium perchlorate to remove water. Next, the sample is cryogenically frozen in two successive LN2 traps; the first purifies the sample and the second cryofocuses the N_2O into a small volume for subsequent injection onto a GC column (PoraPlot Q). The GC separates N_2O from any impurities, in particular any residual CO_2 in the sample or the helium carrier gas, which is isobaric with N_2O and would result in isotopic artifacts. Nitrous oxide eluted from the column at a retention time of approximately 270 seconds, and is then introduced through an open split into the ion source of the IRMS. There, the sample gas is ionized by electron impact ionization with electrons at 100 eV. The ions are then accelerated out of the source with a 10 kV potential, through focusing lenses and are separated in space using an electromagnet. The ion beams are collected in Faraday cups, placed specifically to collect the ion beams at m/z ratios of 44, 45, and 46 or 30 ad 31 for the isotopic analogs ("isotopologs") of N_2O^+ and NO^+ (see below). As required for IRMS for sensitive and accurate analysis of isotope ratios, the resistance of each Faraday cup signal is configured such that the ion beam voltages are roughly equal despite the large differences in isotopic abundances between the rare, heavy isotopes and the common isotopes (The natural abundance of ^{15}N is 0.366% and that for ^{18}O is 0.205%). Two aliquots of the same sample were required to determine, first, the average $\delta^{15}N$ value – that is, the average of the isotopic composition across both the central (α) and terminal (β) nitrogen atom positions in NNO – and the $\delta^{18}O$ value and, second, the "site-specific" $\delta^{15}N^{\alpha}$ and $\delta^{15}N^{\beta}$ values. The δ values are defined in Equation (1) for $\delta^{15}N$ as:

$$\delta^{15}N = \left(\frac{^{15}R_{Sample}}{^{15}R_{Standard}} - 1\right) \times 1000 \qquad (1)$$

In Equation (1), ^{15}R represents the measured $^{15}N/^{14}N$ ratio – that is, the ratio of m/z 45 to m/z 44 for the N_2O^+ ion in the IRMS, for the sample and for the standard as indicated, and the factor of 1000 yields a δ value in per mil (‰). For $\delta^{18}O$, ^{18}R is substituted for ^{15}R in Equation (1) and represents the measured $^{18}O/^{16}O$ ratio – that is, the ratio of m/z 46 to m/z 44 for N_2O^+, for the sample and the standard. Simply put, the δ values represent the part-per-thousand difference in the heavy to light isotopologs between a sample and an international standard. For this study, we have assumed that the standard mass-dependent correction for the contribution of m/z 45 from $^{14}N^{14}N^{17}O$ based on the measured m/z 46/44 ratio holds.

By measuring the ratio of m/z 31 to m/z 30 – which are the NO^+ fragment ions from electron impact ionization of N_2O in the ion source of the IRMS – on a second aliquot of a sample, we can determine the nitrogen isotopic composition at the central (α) versus the terminal (β) atom positions in N_2O, or the $\delta^{15}N^{\alpha}$ and $\delta^{15}N^{\beta}$ values (Toyoda & Yoshida, 1999). Here, we report all values for the N_2O isotopic composition relative to the international standards air N_2 and air O_2; this happens to be especially convenient in this study since the isotopic composition of the reactants in our zero air are the equal to the international air O_2 and air N_2 standards (to within ± 2‰; see (Smith et al., 2021)). Previous studies of our IRMS measurement precision for tropospheric N_2O in whole air samples (Croteau et al., 2010; Park, 2004; Park et al., 2012) have

determined single measurement precisions of ±0.2‰ for $\delta^{15}N$, ±0.25‰ for $\delta^{18}O$, ±0.8‰ for $\delta^{15}N^{\alpha}$, and ±1.0‰ for $\delta^{15}N^{\beta}$ (1σ). To decrease the uncertainty, multiple measurements of N_2O from the same run were made on most discharge samples.

In the cases in which some NO and O_3 may have remained in the sample (and thus that the manometric determination of total gas yield on the discharge line might not equal the total amount of N_2O produced), the yield of N_2O can also be determined using the IRMS peak area for N_2O^+. This approach was calibrated using the concentration of N_2O in tropospheric samples (of ~330 ppbv) and calculations of the aliquot sizes in the sample preparation for IRMS analysis on the gas transfer line.

2.2.3 Atmospheric Plasma Sample Generation and Analysis

The additional NEPs generating N_2O that are investigated in this study are those designed and built by the Graves group in the Department of Chemical and Biomolecular Engineering at the University of California, Berkeley. They include a plasma flashlight (Pei et al., 2014; Pei et al., 2012), surface microdischarge (Pavlovich, Chang, et al., 2013; Pavlovich et al., 2014; Pavlovich, Sakiyama, et al., 2013) and a nanosecond pin-to-plane plasma (Anderson et al.). Important details as well as the main differences between these NEPs are described briefly here. The first atmospheric pressure NEP studied – the plasma flashlight (PF) – is a handheld device described in Pei *et al.* (2012); it has a needle-type electrode placed in a plastic nozzle and is powered by a 12 V battery. This DC voltage is then amplified by a booster circuit to 10 kV and the current is limited by two 50 MΩ ballast resistors. The second atmospheric pressure NEP – the surface microdischarge (SMD) – is the same as the apparatus described in Pavlovich *et al.* (2013). Briefly, it is a cylindrical copper block, with a diameter of 47 mm, that is covered by a 1mm thick quartz plate. A wire mesh made of woven stainless steel is attached to the plate to serve as the grounded electrode. The mesh has a density of 8 x 8 meshes per cm^2 and the wire diameter is 0.5 mm. A high voltage sinusoidal alternating current between 2-6 kV is applied with a frequency of 10 kHz. The third atmospheric pressure NEP studied – the pin-to-plane (PP) is described in Anderson *et al.* (2016) and is a direct current discharge in air with a positive voltage applied to the pin electrode with the plane as the grounded electrode. The parameters under which the discharge was run in these experiments are with a 16 kV applied voltage, 1 kHz frequency, 220 ns pulse width, a 0.56 cm gap between the pin and the plane, and a mΩ resistor. The reaction products generated from each of these 3 atmospheric pressure discharges were each sampled for isotopic analysis using the procedure described below.

To ensure effective sampling of the discharge-generated species, each NEP are generated in a confined acrylic chamber at atmospheric pressure. The chamber has a sample port leading to a chemical trap packed with silver wool (Sigma-Aldrich, St. Louis, MO) and NaOH-coated silica (Ascarite, Sigma-Aldrich, St. Louis, MO) to remove ozone and NO_2 created in the discharge attached to a 1.4-liter silonite-coated mini-canister (Entech Instruments, Inc, Simi Valley, CA). The collection flasks are evacuated the previous night by a diffusion pump and then leak checked before use. Due to differences in the amounts of N_2O generated by the different NEPs, the length of time that the discharge is on varied between each type of plasma. For the results reported here, the surface microdischarge and the plasma flashlight were run for one minute before a sample was

collected, and the pin-to-plane plasma was run for three minutes since the pin-to-plane produced significantly less N_2O. Once the desired time has elapsed with the plasma operating, the evacuated canister is opened, drawing the air in the chamber into the flask. The flask is then closed and brought back to the Boering laboratory for IRMS analysis.

Back in the Boering laboratory, the canister is attached to the gas transfer line (Figure S2.1) with a 100 mL IRMS flask (the typical sized flask used for IRMS analysis of tropospheric N_2O in whole air samples). An aliquot of sample is taken, expanded into the IRMS flask and part of the gas transfer line volume, and the pressure is recorded. Then the sample in the IRMS flask is removed and analyzed on the IRMS, as described in Section 2.2.2 for the corona discharge samples. Three aliquots each were measured for both the N_2O^+ and NO^+ fragment isotopic analysis, and the results were averaged. Each type of atmospheric pressure plasma was sampled three times under the same conditions and analyzed through the same process. These three analyses were averaged and reported as a single set of data for each type of discharge – the PF, SMD, and the PP plasmas.

To correct for the isotopic composition of N_2O in background air in the Graves laboratory, three samples of the lab air were taken and analyzed by IRMS using an identical method to the plasma sample analysis. The isotopic values of the plasma discharges were weighted by concentration and the N_2O in background air was subtracted following the weighted difference equation:

$$\delta^{15}N_{bckg\ correc} = \left(\frac{C_{N2O,plasma} \times \delta^{15}N_{plasma} - C_{N2O,bckg} \times \delta^{15}N_{bckg}}{C_{N2O,plasma} + C_{N2O,bckg}}\right) \qquad (2)$$

In equation (2), $C_{N2O,plasma}$ represents the concentration of N_2O produced in the plasma determined from the FTIR measurements described below for the SMD and plasma flashlight and determined from the N_2O sample IRMS peak area for the pin-to-plane. $C_{N2O,bckg}$ represents the concentration of background N_2O in the lab air, which was determined based on the IRMS peak area of the background sample, and was in fact close to the atmospheric concentration of N_2O of ~330 ppbv, as expected. The $\delta^{15}N$ values used in Equation (2) are those determined from IRMS analysis for the plasma-generated sample and the laboratory background sample. The same equation was followed for ^{18}O and site specific ^{15}N with those δ values substituted for $\delta^{15}N$ in Equation (2).

2.2.4 FTIR measurements of gases generated by the atmospheric pressure plasmas

To measure the total amount of N_2O generated by each type of plasma, a gas phase Fourier Transform Infrared (FTIR) spectrum was taken using the same discharge operation time as was done for sample collection and subsequent IRMS analysis (Pavlovich, Chang, et al., 2013). The FTIR instrument was first calibrated by flowing a gas mixture of 10 ppm N_2O in N_2 into a gas sample cell. The peaks used to determine N_2O concentrations are 2240 and 2210 cm^{-1}(*Nitrous oxide*, 2018; Pavlovich, Chang, et al., 2013; Sakiyama et al., 2012). Each NEP discharge was run for the same length of time as was used for sample collection in the modified acrylic chamber with ZnSe IR-transparent windows and FTIR spectra were collected.

These spectra were analyzed to get the amplitude, A, of the peak using Matlab (MATLAB, 2019) by fitting a Gaussian function to each plasma discharge N_2O peak in the form:

$$F = A\, e^{-(x-b)^2/2c^2} + D \qquad (3)$$

In equation (3), F is the absorbance, A is the amplitude, x is the wavenumber, and the terms b, c, and D are all factors for the fit. Beer's law was then used to determine the molar absorption coefficient of the peak at 2240 cm^{-1} from the calibration gas with a known concentration. These factors were then used to determine the concentrations of N_2O produced in the 3 atmospheric pressure NEPs of this study.

2.2.5 Optical Emission Spectra (OES) Measurements

OES has been shown to be a valuable characterization method to determine rotational and vibrational temperatures in NEPs (Gidon et al., 2019; Laux et al., 2003; Machala et al., 2007). Measurements using a UV-VIS spectrometer (Ocean Insight, Ocean Optics, Inc USB2000) were conducted for the corona discharge and for each of the atmospheric plasma systems under the operating conditions used to collect samples for IRMS analysis. Spectra collected were analyzed using the Massive OES program to fit a Lorentzian between 365 and 382 nm, the location of the N_2 ($C^3\Pi_u \rightarrow B^2\Pi_g$) emission band to yield values for T_{rot} and T_{vib} for each of the NEPs (Voráč et al., 2017). These data were then used to estimate the energies of the rotationally and vibrationally excited species in each NEP and to compare these energies between them.

2.2.6 Kinetics modeling details: Sensitivity runs including hypothetical KIEs

The chemistry and kinetics of NEP systems similar to those in our experiments reported here have been simulated previously in modeling efforts by various groups before, as cited below. However, just as isotopic composition measurements on NEP reaction products have been rare, so too are modeling studies that include kinetic isotope effects; this is discussed in Section 2.3.3. The different NEPs exhibit differences in reaction sets that are included and, in some cases, reaction rate coefficients due to differences in the voltage, current, and configuration of the particular plasma. For this study, chemical kinetics models for each plasma system were created in Kintecus (Ianni, 2017) using the chemical reaction sets and rate coefficients from the respective literature sources as described below.

For the corona discharge and plasma flashlight (which is also a type of corona discharge), chemical reactions and rate coefficients from the kinetics model by Chen and Davidson (2002b) and references therein are used. The relevant N_2O formation reactions in this model are R1a, R2, and R3 in Table 2.1. For the surface microdischarge, the reaction set in the model by Sakiyama *et al.* (2012) is used; key differences from the corona discharge model include the fact that the N_2O formation reactions in this model are R2, R4, and R5 (Table 2.1). For the pin-to-plane plasma, the reaction set in the models by Adamovich *et al.* (2015) and Shkurenkov *et al.* (2014) is used; the pin-to-plane NEP is similar to a spark discharge and is therefore expected to be hotter than the corona discharge and the other discharges. The N_2O formation reactions in the pin-to-plane model are R1a, R2, and R4 (Table 2.1). (Note that additional reactions of interest that will be discussed in Section 2.3 are also shown in Table 2.1.)

In each NEP model, electron impact reactions (e.g., R10 and R11) are included for the excitation and dissociation of O_2 and N_2. The rate coefficients, which depend on the electron energy, ε, are taken from the literature (for the pin-to-plane and surface microdischarge plasmas) or were calculated using the equation (17) in Chen and Davidson (Chen & Davidson, 2002a) from the relationship between ε and the electric field of the discharge (see footnote in Table 2.1). The SMD model also includes species containing hydrogen (such as HNO), so the initial atmospheric concentration of H_2 (0.5 ppmv) is used to initiate the model runs. (In the next model runs H_2O should also be included as an initial condition but was overlooked here). Finally, we note that, to good approximation under the experimental conditions, only reactions with neutral molecules are included in each of these models, based on the original modeling studies cited above.

Table 2.1: Selected reactions of interest in plasma discharges

	Reaction	Reaction rate coefficient, k	References	Discharge model
R1a	$N_2(A^3\Sigma, v=0, 1, 2) + O_2 \rightarrow N_2O + O(^3P)$	5.97×10^{-14} cm^3 s^{-1}	(Fraser & Piper, 1989; Iannuzzi et al., 1982; Edward C Zipf, 1980)	CD, PF, PP
R1b	$N_2(A^3\Sigma) + O_2 \rightarrow N_2 + 2O$	2.5×10^{-12} cm^3 s^{-1}	(Kossyi et al., 1992)	SMD, PP
R1c	$N_2(A^3\Sigma) + O_2 \rightarrow N_2 + O_2(a^1\Delta)$	8.68×10^{-15} T$^{0.55}$	(Kossyi et al., 1992)	CD, PF, SMD, PP
R1d	$N_2(A^3\Sigma) + O_2 \rightarrow N_2 + O_2(b^1\Sigma)$	8.68×10^{-15} T$^{0.55}$	(Kossyi et al., 1992)	CD, PF, SMD, PP
R2	$N(^4S) + NO_2 \rightarrow N_2O + O(^3P)$	2.77×10^{-12} cm^3 s^{-1}	(Wennberg et al., 1994)	CD, PF, SMD, PP
R3	$O(^1D) + N_2 + M \rightarrow N_2O + M$	2.81×10^{-36} cm^6 s^{-1}	(DeMore & Raper, 1962; Estupinán et al., 2002)	CD, PF
R4	$N(^2D) + NO \rightarrow N_2O$	6.00×10^{-11} cm^3 s^{-1}	(Kossyi et al., 1992)	SMD, PP
R5	$HNO + HNO \rightarrow N_2O + H_2O$	3.0×10^{-13} cm ^{3} s^{-1}	(Mätzing, 1991)	SMD
R6	$N_2 (v \geq 12) + O \rightarrow NO + N$	10^{-11} cm^3 s^{-1}	(Gordiets et al., 1995; Nguyen et al., 2011)	CD, PF, SMD, PP
R7	$NO + NO_3 \rightarrow 2NO_2$	1.5×10^{-11} cm^3 s^{-1}	(Atkinson et al., 1997; Herron & Green, 2001)	CD, PF, PP
R8	$NO + O_3 \rightarrow NO_2 + O_2$	3×10^{-12} cm^3 s^{-1}	(Burkholder et al., 2015)	CD, PF, PP
R9	$NO + O + M \rightarrow NO_2$	4.68×10^{-28} T$^{-1.5}$ cm^6 s^{-1}	(Atkinson et al., 1997)	CD, PF, PP
R10	$N_2 + e^- \rightarrow N_2 (A^3\Sigma) + e^-$	3.34×10^{-16} ε $^{-0.06}$ e$^{(-8.50/\varepsilon)}$ [a]	(Adamovich et al., 2015; Chen & Davidson, 2002a; Sakiyama et al., 2012)	CD, PF, SMD, PP
R11	$N_2 + e^- \rightarrow N(^2D) + N + e^-$	3.88×10^{-17} ε $^{2.24}$ e$^{(-9.10/\varepsilon)}$ [a]	(Sakiyama et al., 2012)	SMD, PP
R12	$^{14}NO + {}^{15}NO_2 \rightarrow {}^{14}NO + {}^{15}NO_2$	8.14×10^{-14} cm^3 s^{-1}	(Freyer et al., 1993; Li et al., 2020; Sharma et al., 1970; Walters et al., 2016)	

CD=corona discharge; PF= plasma flashlight; PP= pin-to-plane; SMD=surface microdischarge

[a] In the equations for the rate coefficient ε represents the electron energy in eV that has been estimated based on equation (17) in (Chen & Davidson, 2002a) for CD and PF; for the SMD from (Sakiyama et al., 2012), and for the PP from (Janda et al., 2014).

As a first step in investigating the mechanisms affecting the isotopic composition of N_2O generated in the various NEP models under different experimental conditions, nitrogen and oxygen isotopologs [e.g., $^{15}N^{14}N^{16}O$, $^{14}N^{15}N^{16}O$, $^{14}N^{14}N^{16}O$, $^{14}N^{14}N^{18}O$, and so on] were expressed in the NEP kinetics models as individual species, including isotopologs for all singly- and doubly-isotopically substituted molecules. In the "base model" runs, the rate coefficients for each chemical reaction are equal for all isotopologs of that species. In other words, the KIEs (where a KIE is defined as chemists as $k_{light}/k_{heavy} = 1$) in the "base" model are all equal to 1. The effect of hypothetical KIEs on the isotopic composition of N_2O can then be tested in different model runs by setting the KIEs to various values for normal ($k_{light}/k_{heavy} > 1$) or inverse ($k_{light}/k_{heavy} < 1$) KIEs. For this initial study, hypothetical inverse nitrogen KIEs of 0.9 in several N_2O-forming reactions were studied (see Table 2.2). In addition to these straightforward hypothetical nitrogen KIEs, in the corona discharge model we also implemented isotopolog-specific populations of vibrationally-excited N_2 in its ground electronic state ($X^1\Sigma_g^+$) which can react with O atoms, producing NO (R6 in Tables 2.1 and 2.2), as previous NEP modeling studies have included this reaction in their reaction set (Gordiets et al., 1995). At the same energies, the vibrational temperature is higher for the heavy isotopologs relative to the light isotopologs due to their closer vibrational spacing, so there will be isotope-specific differences in the population of N_2 in vibrational states higher than v=12, the energetic threshold for this reaction (Gordiets & Mamedov, 1975) and thus some isotope effects might be expected from this reaction. For these sensitivity runs for R6, the isotope-specific populations of $N_2(v>12)$ were estimated using the partition function for vibrations at the vibrational temperature measured by OES for the corona discharge. The effect of oxygen KIEs on the isotopic composition of plasma-generated N_2O will be reported in a future publication. A summary of sensitivity tests for various nitrogen KIEs implemented in different model scenarios performed in this work is given in full in Table 2.2.

Table 2.2: Summary of modeled sensitivity tests

	Reaction	Discharge model	$k_{(light)}/k_{(heavy)}$	Change in $\delta^{15}N$-N_2O[a] relative to $k_{(light)}/k_{(heavy)}$ =1
R1a	$N_2(A^3\Sigma) + O_2 \rightarrow N_2O + O(^3P)$	CD, PF, PP	0.9 for both $^{14}N^{15}N(A^3\Sigma) + OO \rightarrow {}^{14}N^{15}NO + O$ $\rightarrow {}^{15}N^{14}NO + O$	100‰
	"	"	0.9 only for $^{14}N^{15}N+OO \rightarrow {}^{14}N^{15}NO + O$	$\delta^{15}N$=50‰ $\delta^{15}N^{\alpha}$ =100‰
R2	$N(^4S) + NO_2 \rightarrow N_2O + O(^3P)$	CD, PF, SMD, PP	0.9	0‰
R3	$O(^1D) + N_2 + M \rightarrow N_2O + M$	CD, PF	0.9	0‰
R4	$N(^2D) + NO \rightarrow N_2O$	SMD, PP	0.9 for both $^{15}N(^2D) + {}^{14}NO \rightarrow {}^{15}N^{14}NO$ $^{14}N(^2D) + {}^{15}NO \rightarrow {}^{14}N^{15}NO$	100‰ in SMD 0‰ in PP
	"	"	0.9 only for $^{14}N(^2D) + {}^{15}NO \rightarrow {}^{14}N^{15}NO$	$\delta^{15}N$=50‰ in SMD $\delta^{15}N^{\alpha}$ =100‰ in SMD
R5	$HNO + HNO \rightarrow N_2O + H_2O$	SMD	0.9	0‰
R6	N_2 (v ≥ 12) + O → NO + N	CD	KIE=1(but OES-determined isotope-specific N_2(v>12) populations)	0‰ ($\delta^{15}N$-NO=118‰ and $\delta^{15}N$-NO_2=118‰)
R10	$N_2 + e^- \rightarrow N_2(A^3\Sigma) + e^-$	CD, PF, PP	0.9	100‰ in CD, PF 6‰ in PP
R11	$N_2 + e^- \rightarrow N(^2D) + N + e^-$	SMD, PP	0.9	$\delta^{15}N$=20‰ $\delta^{15}N^{\beta}$ = 40‰

[a] $\delta^{15}N = \delta^{15}N^{\beta} = \delta^{15}N^{\alpha}$ from modeling results unless explicitly stated otherwise.

2.2 Results and Discussion

2.3.1 Corona Discharge Results

New results for the amounts and isotope compositions of N_2O generated in the corona discharge experiments are given in Table 2.3, and the N_2O isotope compositions are plotted and compared with those from Smith *et al.* (2021) in Figures 2.2 and 2.3. The isotope compositions of plasma-generated N_2O are distinct from those of the reactant N_2 and O_2, with large enrichments in nitrogen up to 35‰ for $\delta^{15}N$ and 82‰ for $\delta^{15}N^{\alpha}$ (i.e., the enrichment at the α, or central, nitrogen atom position in N_2O) and large depletions in oxygen as large as 67‰. The isotope-isotope relationships are similar to our earlier work (Smith et al., 2021) but extend to higher pressures and different flow rates and residence times, which were measured in this study. The nitrogen isotope enrichments are not just large but also interesting in that the $\delta^{15}N^{\alpha}/\ \delta^{15}N$ slope of 2.34±0.07(1σ) indicates that essentially all the enrichment is occurring at the central atom position of N_2O. In fact, by mass balance arguments, because the $\delta^{15}N^{\alpha}/\ \delta^{15}N$ slope is larger than 2 (with a value of 2 indicating that ^{15}N is "added" only at the central atom position), the same or another process must also deplete ^{15}N at the β (or terminal) nitrogen atom site. These characteristics of the ^{15}N enrichments will ultimately provide strong constraints on the chemical reaction pathways by which N_2O is generated in the corona discharge and under different conditions.

The $\delta^{18}O$:$\delta^{15}N$ relationships for N_2O in Figure 2.3 are also interesting, and more complex than for $\delta^{15}N^{\alpha}$:$\delta^{15}N$. At the lowest ^{15}N enrichments (corresponding to the lowest experimental pressures), N_2O is enriched in ^{18}O relative to the reactant O_2 isotope composition; the ^{18}O enrichment then decreases as the ^{15}N enrichment increases (and roughly as pressure increases) until ^{18}O becomes depleted in N_2O. The $\delta^{18}O$:$\delta^{15}N$ slope in this region is –8.0±0.2. As $\delta^{15}N$ increases, $\delta^{18}O$ decreases, but at a slower rate of about –2.5. Intriguingly, this change in slope may indicate a transition from the ozone- to the NO_x-producing regime (e.g., Schmidt-Bleker et al., 2016) – a transition that is still not well understood (Pavlovich, Chang, et al., 2013) despite decades of study. These isotope constraints may thus hold entirely new information on the chemistry underlying this well-known but not understood transition in NEPs.

Table 2.3: Summary of results from the corona discharge experiments

Date Generated	**Pressure, Torr**	**Flow, sccm**	**Condensed Yield, nmol**	**N_2O Yield, nmol**	**$\delta^{15}N$ vs. air N_2, ‰**	**$\delta^{18}O$ vs. air O_2, ‰**	**$\delta^{15}N^{\alpha}$ vs. air N_2, ‰**	**$\delta^{15}N^{\beta}$ vs. air N_2, ‰**
7/20/2017	0.94±0.02	N/A	2536	1018±45	6.6±0.1	-1.8±0.07	18.5±1.5	-5.5±1.4
12/11/2017	10.5±3.2	0±2	543	201±9	19.2±0.4	-51.4±0.02	49.3±0.8	-11.6±1.5
12/12/2017	10.5±0.25	Static	2799	2272±100	4.3±0.2	-8.3±0.6	5.6±1.1	3.0±1.1
12/13/2017	10±0.5	N/A	1968	1706±75	14.4±0.2	-36.4±0.5	31.4±1.4	-3.0±1.5
12/20/2017	10±0.25	N/A	6158	481±21	8.1±0.8	-14.0±0.4	17.0±2.3	-1.0±3.6
12/20/2017	7.45±0.05	N/A	9080	301±13	7.2±0.1	-4.8±0.9	11.9±1.7	2.5±1.6
12/21/2017	7.8±0.05	N/A	10208	343±15	5.4±0.3	-4.0±1	8.6±2.7	2.3±3.3
5/4/2018	5.1±0.05	N/A	4618	1593±70	6.5±1.1	9.0±0.9	17.6±0.5	-4.9±2.5
5/3/2018	4.52±3	Static	231	280±12	9.1±2.4	7.1±2.2	14.5±8.7	3.5±4.5
5/7/2018	7.75±3	Static	362	431±19	8.3±2.9	4.8±3	12.9±3.7	3.6±2.3
9/14/2018	50.5±0.25	N/A	35186	4328±190	25.6±0.3	-43.2±0.6	59.5±0.6	-9.0±0.5
9/13/2018	21.5±0.5	N/A	10291	3735±164	4.8±0.2	-8.0±0.7	6.3±0.5	3.4±0.2
9/18/2018	30.5±0.5	N/A	8356	1960±86	6.8±0.8	-15.3±0.8	14.6±1.6	-1.1±3.2
2/21/2019	11.5±0.25	6±1	2865	1521±67	17.7±0.2	-30.4±0.5	33.1±1.2	1.9±1.1
2/22/2019	13.5±0.5	10±0.5	2050	1757±77	16.6±0.3	-43.4±1	32.6±1.9	0.2±1.4
2/25/2019	11±1	Static	1013	530±23	19.7±1.0	-42.3±2.4	39.5±2.0	-0.5±3.7
3/11/2019	15.5±0.5	13.5±0.5	4520	1245±55	16.8±0.5	-46.3±1.8	39.9±1.9	-6.8±2.7
3/12/2019	17.5±0.25	19.5±0.5	6108	1480±65	19.3±0.3	-54.8±3.5	43.6±0.8	-5.6±0.6
3/13/2019	20.5±0.5	29±0.5	3054	2568±113	19.1±0.4	-55.2±0.6	43.0±1.1	-5.4±1.3
3/22/2019	25.5±0.25	34±0.5	6364	2069±91	21.7±2.4	-48.3±2.9	44.6±0.8	-1.7±5.5
3/25/2019	31±0.25	51±0.5	7450	2152±94	19.0±0.5	-38.2±1.3	40.5±0.4	-2.9±1.2
3/26/2019	40.5±0.25	102±0.5	18062	2382±105	35.3±0.6	-67.4±0.8	82.5±2.9	-12.9±2.8
4/2/2019	28±0.5	41±0.5	7821	2160±95	17.8±0.6	-46.1±1.5	38.8±0.2	-3.8±0.9
4/3/2019	35.5±0.5	68±0.5	10538	2263±99	19.8±0.9	-38.2±1.7	41.8±0.4	-2.8±1.8
4/11/2019	23.5±0.5	32±0.5	6339	1664±73	19.7±0.5	-54.4±2.3	45.8±0.6	-6.9±1.1
4/25/2019	38±0.5	82±1	11171	2621±115	19.9±0.6	-40.4±1	44.1±3.7	-4.7±3.7
4/26/2019	43±0.25	124±1	12340	2682±118	34.8±0.6	-62.8±1.9	80.0±0.2	-11.5±1.0
6/11/2019	1.08±0.04	N/A	930	474±80	10.1±0.2	-6.3±0.2	23.9±0.9	-4.1±1.2

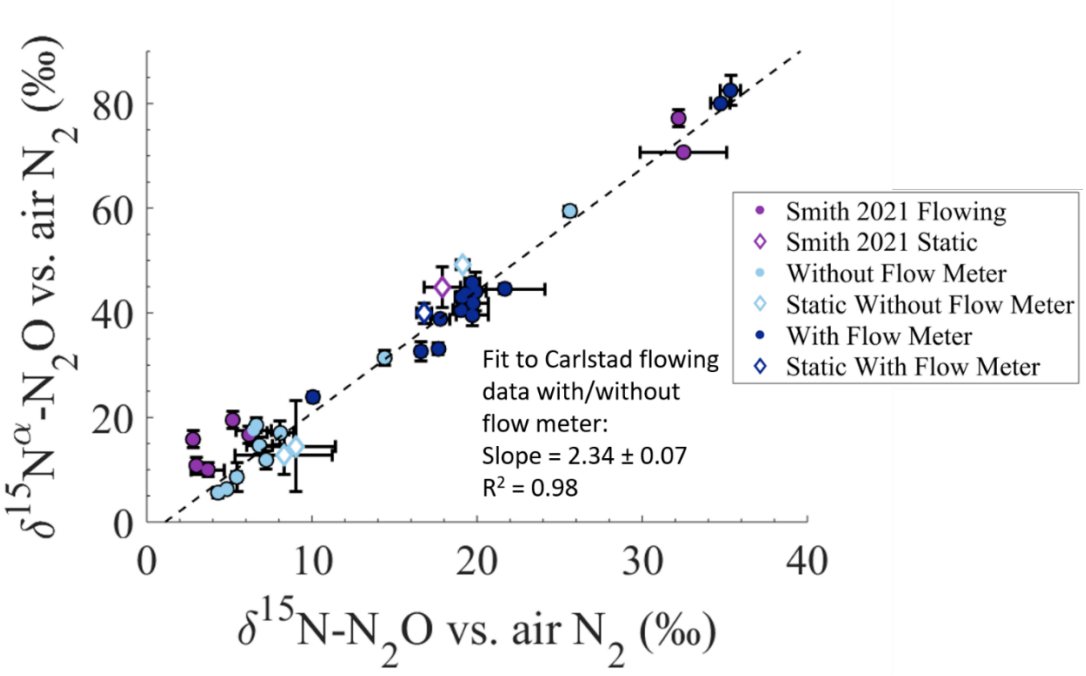

Figure 2.2: Measurements of the isotopic composition of N_2O generated in the corona discharge apparatus isotopic composition, for which $\delta^{15}N$ is the "bulk" nitrogen isotopic composition averaged over the two nitrogen atom positions and $\delta^{15}N^{\alpha}$ is the isotopic composition at the central (or α) nitrogen atom position in NNO, both on the air N_2 scale.

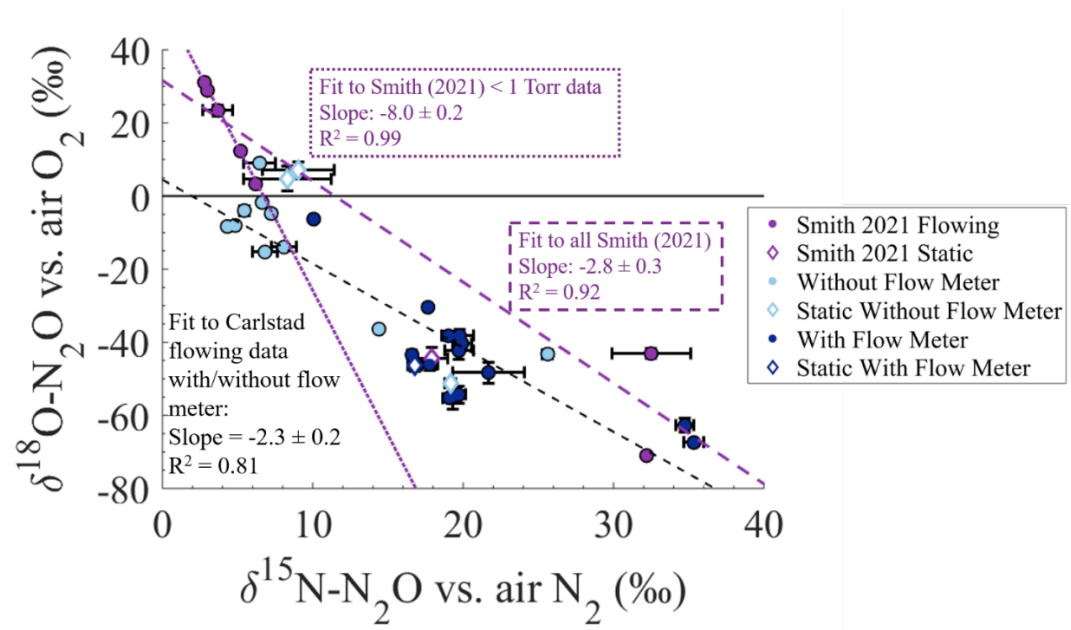

Figure 2.3: Measurements of the isotopic composition of N_2O generated in the corona discharge apparatus isotopic composition, for which $\delta^{15}N$ is the "bulk" nitrogen isotopic composition averaged over the two nitrogen atom positions on the air N_2 scale and $\delta^{18}O$ is the oxygen isotopic composition on the air O_2 scale.

Further mechanistic insights can be gleaned from Figure 2.4, showing the relationship between $\delta^{15}N^{\alpha}$ and $\delta^{15}N^{\beta}$ versus $\delta^{18}O$ for N_2O. A correlation between $\delta^{15}N^{\alpha}$ versus $\delta^{18}O$ and the lack of one (or a weaker one for some of the data at high $\delta^{15}N^{\alpha}$ values) between $\delta^{15}N^{\beta}$ and $\delta^{18}O$ indicates that a predominant effect is likely an isotope effect leading during the formation or destruction of the N—O bond in N_2O. This relationship was discussed in Smith *et al*. (2021), and the new results presented here continue to support the empirical conclusions drawn previously – that the relationships shown between $\delta^{15}N^{\alpha}$ and $\delta^{18}O$ and $\delta^{15}N^{\beta}$ and $\delta^{18}O$ indicate that the predominant isotope effect leading to the enrichment in ^{15}N and depletion in ^{18}O is likely due to the formation (and/or destruction) of the bond between NN—O. Future modeling work may also help to distinguish some of the more subtle correlations and anti-correlations in different regions of the plot.

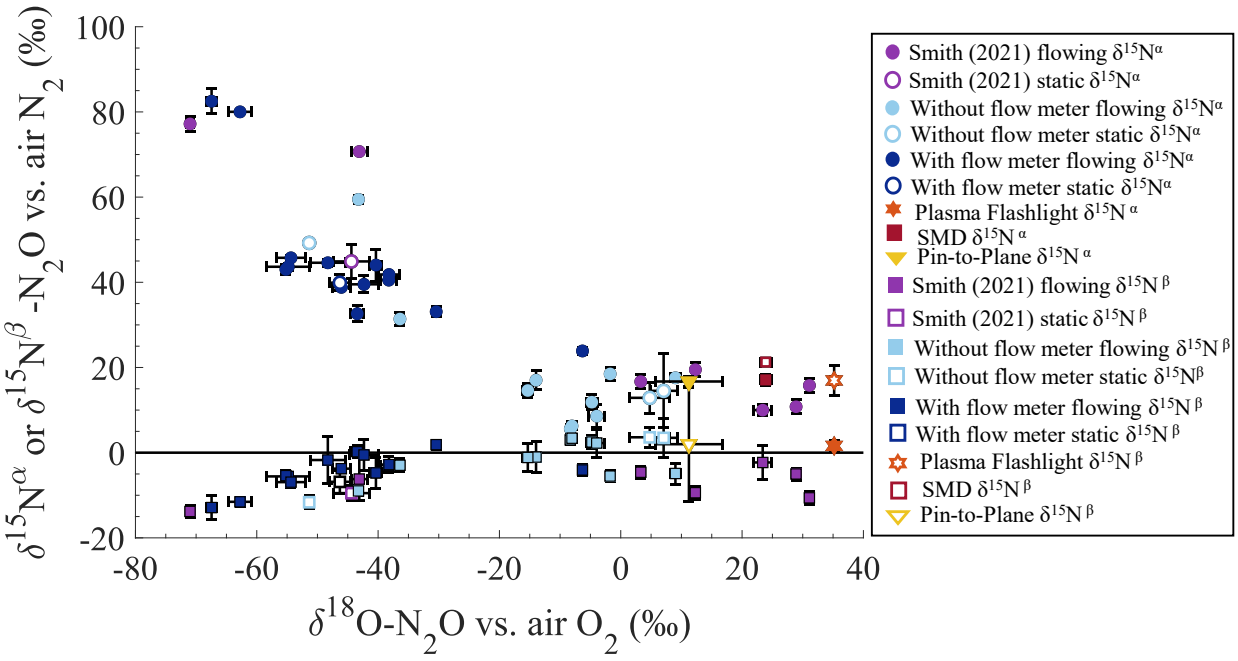

Figure 2.4: Relationship between $\delta^{18}O$ and $\delta^{15}N^{\alpha}$ (circles) or $\delta^{15}N^{\beta}$ (squares) for all the corona discharge data (cool colors) and for the 3 types of atmospheric pressure plasmas studied (plasma flashlight, surface microdischarge, and pin-to-plane). There is an anti-correlation between $\delta^{15}N^{\alpha}$ and $\delta^{18}O$ and only a weak correlation between $\delta^{15}N^{\beta}$ and $\delta^{18}O$ for the corona discharge data indicating that there is an isotope effect in a reaction that creates or destroys the N—O bond of N_2O.

Additional plots showing the amounts of N_2O produced in each experiment and the N_2O isotope compositions as a function of pressure and residence time in the corona discharge region are shown in Supplementary Figures (S2.5-2.8) and compared with the Smith *et al.* (2021) results. These scatterplots are much noisier than the isotope:isotope relationships shown in Figures 2.2 and 2.3, for several reasons. First, we found that installing a flow meter changed the relationship between the measured pressure and the measured flow rates (and hence discharge cell residence times), which likely altered the isotope compositions as a function of measured pressure with and

without the flow meter. Second, we found that, in the Smith *et al.* experiments, because the pressures were measured much further downstream from the corona discharge region than in this study, the pressures reported in Smith *et al.* (and plotted in the Supplementary figures) were likely not, in retrospect, representative of the actual cell pressure. In fact, because the $\delta^{15}N^{\alpha}$:$\delta^{15}N$ relationship is so robust, we can use the isotope relationships in our more systematic pressure and flow rate study here to infer that the actual corona discharge cell pressures in the "5 and 10 Torr" experiments in Smith *et al.* were more likely to be between 40 and 60 Torr. Third, we also found that the flow rates were difficult to control at pressures less than 10 Torr, likely leading to some additional variability. But, even with the greater variability in the isotope compositions as a function of pressure and residence time shown in the supplementary figures, we can still make the following general remarks. The nitrogen and oxygen isotopic composition of N_2O as a function of residence times (shown in Figure S2.8 for those experiments in which flow rates were measured directly) show largely the same relationship as those as a function of pressure, with shorter residence times corresponding to higher pressures, larger enrichments in ^{15}N, and larger depletions in ^{18}O since the experimental design under which these measurements were made prevented pressure and residence time from being independently varied (see Methods). Also, flowing experiments produced more N_2O than the static experiments, as there may have been more destruction of N_2O in the discharge region, as suggested by Smith *et al.,* or perhaps alternatively, there is more N_2O formation in the immediate outflow from the discharge region (Gorshunov & Gudenko, 2003). One optical emission spectrum of the corona discharge has been collected with the discharge cell pressure at 16.5 Torr and a flow rate of 15 sccm, finding T_{rot}=587±84K and T_{vib}=3095±190K. Future experiments will benefit from the additional modifications to the corona discharge apparatus noted in the Methods section that will now allow much finer independent control of the flow rates and cell pressure and will help to further elucidate how the N_2O isotopic composition and OES depends on the residence time and on static versus flowing conditions.

2.3.2 Results of Atmospheric Pressure Discharges

Concentrations and isotope composition data for N_2O as well as OES measurement results for the three atmospheric pressure plasma discharges are given in Table 2.4, while the isotope relationships are shown in Figures 2.5 and 2.6. In Figure 2.5, the surface microdischarge shows the largest enrichment in ^{15}N, the pin-to-plane discharge is enriched in ^{15}N and is preferentially enriched at the central nitrogen atom position, and the plasma flashlight is enriched in ^{15}N but has very small enrichments at the central position. In Figure 2.6, all the atmospheric pressure NEPs are enriched in both ^{15}N and ^{18}O. The plasma flashlight is the most enriched in ^{18}O of all the plasmas including the corona discharge, and the surface microdischarge is the most enriched in ^{15}N of the atmospheric pressure plasmas. The relationships between $\delta^{15}N^{\alpha}$ and $\delta^{15}N^{\beta}$ versus $\delta^{18}O$ for each atmospheric pressure discharge are shown in Figure 2.4. The pin-to-plane results appear to fall within the same $\delta^{15}N^{\alpha}$: $\delta^{18}O$ and $\delta^{15}N^{\beta}$:$\delta^{18}O$ relationships as those for the corona discharge, showing an enrichments in $^{15}N^{\alpha}$ and approximately neutral in $^{15}N^{\beta}$. But the plasma flashlight and SMD results exhibit the opposite relationship, in which $^{15}N^{\beta}$ is more enriched than $^{15}N^{\alpha}$.

Table 2.4: Summary of atmospheric plasma discharge yields and isotope composition for N_2O

Plasma Source	Concentration of N_2O, nmol	Mixing Ratio of N_2O, ppm	$\delta^{15}N$ vs. air N_2, ‰	$\delta^{18}O$ vs. air O_2, ‰	$\delta^{15}N^{\alpha}$ vs. air N_2, ‰	$\delta^{15}N^{\beta}$ vs. air N_2, ‰	T_{rot}, K	T_{vib}, K
Plasma Flashlight	46,800 [a]	31.2 [a]	9.2±1.1	35.2±0.6	1.6±1.4	17.0±3.6	310	2600
Surface Microdischarge	1,085,250 [a]	723 [a]	18.9±0.6	23.9±0.9	17.1±1.2	21.3±0.9	300	2044
Pin-to-Plane	10,100 [b]	< 1 [b]	9.8±4.2	11.3±5.6	18.8±2.9	1.3±8.9	450	4100

[a] Concentration and mixing ratios for the surface microdischarge and plasma flashlight were determined from the FTIR spectra. [b] Concentration and mixing ratio for the pin-to-plane were determined from the IRMS peak area because the amount of N_2O was below the 1 ppm detection limit of the FTIR.

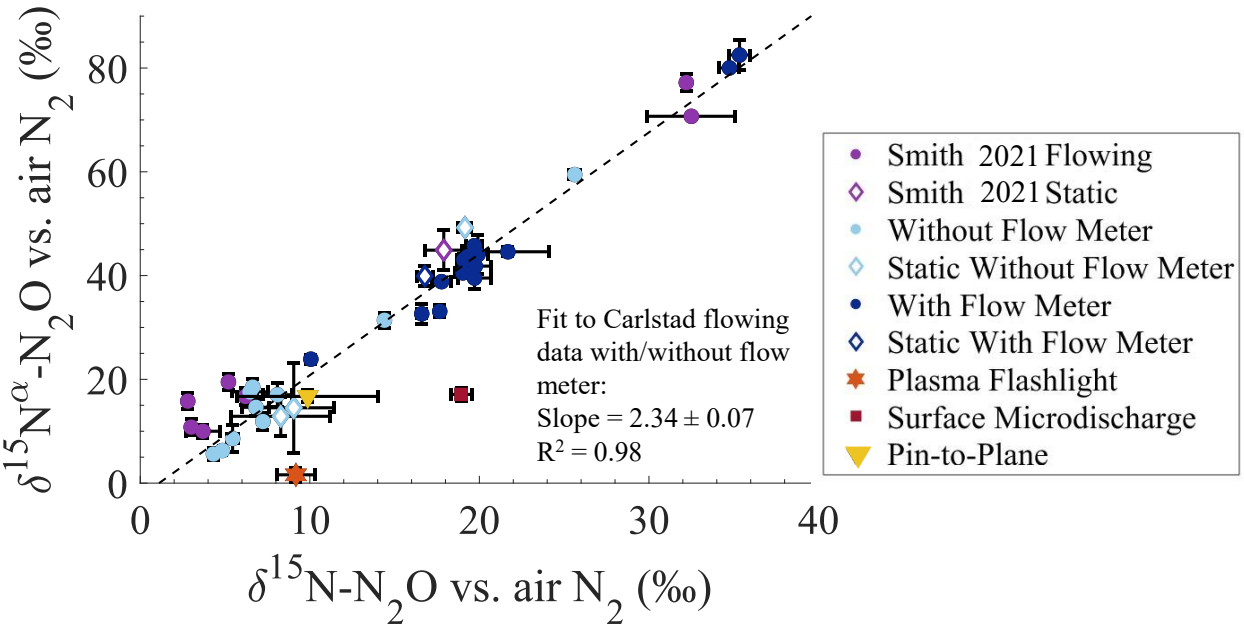

Figure 2.5: Same as Figure 2.3 with measurements of the atmospheric pressure NEPs added. Corona discharge data from Smith *et al.* (2021) are shown as purple circles, that of this work are shown in dark and light blue circles, surface microdischarge is shown as a red square, plasma flashlight is shown as an orange star, and pin-to-plane is shown as a yellow triangle.

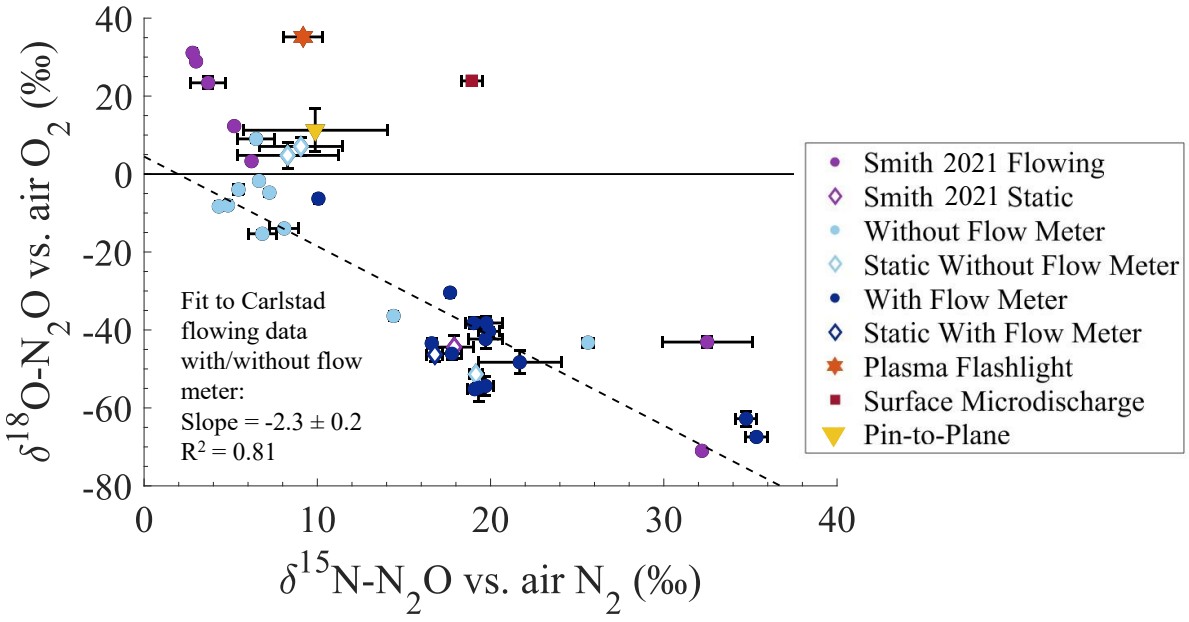

Figure 2.6: Same as Figure 2.4 measurements of the three atmospheric pressure NEPs added. Corona discharge data from Smith *et al.* (2021) are shown as purple circles, that of this work are shown in dark and light blue circles, surface microdischarge is shown as a red square, plasma flashlight is shown as an orange star, and pin-to-plane is shown as a yellow triangle.

The FTIR spectra for the atmospheric pressure discharges are shown in Figure 2.7. From these spectra, the concentration of N_2O produced for each discharge was determined. The surface microdischarge produces the most N_2O, while the pin-to-plane produces the least (with N_2O produced below the detection limit of 1 ppm for the FTIR, hence the concentration was estimated from the IRMS peak area). Other species are apparent in the FTIR spectra, including O_3, HNO_3, and NO_2 (Pavlovich, Chang, et al., 2013; Sakiyama et al., 2012). Since the FTIR spectra were not calibrated to obtain mixing ratios for these species (as was done for N_2O), we can still interpret the relative amounts of these gases produced in the different discharges. The plasma flashlight produces the most ozone, while the surface microdischarge produces the most NO_2. (The observed CO_2 in the PP spectrum is likely due to variable amounts of background CO_2 in the lab air that were not corrected for by the background FTIR subtraction).

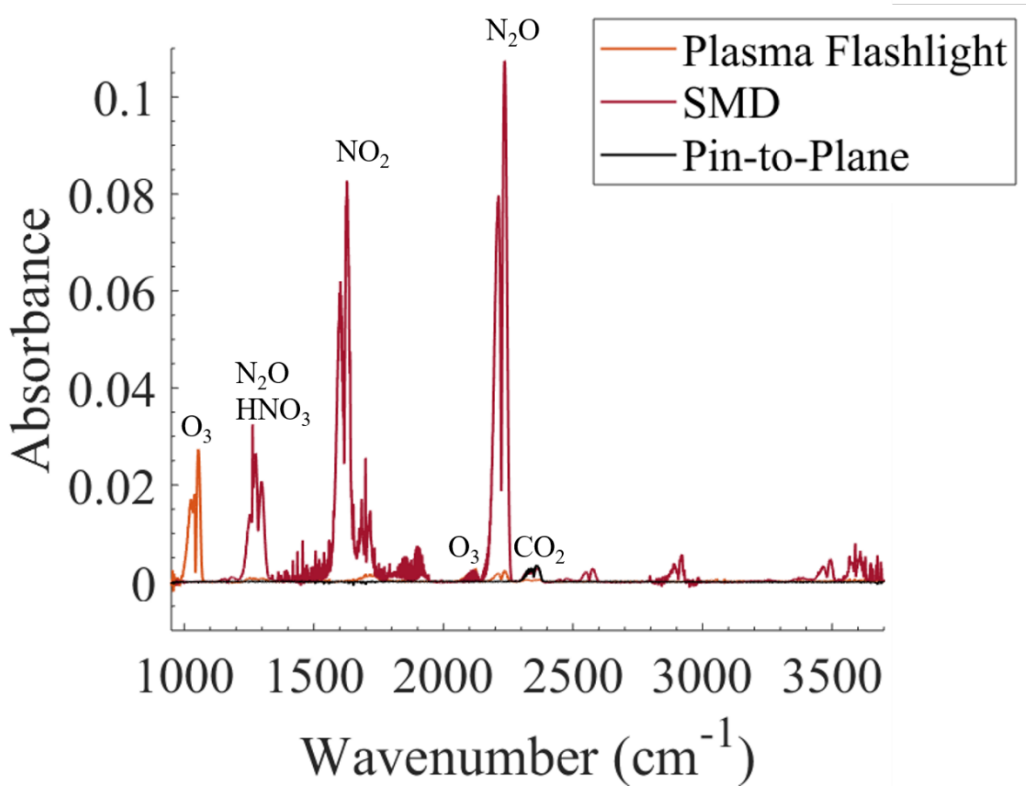

Figure 2.7: FTIR spectra of the gases produced in the atmospheric pressure NEPs. Peaks are labeled based on the molecule(s) that are inferred at particular wavenumbers.

2.3.3 Insights into Chemical Mechanisms

Based solely on the very different isotopic compositions of N_2O generated in the different NEPs of this study, there are clearly differences in the chemical mechanisms and kinetics for each plasma, as well as changes as function of discharge pressure and/or flow rates, as expected. The exciting part of this new work is that the measured N_2O isotopic compositions provide additional and complementary information to the more traditional concentration measurements alone. For example, all plasma-generated N_2O is enriched in ^{15}N but to varying degrees, and the magnitude of the enrichments at the central nitrogen are different for each (Figure 2.5). The atmospheric pressure plasma discharges are enriched in ^{18}O while the corona discharge is depleted in ^{18}O (Figure 2.6). The $\delta^{15}N^{\alpha}$:$\delta^{18}O$ and $\delta^{15}N^{\beta}$:$\delta^{18}O$ correlations shown in Figure 2.4 also provide further evidence that there are different chemical mechanisms creating N_2O, especially in the plasma flashlight and SMD which are different from each other, and fall well outside of the relationships between $\delta^{15}N^{\alpha}$ versus $\delta^{18}O$ for the corona and pin-to-plane NEPs. Empirically, the strong $\delta^{15}N^{\alpha}$:$\delta^{18}O$ correlation and weak $\delta^{15}N^{\beta}$:$\delta^{18}O$ correlation for the corona discharge data suggest that reactions that form or break N–O bonds may be responsible, which include N–O bond formation in R1a, R3 and R6 and N–O bond breakage in R2, but not solely or dominantly R4 in which only an N–N is formed.

To gain further insight, results for the isotopic sensitivity tests using the NEP models described in the Methods section are shown in Table 2.2. Of particular interest is whether hypothetical KIEs in the reactions in Table 2.1 that produce N_2O might lead to the N_2O isotope composition relationships that we measured. We note first that, while there have been many simulations of the kinetics and mechanisms of NEP-generated products (and upon which we based our kinetics sensitivity studies for plasma-generated isotopologs using KINTECUS, as described in the Methods section), few experimental and few theoretical studies of ^{15}N enrichment in NEP-generated species exist. The 4 experimental studies, prior to Smith *et al.* (2021), were discussed in the introduction. The handful of theoretical studies mostly focus on theoretical predictions of ^{15}N (or ^{13}C) separation factors for isotope enrichment applications via plasmas (or lasers) rather than full kinetics simulations of NEP products (e.g., Belenov et al., 1973; Gordiets & Mamedov, 1975; Gorshunov & Gudenko, 2003; McLaughlin & Christiansen, 1986; Nguyen et al., 2011). To our knowledge, then, the results presented here are the first simulations exploring potential KIEs in the formation of NEP reaction products in various discharges – using the same reaction sets and reaction rate coefficients as models used extensively for modern simulations of the concentrations of various species, such as O_3, NO_x, and N_2O (e.g., Mesbah & Graves, 2019; National Academies of Sciences & Medicine, 2021; Pavlovich, Chang, et al., 2013).

From the model scenario results in Table 2.2, in the corona discharge, plasma flashlight, and pin-to-plane discharges, if is found that N_2O production is dominated by reaction R1a: $N_2(A^3\Sigma) + O_2 \rightarrow N_2O + O(^3P)$ over any other reactions by several orders of magnitude (see Figure S2.9 for the rate of N_2O produced by R1a, R2, and R3 in a corona discharge) and that R1a is the only N_2O formation reaction that leads to ^{15}N enrichment in the product N_2O in these 3 types of NEPs under the measured conditions. For example, with an inverse KIE of 0.9 (or 10%) in R1a, a 100‰ enrichment in ^{15}N of N_2O – equally distributed at the α and β positions – relative to the model results for N_2O with a KIE=1 is the result. When we restrict the KIE of 0.9 to only the $^{14}N^{15}N + OO \rightarrow {}^{14}N^{15}NO + O$ reaction, leaving the KIE for the $^{14}N^{15}N + OO \rightarrow {}^{15}N^{14}NO + O$ reaction at a value of 1, the model predicts an N_2O isotopic composition of $\delta^{15}N$=50‰ and $\delta^{15}N^{\alpha}$=100‰ relative to the model results for N_2O with KIEs of 1. Because the other reactions (R2 and R3) produce so little N_2O (due to small abundances of reactants needed for R2 and the very small rate coefficient for R3), the KIEs in these reactions produce no detectable change in the modeled isotopic composition of N_2O relative to the model scenario in which all KIEs are equal to 1. Given the simplicity of one dominant N_2O-forming reaction, there is a simple correspondence between the model KIEs and the resulting N_2O isotopic composition. This will not be the case for all possible scenarios when multiple processes can alter the isotope distribution in N_2O.

In the surface microdischarge, the dominant N_2O-producing reaction in the model as initially set up as in Sakiyama *et al.* (2012) is R4: $N(^2D) + NO \rightarrow N_2O$ for which an inverse KIE of 0.9 also leads to a 100‰ ^{15}N enrichment in N_2O at both the α and β positions relative to model results with a KIE of 1 (or to $\delta^{15}N$=50‰ and $\delta^{15}N^{\alpha}$=100‰ if the KIE is restricted to only reactions producing $^{14}N^{15}NO$). Interestingly, R1a was not originally included in the surface microdischarge model, because it is not included in the model (Sakiyama et al., 2012) on which our study was based. But, upon adding it to our kinetics model for the SMD, R1a becomes the dominant production pathway for N_2O over R4. The conditions under which R1a should occur is at electron

energies of 15 eV (Edward C. Zipf, 1980), which is large enough to excite N_2 to $N_2(A^3\Sigma)$; the estimated maximum electron energy of the SMD is 7.5 eV (Sakiyama et al., 2012), although it is known that electron energies in these NEP discharges are often non-Maxwellian (Fridman, 2008). While there are other channels for R1 (see Table 2.1), our modeling suggests that R1a should still be the dominant N_2O production mechanism in the SMD, because of the low concentrations of NO and NO_2 reactants in R2, R4, and R5. While we did not include a model scenario here for this idea, it is interesting to consider how vibrational excitations could impact R1a and the isotopic composition of N_2O produced through this reaction. R1a has been previously studied with N_2 in the v'=0, 1, 2 states (Edward C. Zipf, 1980), and Fraser and Piper (1989) note that the branching ratio of the reaction forming N_2O is <0.2% at vibrational levels less than or equal to 2, but they acknowledge that the reaction could be important at higher vibrational levels. If R1a proceeds through higher vibrational levels, the vibrational excitations in this reaction could also lead to an isotope effect, favoring the excitation of $^{15}N^{14}N$ and leading to ^{15}N enrichments in N_2O (based on reasoning presented in the Methods section: that heavy isotopologs have a higher vibrational temperature than the light isotopologs for a given energy due to their closer vibrational energy level spacing). In Figure 2.4, a correlation between $\delta^{15}N^{\alpha}$ and $\delta^{18}O$ is observed for the corona discharge and pin-to-plane discharge, which is also consistent with an isotope effect in R1a where an N—O bond is created. With our modeling results showing that R1a is a dominant production pathway for N_2O in all of the plasma discharges, even the SMD, it is possible that there is a process such as vibrational excitation of $N_2(A^3\Sigma)$ that is also leading to ^{15}N enrichments in N_2O.

Another reaction that has been suggested by other researchers to contribute to ^{15}N enrichments in plasma-generated nitrogen oxides is R6: N_2 ($v \geq 12$) + O → NO + N (Gordiets et al., 1995; Nguyen et al., 2011). R6 was incorporated into the kinetics simulation for the corona discharge by estimating the population of each vibrational state of the isotopologs of N_2 using the measured T_{vib} determined from our OES measurements (see Methods section). Then sensitivity studies were performed, by including just the population distribution differences between the heavy and light N_2 isotopologs, testing a KIE=1 in R6, and finding no enrichment in ^{15}N in N_2O. Enrichments were found, however, in NO and NO_2 with $\delta^{15}N$=118‰ for both (see Table 2.2). The highly ^{15}N-enriched NO produced in this reaction can produce enriched NO_2 through R7, R8, and R9 in Table 2.1. ^{15}N-Enriched NO_2 can then go on to produce N_2O in all NEPs through R2, although in the corona discharge model this reaction does not lead to significant production of N_2O at short residence times of <1 minute such as those in the flowing experiments performed here.

Another potential pathway to produce ^{15}N-enriched NO_2 from NO, such as that produced in R6, is through R12: ^{15}N isotopic exchange between NO and NO_2, which has been measured previously (Freyer et al., 1993; Li et al., 2020; Sharma et al., 1970; Walters et al., 2016), but has not yet been implemented into our NEP kinetics models. This could lead to even larger enrichments in NO_2 than are presently modeled. If the concentration of NO_2 builds up over time, then R2 could become a significant reaction mechanism for the production of N_2O. In our simulations, at early reaction times R2 is the slowest reaction, but when the reaction time is longer than 10 minutes the concentration of NO_2 increases, and the reaction rate of R2 becomes the second most significant reaction after R1 (Figure S2.9). This indicates that, for the static experiments in which the residence time in the discharge cell was 15 minutes, a significant concentration of NO_2 could build

up and lead to more production of N_2O through R2. This series of reactions, beginning with R6, is also consistent with experimental results for the corona discharge, and pin-to-plane in Figure 2.4. The relationship observed between $\delta^{15}N^{\alpha}$ and $\delta^{18}O$ and that of $\delta^{15}N^{\beta}$ and $\delta^{18}O$, discussed previously, is an indication of an isotope effect in the creation or destruction of the N—O bond, and could be due to a series of reactions that begins with an isotope effect in R6, in which the NO produced in R6 goes on to form N_2O through R2.

An additional potential pathway to produce a ^{15}N enrichment in N_2O could be through isotope effects in the electron impact excitation and dissociation reactions occurring in the discharges. In the plasma flashlight, pin-to-plane, and corona discharge, an inverse KIE=0.9 in R10: $N_2 + e^- \rightarrow N_2\ (A^3\Sigma) + e^-$ leads to $\delta^{15}N\text{-}N_2O$=100‰ in the corona discharge and plasma flashlight models and $\delta^{15}N\text{-}N_2O$=6‰ in the pin-to-plane relative to a KIE=1, and this enrichment is equally distributed across the alpha and beta positions in all NEPs. The lower $\delta^{15}N\text{-}N_2O$ value in the pin-to-plane simulation is the result of a smaller rate coefficient for R10 in the pin-to-plane than in the corona discharge and plasma flashlight models. Experimentally, isotope effects have been observed in similar processes. For example, Govers (1973) found that N_2 excited by electron impact to the $C^2\Sigma_u^+$ state of N_2^+ pre-dissociates 6 to 10 times more rapidly for $^{14}N^{14}N$ than $^{14}N^{15}N$ and $^{15}N^{15}N$, which led to ^{15}N enrichments in the remaining electronically excited N_2 molecules, and a similar pathway could lead to ^{15}N-enrichments in $N_2(A^3\Sigma)$ that produces N_2O through R1a. Looking at electron impact dissociation reactions, in the SMD model, when an inverse KIE=0.9 is included in the electron impact reaction R11: $N_2 + e^- \rightarrow N(^2D) + N + e^-$, the resulting N_2O has an isotope composition of $\delta^{15}N$=20‰, and the enrichment is fully at the beta position, with $\delta^{15}N^{\beta}$=40‰. However, the SMD measurements show ^{15}N enrichment at the alpha position, with $\delta^{15}N^{\alpha}$=17.1‰, so this reaction alone is unlikely to lead to the experimental results for the SMD. There is additional experimental evidence suggesting that ^{15}N enrichments can occur through dissociation processes, such as through UV photodissociation of N_2 (Chakraborty et al., 2016; Chakraborty et al., 2014). In a pulsed glow discharge, Gorshunov & Gudenko (2003) measured huge ^{15}N enrichments in nitrogen atoms and suggested the enrichment results from the vibrational excitation of ^{15}N-substituted N_2 in the $N_2(B^2\Pi_g)$ electronic excited state, that then dissociates. The isotope effect described by Gorshunov & Gudenko (2003) has not been tested in modeling here but, in principle, could be an additional pathway to produce ^{15}N-enrichments in N_2O.

For the new oxygen isotope composition measurements, the N_2O generated in the corona discharge is isotopically depleted in ^{18}O to a significant degree at higher discharge pressures, while the other atmospheric pressure discharges are enriched in ^{18}O, indicating that there are key differences in the production pathways. In the corona discharge, the ^{18}O depletion could be due to either 'normal' KIEs in which the light isotopologs react faster than the heavy isotopologs or to sequestering of the heavy oxygen isotopes (^{18}O and ^{17}O) in the ozone formed in the discharge, as first noted by Smith *et al.* (2021), due to large (and mass-independent) KIEs in the ozone formation reaction, $O+O_2+M$ (Thiemens & Heidenreich, 1983). Indeed, the experiments by Nguyen *et al.* (2011) in a glow discharge, show that, at an O_2 mixing ratio of 5% and above, all of the O_2 in the discharge air is converted to ozone. By mass balance, this 'reservoir' effect could lead to isotopically light N_2O. Measurements of $\delta^{17}O$ of plasma-generated N_2O could therefore be a useful diagnostic for which mechanism is operative in the corona discharge experiments. In contrast, N_2O

generated in the atmospheric pressure plasmas are enriched in ^{18}O, which could be due to less ozone production sequestering the heavy isotopes or a different mechanism altogether. These differences in the oxygen isotopic compositions in N_2O may also be indicative of different chemical mechanisms or regimes, such as the transition between an ozone-producing versus NO_x-producing regime. Model scenarios for oxygen KIEs are beyond the scope of this chapter.

2.3.4 Atmospheric Applications

In addition to the importance of these findings for plasma chemistry, the results of this work are also potentially relevant for the upper troposphere, where lightning storms may create N_2O (Levine & Shaw, 1983), and for the upper atmosphere where N_2O is now known to be produced in the mesosphere through auroral precipitation events (Semeniuk et al., 2008) and transient luminous events (Pérez-Invernón et al., 2020). All these processes create high energy electrons that can react through electron impact with air to generate electronically, rotationally, vibrationally, and translationally excited atoms and molecules, similar to that of the discharges studied here. While none of these sources impact global concentrations of N_2O, a source of N_2O with unusual isotope compositions, such as those of the discharges measured here, could impact the conclusions of researchers measuring the isotopic composition of N_2O in the free troposphere influenced by lightning, and in the upper atmosphere.

Previous atmospheric modeling and satellite measurements have led to the suggestion that R1 creates N_2O in the mesosphere, but that the reaction R1a may not have a large enough branching ratio to produce large amounts of N_2O (de Sousa et al., 1985; Funke, López-Puertas, et al., 2008; Iannuzzi et al., 1982; Edward C Zipf, 1980), so R2 is also proposed as a potential source of N_2O (Funke, García-Comas, et al., 2008; Funke, López-Puertas, et al., 2008; Semeniuk et al., 2008). It is suggested by Semeniuk *et al.* (2008) that the reactant NO_2 in the mesosphere that goes on to produce N_2O through R2, is created during the polar night from the reaction of NO with ozone (R8). Recent advancements have allowed for ^{15}N isotopic analysis of the N_2O in the upper stratosphere from satellites, providing an exciting new tracer for chemistry and circulation in the atmosphere. Measurements from 2004-2013 across all seasons at 40-50° latitudes found large enrichments in ^{18}O and ^{15}N at the alpha and beta positions of N_2O that increase with altitude and latitude, with the largest enrichments over the poles in the stratosphere (Bernath et al., 2017). While the most recent ACE satellite measurements of the isotopic enrichments of N_2O follow the well-known fractionation patterns of photolysis and photo-oxidation of N_2O in the stratosphere, future work seeks to separate out the isotopic signature of N_2O produced by solar wind in the mesosphere, that can mix down into the upper stratosphere, particularly at the poles, and potentially impacting the isotopic composition of N_2O observed in the stratosphere (Bernath et al., 2017). Such transport might also be important for the multiply-substituted isotopic composition of N_2O measured in the stratosphere (also known as 'clumped' isotope composition), especially in the polar vortex, where air from the upper atmosphere mixes down as it is entrained from the mesosphere. The results of the discharge experiments could be used to give insights into the singly- and doubly- substituted isotopic fingerprints in N_2O, which would have implications for the polar stratospheric isotopic composition of N_2O and other trace gases. For example, Yeung *et al.* (2009) measured the clumped isotopic composition of CO_2 in the stratosphere, which required a correction

to account for isobaric interferences from the stratospheric N_2O that remained in the cryogenically separated gases from the original whole air samples from the stratosphere. The clumped isotope signal in polar vortex CO_2 was unusual compared to the well-described non-vortex data, and several mechanisms were proposed to account for the unusual vortex data (e.g., unknown reactions on PSCs, or transport of unusually isotopically fractionated CO or CO_2 from the mesosphere into the stratospheric vortex), but none seemed satisfactory. One possibility that was not considered at the time is that the charged particle-induced source of N_2O in the upper atmosphere could have a very unusual clumped isotope composition, which, if not accounted for properly, could skew the clumped CO_2 isotope measurements. Producing large amounts of N_2O in NEPs and analyzing the results for the clumped isotope composition might inform such clumped isotope studies, for N_2O and for isobaric CO_2, since the chemical mechanisms may be similar to those studied in NEPs. This work, in combination with the new discoveries of an upper atmospheric sources of N_2O, highlights the importance of understanding the underlying physical chemistry of R1, R2, and electron impact reactions, and the isotopic fingerprints in these discharges.

2.4 Conclusions and Future Work

Four different low-temperature, non-equilibrium plasma (NEP) discharges – three at atmospheric pressure and one over a range of sub-atmospheric pressures – were used to generate N_2O, and the ^{15}N and ^{18}O compositions were measured by IRMS and compared. All plasmas lead to N_2O that is enriched in ^{15}N to different degrees, and the N_2O generated in the atmospheric pressure plasmas studied are enriched in ^{18}O while that generated in the corona discharge is, except at very low pressures, depleted in ^{18}O. The large differences in isotope compositions provide strong evidence of mechanistic differences between the different types of plasma discharges – as expected but never shown by isotope measurements before - and demonstrate that isotope measurements at natural abundances are poised to serve as a new breakthrough in low-temperature NEP diagnostics.

Through the incorporation of nitrogen and oxygen isotopic analogs into NEP kinetics models, we provide some preliminary insights into the mechanisms that may be responsible for the measured isotope compositions of N_2O. In the modeling work presented here, R1a: $N_2(A^3\Sigma) + O_2 \rightarrow N_2O + O(^3P)$, has a high reaction rate and, if an isotope effect is present in this reaction, it is likely to greatly influence the nitrogen isotopic composition of N_2O. Vibrational excitation of N_2 is also likely to be an important mechanism for the enrichment of ^{15}N in N_2O and potentially other nitrogen oxides, as it has been suggested through previous isotope separation studies that are roughly consistent with measurements here (Gorshunov & Gudenko, 2003; Nguyen et al., 2011). In the corona discharge results, ozone formation may pay a role in sequestering heavy oxygen isotopes in the system, leading to ^{18}O depletions in N_2O. The new modeling and experimental results presented here can inform experimental conditions and modeling in future studies to better understand the isotopic fractionation and reactions that lead to the production of N_2O.

There is extensive work ongoing and planned to continue to understand the isotopic composition of gases formed in plasma discharges. This includes expanded modeling studies to test a greater number of reaction pathways under different conditions, including an expanded analysis of the vibrationally excited species in each discharge and a consideration of ion-molecule reactions. This will be combined with continued systematic experiments at higher pressures with

the corona discharge and measurements of all plasmas over different operation times and conditions. There are also plans for analysis of the ^{17}O isotopic composition of N_2O, which will provide further information about the importance of ozone in the discharges, and the measurement of the isotopic composition of the NO_x produced, which can now be analyzed with recent sampling and analysis developments (Fibiger et al., 2014). In addition, ongoing collaborations across the College of Chemistry at UC Berkeley will allow for the measurement of two new plasma discharges, the plasma jet and pin-to-pin plasma, and through this collaboration artificial intelligence and machine learning will be used to analyze how the plasma discharges change under different conditions and identify gaps of knowledge that can help design laboratory experiments to continue to further the understanding of these systems. This future work will continue to enhance understanding of fundamental plasma chemistry and atmospheric processes, and also other environmental applications such as nitrogen fixation and applications in healthcare.

References

Adamovich, I. V., Li, T., & Lempert, W. R. (2015). Kinetic mechanism of molecular energy transfer and chemical reactions in low-temperature air-fuel plasmas. *Philosophical Transactions of the Royal Society A: Mathematical, Physical and Engineering Sciences*, *373*(2048), 20140336. https://doi.org/doi:10.1098/rsta.2014.0336

Anderson, C. E., Cha, N. R., Lindsay, A. D., Clark, D. S., & Graves, D. B. (2016). The Role of Interfacial Reactions in Determining Plasma–Liquid Chemistry. *Plasma Chemistry and Plasma Processing*, *36*(6), 1393-1415. https://doi.org/10.1007/s11090-016-9742-1

Atkinson, R., Baulch, D. L., Cox, R. A., Jr., R. F. H., Kerr, J. A., Rossi, M. J., & Troe, J. (1997). Evaluated Kinetic, Photochemical and Heterogeneous Data for Atmospheric Chemistry: Supplement V. IUPAC Subcommittee on Gas Kinetic Data Evaluation for Atmospheric Chemistry. *Journal of Physical and Chemical Reference Data*, *26*(3), 521-1011. https://doi.org/10.1063/1.556011

Basov, N., Belenov, E., Gavrilina, L., Isakov, V., Markin, E., Oraevskii, A., Romanenko, V., & Ferapontov, N. (1974). *Isotope separation in chemical reactions occurring under thermodynamic nonequilibrium conditions*.

Belenov, E., Markin, E., Ovaevskii, A., & Romanenko, V. (1973). *Isotope separation by infrared laser radiation*.

Bernath, P. F., Yousefi, M., Buzan, E., & Boone, C. D. (2017). A Near-Global Atmospheric Distribution of N_2O Isotopologues. *Geophysical Research Letters*, *44*(20), 10,735-710,743. https://doi.org/10.1002/2017gl075122

Brenninkmeijer, C. A. M., & Röckmann, T. (1996). Russian Doll Type Cryogenic Traps: Improved Design and Isotope Separation Effects. *Analytical Chemistry*, *68*(17), 3050-3053. https://doi.org/10.1021/ac960208w

Burkholder, J., Sander, S., Abbatt, J., Barker, J., Huie, R., Kolb, C., Kurylo, M., Orkin, V., Wilmouth, D., & Wine, P. (2015). *Chemical kinetics and photochemical data for use in atmospheric studies: evaluation number 18*.

Chakraborty, S., Jackson, T. L., Rude, B., Ahmed, M., & Thiemens, M. H. (2016). Nitrogen isotopic fractionations in the low temperature (80 K) vacuum ultraviolet photodissociation of N_2. *The Journal of Chemical Physics*, *145*(11), 114302. https://doi.org/10.1063/1.4962447

Chakraborty, S., Muskatel, B. H., Jackson, T. L., Ahmed, M., Levine, R. D., & Thiemens, M. H. (2014). Massive isotopic effect in vacuum UV photodissociation of N_2O and implications for meteorite data. *Proceedings of the National Academy of Sciences*, *111*(41), 14704-14709. https://doi.org/10.1073/pnas.1410440111

Chen, J., & Davidson, J. H. (2002a). Electron Density and Energy Distributions in the Positive DC Corona: Interpretation for Corona-Enhanced Chemical Reactions. *Plasma Chemistry and Plasma Processing*, *22*(2), 199-224. https://doi.org/10.1023/A:1014851908545

Chen, J., & Davidson, J. H. (2002b). Ozone Production in the Positive DC Corona Discharge: Model and Comparison to Experiments. *Plasma Chemistry and Plasma Processing*, *22*(4), 495-522. https://doi.org/10.1023/A:1021315412208

Croteau, P., Atlas, E. L., Schauffler, S. M., Blake, D. R., Diskin, G. S., & Boering, K. A. (2010). Effect of local and regional sources on the isotopic composition of nitrous oxide in the tropical free troposphere and tropopause layer. *Journal of Geophysical Research: Atmospheres*, *115*(D10). https://doi.org/https://doi.org/10.1029/2009JD013117

de Sousa, A. R., Touzeau, M., & Petitdidier, M. (1985). Quenching reactions of metastable $N_2(A\ ^3\Sigma, \upsilon = 0, 1, 2)$ molecules by O_2. *Chemical Physics Letters*, *121*(4), 423-428. https://doi.org/https://doi.org/10.1016/0009-2614(85)87207-9

DeMore, W., & Raper, O. (1962). Reaction of O (^{1}D) with nitrogen. *The Journal of Chemical Physics*, *37*(9), 2048-2052.

Estupinán, E., Nicovich, J., Li, J., Cunnold, D., & Wine, P. (2002). Investigation of N_2O production from 266 and 532 nm laser flash photolysis of $O_3/N_2/O_2$ mixtures. *The Journal of Physical Chemistry A*, *106*(24), 5880-5890.

Fibiger, D. L., Hastings, M. G., Lew, A. F., & Peltier, R. E. (2014). Collection of NO and NO_2 for Isotopic Analysis of NO_x Emissions. *Analytical Chemistry*, *86*(24), 12115-12121. https://doi.org/10.1021/ac502968e

Fraser, M. E., & Piper, L. G. (1989). Product branching ratios from the nitrogen ($A^3\Sigma_u^+$) + oxygen interaction. *The Journal of Physical Chemistry*, *93*(3), 1107-1111.

Freyer, H. D., Kley, D., Volz-Thomas, A., & Kobel, K. (1993). On the interaction of isotopic exchange processes with photochemical reactions in atmospheric oxides of nitrogen. *Journal of Geophysical Research: Atmospheres*, *98*(D8), 14791-14796. https://doi.org/https://doi.org/10.1029/93JD00874

Fridman, A. (2008). *Plasma chemistry*. Cambridge university press.

Funke, B., García-Comas, M., López-Puertas, M., Glatthor, N., Stiller, G. P., Von Clarmann, T., Semeniuk, K., & McConnell, J. C. (2008). Enhancement of N_2O during the October–November 2003 solar proton events. *Atmospheric Chemistry and Physics*, *8*(14), 3805-3815. https://doi.org/10.5194/acp-8-3805-2008

Funke, B., López-Puertas, M., Garcia-Comas, M., Stiller, G., Clarmann, T. v., & Glatthor, N. (2008). Mesospheric N_2O enhancements as observed by MIPAS on Envisat during the polar winters in 2002–2004. *Atmospheric Chemistry and Physics*, *8*(19), 5787-5800.

Gidon, D., Pei, X., Bonzanini, A. D., Graves, D. B., & Mesbah, A. (2019). Machine Learning for Real-Time Diagnostics of Cold Atmospheric Plasma Sources. *IEEE Transactions on Radiation and Plasma Medical Sciences*, *3*(5), 597-605. https://doi.org/10.1109/TRPMS.2019.2910220

Gordiets, B. F., Ferreira, C. M., Guerra, V. L., Loureiro, J. M. A. H., Nahorny, J., Pagnon, D., Touzeau, M., & Vialle, M. (1995). Kinetic model of a low-pressure N_2-O_2 flowing glow discharge. *IEEE Transactions on Plasma Science*, *23*(4), 750-768. https://doi.org/10.1109/27.467998

Gordiets, B. F., & Mamedov, S. S. (1975). Isotope separation in chemical reactions of vibrationally excited molecules. *Soviet Journal of Quantum Electronics*, *5*(9), 1082-1084. https://doi.org/10.1070/qe1975v005n09abeh011907

Gorshunov, N. M., & Gudenko, S. V. (2003). Enrichment of the nitrogen atomic component with the ^{15}N isotope in a post-discharge zone. *Journal of Experimental and Theoretical Physics Letters*, *77*(4), 162-166. https://doi.org/10.1134/1.1571874

Govers, T. R., Runstraat, C. A. v. d., & Heer, F. J. d. (1973). Isotope effects in the predissociation of the $C^2\Sigma_u^+$ state of N_2^+. *Journal of Physics B: Atomic and Molecular Physics*, *6*(4), L73-L76. https://doi.org/10.1088/0022-3700/6/4/007

Graves, D. B., Bakken, L. B., Jensen, M. B., & Ingels, R. (2019). Plasma Activated Organic Fertilizer. *Plasma Chemistry and Plasma Processing*, *39*(1), 1-19. https://doi.org/10.1007/s11090-018-9944-9

Herron, J. T., & Green, D. S. (2001). Chemical Kinetics Database and Predictive Schemes for Nonthermal Humid Air Plasma Chemistry. Part II. Neutral Species Reactions. *Plasma Chemistry and Plasma Processing*, *21*(3), 459-481. https://doi.org/10.1023/A:1011082611822

Ianni, J. C. (2017). *Kintecus*. Retrieved 2017 from www.kintecus.com

Iannuzzi, M., Jeffries, J., & Kaufman, F. (1982). Product channels of the N_2 ($A^3\Sigma^+_u$) + O_2 interaction. *Chemical Physics Letters*, *87*(6), 570-574.

Isbary, G., Zimmermann, J. L., Shimizu, T., Li, Y. F., Morfill, G. E., Thomas, H. M., Steffes, B., Heinlin, J., Karrer, S., & Stolz, W. (2013). Non-thermal plasma—More than five years of clinical experience. *Clinical Plasma Medicine*, *1*(1), 19-23. https://doi.org/https://doi.org/10.1016/j.cpme.2012.11.001

Janda, M., Martišovitš, V., Hensel, K., Dvonč, L., & Machala, Z. (2014). Measurement of the electron density in Transient Spark discharge. *Plasma Sources Science and Technology*, *23*(6), 065016. https://doi.org/10.1088/0963-0252/23/6/065016

Kossyi, I. A., Kostinsky, A. Y., Matveyev, A. A., & Silakov, V. P. (1992). Kinetic scheme of the non-equilibrium discharge in nitrogen-oxygen mixtures. *Plasma Sources Science and Technology*, *1*(3), 207-220. https://doi.org/10.1088/0963-0252/1/3/011

Laux, C., Spence, T., Kruger, C., & Zare, R. (2003). Plasma Sources Sci. Technol. In.

Levine, J. S., & Shaw, E. F. (1983). In situ aircraft measurements of enhanced levels of N_2O associated with thunderstorm lightning. *Nature*, *303*(5915), 312-314. https://doi.org/10.1038/303312a0

Li, J., Zhang, X., Orlando, J., Tyndall, G., & Michalski, G. (2020). Quantifying the nitrogen isotope effects during photochemical equilibrium between NO and NO_2: implications for $\delta^{15}N$ in tropospheric reactive nitrogen. *Atmos. Chem. Phys.*, *20*(16), 9805-9819. https://doi.org/10.5194/acp-20-9805-2020

Machala, Z., Janda, M., Hensel, K., Jedlovský, I., Leštinská, L., Foltin, V., Martišovitš, V., & Morvova, M. (2007). Emission spectroscopy of atmospheric pressure plasmas for bio-medical and environmental applications. *Journal of Molecular Spectroscopy*, *243*(2), 194-201.

Manuccia, T. J., & Clark, M. D. (1976). Enrichment of N^{15} by chemical reactions in a glow discharge at 77 °K. *Applied Physics Letters*, *28*(7), 372-374. https://doi.org/10.1063/1.88785

MATLAB. (2019). *Version 9.6.0.1135713 (2019a)* The MathWorks Inc.

Mätzing, H. (1991). Chemical kinetics of flue gas cleaning by irradiation with electrons. *Advances in chemical physics*, *80*, 315-402.

McLaughlin, D. F., & Christiansen, W. H. (1986). Isotope separation and yield calculations for vibrationally enhanced oxidation of nitrogen. *The Journal of Chemical Physics*, *84*(5), 2643-2648. https://doi.org/10.1063/1.450335

Mesbah, A., & Graves, D. B. (2019). Machine learning for modeling, diagnostics, and control of non-equilibrium plasmas. *Journal of Physics D: Applied Physics*, *52*(30), 30LT02.

Metelmann, H.-R., Seebauer, C., Rutkowski, R., Schuster, M., Bekeschus, S., & Metelmann, P. (2018). Treating cancer with cold physical plasma: On the way to evidence-based medicine. *Contributions to Plasma Physics*, *58*(5), 415-419. https://doi.org/https://doi.org/10.1002/ctpp.201700085

National Academies of Sciences, E., & Medicine. (2021). *Plasma Science: Enabling Technology, Sustainability, Security, and Exploration*. The National Academies Press. https://doi.org/doi:10.17226/25802

Nguyen, N. T. A., Ichikawa, M., Mori, S., & Suzuki, M. (2011). Nitrogen Isotope Separation by Plasma Chemical Reaction in N_2-O_2 DC Glow Discharge. Journal of Chemical Engineering of Japan, 1105240208-1105240208.

Nitrous oxide. (2018). NIST Chemistry WebBook, U.S. Secretary of Commerce.

Park, S. (2004). Measurements of N_2O isotopologues in the stratosphere: Influence of transport on the apparent enrichment factors and the isotopologue fluxes to the troposphere. *Journal of Geophysical Research*, *109*(D1). https://doi.org/10.1029/2003jd003731

Park, S., Croteau, P., Boering, K. A., Etheridge, D. M., Ferretti, D., Fraser, P. J., Kim, K. R., Krummel, P. B., Langenfelds, R. L., Van Ommen, T. D., Steele, L. P., & Trudinger, C. M. (2012). Trends and seasonal cycles in the isotopic composition of nitrous oxide since 1940. *Nature Geoscience*, *5*(4), 261-265. https://doi.org/10.1038/ngeo1421

Pavlovich, M. J., Chang, H.-W., Sakiyama, Y., Clark, D. S., & Graves, D. B. (2013). Ozone correlates with antibacterial effects from indirect air dielectric barrier discharge treatment of water. *Journal of Physics D: Applied Physics*, *46*(14), 145202. https://doi.org/10.1088/0022-3727/46/14/145202

Pavlovich, M. J., Clark, D. S., & Graves, D. B. (2014). Quantification of air plasma chemistry for surface disinfection. *Plasma Sources Science and Technology*, *23*(6), 065036. https://doi.org/10.1088/0963-0252/23/6/065036

Pavlovich, M. J., Sakiyama, Y., Clark, D. S., & Graves, D. B. (2013). Antimicrobial Synergy Between Ambient-Gas Plasma and UVA Treatment of Aqueous Solution. *Plasma Processes and Polymers*, *10*(12), 1051-1060. https://doi.org/https://doi.org/10.1002/ppap.201300065

Pei, X., Liu, J., Xian, Y., & Lu, X. (2014). A battery-operated atmospheric-pressure plasma wand for biomedical applications. *Journal of Physics D: Applied Physics*, *47*(14), 145204. https://doi.org/10.1088/0022-3727/47/14/145204

Pei, X., Lu, X., Liu, J., Liu, D., Yang, Y., Ostrikov, K., Chu, P. K., & Pan, Y. (2012). Inactivation of a 25.5 μmEnterococcus faecalisbiofilm by a room-temperature, battery-operated, handheld air plasma jet. *Journal of Physics D: Applied Physics*, *45*(16), 165205. https://doi.org/10.1088/0022-3727/45/16/165205

Pérez-Invernón, F. J., Malagón-Romero, A., Gordillo-Vázquez, F. J., & Luque, A. (2020). The Contribution of Sprite Streamers to the Chemical Composition of the Mesosphere-Lower Thermosphere. *Geophysical Research Letters*, *47*(14), e2020GL088578. https://doi.org/https://doi.org/10.1029/2020GL088578

Sakiyama, Y., Graves, D. B., Chang, H.-W., Shimizu, T., & Morfill, G. E. (2012). Plasma chemistry model of surface microdischarge in humid air and dynamics of reactive neutral species. *Journal of Physics D: Applied Physics*, *45*(42), 425201. https://doi.org/10.1088/0022-3727/45/42/425201

Schmidt-Bleker, A., Bansemer, R., Reuter, S., & Weltmann, K.-D. (2016). How to produce an NO_x- instead of O_x-based chemistry with a cold atmospheric plasma jet. *Plasma Processes and Polymers*, *13*(11), 1120-1127. https://doi.org/https://doi.org/10.1002/ppap.201600062

Semeniuk, K., McConnell, J. C., Jin, J. J., Jarosz, J. R., Boone, C. D., & Bernath, P. F. (2008). N_2O production by high energy auroral electron precipitation. *Journal of Geophysical Research*, *113*(D16). https://doi.org/10.1029/2007jd009690

Sharma, H., Jervis, R., & Wong, K. (1970). Isotopic exchange reactions in nitrogen oxides. *The Journal of Physical Chemistry*, *74*(4), 923-933.

Shkurenkov, I., Burnette, D., Lempert, W. R., & Adamovich, I. V. (2014). Kinetics of excited states and radicals in a nanosecond pulse discharge and afterglow in nitrogen and air. *Plasma Sources Science and Technology*, *23*(6), 065003. https://doi.org/10.1088/0963-0252/23/6/065003

Smith, M. C., Carlstad, J. M., Hunter, P. Q., Randazzo, J., & Boering, K. A. (2021). Nitrous Oxide Formation by Corona Discharge: Isotopic Composition Measurements and Atmospheric Applications. *Journal of Geophysical Research: Atmospheres*, *126*(8). https://doi.org/10.1029/2020jd033927

Thiemens, M. H., & Heidenreich, J. E. (1983). The Mass-Independent Fractionation of Oxygen: A Novel Isotope Effect and Its Possible Cosmochemical Implications. *Science*, *219*(4588), 1073-1075. https://doi.org/10.1126/science.219.4588.1073

Toyoda, S., & Yoshida, N. (1999). Determination of Nitrogen Isotopomers of Nitrous Oxide on a Modified Isotope Ratio Mass Spectrometer. *Analytical Chemistry*, *71*(20), 4711-4718. https://doi.org/10.1021/ac9904563

Voráč, J., Synek, P., Potočňáková, L., Hnilica, J., & Kudrle, V. (2017). Batch processing of overlapping molecular spectra as a tool for spatio-temporal diagnostics of power modulated microwave plasma jet. *Plasma Sources Science and Technology*, *26*(2), 025010. https://doi.org/10.1088/1361-6595/aa51f0

Walters, W. W., Simonini, D. S., & Michalski, G. (2016). Nitrogen isotope exchange between NO and NO_2 and its implications for $\delta^{15}N$ variations in tropospheric NO_x and atmospheric nitrate. *Geophysical Research Letters*, *43*(1), 440-448. https://doi.org/https://doi.org/10.1002/2015GL066438

Wennberg, P. O., Anderson, J. G., & Weisenstein, D. K. (1994). Kinetics of reactions of ground state nitrogen atoms ($^4S_{3/2}$) with NO and NO_2. *Journal of Geophysical Research: Atmospheres*, *99*(D9), 18839-18846. https://doi.org/https://doi.org/10.1029/94JD01823

Yeung, L. Y., Affek, H. P., Hoag, K. J., Guo, W., Wiegel, A. A., Atlas, E. L., Schauffler, S. M., Okumura, M., Boering, K. A., & Eiler, J. M. (2009). Large and unexpected enrichment in stratospheric $^{16}O^{13}C^{18}O$ and its meridional variation. *Proceedings of the National Academy of Sciences*, *106*(28), 11496-11501. https://doi.org/10.1073/pnas.0902930106

Zipf, E. C. (1980). A laboratory study on the formation of nitrous oxide by the reaction $N_2(A^3\Sigma_u^+) + O_2 \rightarrow N_2O + O$. *Nature*, *287*(5782), 523-524. https://doi.org/10.1038/287523a0

Appendix: Supplemental Material

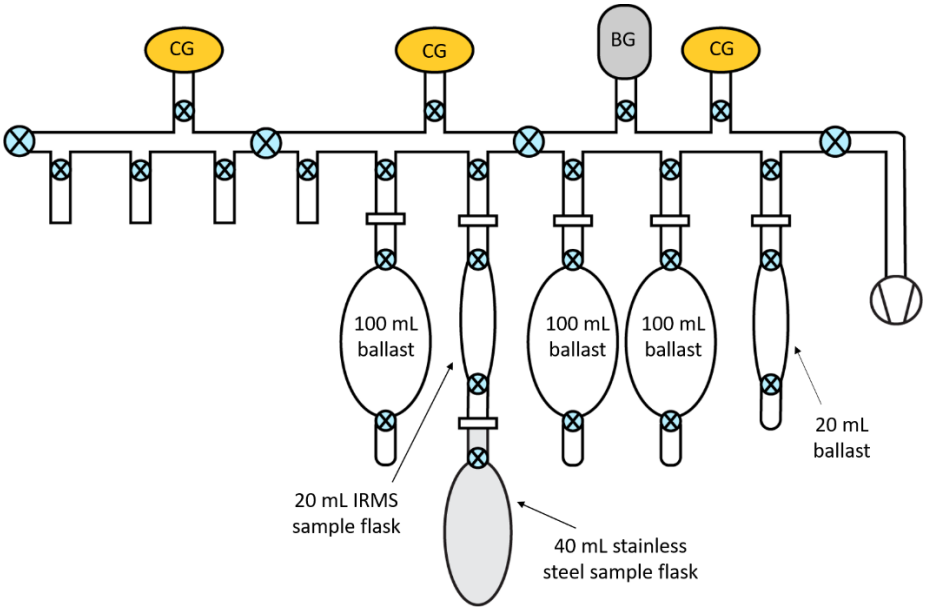

Figure 2.S1: Diagram of the gas transfer line used for sample aliquot preparation before analysis on the IRMS.

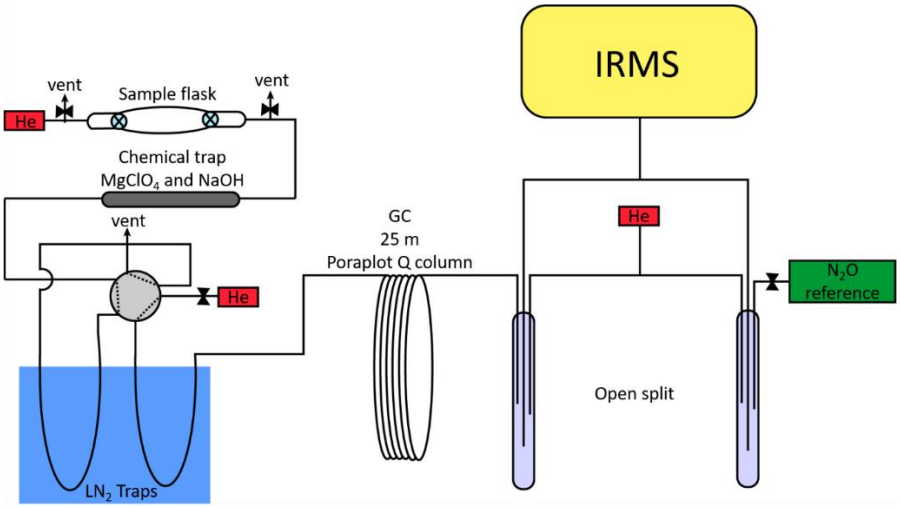

Figure 2.S2: Schematic of the preconcentrator, GC, and open split interface for N_2O as part of the online continous-flow IRMS apparatus for analysis of the isotope composition of N_2O.

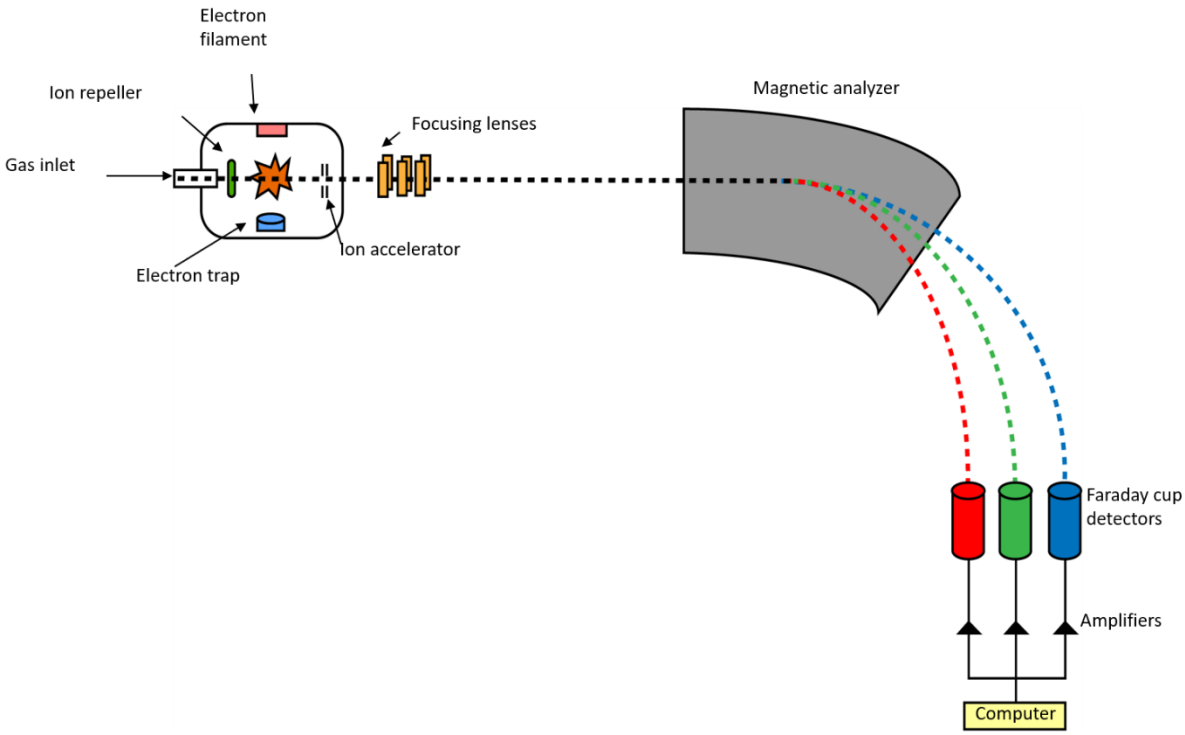

Figure 2.S3: Diagram of the IRMS used for isotopic analysis.

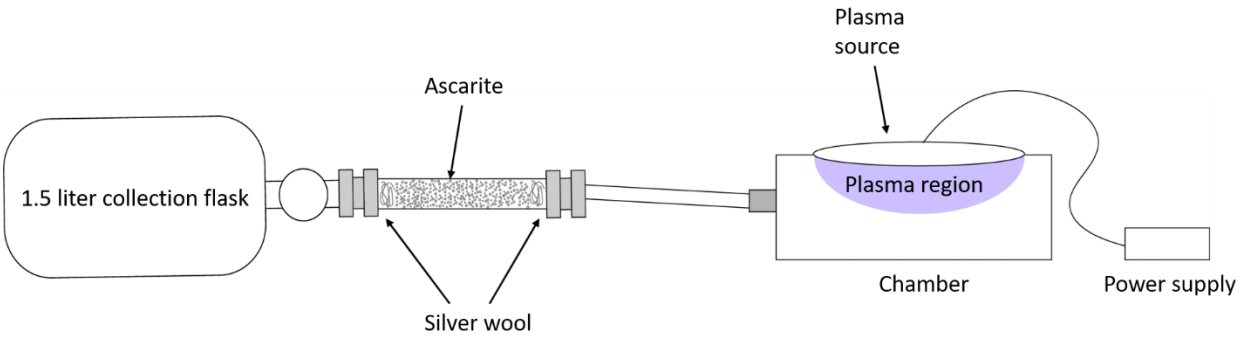

Figure 2.S4: Diagram of setup for plasma sample generation and collection.

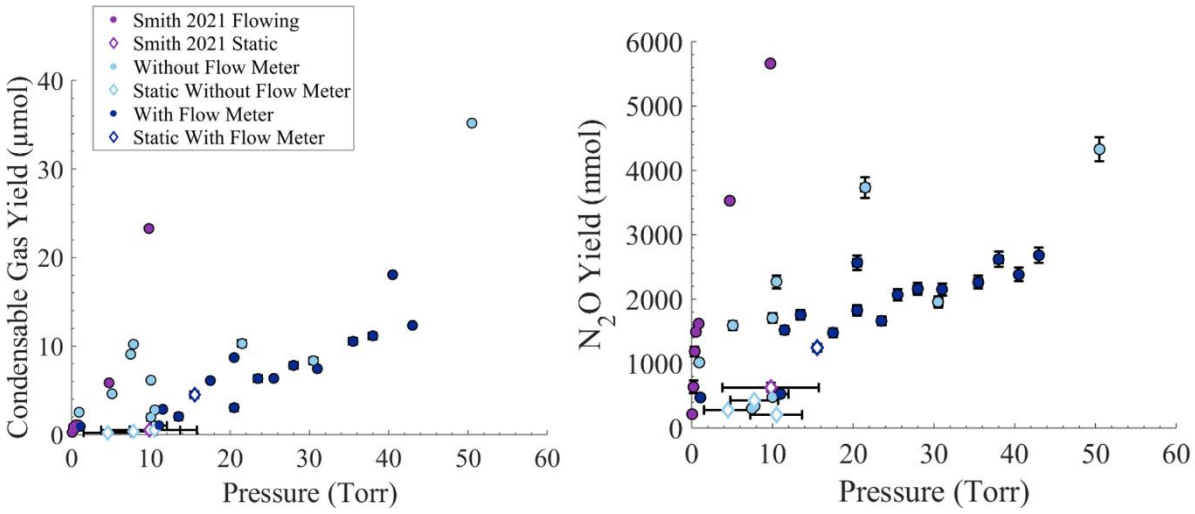

Figure 2.S5: Yield of (a) condensable gas (largely NO and N_2O) from the manometric calibration on the corona discharge line and (b) N_2O from the IRMS peak area, both as a function of measured pressure in the corona discharge cell. Note that the Smith *et al.* (2021) pressures at 5 and 10 Torr are likely much higher (40 to 60 Torr); see text.

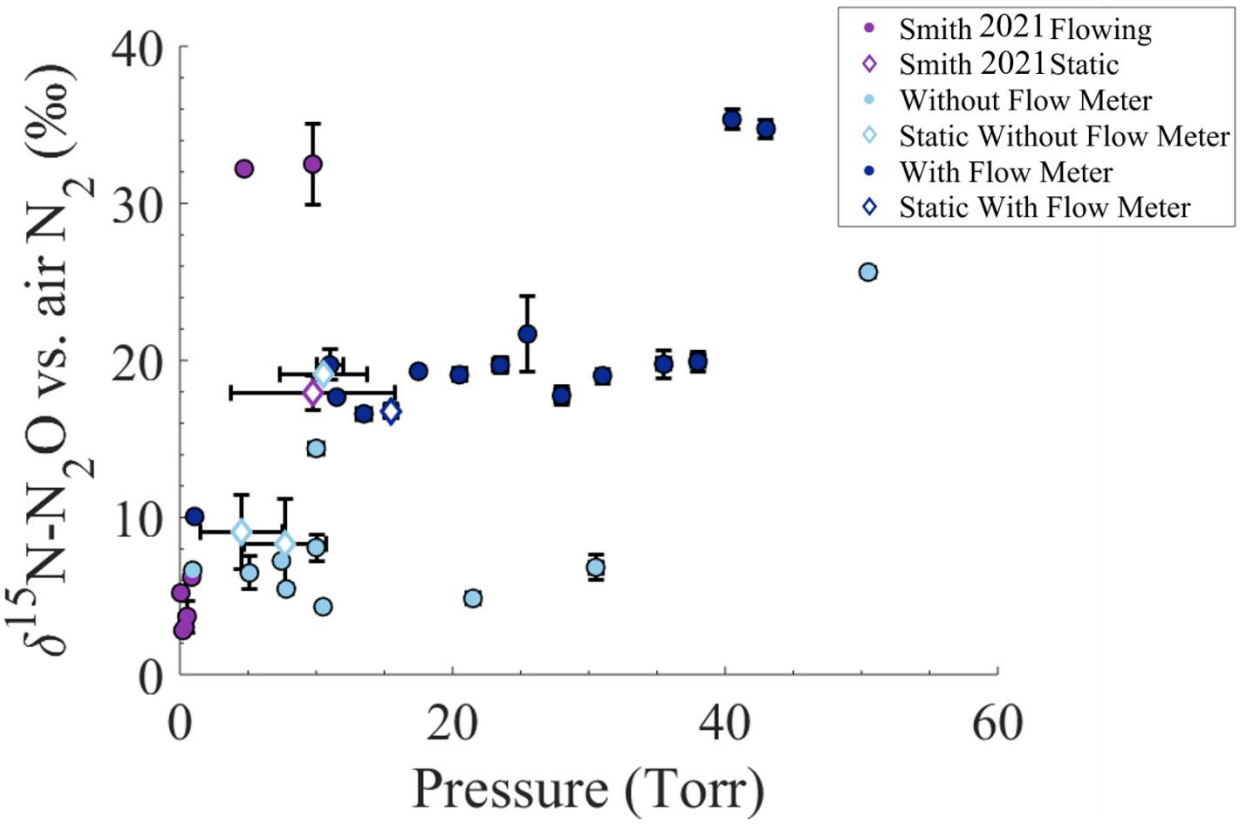

Figure 2.S6: Plot of $\delta^{15}N$ bulk versus pressure in the corona discharge cell.

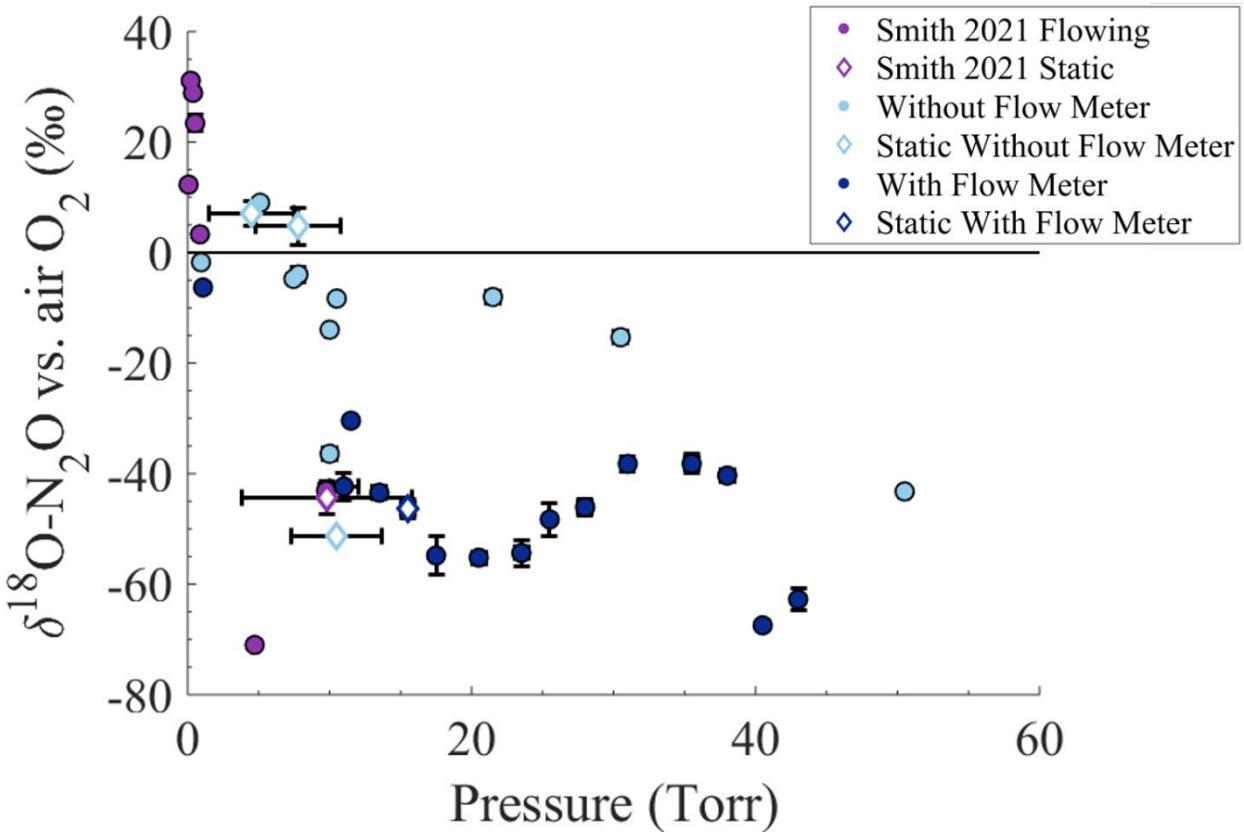

Figure 2.S7: Plot of $\delta^{18}O$ versus pressure in the corona discharge cell for the corona discharge experiments.

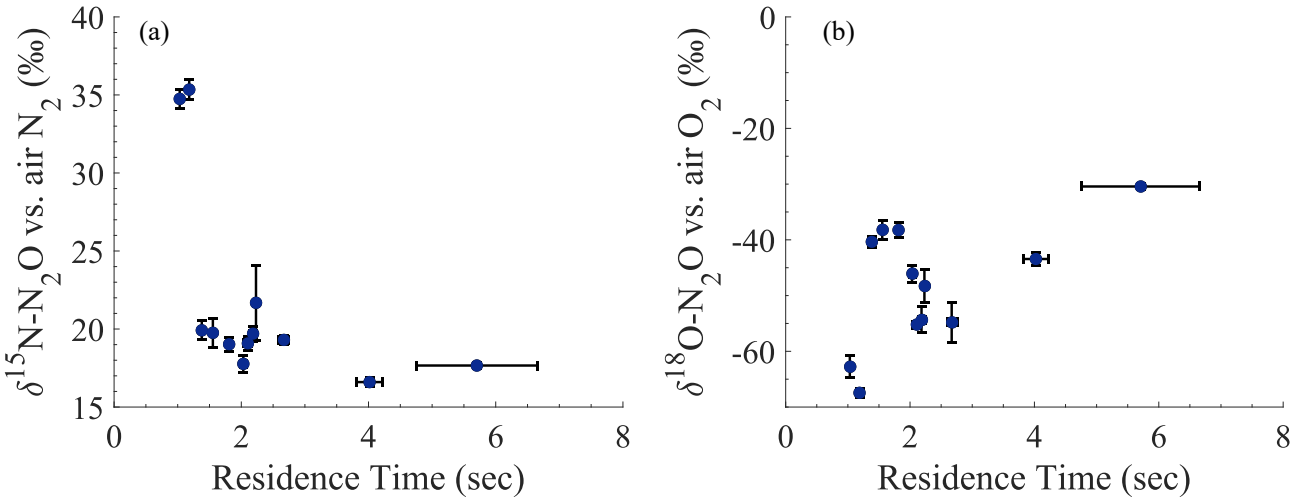

Figure 2.S8: Plots of (a) $\delta^{15}N$ and (b) $\delta^{18}O$ of N_2O generated in the corona discharge versus residence time measured with the flow meter.

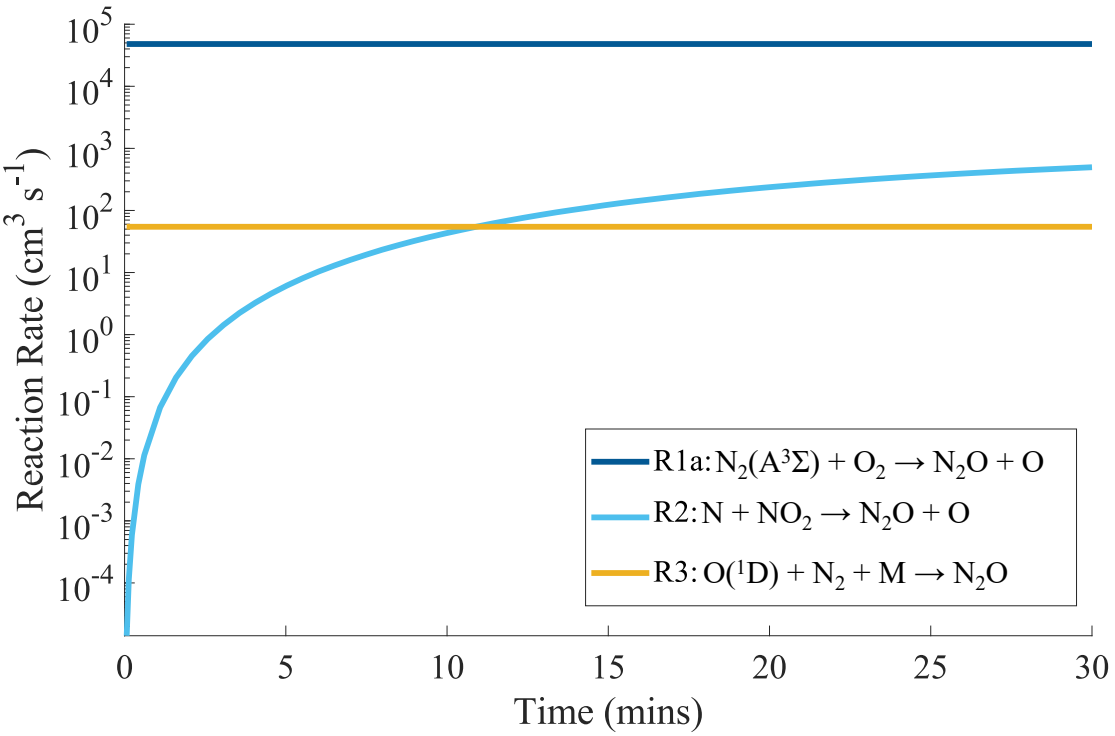

Figure 2.S9: Reaction rates from the Kintecus-based NEP simulations for the corona discharge over 30 minutes. R1a is plotted in dark blue, R2 is plotted in light blue, and R3 is plotted in yellow.

Chapter 3

High Latitude Vertical Profiles of $^{14}CO_2$ across the tropopause from the Atmospheric Tomography (ATom) Mission

Key Points

- A series of whole air samples that span the tropopause at high latitudes in both the northern and southern hemisphere in May 2018 were measured for $\Delta^{14}C\text{-}CO_2$.
- Key hemispheric differences in the lowermost stratosphere include higher ^{14}C in the south and lower N_2O in the north, informing differences in transport.
- Inferred global ^{14}C production rates are skewed high, consistent with recent isentropic transport of air into the lowermost stratosphere.

Abstract

Measurements of $\Delta^{14}C\text{-}CO_2$ on whole air samples collected by the NASA DC-8 aircraft during the fourth Atmospheric Tomography Mission deployment (ATom-4) in May 2018 provide the first near-simultaneous vertical profiles of $\Delta^{14}C\text{-}CO_2$ across the tropopause at high latitudes in both hemispheres. The measurements span latitudes of 62 to 69°N and altitudes of ~0.2 to 12 km, with a maximum potential temperature, θ, of 366 K in the north, and 57 to 81°S and ~0.2 to 11.5 km, with a maximum θ of 350 K, in the south. In addition to providing new vertical constraints at high latitudes for inverse models, the measurements show interesting hemispheric differences. A hemispheric offset of 8±1‰ in radiocarbon in the lowermost stratosphere (i.e., $\theta < \sim 380$ K) could result from seasonal and hemispheric differences in factors such as: the amounts of isentropic transport from the subtropical upper troposphere into the lowermost stratosphere, the magnitudes of downwelling from the overworld (i.e., $\theta > 380$ K), tropospheric radiocarbon levels, or some combination of these factors. These data are thus both unique from and complementary to other troposphere-to-stratosphere tracers, which together provide constraints on the balance of these convolved dynamical factors that determine the chemical composition of the lowermost stratosphere. Further, the new radiocarbon data and a comparison with data from past missions – including SEAC^{4}RS (2013), DC-3 (2012), Pre-AVE (2004), SOLVE (2000), POLARIS (1997), and balloon flights in 2003, 2004, and 2005 – reveal that inferring global ^{14}C production rates empirically from measured $\Delta^{14}C\text{-}CO_2$:N_2O relationships is not robust for the lowermost stratosphere, due to the substantial contribution of isentropic mixing in of new air from the troposphere that short-circuits the Brewer-Dobson circulation into the stratospheric overworld.

3.1 Introduction

Radiocarbon is produced in the extratropical upper troposphere and lower stratosphere by the reaction of neutrons from cosmic rays (or atmospheric nuclear weapon detonations in the middle of the last Century) with ^{14}N nuclei, producing ^{14}C, which has a half-life of 5780 years. Discovered in nature by Libby in 1947 [Libby, 1947], ^{14}C has been extensively used in the earth sciences as a tracer of the magnitudes and rates of exchange of carbon between various atmospheric, oceanic, and biospheric reservoirs [e.g., Naegler & Levin, 2006; Randerson et al. 2002, Shi et al. 2020;

Kusch et al.. 2021], of the oceanic [e.g., Broecker et al., 1988, Alves et al., 2018, Guilderson et al., 2021] and stratospheric [e.g., Johnston 1989; Kinnison et al., 1994] circulations, and of the human impact on the atmosphere from fossil fuel burning [e.g., Suess 1955; Basu et al., 2016, 2020].

Until recently, most stratospheric $^{14}CO_2$ measurements were made prior to 1975 on very large whole air samples collected by aircraft such as the WB57 and by high altitude balloons [e.g., Johnston 1989], and at a time when the stratosphere was still influenced by ^{14}C produced by atmospheric nuclear weapons testing in the 1950s and 1960s. With the advent of ^{14}C analysis by accelerator mass spectrometry (AMS) enabling precise measurements on much smaller samples [Povinec et al., 2009], as well as renewed interest in the stratospheric circulation [e.g., Butchart 2014; Oman et al., 2009] and its influence on measurements made at Earth's surface [e.g., Randerson et al., 2002; Garofalo et al., 2019], we began analyzing small whole air samples collected in the upper troposphere and stratosphere for $^{14}CO_2$ [e.g., Kanu et al., 2016; Garofalo et al., 2019]. These "post-Post-Bomb era" $^{14}CO_2$ measurements currently span the years from 1997 to 2013 from samples collected during NASA missions from POLARIS [Newman et al., 1999] to SEAC4RS [Toon et al., 2016], respectively. Using a combination of $\Delta^{14}C\text{-}CO_2$ and nitrous oxide (N_2O) measurements from these whole air samples has allowed for investigation of stratospheric transport, as well as entirely empirical calculations of the natural cosmogenic ^{14}C production rate [Kanu et al., 2016; Garofalo et al., 2019] to compare with ^{14}C production rates from physics-based models of the cascade of particles induced by galactic cosmic rays penetrating to different depths of the atmosphere [e.g., Lal and Peters, 1967, Kovaltsov et al., 2012] and from mass balance reservoir models from observations of the redistribution of bomb radiocarbon [Naegler & Levin, 2006]. These modern measurements of $\Delta^{14}C\text{-}CO_2$ in the free troposphere to the stratosphere have also provided important new vertical constraints for inverse models that seek to constrain the sources and sinks of CO_2 [e.g. Basu et al., 2016; Graven et al., 2015; Levin et al., 2003, 2010; Turnbull et al., 2011; Randerson et al., 2002].

In this chapter, I report measurements of $\Delta^{14}C\text{-}CO_2$ on samples collected from the NASA DC-8 aircraft during the fourth deployment of the NASA Atmospheric Tomography (ATom) mission in May 2018. Samples were collected near-simultaneously at high latitudes in both hemispheres, resulting in vertical profiles of $\Delta^{14}C\text{-}CO_2$ from altitudes of ~0.2 km to across the tropopause, and thus provide new vertical constraints needed for inverse models to deduce the magnitudes and distributions of surface sources and sinks of CO_2. The maximum altitude of the DC-8 of ~13 km allowed sampling well into the high latitude "stratospheric middleworld" (also known as the "lowermost stratosphere") – a region defined as the part of the stratosphere that is above the local tropopause but with a potential temperature (θ) less than 380K, which is the potential temperature of the typical tropopause temperature in the tropics, as illustrated in Figure 3.1. This region of the stratosphere is arguably more chemically and dynamically complex than the "overworld" (i.e., θ>380 K) since air can enter the lowermost stratosphere by downwelling from the overworld, by isentropic (i.e., quasi-horizontal) transport from the upper troposphere across the subtropical jet, and in some cases [e.g., Holton 1995; Anderson et al., 2012] by episodic diabatic transport through deep convection in the northern hemisphere in summer. The balance of these different transport processes into and out of the lowermost stratosphere and how they may be changing over time is not well-known and yet has important implications for dynamical, chemical, and climate feedbacks, such as the amount of ozone and water vapor in the upper troposphere/lower stratosphere (UT/LS) [e.g., Rind et al., 1990; Solomon et al., 2010; Dessler et al., 2013; Wang &

Huang, 2020]. Since $^{14}CO_2$ can build up in the stratosphere (due to its stratospheric source and tropospheric sink) and is typically lower in the northern than the southern hemisphere due to differences in fossil fuel emissions (which contain no $^{14}CO_2$ molecules due to the fossil source of the carbon), $\Delta^{14}C\text{-}CO_2$ is thus both unique from, and complementary, to other tracers typically used to investigate stratosphere-troposphere exchange and the controls on the chemical composition of the lowermost stratosphere, which I explore below. The new data obtained in the lowermost stratosphere also allow a test of whether the Plumb [2007] and Plumb and Ko [1992] method for determining the net vertical flux of $^{14}CO_2$ from the stratosphere to the troposphere (and hence the cosmogenic ^{14}C production rate, as in Kanu *et al.* [2016]) from the empirical correlation between measurements of $\Delta^{14}C\text{-}CO_2$ and N_2O is valid below the 'overworld.'

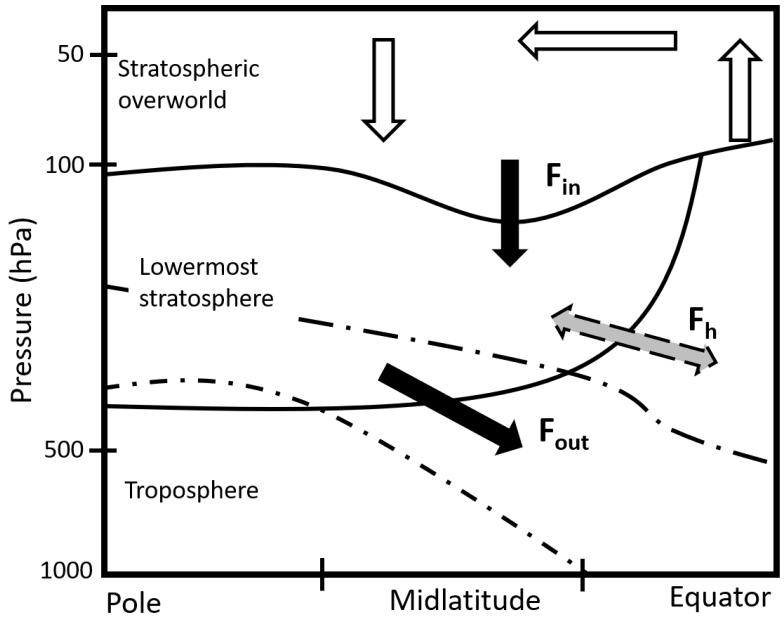

Figure 3.1: Schematic of the troposphere, different regions of the stratosphere, and the mass fluxes between them: Air enters the stratospheric "overworld" in the tropics across the tropical tropopause (θ~380K) and follows the global-scale meridional stratospheric circulation (open arrows), also known as the Brewer-Dobson circulation (BDC). Air descends from the overworld across the 380K surface that separates the "stratospheric overworld" from the "lowermost stratosphere" (shown as the top solid curve) with flux F_{in}. The magnitude of F_{in} varies seasonally and, thus, the mass of the lowermost stratosphere varies seasonally as well. Air leaves the lowermost stratosphere across the extratropical tropopause (denoted by the lower solid line) via the flux indicated by F_{out}. Air can also be transported isentropically (or "quasi-horizontally") into and out of the lowermost stratosphere without ever having entered the stratospheric overworld, with a flux indicated by F_h, in effect "short-circuiting" the BDC. [Adapted from Figure 1 of *Appenzeller* (1996).]

3.2 Methods

Whole air samples were collected aboard the NASA DC-8 aircraft during the ATom-4 mission in May 2018 [Wofsy et al., 2018]. The DC-8 has a maximum flying altitude of 13 km so samples were limited to altitudes between ground level and 13 km, roughly corresponding to a

potential temperature, θ, of ~360 K and a pressure of ~165 hPa at midlatitudes based on the US standard atmosphere [Stepaniak, 2012]. This maximum altitude is often in the lowermost stratosphere at middle and high latitudes.

After sample collection, the mixing ratios of ~50 different trace gases, including n-pentane, i-pentane, and many others, were measured by gas chromatography at UC Irvine [Colman et al., 2001]. For a subset of samples that were collected at high latitudes in both hemispheres, samples were shipped to UC Berkeley where CO_2 was cryogenically extracted and stored in flame-sealed glass ampoules [e.g., Boering et al., 2004; Wiegel et al., 2013]. These samples were selected from Flight 7 on 5/9/2018 (latitudes from –57°S to –82°S), Flight 10 on 5/17/2018 (latitudes from 68°N to 75°N), and Flight 12 on 5/19/2018 (latitudes from 62°N to 69°N). At the Lawrence Livermore National Laboratory Center for Accelerator Mass Spectrometry (LLNL-CAMS), the CO_2 was reduced to graphite through a catalytic reduction by Fe in H_2; the graphite was pressed into aluminum targets; and the $\Delta^{14}C\text{-}CO_2$ was measured by AMS with an uncertainty (depending on sample size) between ± 1.6 ‰ and ± 2.0 ‰ [e.g. Graven et al., 2012a; b]. The $\Delta^{14}C\text{-}CO_2$ values reported are $\Delta^{14}C$ for geochemical samples that include corrections for fractionation and age of the sample [Stuiver & Polach [1977].

For additional information on the chemical and dynamical context of the samples for which $\Delta^{14}C\text{-}CO_2$ was measured, simultaneous measurements of the mixing ratios of N_2O, ozone (O_3), and water vapor (H_2O) are used here, measured *in situ* by the NOAA UCATS instrument [Hintsa et al., 2021]. UCATS measured O_3 using a dual beam ozone photometer with accuracy of ±5 ppb and precision of ±3 ppb; N_2O was measured using a two-channel gas chromatograph with precision reported for each measurement between ± 1.3 ppb and ± 1.4 ppb and accuracy of ±1%; and water vapor was measured *in situ* by a tunable diode laser hygrometer with an accuracy of ±3-5%and precision of ±2-3%.

As in Kanu *et al.* [2016] and Garofalo *et al.* [2019], global cosmogenic production rates for ^{14}C are evaluated here from the correlation of stratospheric $\Delta^{14}C\text{-}CO_2$ measurements with simultaneous measurements of N_2O mixing ratios: First, the global annual mean flux of ^{14}C from the stratosphere to the troposphere is proportional to the slope of the observed $\Delta^{14}C\text{-}CO_2$:N_2O relationship, which, according to Plumb [2007] and Plumb and Ko [1992] is the ratio of their global net vertical fluxes equation (1).

$$\text{Global annual mean net } ^{14}C \text{ flux} = [CO_2]\ m\ (-(\ L + G_{strat}\ )) \qquad (1)$$

In equation (1), m is the slope of the $\Delta^{14}C\text{-}CO_2$:N_2O relationship, $[CO_2]$ is the mixing ratio of carbon dioxide at the tropical tropopause [Andrews et al., 2001] when the samples were collected in 2018 based on ground-based data [NOAA ESRL, 2018], L is the loss rate of N_2O, or 4.5×10^{11} mol N_2O yr^{-1} [Minschwaner et al., 1993; Prather and Ehhalt, 2001], and G_{strat} is the stratospheric growth rate of N_2O, or 1.1×10^{10} mol N_2O yr^{-1} [Denman and Brasseur, 2007]. Here, the slope was calculated using a Williamson-York (WY) bivariate fit to account for the errors in the x and y data [Cantrell, 2008]. In order to reduce the potential artifact on the $\Delta^{14}C\text{-}CO_2$:N_2O slope from the influence of air that has very recently entered the lowermost stratosphere by "short-circuiting" the Brewer-Dobson (i.e., by entering via quasi-horizontal transport, F_h, in Figure 3.1 rather than by the open arrows, for which the Plumb [2007] method to determine the net vertical fluxes was derived), only stratospheric samples with low water vapor mixing ratios were used for the WY

regression. For this work, "low water vapor" was defined in the northern hemisphere (NH) as $H_2O(v) < 9$ ppmv and in the southern hemisphere (SH) as $H_2O(v) < 10$ ppmv. Slightly higher water mixing ratios were included in SH because of sparse sampling at high altitudes, where all samples collected were at altitudes below 11.5 km and $\theta \leq 350$ K. As discussed in detail in Kanu *et al.* [2016] and Garofalo *et al.* [2019], the global mean ^{14}C production rate is the global annual mean net ^{14}C flux from the stratosphere to the troposphere (Equation 1) multiplied by 2 given that half of the ^{14}C atoms produced in the extratropical upper troposphere and lower stratosphere are produced in the stratosphere [Masarik & Beer, 1999, 2009].

3.3 Results and Discussion

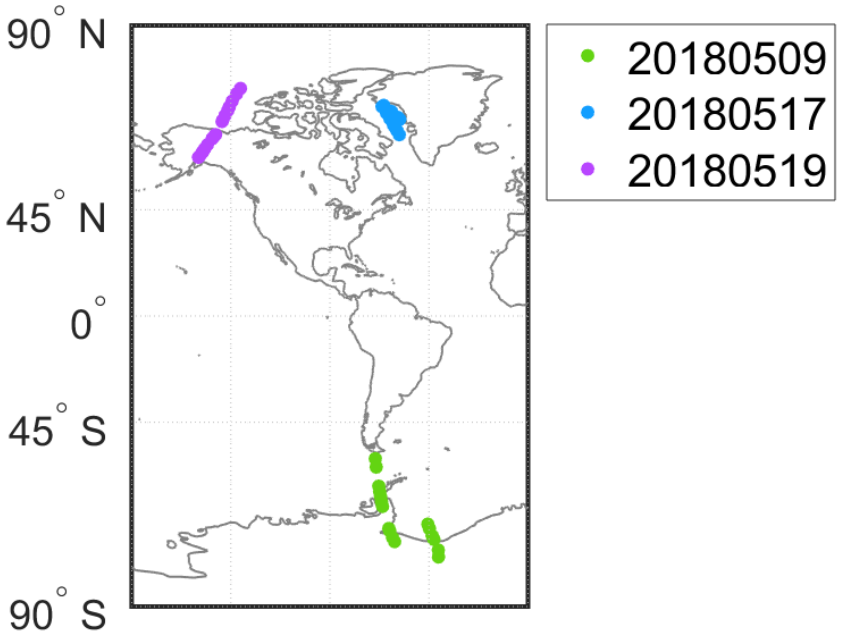

Figure 3.2: Map of the NASA DC-8 flight tracks for which samples were collected and analyzed for $\Delta^{14}C\text{-}CO_2$: Flight 7 (20180509), Flight 10 (20180517), and Flight 12 (20180519).

ATom-4 flight tracks for the DC8 aircraft for which whole air samples were analyzed for $\Delta^{14}C\text{-}CO_2$ are shown in Figure 3.2, while vertical profiles of the resulting $\Delta^{14}C\text{-}CO_2$ observations are shown in Figure 3.3. These new high latitude, vertical profiles from the NH and SH provide vertical constraints for inverse models that aim to make top-down estimates of the magnitude and geographic distribution of CO_2 sources and sinks from atmospheric observations. The transition from the troposphere to the stratosphere – from lower values of $\Delta^{14}C\text{-}CO_2$ in the troposphere to higher values in the stratosphere (where ^{14}C levels can build up due to cosmogenic ^{14}C production there and stratospheric residence times of ~ 3-5 years [Holton 1990; Hall & Waugh 2000; Andrews et al. 2001]) – are generally smooth.

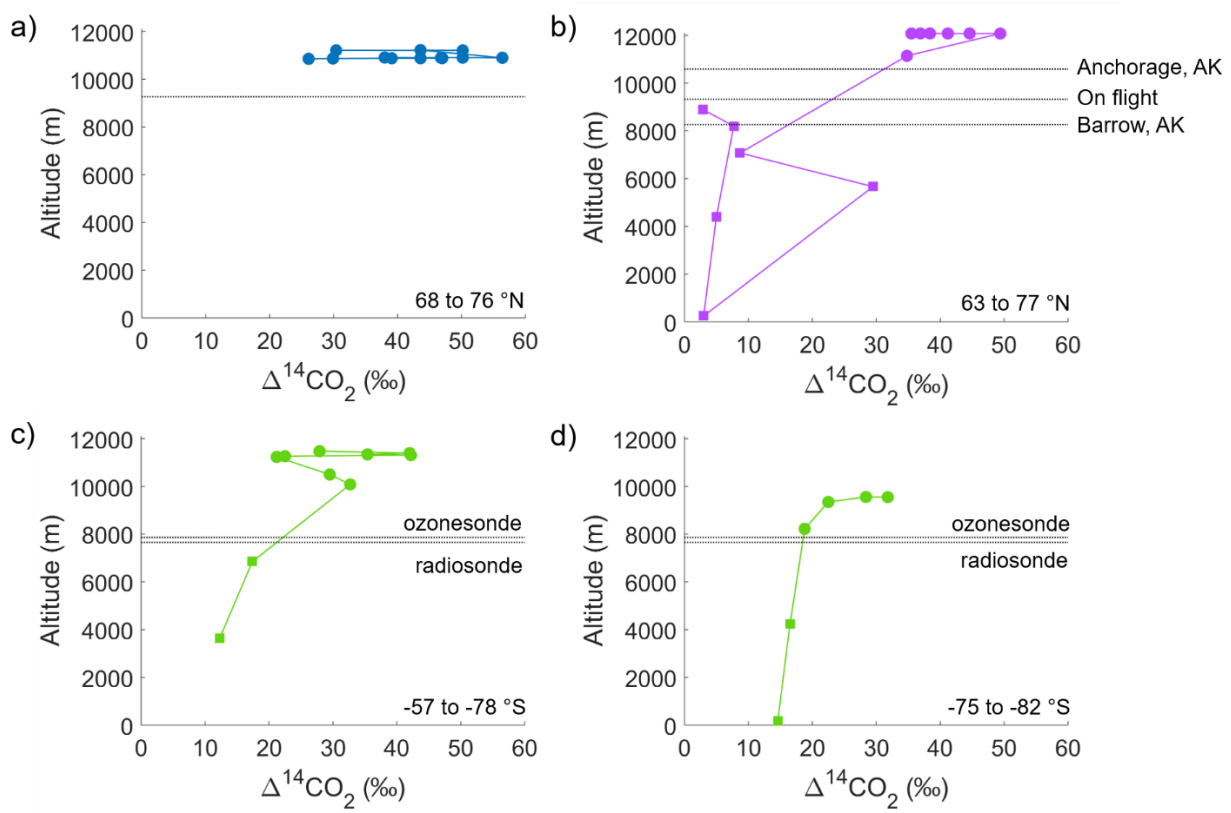

Figure 3.3: Vertical profiles of Δ^{14}C-CO_2 (N=41) measured on samples collected below (squares) and above (circles) the regional tropopause (black dotted lines) for (a) Flight 10=20180517, (b) Flight 12=20180519, and (c, d) Flight 7=20180509. The latitude range of the observations are given in the lower right of each figure. The tropopauses indicated by thin solid lines were determined by (a) a radiosonde launch at BGEM within 6 hours, (b) radiosondes at PANC (Anchorage) and PABR (Barrow) as well as a mid-flight temperature profile, and (c, d) by a radiosonde launch at Rothera and an ozonesonde launch at the Amundsen-Scott South Pole station. Profiles as a function of potential temperature are shown in Figure 3.S1, and additional tropospheric samples not plotted here are shown in Figure 3.S3 of Supplementary Materials.

However, there is one notable outlier in the samples extracted on Flight 12 (Figure 3.3(b)). Δ^{14}C-CO_2 for this sample is 29.5‰, or about 25‰ higher than other tropospheric samples on this flight date. It was collected at 72.25°N and −138.67°W at a potential temperature of 300 K and altitude of 5661 m, while the tropopause was at ~9300 m and θ=316 K. Simultaneous measurements of ozone (71 ppb) and water vapor (126 ppm) indicate that this sample collected in the troposphere had not recently returned from the stratosphere. Instead, the high Δ^{14}C-CO_2 is likely due to the influence of biomass burning. Biomass that was fixed by plants when radiocarbon in the atmosphere was higher due to atmospheric nuclear weapons testing can produce CO_2 with high ^{14}C content when burned, as previously observed by Vay *et al.* [2011] during the ARCTAS/POLARCAT mission in 2008. Short-lived biomass burning tracers – such as n-pentane ($\tau_{n\text{-pent}}$ ~ 3 days), black carbon (τ_{BC} ~ 1 week), CH_3CN (τ_{CH3CN} ~ 11 days) and convection tracers such as the [NO_x]/[HNO_3] ratio [Bertram et al., 2007] – were not above background when this sample was collected, nor was the ratio of CO to CO_2. The longer-lived tracer, HCN (τ_{HCN} ~ 2-4

weeks), was elevated, however, measured at 540 pptv in this region by the Caltech Chemical Ionization Mass Spectrometer (CIT CIMS). Together, these observations are consistent with this high $\Delta^{14}C\text{-}CO_2$ tropospheric sample being influenced tens of days ago by biomass burning. A NOAA HYSPLIT back trajectory [Stein et al., 2015; Rolph et al., 2017] calculated for this sample (Figure 3.S2) indicates that this air mass spent time over Russia, and during the time of this flight there were forest fires occurring across Russia and Alaska [e.g., ESRI USGS, 2019; Siberian Times Reporter, 2018]. Increases in biomass burning and, in particular, of older boreal vegetation that had assimilated bomb radiocarbon more than 40 years ago may thus complicate the use of tropospheric $\Delta^{14}C\text{-}CO_2$ observations to infer emissions from fossil fuel burning [e.g., Vay et al., 2011; Levin et al., 2010].

To investigate potential hemispheric and seasonal differences in the composition of the lowermost stratosphere, the stratospheric $\Delta^{14}C\text{-}CO_2$ measurements were separated into northern and southern hemispheric data, and plotted as a function of simultaneous measurements of N_2O mixing ratios (Figure 3.4). While on average higher $\Delta^{14}C\text{-}CO_2$ and lower N_2O values are observed in the NH than in the SH lowermost stratosphere, Williamson-York regressions of the $\Delta^{14}C\text{-}CO_2$:N_2O relationships show that the slopes are the same to within 1σ, with a constant offset of -8 ± 1‰ in $\Delta^{14}C\text{-}CO_2$ between the northern and southern lowermost stratospheric data in May 2018. (The $\Delta^{14}C\text{-}CO_2$:N_2O regressions are plotted and the equations listed in Figure 3.4 and its caption.) Although the sampling is sparse, these hemispheric differences in the lowermost stratospheric observations, if robust, may be due to north-south differences in (1) the magnitudes of the downwelling fluxes from the overworld; (2) the amount of isentropic transport across the subtropical jet from the subtropical troposphere into the lowermost stratosphere; (3) $\Delta^{14}C\text{-}CO_2$ of upper tropospheric air that enters the lowermost stratosphere isentropically; or (4) some combination of factors (1) through (3). Each of these processes, and the balance between them, can affect the composition of the lowermost stratosphere.

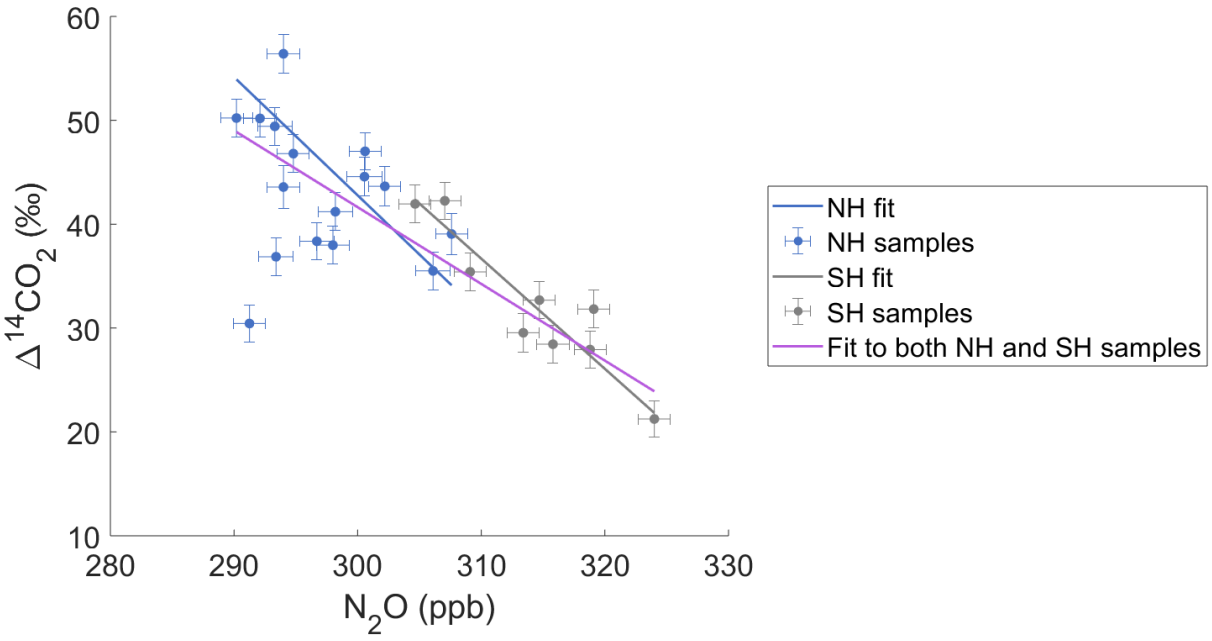

Figure 3.4: Measurements of $\Delta^{14}C\text{-}CO_2$ versus N_2O mixing ratio for samples collected in the lowermost stratosphere in the northern and southern hemispheres. The Williamson-York regressions are: for the NH (N=16): $\Delta^{14}C\text{-}CO_2 = (-1.15 \pm 0.14)[N_2O] + (384 \pm 42)$; for the SH (N=9): $\Delta^{14}C\text{-}CO_2 = (-1.06 \pm 0.13)\ [N_2O] + (366 \pm 41)$; for the combined stratospheric dataset (N=25): $\Delta^{14}C\text{-}CO_2 = (-0.74 \pm 0.04)\ [N_2O] + (263 \pm 13)$. The regressions yield an offset of -8 ± 1‰ for the NH compared to the SH. (Samples collected above the tropopause and with low water vapor (NH with $H_2O(v) < 9$ ppmv and in SH with $H_2O(v) < 10$ ppmv) were included in the fits; see text.) All uncertainties given are 1σ.

For the first factor, differences in the magnitudes of downwelling from the overworld into the lowermost stratosphere can be visualized as F_{in} in Figure 3.1. In the atmosphere, the magnitude of F_{in} exhibits both a seasonal and a N-S difference [e.g., Appenzeller et al., 1996]. Seasonally, in either hemisphere, downwelling has a maximum in winter and a minimum in late spring to early summer. In addition to this seasonal difference, both the annual and the seasonal magnitudes are larger in the NH than in the SH. These seasonal and hemispheric differences in downwelling are consistent with the lower N_2O (and higher $\Delta^{14}C\text{-}CO_2$) observations in the NH lowermost stratosphere in May 2018, which could result from more downwelling over the winter and, with the known delay in F_{out} [e.g., Holton 1995], would still be observable during the ATom-4 sampling in May. For the SH observations, May corresponds to the late fall, so the magnitude of downwelling over the previous several months was smaller than that in the NH over the same time period. These differences would be consistent with higher N_2O and lower $\Delta^{14}C\text{-}CO_2$ observations in the SH because there was less mixing in of older air entering from the overworld where N_2O had been photochemically lost and ^{14}C levels had built up. Thus, factor (1) could account for the distribution of N_2O and $\Delta^{14}C\text{-}CO_2$ values observed in May 2018, although not the slope offset we observe.

For the second factor, the amount of isentropic transport from the upper subtropical troposphere into the lowermost stratosphere, represented by F_h in Figure 3.1, may also have a seasonal and a N-S difference [Holton, 1995], which could result in different amounts of tropospheric air mixing into the lowermost stratosphere. Chen [1995] reported modelled isentropic troposphere-to-stratosphere transport on the 320 K isentrope peaking in winter in each hemisphere. In this same study, a different pattern was seen on the 350 K isentrope, where a small amount of transport occurred into the lowermost stratosphere in DJF in both hemispheres; whereas in JJA on the 350 K isentrope, there was a large amount of transport into the lowermost stratosphere in the NH and only a small amount into the SH. If this scenario is applied to ATom-4, higher N_2O and lower $\Delta^{14}C\text{-}CO_2$ would be consistent with a larger amount of isentropic transport into the lowermost stratosphere, diluting air from the overworld with tropospheric air with high N_2O and low $\Delta^{14}C\text{-}CO_2$. At the time of sampling in May, isentropic transport would likely not be peaking in either hemisphere based on Chen [1995], and, furthermore, this process alone applied in a JJA time frame would likely produce the opposite of the observations given the lower N_2O values in the NH lowermost stratosphere relative to the SH.

For the third factor, differences in tropospheric $\Delta^{14}C\text{-}CO_2$ in each hemisphere for air that enters the lowermost stratosphere via isentropic transport across the subtropical jet or via diabatic processes near the extratropical tropopause could lead to the lower $\Delta^{14}C\text{-}CO_2$ values observed on average in the NH than the SH. For ATom-4 samples, for example, the average of all NH tropospheric points (shown as vertical profiles of tropospheric $\Delta^{14}C\text{-}CO_2$ in Figure 3.S3) is 6±2‰ (N=9) without the biomass burning outlier (or 8±7‰ with the biomass burning outlier included), while the average of just the SH tropospheric data is 14±4‰ (N=5). This north-south difference in tropospheric $\Delta^{14}C\text{-}CO_2$ of 6 to 8‰ during ATom-4 is similar in sign and magnitude to the meridional gradients deduced in other studies at the surface [e.g., Levin et al., 2010; Graven et al., 2012b] and is due to greater emissions from fossil fuel burning in the north (for which the emitted CO_2 is devoid of ^{14}C [Suess 1955]), as well as annual and seasonal differences in the air-sea exchange of CO_2 between the two hemispheres [e.g., Levin et al., 2010; Graven et al., 2012b]. Indeed, the difference between the NH and SH tropospheric ATom-4 data of 6 to 8‰ is also consistent with the north-south offset in the ATom-4 $\Delta^{14}C\text{-}CO_2$:N_2O relationships in the lowermost stratosphere of −8±1‰. Thus, isentropic mixing of air from the upper troposphere into the lowermost stratosphere in each hemisphere could result in lower $^{14}CO_2$ levels in the NH than the SH due to the meridional gradient in tropospheric $\Delta^{14}C\text{-}CO_2$ values observed in this and other studies.

Overall, the new $^{14}CO_2$ observations from ATom-4 at high latitudes in both hemispheres in May 2018, combined with simultaneous N_2O measurements, are most consistent with a combination of the three factors above in determining the composition of the lowermost stratosphere. In particular, since $\Delta^{14}C\text{-}CO_2$ is both very long-lived (and with a sink only at Earth's surface) and can be measured very precisely, it provides a unique signature that points to a significant influence of a "short-circuiting" of the BDC even after other tropospheric tracers have mixed into the background or been photochemically removed. Below, we explore two more aspects of the new dataset that support this idea.

Figure 3.4 shows two $\Delta^{14}C\text{-}CO_2$ outliers in the NH lowermost stratosphere in samples collected at 354-355 K, well above the tropopause at 312K, on 17 May 2018 and with $H_2O < 9$ ppmv. One sample has the highest $\Delta^{14}C\text{-}CO_2$ value in the entire dataset (56‰) and one has the

lowest value (30.4‰) in this grouping, while their N_2O values are 294 and 291 ppbv, respectively; hence, these outliers are clearly not a simple case of varying transport from the overworld only since $\Delta^{14}C\text{-}CO_2$ and N_2O are anti-correlated there [Kanu et al., 2016]. (Two other samples collected above the tropopause on the same flight have low $\Delta^{14}C\text{-}CO_2$ values of 26.1‰ and 29.9‰, shown in Figure 3.3, but H_2O is 10 ppmv, clearly showing a short-circuiting of the BDC and thus they were excluded from Figure 3.4; see Methods.) Indeed, this much of a range in $\Delta^{14}C\text{-}CO_2$ values in the lowermost stratosphere is somewhat surprising and was not observed during the SEAC4RS mission, for which an extensive set of samples from the NASA ER-2 aircraft were analyzed for radiocarbon [Garofalo et al., 2019]. Furthermore, these ATom-4 samples did not show any anomalous tracer concentrations (e.g., CO, O_3, H_2O, CO_2, and CH_4). HYSPLIT back trajectories provide some useful insights (Figure 3.5), showing these air masses have quite different transport histories. Air from both samples had been at altitudes just below 10 km a few days before sampling, in a region greatly influenced by diurnal fluctuations in the local tropopause. Prior to that, the back trajectories are quite different, and suggest that different amounts of tropospheric and stratospheric air may have mixed together or that tropospheric air with quite different $\Delta^{14}C\text{-}CO_2$ values (e.g., from biomass burning influences) was involved. Based on these back trajectories, it is thus likely that there is sufficient mixing in of new tropospheric air, leading to an interestingly large range in $\Delta^{14}C\text{-}CO_2$ values and the departures from the compact $\Delta^{14}C\text{-}CO_2$:N_2O relationships expected for the stratospheric overworld.

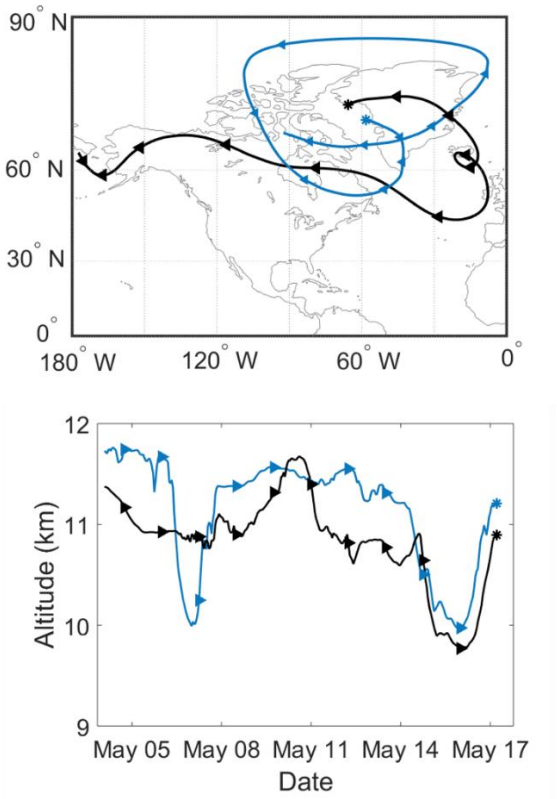

Figure 3.5: Back trajectories calculated using NOAA HYSPLIT for the $\Delta^{14}C\text{-}CO_2$ outliers in Figure 3.4 as a function of (a) latitude and longitude and (b) altitude: Asterisks denote the sampling location, triangles the location at 30 hours back in time, black indicates the back trajectory for the

high outlier with $\Delta^{14}C\text{-}CO_2$ of 56‰, and blue indicates the back trajectory for the low outlier with $\Delta^{14}C\text{-}CO_2$ of 30‰.

This evidence for significant admixture of tropospheric air into the lowermost stratosphere has implications for whether the global mean ^{14}C production rate from the slope of the $\Delta^{14}C\text{-}CO_2$:N_2O relationships using the Plumb [2007] method can in fact be determined from observations in the lowermost stratosphere or not. Table 1 compares the global mean ^{14}C production rates from the new ATom-4 samples collected in the lowermost stratosphere in 2018 with those from previous NASA missions for which almost all samples were collected in the stratospheric overworld between 1997 and 2013 [Garofalo et al., 2019]. The inferred ^{14}C production rates for ATom-4 separated by hemisphere are skewed quite high compared with previous datasets made up of predominantly overworld data. The combined ATom-4 dataset from both hemispheres appears to yield a ^{14}C production rate that is consistent with those from previous missions but, given all the north-south differences discussed above (from the N_2O distribution between the north and south and the wide range of $\Delta^{14}C\text{-}CO_2$ for a given N_2O value in the north), we believe this is simply a coincidence. Rather, the dynamical basis for the Plumb [2007] method – such that the slope of the correlation of two long-lived tracers representing the net vertical flux of the two species – requires that the observations used be obtained in the stratospheric overworld. Thus, even though the solar cycle is at a minimum in 2018 – corresponding to a maximum in the cosmogenic ^{14}C production rate [Solar cycle progression, 2018] – the lowermost stratospheric $\Delta^{14}C\text{-}CO_2$ and N_2O data from ATom-4 cannot be used to empirically assess any solar-cycle enhanced cosmogenic production rate. For the latter, a more appropriate tracer would be a time series of ^{14}CO measurements [e.g., Jökel & Brenninkmeijer, 2002].

Table 3.1: Global annual mean ^{14}C production rates calculated for ATom-4 compared with previous missions.

	Year	$\Delta^{14}C\text{-}CO_2$ flux, 10^{17} ‰ mol C yr^{-1}	^{14}C Production rate 10^{17} ‰ mol C yr^{-1}	^{14}C Production rate 10^{26} atoms yr^{-1}
POLARIS [a]	1997	1.7 ± 0.4	3.3 ± 0.8	2.3 ± 0.6
SOLVE [a]	2000	1.2 ± 0.5	2.3 ± 1.0	1.6 ± 0.7
AVE [a]	2004	1.4 ± 0.3	2.9 ± 0.6	2.0 ± 0.4
Balloon [a]	2004/2005	1.6 ± 0.2	3.1 ± 0.4	2.2 ± 0.2
SEAC4RS [a]	2013	1.5 ± 0.1	3.0 ± 0.2	2.1 ± 0.2
ATom-4 (N= 25)	*2018*	*1.4 ± 0.1**	*2.8 ± 0.2**	*2.0 ± 0.1**
ATom-4 SH (N=9)	*2018*	*2.0 ± 0.2**	*4.0 ± 0.5**	*2.9 ± 0.3**
ATom-4 NH (N=16)	*2018*	*2.2 ± 0.3**	*4.3 ± 0.5**	*3.0 ± 0.4**

[a] Data from Garofalo *et al.* (2019)

* Results for samples collected exclusively from the lowermost stratosphere are skewed due to substantial short-circuiting of air entering the stratosphere isentropically (quasi-horizontally) from the troposphere into the lowermost stratosphere, demonstrating that robust global annual mean ^{14}C production rates require sampling in the stratospheric overworld.

As a quick test of how this mixing in of tropospheric air could skew the ^{14}C production rates inferred from the Plumb [2007] method, we set up illustrative vertical profiles of $\Delta^{14}C\text{-}CO_2$ and N_2O and mixed them incrementally with tropospheric air with N_2O mixing ratio of 333 ppb and $\Delta^{14}C\text{-}CO_2$ of 8‰ based on a tropospheric sample collected during ATom-4. The profile values with lower N_2O, representing higher altitude samples, were mixed with a smaller percentage of tropospheric air than those representing lower altitude samples with higher N_2O, which is similar to patterns in the atmosphere in which more mixing occurs on lower isentropic surfaces than on higher [Chen, 1995]. In this conceptual illustration, the slope of the $\Delta^{14}C\text{-}CO_2$:N_2O relationship

increased from 1% to 20%, with the larger increases occurring when there is more mixing in of tropospheric air at low altitudes and much less at high altitudes. This conceptual example illustrates that significant mixing in of tropospheric air that short-circuits the BDC in the overworld will skew the ^{14}C production rates inferred from the $\Delta^{14}C$-CO_2:N_2O correlation artificially high. We conclude that robust empirical ^{14}C production rates derived from the observed $\Delta^{14}C$-CO_2:N_2O correlation require that most observations used as input be for air from the stratospheric 'overworld.'

3.4 Conclusions

Measurements of $\Delta^{14}C$-CO_2 were made on 46 whole air samples collected from the NASA DC-8 during the ATom-4 mission in May 2018. These samples provide the first near-simultaneous vertical profiles of $\Delta^{14}C$-CO_2 across the tropopause at high latitudes in both hemispheres, ranging from ~0.2 km up to potential temperatures of 350-366K, well into the lowermost stratosphere. In addition to providing new vertical constraints at high latitudes for inverse models, the measurements show interesting hemispheric differences. For example, a north-south hemispheric offset in $\Delta^{14}C$-CO_2 of −8±1‰ in the lowermost stratosphere (θ<380 K) could result from seasonal and hemispheric differences in factors such as: the amounts of isentropic transport from the subtropical troposphere into the lowermost stratosphere, the magnitudes of downwelling from the overworld (θ>380 K), meridional gradients in tropospheric $\Delta^{14}C$-CO_2, or some combination of these. These data thus provide interesting new constraints for models that are unique and complementary to other troposphere-to-stratosphere tracers on the balance of these convolved dynamical factors that determine the chemical composition of the lowermost stratosphere. The addition of $\Delta^{14}C$-CO_2 measurements adds a unique dimension to other tracers, given the fact that the $^{14}CO_2$ signal is long-lived and appears to remain above background levels longer than short-lived tracers of troposphere-to-stratospheric transport (such as HCN or hydrocarbons) or anomalous tracer:tracer relationships provided by the combination of N_2O, H_2O, O_3, CO, CO_2, and CH_4 observations. Beyond the empirical investigation reported here, the next steps are to use $^{14}CO_2$ as a tracer in models in order to help quantify the transport differences leading to the observed north-south differences in the $\Delta^{14}C$-CO_2:N_2O relationships during ATom-4. Finally, we note that the new ATom $\Delta^{14}C$-CO_2:N_2O observations from the lowermost stratosphere demonstrate that inferring global ^{14}C production rates empirically from measured $\Delta^{14}C$-CO_2:N_2O relationships is not robust when overworld data are absent, due to substantial isentropic mixing in of new air from the troposphere that short-circuits the BDC. In other words, the Plumb {, 2007 #537} approach for determining net vertical fluxes from tracer observations is not valid in the lowermost stratosphere; rather, samples must be collected from aircraft and balloons platforms that can include samples collected above θ=380K.

References

Alves, E.Q., Macario, K., Ascough, P., and BronkRamsey, C. (2018). The worldwide marine radiocarbon reservoir effect: Definitions, mechanisms, and prospects. Reviews of Geophysics *56*, 278-305. doi: 10.1002/2017rg000588.

Anderson J.G., Wilmouth D.M., Smith J.B., Sayres D.S. (2012). UV Dosage Levels in Summer: Increased Risk of Ozone Loss from Convectively Injected Water Vapor. Science 337: 835-9.

Andrews, A. E. et al. (2001), Mean ages of stratospheric air derived from in situ observations of CO_2, CH_4, and N_2O, *J. Geophys. Res.*, 106(D23), 32295–32314, doi:10.1029/2001JD000465.

Appenzeller, C., J. R. Holton, and K. H. Rosenlof (1996), Seasonal variation of mass transport across the tropopause, *J. Geophys. Res. Atmos.*, 101(D10), 15071–15078, doi:10.1029/96JD00821

Basu, S., J. B. Miller, and S. Lehman (2016), Separation of biospheric and fossil fuel fluxes of CO_2 by atmospheric inversion of CO_2 and $^{14}CO_2$ measurements: Observation System Simulations, *Atmos. Chem. Phys.*, 16, 5665–5683, doi:10.5194/acp-16-5665-2016.

Basu, S., Lehman, S.J., Miller, J.B., Andrews, A.E., Sweeney, C., Gurney, K.R., Xu, X., Southon, J., and Tans, P.P. (2020). Estimating us fossil fuel CO_2 emissions from measurements of ^{14}C in atmospheric CO_2. *Proceedings of the National Academy of Sciences 117*, 13300-13307. doi: 10.1073/pnas.1919032117.

Bertram, T. H. et al. (2007), Direct measurements of the convective recycling of the upper troposphere, *Science*, 315, 816–820, doi:10.1126/science.1134548.

Boering, K. A., T. Jackson, K. J. Hoag, A. S. Cole, M. J. Perri, M. Thiemens, and E. Atlas (2004), Observations of the anomalous oxygen isotopic composition of carbon dioxide in the lower stratosphere and the flux of the anomaly to the troposphere, *Geophys. Res. Lett.*, 31, L03109, doi:10.1029/2003GL018451.

Butchart, N. (2014), The Brewer-Dobson circulation, *Reviews of Geophysics*, *52*(2), 157-184, doi:10.1002/2013rg000448.

Cantrell, C. A. (2008), Technical Note: Review of methods for linear least-squares fitting of data and application to atmospheric chemistry problems, *Atmos. Chem. Phys.*, 8, 5477–5487, doi:10.5194/acp-8-5477-2008.

Chen, P., (1995), Isentropic cross-tropopause mass exchange in the extratropics, *J. Geophys. Res.*, 100(D8), 16661–16673, doi:10.1029/95JD01264.

Colman, J. J., A. L. Swanson, S. Meinardi, B. Sive, D. R. Blake, and F. S. Rowland (2001), Description of the analysis of a wide range of volatile organic compounds in whole air samples collected during PEM-Tropics A and B, *Anal. Chem., 73*, 3723-3731.

Siberian Times Reporter, Concern over raging wildfires as smoke from Siberia crosses Alaska and Canada, reaching New England. (2018, July 13). *The Siberian Times*. https://siberiantimes.com/ecology/others/news/concern-over-raging-wildfires-as-smoke-from-siberia-crosses-alaska-and-canada-reaching-new-england/.

Denman, K.L., G. Brasseur, A. Chidthaisong, P. Ciais, P.M. Cox, R.E. Dickinson, D. Hauglustaine, C. Heinze, E. Holland, D. Jacob, U. Lohmann, S Ramachandran, P.L. da Silva Dias, S.C. Wofsy and X. Zhang, 2007: Couplings Between Changes in the Climate System and Biogeochemistry. In: Climate Change 2007: The Physical Science Basis. Contribution of Working Group I to the Fourth Assessment Report of the Intergovernmental Panel on Climate Change [Solomon, S., D. Qin, M. Manning, Z. Chen,

M. Marquis, K.B. Averyt, M.Tignor and H.L. Miller (eds.)]. Cambridge University Press, Cambridge, United Kingdom and New York, NY, USA

Dessler, A. E., M. R. Schoeberl, T. Wang, S. M. Davis, and K. H. Rosenlof (2013), Stratospheric water vapor feedback, *Proceedings of the National Academy of Sciences*, 110(45), 18087-18091, doi:10.1073/pnas.1310344110.

ESRI USGS. (26 Nov 2019). *Wildland Fires.* Alaska Wildland Fire Information. https://www.arcgis.com/apps/MapSeries/index.html?appid=32ec4f34fb234ce58df6b1222a207ef1.

Garofalo, L.A., Kanu, A., Hoag, K.J., Atlas, E.A., and Boering, K.A. (2019). The effects of stratospheric chemistry and transport on the isotopic compositions of long-lived gases measured at earth's surface. Advances in Atmospheric Chemistry *2*, 529-587. doi: doi.org/10.1142/9789813271838_0007.

Graven, H. D. (2015), Impact of fossil fuel emissions on atmospheric radiocarbon and various applications of radiocarbon over this century, *Proc. Natl. Acad. Sci.* U. S. A., 112(31), 9542–9545, doi:10.1073/pnas.1504467112.

Graven, H. D., T. P. Guilderson, and R. F. Keeling (2012a), Observations of radiocarbon in CO_2 at La Jolla, California, USA 1992-2007: Analysis of the long-term trend, *J. Geophys. Res.*, 117, D02302, doi:10.1029/2011JD016533.

Graven, H. D., T. P. Guilderson, and R. F. Keeling (2012b), Observations of radiocarbon in CO_2 at seven global sampling sites in the Scripps flask network: Analysis of spatial gradients and seasonal cycles, *J. Geophys. Res.*, 117, D02303, doi:10.1029/2011jd016535.

Guilderson, T.P., Schrag, D.P., Druffel, E.R.M., and Reimer, R.W. (2021). Post-bomb subtropical north pacific surface water radiocarbon history. Journal of Geophysical Research-Oceans *126*, 10. doi: 10.1029/2020jc016881.

Hall, T. M., and D. W. Waugh (2000), Stratospheric residence time and its relationship to mean age, *J. Geophys. Res.*, 105(D5), 6773–6782, doi:10.1029/1999jd901096.

Hintsa, E. J., Moore, F. L., Hurst, D. F., Dutton, G. S., Hall, B. D., Nance, J. D., Miller, B. R., Montzka, S. A., Wolton, L. P., McClure-Begley, A., Elkins, J. W., Hall, E. G., Jordan, A. F., Rollins, A. W., Thornberry, T. D., Watts, L. A., Thompson, C. R., Peischl, J., Bourgeois, I., Ryerson, T. B., Daube, B. C., Pittman, J. V., Wofsy, S. C., Kort, E., Diskin, G. S., & Bui, T. P. (2021). UAS Chromatograph for Atmospheric Trace Species (UCATS) - a versatile instrument for trace gas measurements on airborne platforms. *Atmos. Meas. Tech. Discuss., 2021*, 1-30. https://doi.org/10.5194/amt-2020-496

Holton, J. R. (1990), On the Global Exchange of Mass between the Stratosphere and Troposphere, *J. Atmos. Sci.*, 47(3), 392–395.

Holton, J. R., P. H. Haynes, M. E. McIntyre, A. R. Douglass, R. B. Rood, and L. Pfister, (1995). Stratosphere–troposphere exchange. *Rev. Geophys.*, **33**, 403–439, doi:10.1029/95RG02097.

Jöckel, P., and C. A. M. Brenninkmeijer (2002), The seasonal cycle of cosmogenic ^{14}CO at the surface level: A solar cycle adjusted, zonal-average climatology based on observations, *J. Geophys. Res.*, 107(D22), 4656, doi:10.1029/2001JD001104.

Johnston, H. (1989), Evaluation of excess C14 and SR90 data for suitability to test Two-dimensional stratospheric models, *J. Geophys. Res.*, 94(D15), 18485–18493, doi:10.1029/JD094iD15p18485.

Kanu, A. M., L. L. Comfort, T. P. Guilderson, P. J. Cameron-Smith, D. J. Bergmann, E. Atlas, S.

Schauffler, and K. A. Boering (2016), Measurements and modeling of contemporary radiocarbon in the stratosphere, *Geophys. Res. Lett.*, 43(3), 1399–1406, doi:10.1002/2013GL058740.

Kinnison, D. E., H. S. Johnston, and D. J. Wuebbles (1994), Model study of atmospheric transport using carbon 14 and strontium 90 as inert tracers, *J. Geophys. Res.*, 99(D10), 20647–20664.

Kovaltsov, G.A., Mishev, A., and Usoskin, I.G. (2012). A new model of cosmogenic production of radiocarbon C-14 in the atmosphere. Earth and Planetary Science Letters *337*, 114-120. doi: 10.1016/j.epsl.2012.05.036.

Kusch, S., Rethemeyer, J., Ransby, D., and Mollenhauer, G. (2021). Permafrost organic carbon turnover and export into a high-arctic fjord: A case study from svalbard using compound-specific C-14 analysis. Journal of Geophysical Research-Biogeosciences *126*, 15. doi: 10.1029/2020jg006008.

Lal, D., and B. Peters (1967), Cosmic Ray produced radioactivity on the Earth, in Kosmische Strahlung II/Cosmic Rays II, edited by K.Sitte, pp. 551–612, Springer, Berlin Heidelberg.

Levin, I., B. Kromer, M. Schmidt, and H. Sartorius (2003), A novel approach for independent budgeting of fossil fuel CO_2 over Europe by $^{14}CO_2$ observations, *Geophys. Res. Lett.*, 30(23), 2194, doi:10.1029/2003GL018477.

Levin, I., T. Naegler, B. Kromer, M. Diehl, R. J. Francey, A. J. Gomez-Pelaez, L. P. Steele, D. Wagenbach, R. Weller, and D. E. Worthy (2010), Observations and modelling of the global distribution and long-term trend of atmospheric $^{14}CO_2$, *Tellus*, 62B, 26–46, doi:10.1111/j.1600- 742 0889.2009.00446.x.

Libby, W. F. (1947). Measurement of Radioactive Tracers. *Analytical Chemistry*, *19*(1), 2-6.

Masarik, J., and J. Beer (1999), Simulation of particle fluxes and cosmogenic nuclide production in the Earth's atmosphere, *J. Geophys. Res.*, 104 (D10), 12099-12111, doi:10.1029/1998JD200091.

Masarik, J., and J. Beer (2009), An updated simulation of particle fluxes and cosmogenic nuclide production in the Earth's atmosphere, *J. Geophys. Res.*, 114, D11103 doi:10.1029/2008jd010557.

Minschwaner, K., R. J. Salawitch, and M. B. McElroy (1993), Absorption of solar radiation by O_2: Implications for O_3 and lifetimes of N_2O, $CFCl_3$, and CF_2Cl_2, *J. Geophys. Res.*, 98(D6), 10543 10561, doi:10.1029/93JD00223.

Naegler, T., and Levin, I. (2006). Closing the global radiocarbon budget 1945-2005. Journal of Geophysical Research-Atmospheres *111*, 14. doi: 10.1029/2005jd006758.

Newman, P. A., D. W. Fahey, W. H. Brune, M. J. Kurylo, and S. R. Kawa (1999), Preface [to special section on Photochemistry of Ozone Loss in the Arctic Region in Summer (POLARIS)], J. Geophys. Res. Atmos., 104(D21), 26481–26495, doi:10.1029/1999JD900832.

NOAA ESRL. (May 2018). *Trends in Atmospheric Carbon Dioxide*. Global Monitoring Laboratory. https://www.esrl.noaa.gov/gmd/ccgg/trends/graph.html.

Oman, L., D. W. Waugh, S. Pawson, R. S. Stolarski, and P. A. Newman (2009), On the influence of anthropogenic forcings on changes in the stratospheric mean age, *Journal of Geophysical Research-Atmospheres, 114*, 15, doi:10.1029/2008jd010378.

Plumb, R. A. (2007), Tracer interrelationships in the stratosphere, *Rev. Geophys.*, 45, RG4005, doi:10.1029/2005RG000179.

Plumb, R. A., and M. K. W. Ko (1992), Interrelationships between mixing ratios of long lived stratospheric constituents, *J. Geophys. Res.*, 97(D9), 10145–10156.

Prather, M. and D. Ehhalt, Atmospheric Chemistry and Greenhouse Gases, in Climate Change 2001: The Scientific Basis. Contribution of Working Group I to the Third Assessment Report of the Intergovernmental Panel on Climate Change, J.T. Houghton et al. (eds.), Cambridge University Press, New York, NY, pp. 239-287, 2001.

Povinec, P. P., Litherland, A. E., & Von Reden, K. F. (2009). Developments in Radiocarbon Technologies: From the Libby Counter to Compound-Specific AMS Analyses. *Radiocarbon*, *51*(1), 45-78. https://doi.org/10.1017/s0033822200033701

Randerson, J. T., I. G. Enting, E. A. G. Schuur, K. Caldeira, and I. Y. Fung (2002), Seasonal and latitudinal variability of troposphere $\Delta^{14}C$: Post bomb contributions from fossil fuels, oceans, the stratosphere, and the terrestrial biosphere, *Global Biogeochem. Cycles*, 16(4), 1112, doi:10.1029/2002GB001876.

Rind, D., R. Suozzo, N. K. Balachandran, and M. J. Prather (1990), Climate change and the middle atmosphere. The doubled CO_2 climate, *Journal of the Atmospheric Sciences*, 47(4), 475-494, doi:10.1175/1520-0469(1990)0472.0.co;2.

Rolph, G., Stein, A., and Stunder, B., (2017). Real-time Environmental Applications and Display sYstem: READY. *Environmental Modelling & Software*, **95**, 210-228, https://doi.org/10.1016/j.envsoft.2017.06.025.

Shi, Z., Allison, S.D., He, Y.J., Levine, P.A., Hoyt, A.M., Beem-Miller, J., Zhu, Q., Wieder, W.R., Trumbore, S., and Randerson, J.T. (2020). The age distribution of global soil carbon inferred from radiocarbon measurements. Nature Geoscience *13*, 555-+. doi: 10.1038/s41561-020-0596-z.

Solomon, S., K. H. Rosenlof, R. W. Portmann, J. S. Daniel, S. M. Davis, T. J. Sanford, and G. K. Plattner (2010), Contributions of Stratospheric Water Vapor to Decadal Changes in the Rate of Global Warming, *Science*, 327(5970), 1219-1223, doi:10.1126/science.1182488.

Stein, A.F., Draxler, R.R, Rolph, G.D., Stunder, B.J.B., Cohen, M.D., and Ngan, F., (2015). NOAA's HYSPLIT atmospheric transport and dispersion modeling system, *Bull. Amer. Meteor. Soc.*, 96, 2059-2077, http://dx.doi.org/10.1175/BAMS-D-14-00110.1.

Stepaniak, D. (17 July 2012). *ERA-Interim Pressure and Isentropic (Theta) Levels.* NCAR. https://rda.ucar.edu/datasets/ds627.1/docs/Pressure_and_isentropic_levels/.

Stuiver, M., and H. A. Polach (1977), Discussion: Reporting of ^{14}C data, *Radiocarbon*, 19(3), 355–363.

Suess, H. E. (1955), Radiocarbon concentration in modern wood, *Science*, 122, 414-417.

Solar cycle progression. Solar Cycle Progression | NOAA / NWS Space Weather Prediction Center. (2018). https://www.swpc.noaa.gov/products/solar-cycle-progression.

Toon, O. B. et al. (2016), Planning, implementation, and scientific goals of the Studies of Emissions and Atmospheric Composition, Clouds and Climate Coupling by Regional Surveys (SEAC^{4}RS) field mission, J. Geophys. Res., 121, 4967–5009, doi:10.1002/2015JD024297.

Turnbull, J. C. et al. (2011), Assessment of fossil fuel carbon dioxide and other anthropogenic trace gas emissions from airborne measurements over Sacramento, California in spring 2009, *Atmos. Chem. Phys.*, 11, 705–721, doi:10.5194/acp-11-705-2011.

Vay, S. A. et al. (2011), Patterns of CO_2 and radiocarbon across high northern latitudes during International Polar Year 2008, *J. Geophys. Res.*, 116, D14301, doi:10.1029/2011JD015643.

Wang, Y., and Y. Huang. (2020), Understanding the Atmospheric Temperature Adjustment to

CO_2 Perturbation at the Process Level, *Journal of Climate*, 33787-803. doi: 10.1175/JCLI-D-19-0032.1.

Wiegel, A. A., A. S. Cole, K. J. Hoag, E. L. Atlas, S. M. Schauffler, and K. A. Boering (2013) Unexpected variations in the triple oxygen isotope composition of stratospheric carbon dioxide, *PNAS*, 110(44), 17680–17685, doi:10.1073/pnas.1213082110

Wofsy, S.C., et al., 2018. ATom: Merged Atmospheric Chemistry, Trace Gases, and Aerosols. ORNL DAAC, Oak Ridge, Tennessee, USA. https://doi.org/10.3334/ORNLDAAC/1581

Appendix: Supplemental Material

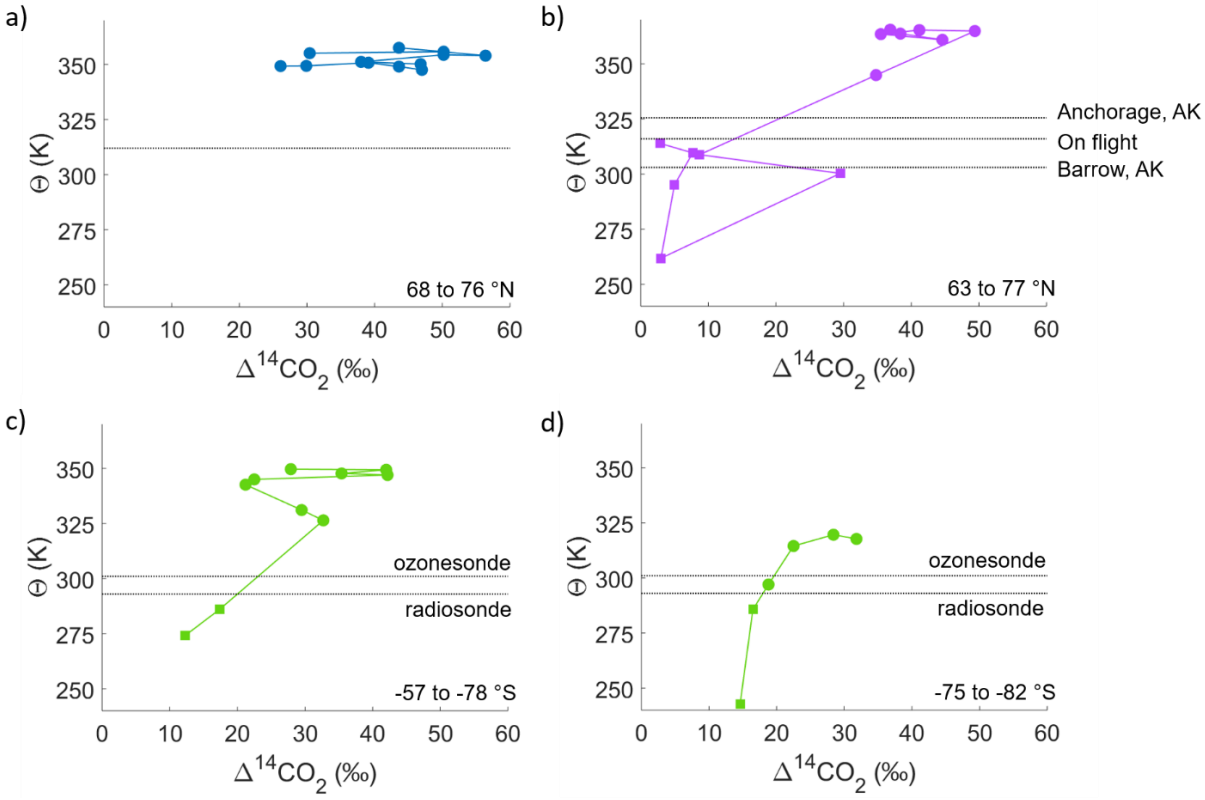

Figure 3.S1: Vertical profiles of $\Delta^{14}C\text{-}CO_2$ (N=41) as a function of potential temperature measured on samples collected below (squares) and above (circles) the regional tropopause (black dotted lines) for (a) Flight 10, (b) Flight 12, and (c, d) Flight 7. The tropopauses were determined by (a) a radiosonde launch at BGEM within 6 hours, (b) radiosondes at PANC and PABR as well as a mid-flight temperature profile, and (c, d) by a radiosonde launch at Rothera and an ozonesonde launch at the Amundsen-Scott South Pole station.

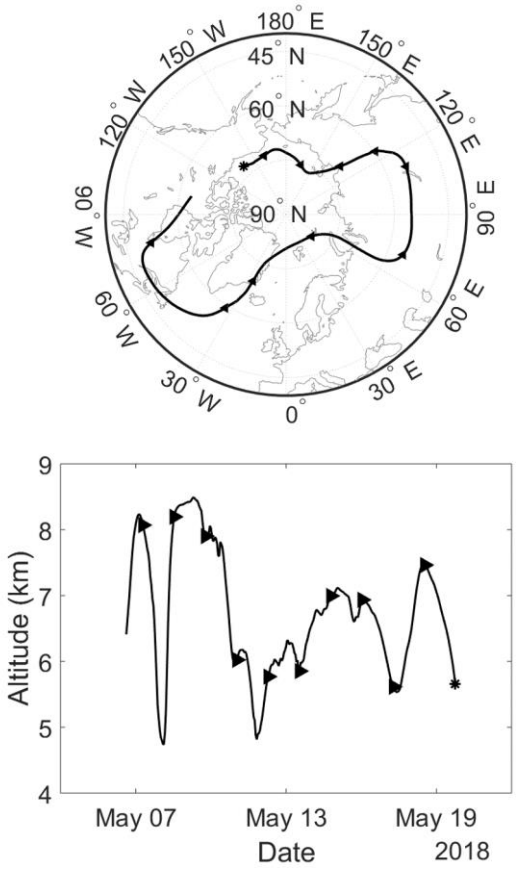

Figure 3.S2: NOAA HYSPLIT back trajectory for the biomass burning outlier with $\Delta^{14}C\text{-}CO_2$ of 30‰ sampled on 19 May 2018 (asterisk) at 72.25°N, −138.67°W at an altitude of 5661 and θ=300 K (the tropopause was at ~9.3 km and θ=316 K).

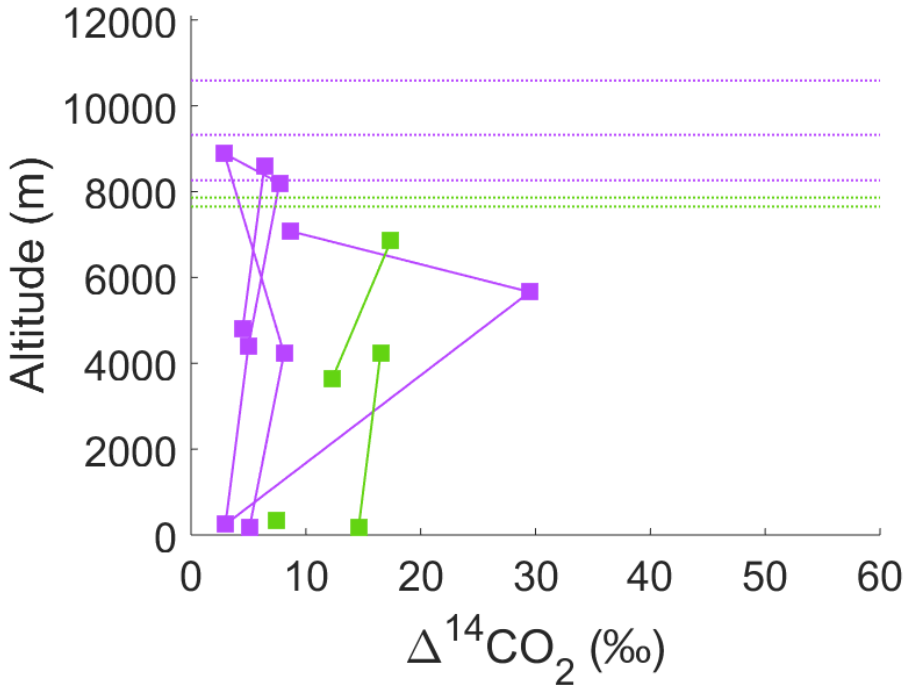

Figure 3.S3: All tropospheric samples collected on Flight 12 (purple) and Flight 7 (green). The tropopauses are the same as in Figure 3.2(b) and (c) and are colorized by flight.

Table 3.S1: Measurements (N=46) of $\Delta^{14}C$-CO_2 on whole air samples collected during ATom-4

Flight Date	Snake #	Can #	CAMS #	Fraction Modern	±	$\Delta^{14}C$	±	Altitude, m	Latitude, °	Longitude, °	Potential Temperature, K	N_2O, ppb	±
5/9/2018	1618	7241	181314	1.0230	0.0018	14.6	1.8	186	-75.12	-45.51	242.75	330.1	1.3
5/9/2018	1604	6359	181315	1.0249	0.0018	16.5	1.8	4227	-76.11	-44.82	285.71	331.1	1.3
5/9/2018	1612	5022	181316	1.0273	0.0019	18.8	1.9	8218	-77.68	-43.53	297.02	327.7	1.3
5/9/2018	1606	6149	181318	1.0310	0.0018	22.5	1.8	9345	-78.43	-42.78	314.51	322.3	1.3
5/9/2018	1607	6115	181319	1.0370	0.0018	28.4	1.8	9556	-80.60	-40.75	319.58	315.8	1.3
5/9/2018	1623	7166	181320	1.0404	0.0018	31.8	1.8	9549	-81.90	-40.69	317.67	319.1	1.3
5/9/2018	5617	8216	181304	1.0208	0.0017	12.3	1.7	3641	-78.89	-60.61	274.17	329.6	1.3
5/9/2018	5615	6275	181305	1.0258	0.0018	17.4	1.8	6849	-78.07	-61.52	286.12	330.0	1.3
5/9/2018	5614	6255	181306	1.0413	0.0018	32.7	1.8	10081	-76.61	-62.85	326.37	314.7	1.3
5/9/2018	5619	8063	181307	1.0381	0.0018	29.5	1.8	10497	-76.10	-63.25	331.05	313.4	1.3
5/9/2018	5605	7056	181308	1.0297	0.0018	21.2	1.8	11231	-70.89	-66.11	342.61	324.0	1.3
5/9/2018	5612	6020	182729	1.0310	0.0019	22.5	1.9	11261	-69.65	-66.58	345.04	326.1	1.3
5/9/2018	5621	8064	181309	1.0509	0.0018	42.2	1.8	11305	-68.28	-67.03	347.04	307.1	1.3
5/9/2018	5606	7225	181311	1.0440	0.0018	35.4	1.8	11337	-67.00	-67.42	347.65	309.1	1.3
5/9/2018	5611	6311	182730	1.0506	0.0018	42.0	1.8	11394	-65.58	-67.79	349.35	304.7	1.3
5/9/2018	5607	7807	182735	1.0365	0.0018	27.9	1.8	11473	-60.04	-68.96	349.64	318.8	1.3
5/9/2018	5608	7156	181313	1.0158	0.0016	7.4	1.6	338	-57.42	-69.36	277.52	330.5	1.3
5/17/2018	4401	8211	181321	1.0346	0.0018	26.1	1.8	10852	68.58	-58.48	349.29	311.8	1.3
5/17/2018	4417	6161	181322	1.0385	0.0018	29.9	1.8	10864	69.56	-59.45	349.40	311.1	1.3
5/17/2018	4402	8278	181323	1.0477	0.0020	39.1	2.0	10874	70.05	-59.96	350.78	307.6	1.3
5/17/2018	4415	6041	182733	1.0523	0.0019	43.6	1.9	10876	70.63	-60.61	349.07	302.2	1.3
5/17/2018	4418	4257	182732	1.0557	0.0018	47.0	1.8	10880	71.10	-61.16	347.57	300.6	1.3

5/17/2018	4419	4058	181328	1.0555	0.0018	46.8	1.8	10896	72.56	-62.71	350.25	294.8	1.3
5/17/2018	4420	4057	181329	1.0466	0.0018	38.0	1.8	10905	73.98	-64.35	351.18	298.0	1.3
5/17/2018	4421	4223	181330	1.0589	0.0018	50.2	1.8	10901	75.41	-66.34	354.36	290.2	1.3
5/17/2018	4411	6109	181332	1.0652	0.0019	56.4	1.9	10894	75.68	-65.53	354.02	294.0	1.3
5/17/2018	4410	6298	182731	1.0522	0.0020	43.6	2.0	11216	74.30	-62.02	357.59	294.0	1.3
5/17/2018	4409	6396	182741	1.0589	0.0018	50.2	1.8	11203	72.89	-59.08	355.81	292.1	1.3
5/17/2018	4424	4200	182736	1.0390	0.0018	30.4	1.8	11206	72.45	-58.26	355.14	291.3	1.3
5/19/2018	4517	6160	181343	1.0134	0.0019	5.1	1.9	183	79.28	-130.60	264.68	331.4	1.4
5/19/2018	4503	4217	181333	1.0165	0.0019	8.1	1.9	4227	78.19	-132.36	295.81	333.0	1.4
5/19/2018	4513	7048	181334	1.0113	0.0018	2.9	1.8	8887	76.61	-134.37	313.93	331.7	1.4
5/19/2018	4505	4148	181335	1.0161	0.0018	7.7	1.8	8199	75.35	-135.67	309.57	327.8	1.4
5/19/2018	4506	4262	181336	1.0134	0.0018	5.0	1.8	4406	74.56	-136.38	295.13	329.9	1.4
5/19/2018	4509	7275	181337	1.0113	0.0017	3.0	1.7	246	73.38	-137.59	261.80	331.2	1.4
5/19/2018	3817	9288	181339	1.0380	0.0021	29.5	2.1	5661	72.25	-138.67	300.27	331.8	1.4
5/19/2018	3802	9293	181340	1.0171	0.0018	8.7	1.8	7074	71.91	-138.97	308.84	331.6	1.4
5/19/2018	3804	9290	181341	1.0434	0.0019	34.8	1.9	11141	68.60	-141.92	344.95	310.0	1.4
5/19/2018	3813	9289	182737	1.0581	0.0018	49.4	1.8	12075	68.04	-142.75	364.89	293.3	1.4
5/19/2018	3820	9302	182738	1.0498	0.0018	41.2	1.8	12076	67.52	-143.51	365.32	298.2	1.4
5/19/2018	3821	9305	181342	1.0441	0.0018	35.5	1.8	12075	65.90	-145.61	363.45	306.1	1.4
5/19/2018	3811	9369	182739	1.0532	0.0019	44.6	1.9	12077	64.80	-146.86	360.91	300.6	1.4
5/19/2018	3822	9313	181325	1.0470	0.0018	38.4	1.8	12079	64.25	-147.45	363.73	296.7	1.4
5/19/2018	3807	9299	182740	1.0455	0.0018	36.9	1.8	12078	63.68	-148.00	365.50	293.4	1.4
5/19/2018	3823	9297	181326	1.0148	0.0017	6.4	1.7	8608	62.71	-149.13	315.12	329.9	1.4
5/19/2018	3808	9296	181327	1.0128	0.0018	4.5	1.8	4815	62.32	-149.66	298.77	331.1	1.4

Chapter 4

Isotope Effects and the Atmosphere

4.1 Introduction

Measurements and modeling of the isotopic composition of atmospheric gases and aerosols provide important constraints on the sources, atmospheric transformations, and sinks of a wide variety of chemically and climatically important atmospheric compounds. Isotopes provide information on atmospheric processes beyond that provided by concentration measurements alone due to the fact that physical and chemical (including biochemical) processes – such as diffusion, phase changes, and chemical reactions – fractionate (i.e., alter) the distribution of isotopes of an element in materials undergoing that process. Often the imprint of these processes are preserved in the isotope compositions even though knowledge of the reactant or product concentrations is no longer available. Indeed, this characteristic enables isotopes to be used to infer not only processes in the current atmosphere but also in atmospheres and climates of the past via isotope measurements on compounds preserved in tree rings, corals, ice and sediment cores, and even rocks and minerals.

For chemical processes, as first explored with the work of Urey in the 1930s and 1940s (Urey, 1947; Urey & Greiff, 1935), substitution of a rare, heavy isotope for a common isotope alters the reaction rate. Typically, for elements heavier than hydrogen but lighter than those for which nuclear field shift effects become pronounced (e.g. Ti, Sr, U reviewed in' Fujii et al., 2009), these equilibrium and kinetic isotope effects –the term given to the change in reaction rate coefficient upon isotopic substitution – are driven primarily by differences in vibrational energies between the isotopic analogs (or 'isotopologs' as they have come to be known). In many cases, equilibrium and kinetic isotope effects and their temperature dependence are well-predicted by statistical mechanics and statistical reaction rate theories, driven by these differences in vibrational energies. But, especially for some interesting systems that we highlight in this review, this is not necessarily the case for many reactions relevant for the atmosphere and climate. This may be due in part to the fact that the molecules of interest tend to be small and thus intra- and intermolecular vibrational energy redistribution may be slow compared to the lifetime of an excited species before dissociation or during the course of a collision with a bath gas. In addition, understanding isotope effects in photolysis or isotopic self-shielding require additional theoretical tools beyond statistical mechanics. Thus, to take full advantage of isotopic constraints on atmospheric composition and chemistry, the physical chemistry underlying the isotope fractionation must be understood.

Highlighted here are systems with isotope effects that are likely to be of particular interest to physical chemists, including isotope effects that result in mass independent fractionation (MIF) in ozone formation and others including kinetic isotope effects (KIEs) and photolysis IEs in reactions or processes involving the trace gases nitrous oxide (N_2O), methane (CH_4), and molecular hydrogen (H_2) that are important in atmospheric chemistry and climate, and for which there are evolving needs for experimental and theoretical chemists to provide some of the critical molecular level details of the underlying isotope effects in order to bring the application of isotope composition measurements to atmospheric processes to fruition. While there are several previous

reviews on this subject or on one of the sub-topics (e.g., Brenninkmeijer et al., 2003; Brinjikji & Lyons, 2021; Johnson et al., 2002; Kaye, 1987; Mauersberger et al., 2005; Thiemens, 2006; Thiemens et al., 2012; Thiemens & Lin, 2019; Weston, 2006; Zhao et al., 2021), our purpose here is not to recreate these detailed reviews but to provide very brief histories and the most relevant updates on outstanding questions. Before discussing the species and processes of interest, we also provide a brief overview on measurement techniques and conventional notation for measurements of isotopic compositions at natural abundances, which has largely been in the domain of isotope geochemists and other Earth scientists until recently.

4.2 Background

The conventions when discussing isotope-specific rate coefficients (i.e., KIEs) are different between fields. Chemists report IEs as k_{light}/k_{heavy} whereas earth scientists use k_{heavy}/k_{light}, and throughout this review we will use the convention of chemists. Chemists have often studied KIEs using highly isotopically enriched reactants, usually to distinguish different possible chemical mechanisms. Except for the occasional enriched tracer study, practical only on relatively small spatial scales, Earth and planetary scientists must usually measure isotope compositions at natural isotope abundances. And, until recently (as outlined below), high precision measurements of isotope abundances were largely measured by specialized isotope ratio mass spectrometers (IRMS) in which the ratio of rare to common isotope of a sample is measured relative to that for an international standard and expressed using "δ" notation. We briefly review these points below so we can later discuss isotope ratios of current scientific interest.

4.2.1 Conventions for reporting isotopes compositions at natural abundances

"Delta" notation represents a measure of the relative abundance of a rare, heavy isotope compared to that for the common, light isotope. For example, for nitrogen isotopes, for which the natural abundance of ^{15}N is 0.366%, an isotope composition in δ notation is given in Equation (1) where $^{15}R_{sample}$ is the $^{15}N/^{14}N$ ratio in the sample and $^{15}R_{std}$ in the standard. Because isotope variations are usually fairly small, the ratios are often close to one. Hence, δ values are usually reported in per mil (‰) and represent the part-per-thousand deviation in the isotope ratio in a sample from that in an international standard (hence the factor of 1000 as in Equation 1):

$$\delta^{15}N = \left(\frac{^{15}R_{sample}}{^{15}R_{standard}} - 1\right) \cdot 1000 \qquad \text{Equation (1)}$$

As such, δ values are like a Taylor series expansion and only valid when the deviations are somewhat small. The ln notation in Equation (2) is thus sometimes used since it is not an approximation to the isotope ratio relationships and thus shows no curvature when the isotope fractionation in a system is large.

$$ln\,^{x}O = \ln\left(\frac{\left(\frac{^{x}O}{^{16}O}\right)_{sample}}{\left(\frac{^{x}O}{^{16}O}\right)_{standard}}\right) \cdot 1000 = \ln(1 + \delta\,^{x}O) \qquad \text{Equation (2)}$$

[The example in Equation (2) is for oxygen, for which there are two stable isotopes: ^{17}O at a natural abundance of 0.038% and ^{18}O at 0.205%; thus Equation 2 represents $\ln^{17}O$ or $\ln^{18}O$ when $x=^{17}O$ or ^{18}O, respectively].

The δ and ln notations arose in part from the fact that absolute isotope abundances are extremely difficult to measure accurately and precisely but isotope ratios can be precisely measured, especially historically, using a specialized isotope ratio mass spectrometer (IRMS). Moreover, the sample and the standard gases are fractionated by effusion of the sample and standard gases into the high vacuum region of the IRMS ion source; by measuring the isotope ratio in a sample relative to that in a standard (and, ideally, at similar delivery pressures), the sample and standard are fractionated in the same way, thus yielding robust ratios of ratios in either the δ or the ln notation. This process requires international standards for each species so that isotope values reported by different researchers can be compared. These standards can be species such as air N_2 (the international standard for nitrogen isotope compositions) or they can be a specific sample maintained by the International Atomic Energy Agency (IAEA) and the National Institute of Standards and Technology (NIST) such as Vienna Standard Mean Ocean Water (VSMOW) for oxygen and hydrogen isotopes. Laboratory intercomparisons are regularly required to ensure that values reported in the literature are comparable across research groups.

4.2.2 Mass Dependent vs Non-Mass Dependent Isotope Effects

Oxygen has three rare stable isotopes that can be measured and compared, ^{16}O, ^{17}O, and ^{18}O with abundances 99.76%, 0.04%, and 0.20% (Thiemens & Lin, 2019). Using oxygen isotopes as an example, a mass dependent fractionation process will result in the relationship in Equation (3):

$$\delta^{17}O \sim \lambda_{MD}\, \delta^{18}O \qquad \text{Equation (3)}$$

where λ_{MD} is the mass-dependent fractionation constant. For oxygen isotopes, $\lambda_{MD} = 0.52$ is typically used since that results from the Bigeleisen & Mayer (1947) and Urey (1947) approximation from a Taylor Series expansion of the ratios of partition functions for $^{17}O/^{16}O$ and $^{18}O/^{16}O$ for the specific reactants or products that simplifies to oxygen atomic masses (Bigeleisen & Mayer, 1947; Urey, 1947; Weston, 2006). The specific value of λ_{MD} depends on the masses of reactants and products and will vary somewhat from 0.52, typically between 0.50 and 0.53 (Luz & Barkan, 2005). Conceptually, the value for λ_{MD} is close to 2 because ^{17}O is one amu heavier than ^{16}O while ^{18}O is 2 amu heavier than ^{16}O and if the ^{17}O-containing species is enriched or depleted relative to ^{16}O, the ^{18}O-containing species will be enriched or depleted relative to ^{16}O by twice that amount. This mass-dependent relationship also means that a plot of $\delta^{17}O$ versus $\delta^{18}O$ will yield a slope of ½, which is shown as the dashed line in Figure 1 and is known as the terrestrial mass-dependent fractionation line.

Because so many processes in nature were originally found to follow the mass-dependent relationship between $\delta^{17}O$ and $\delta^{18}O$, and because $\delta^{17}O$ is more difficult to measure than $\delta^{18}O$ (due to the very low abundance as well as some prominent isobaric interferences from ^{13}C, ^{15}N, or ^{2}H in traditional IRMS), for some decades $\delta^{17}O$ was only measured on extraterrestrial materials (e.g.,

Clayton et al., 1973) since the $\delta^{17}O$ value could simply be calculated from the measured $\delta^{18}O$ value for most terrestrial and lunar materials. However, there are now known to be a number of isotope compositions and several reactions that result in large deviations from the mass-dependent relationship in Equation (3), as clear from the measurements shown in Figure 1. Notably, most of the non-mass-dependent deviations are found in oxygen-bearing species in the atmosphere. In addition to the deviation from the slope=0.5 line visible in $\delta^{17}O$ vs $\delta^{18}O$ plots as in Figure 1, this deviation from mass-dependence can be expressed numerically as $\Delta^{17}O$ in Equation (4) (and for which either the δ notation or the ln notation can be used):

$$\Delta^{17}O = \ln {}^{17}O - 0.52 \ln {}^{18}O \qquad \text{Equation (4)}$$

In the context of this review, we will describe a non-zero value for $\Delta^{17}O$ as 'non-mass-dependent,' although we may also refer to this in shorthand as "MIF" or "O-MIF" (for Oxygen Mass-Independent Fractionation). Technically speaking, the term "mass independent" applies if $\delta^{17}O=\delta^{18}O$, as for ozone formed when any mass-dependent isotope effects in ozone photolysis or ozone loss processes are small or when ideal isotopic self-shielding occurs, both of which will be discussed further below. (Hence, we are ignoring what some researchers study in detail: deviations due to the very small variations in λ_{MD} which may also exhibit non-zero $\Delta^{17}O$ values in systems in which more than one reaction or process is occurring but all are mass-dependent.)

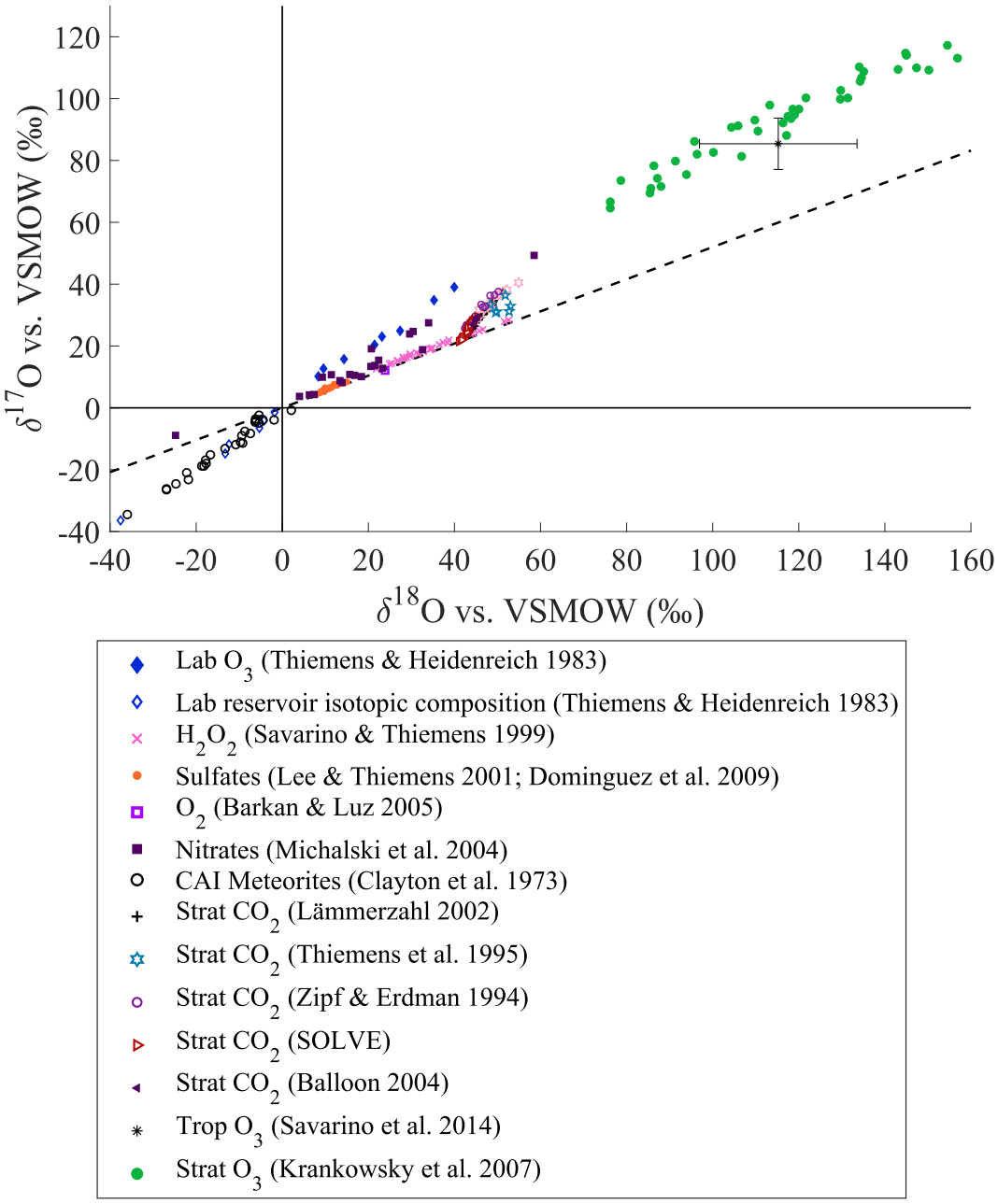

Figure 1: Triple isotope plot ($\delta^{17}O$ vs $\delta^{18}O$) for selected species including laboratory (Thiemens & Heidenreich, 1983), stratospheric (Krankowsky et al., 2007), and tropospheric ozone (Vicars & Savarino, 2014); atmospheric H_2O_2 (Savarino & Thiemens, 1999); atmospheric O_2 (Barkan & Luz, 2005); sulfates (Dominguez et al., 2008; Lee & Thiemens, 2001); nitrates (Michalski et al., 2004); stratospheric CO_2 (Garofalo et al.; Lämmerzahl et al., 2002; Thiemens, Jackson, Zipf, et al., 1995), and calcium aluminum inclusions (CAI) in carbonaceous chondrite meteorites (Clayton et al., 1973). The dashed line with slope of ½ corresponds to mass-dependent fractionation.

4.2.3 Instrumentation

Isotope compositions can be measured using mass spectrometry, nuclear magnetic resonance (NMR), and spectroscopy. The Isotope Ratio Mass Spectrometer (IRMS) is the most commonly used instrument for the precise measurement of stable isotopes at natural abundance throughout Earth and planetary sciences. In atmospheric science, it can be used to measure the isotopic composition of trace gases including N_2O, CH_4, H_2, O_2, CO_2. Since it is a large magnetic sector instrument, samples are usually brought into a laboratory to be measured rather than measured in the field. Less commonly used in atmospheric sciences, NMR (reviewed in Akoka & Remaud, 2020) is ideal for measuring the isotopic composition at particular positions in a non-gas-phase molecule, and both enriched samples (typical in chemical mechanism studies) and natural abundance samples can be analyzed. The most common natural abundance application is analysis of ^{2}H, ^{18}O and ^{13}C compositions for food, wine, and medicine authentication.

More recent advancements in the measurement of isotolog abundances include optical spectroscopy techniques which allow for *in situ* measurements, such as in the field at the site of sampling including, most recently, on aircraft for direct atmospheric sampling and measurement. They utilize the shift in absorption wavelength of different isotopologs to measure the abundance of each and typically have lower precisions than traditional IRMS, although in some cases the direct *in situ* measurement of isotopolog abundances results in similar precisions since the samples do not have to be handled or chemically processed for IRMS analysis, which can introduce additional noise. Spectroscopic techniques were first applied to water vapor isotopes (Moyer et al., 1996; Sayres et al., 2009) since the interesting scientific questions could be addressed with lower precisions due to the very large isotope fractionations associated with water's phase changes. Precisions of spectroscopic techniques have since been improved so they can now be used to more precisely measure the relative isotopolog abundances of CO_2 (e.g. Wehr et al., 2016), CH_4 (Xueref-Remy et al., 2020), and N_2O (Yu et al., 2020) with commercially available instruments from Aerodyne, Picarro, and Los Gatos. Due to the specifics of absorption features, each instrument typically measures the isotopic composition of only one dedicated species.

New instruments using both optical and magnetic sector mass spectrometry techniques have also been recently developed to perform measurements at natural abundances of very rare multiply-isotopically substituted species – that is, species containing more than one rare, heavy isotope of an element (such as $^{13}C^{18}O^{16}O$); since the rare isotopes are 'clumped' together in one molecule or kind of material analyzed, these species are referred to as 'clumped isotopes.' Optically-based laser spectroscopic instrument have been developed for the measurement of clumped isotopes in CH_4 (Ono et al., 2014), CO_2 (Prokhorov et al., 2019), and N_2O (Kantnerová, Yu, et al., 2020). Magnetic sector instruments have also been developed to measure clumped isotope compositions of gaseous species at natural abundances. This technique requires very high mass resolution so that species such as CH4 can be measured directly and distinguished from H_2O isotopologs and other interfering species that would be 'isobaric' in the lower mass resolution traditional IRMS instruments. The 253 Ultra high-resolution gas-source IRMS was developed by Thermo Scientific and Caltech (Eiler et al., 2013) and is now commercially available. The PANORAMA high resolution IRMS was developed through a collaboration between Nu

Instruments, UCLA, and Carnegie Science Geophysical Laboratory (Young et al., 2016). These new methods expand the scope of questions that can be addressed by isotope analysis of atmospheric gases, and their applications will be discussed in the sections below.

4.3 Oxygen Non-Mass-Dependent Isotope Effects and Isotope Compositions (O-MIF) Relevant to Planetary Atmospheres

4.3.1 Ozone

Prior to the discovery in 1983 of the impressively large and mass-independent oxygen isotope fractionation (O-MIF) in the formation of ozone by Thiemens and Heidenreich (1983), MIF observed in 4.5 billion-year-old meteorites was ascribed to nuclear processes, such as a supernova explosion injecting large amounts of material into the proto-solar nebula just before condensation of the solar system (Clayton et al., 1973). This attribution for O-MIF in meteorites was made because there was no known chemical mechanism that could mass independently fractionate oxygen isotopes (and there are unusual isotope compositions in other elements, such as those derived from very short-lived isotopes, that in fact must be derived from nucleosynthetic processes as in a supernova). Yet the Thiemens discovery showed that a chemical mechanism for O-MIF must indeed be occurring. (The Thiemens laboratory measurements are shown in Figure 1, and fall on a $\delta^{17}O$:$\delta^{18}O$ slope of 1.)

Over the decades since then, experimental and theoretical work has shown that the large O-MIF in ozone occurs in the ozone formation reaction with all reactants in their ground electronic states via the energy transfer mechanism (R1):

$$O(^3P) + O_2(^3\Sigma_g^-) \rightleftharpoons O_3^* \qquad \text{(R1a)}$$

$$O_3^* + M \rightarrow O_3(X^1A') \qquad \text{(R1b)}$$

where O_3^* denotes rovibrationally-excited metastable collision complexes which can form a stable ozone product if enough energy is transferred in collisions with a bath gas "M" in this three-body reaction. Although other mechanisms that may mass-independently enrich or deplete the reactants in R1a have been explored (e.g., Cicerone & McCrumb, 1980; Geiser et al., 2000; Klais et al., 1980; Valentini, 1983), the kinetics governing the atmosphere and most laboratory experiments (if not cleverly designed) means that oxygen isotope exchange in R1a rapidly re-establishes the $O(^3P)$ isotope distribution back to that of the large O_2 reservoir (Kaye, 1986). In other words, because the reversible R1a reaction happens about ~5 orders or magnitude faster than R1b under typical atmospheric and experimental conditions, the O-MIF must originate in ozone formation and not in any MIF that might affect the $O(^3P)$ isotope composition, such as ozone photolysis or other sources of O atoms in their ground or electronically excited states ($O(^1D)$ or $O(^1S)$). (Note that, under some conditions, especially very high pressures, ozone may also form by the chaperon mechanism (Luther et al., 2005); there is some controversy over whether this mechanism for ozone formation is relevant for the atmosphere or typical laboratory experiments, so a discussion of this second mechanism for forming ozone is deemed beyond the scope of this dissertation chapter and does not affect the discussion herein.)

Statistical reaction rate theories (Kaye, 1986) predict that there should be small, mass-dependent depletions in ^{17}O and ^{18}O in ozone formed (of ~1 and 2%, respectively), but experiments show that there are huge, mass-independent enrichments (of ~15% depending on experimental conditions) in ozone formed. This is an enormous isotope effect for elements heavier than hydrogen (for which tunneling effects as well as the factor of 2 mass difference between ^{1}H and ^{2}H come into play). Thus, statistical theories for ozone formation predict the wrong magnitude, sign, and mass dependence. Indeed, measurements of the ^{18}O abundance in stratospheric ozone using a molecular beam mass spectrometer by Mauersberger and co-workers that predate the Thiemens MIF experiments showed large enrichments in ^{18}O in ozone (Mauersberger, 1981). (We note that ozone formed in the gas phase anywhere in the atmosphere and in the laboratory will have a MIF character; the first measurements were made in the stratosphere simply because the ozone concentrations are so high there, not because there is anything else special about stratospheric ozone and its isotopic composition.)

Thiemens and Heidenreich (1983) first suggested isotopic self-shielding (see below) as a potential source of the MIF in their discharge-in-O_2 experiments, but they also noted that the symmetric isotopologs of ozone (e.g., $^{16}O^{16}O^{16}O$, $^{16}O^{17}O^{16}O$, and $^{16}O^{18}O^{16}O$) have half the complement of rovibrational states as the asymmetric species (e.g., $^{17}O^{16}O^{16}O$ and $^{18}O^{16}O^{16}O$) due to symmetry restrictions, which could result in differences in the lifetimes or relaxation rates of the symmetric versus asymmetric O_3* complexes. However, we note here that symmetry numbers already appear in RRKM and other statistical reaction rate theories, so a simple density of states difference for symmetric versus asymmetric species is already accounted for in statistical theories, and a more subtle dependence on symmetry, if symmetry is the origin of the O-MIF in ozone formation, is thus required to explain the isotope composition measurements. Indeed, tunable diode laser experiments by Mauersberger and coworkers (Anderson et al., 1989) showed that the ^{17}O and ^{18}O enrichments in ozone were largely carried by the terminal oxygen atom – thus, by the asymmetric ^{17}O and ^{18}O isotopologs of ozone. Furthermore, in careful and detailed experimental work, Mauersberger and co-workers measured isotope-specific rate coefficients for ozone formation by R1 (Janssen et al., 2001; Mauersberger et al., 1999). Their measurements showed large but essentially *mass-dependent* KIEs for the formation of asymmetric ozone isotopologs – of up to 50% for $^{16}O + {}^{18}O^{18}O$ relative to that for $^{16}O^{16}O^{16}O$ – that were dependent on the difference in zero point energies for the different isotopologs of O_2 in the two reactant channels forming the same ozone isotopolog (e.g., the "ΔZPE" between $^{18}O^{18}O$ and $^{16}O^{18}O$ in R2), while the rate coefficients for formation of the symmetric isotopologs of ozone were similar to those for $^{16}O^{16}O^{16}O$ formation.

$$^{16}O + {}^{18}O^{18}O \rightarrow [{}^{16}O^{18}O^{18}O]^* + M \rightarrow {}^{16}O^{18}O^{18}O, \qquad \text{KIE=1.50} \qquad \text{(R2a)}$$

$$^{18}O + {}^{16}O^{18}O \rightarrow [{}^{16}O^{18}O^{18}O]^* + M \rightarrow {}^{16}O^{18}O^{18}O, \qquad \text{KIE=0.92} \qquad \text{(R2b)}$$

$$^{16}O + {}^{17}O^{17}O \rightarrow [{}^{16}O^{17}O^{17}O]^* + M \rightarrow {}^{16}O^{17}O^{17}O, \qquad \text{KIE=1.23} \qquad \text{(R2c)}$$

At first, these differences between the apparently *mass-dependent* KIEs (e.g., compare R2a with R2c) for ozone formation of individual isotope channel formation pathways that depend on ΔZPE

and not symmetry (e.g., compare R2a with R2b) and the apparent 'symmetry-dependent' (and hence mass-independent) ozone isotope compositions were mysterious.

A number of theoretical studies have explored the origin of the O-MIF in ozone, which are, impressively, beyond the scope of this review, and the reader is referred back to previous isotope reviews for some of the earlier work (Mauersberger et al., 2005; Schinke et al., 2006; Thiemens et al., 2012). The highlights that withstand the test of time are the approaches by Marcus and co-workers (Gao & Marcus, 2001, 2007; Hathorn & Marcus, 1999, 2000) using a modified RRKM approach and the quasi-classical trajectory approach of Schinke and co-workers (e.g., Qu et al., 2005a; Qu et al., 2005b; Schinke & Fleurat-Lessard, 2005) which both draw heavily on the key isotope-specific rate coefficients measured for R1 by Mauersberger and co-workers (Janssen et al., 2003; Janssen et al., 2001; Mauersberger et al., 1999) and the isotope composition measurements by Thiemens and co-workers (Heidenreich & Thiemens, 1983, 1986; 1983; Thiemens & Jackson, 1988, 1990). Marcus and co-workers were the first to resolve the apparent discrepancies between the experimental Mauersberger KIEs for ozone formation and the Thiemens ozone isotope composition measurements. In a modified RRKM approach, Marcus separated the ozone isotope effects into two isotope effects: the ΔZPE effect and the η ("eta") effect. Their 2001 paper (Gao & Marcus, 2001) lays out the reasoning and results in a readable and straightforward manner, so the reader is referred to that paper in particular. In short, Marcus showed that enormous differences in KIEs can result when forming one ozone isotopolog from two different isotope-specific reactant channels (e.g., compare the large difference in KIE when forming $^{16}O^{18}O^{18}O$ in R2a versus R2b). These different KIEs can only be measured in "unscrambled" laboratory conditions under which $O+O_2$ isotope exchange (R1a) is slow and/or the experiment is stopped before significant scrambling of the isotopes in, for example, the $^{18}O^{18}O$ reactant in R2a occurs (via ozone formation and subsequent photolysis to form O atoms, which then 'scramble' the reactant O_2 to now include $^{16}O^{18}O$ reactant as well as the initial $^{18}O^{18}O$). When ozone can form from either channel (e.g., R2a and R2b), which occurs under 'scrambled' conditions, then the ΔZPE isotope effect cancels out and what remains is the η effect for symmetric versus asymmetric isotopologs of ozone, as described below.

The second isotope effect in Marcus' modified RRKM approach to the ozone formation reaction is the η effect. After accounting for the ΔZPE effect using RRKM theory, Marcus noted that, while neither the symmetric nor the asymmetric isotopologs of ozone behaved statistically, the symmetric isotopologs were 18% less statistical than the asymmetric isotopologs. When he applied this empirical difference between the symmetric and asymmetric ozone isotopologs in his RRKM approach – that is, using a phenomenological difference of 18% in the densities of states of the symmetric versus asymmetric isotopologs based on an empirical fit in his analysis to the Mauersberger KIEs – he could reproduce the Thiemens ozone isotope compositions, including their observed temperature and pressure dependence (Gao & Marcus, 2001, 2007). He called this 18% difference the "η effect." Since the ΔZPE effect cancels out under "scrambled" conditions, the only isotope effect that remains in the atmosphere and under most laboratory conditions (since 'scrambling' is efficient through R1a) is the η effect, which is somehow related to the symmetry of the excited ozone complex, O_3* or at least the fact that the heavy isotope enrichments appear on the terminal atom.

Schinke and co-workers (Babikov et al., 2003a; Grebenshchikov et al., 2007; Grebenshchikov & Schinke, 2009; Ivanov et al., 2009; Ivanov & Schinke, 2005; Ivanov & Schinke, 2010; Qu et al., 2005a, 2005b; Schinke & Fleurat-Lessard, 2005; Schinke & Grebenshchikov, 2008; Schinke et al., 2009; Siebert et al., 2001) had the same aim, and they performed quasi-classical trajectory calculations to predict differences in the formation rates of some key ozone isotopologs. They, too, found that they could explain the Mauersberger ozone formation KIEs via zero-point energy differences in the isotope-specific O_2 reactants and also that an empirical ~15% difference in the lifetimes of the symmetric and the asymmetric isotopologs of O_3* could reproduce the Mauersberger KIEs. The origin of the η effect in the ozone formation reaction, however, remains elusive, almost 40 years since its discovery and about 20 years after the resolution of the apparent discrepancies between the ozone KIE and ozone isotope compositions by Marcus and by Schinke.

Among the promising theoretical studies of ozone formation, Babikov and co-workers have performed a number of approximate or full quantum mechanical calculations (e.g., Ayouz & Babikov, 2013; Babikov, 2003; Babikov et al., 2003a, 2003b; Gayday et al., 2020; Teplukhin et al., 2018) for O_3* in R1a (and often including master equation modeling for the subsequent ozone stabilization in R1b). Their work has provided insights into the ΔZPE effect but not yet – quantitatively at least – the η effect. One interesting set of quantum calculations (Ivanov & Babikov, 2013) suggested that placement of a heavy isotope at the terminal position of ozone could distort the vibrational wavefunctions and result longer tunneling lifetimes into and out of O_3* for asymmetric O_3* than for symmetric O_3*. While this was promising for $^{16}O^{16}O^{18}O$ and $^{16}O^{18}O^{16}O$, it did not work for $^{16}O^{18}O^{18}O$, so Babikov has moved on to other calculations (referenced below), as well as providing important new 'guides' for researchers interested in calculating ozone KIEs and isotope compositions, which we refer the reader to here (Teplukhin & Babikov, 2018a, 2018b).

Other theoretical work of note over the past decade includes the following: quantum scattering calculations of state-to-state differential and integral cross-sections for the O + O_2 reaction which are highly nonstatistical (Sun et al., 2010); calculation of non-RRKM effects that arise from diffusive energy exchange between vibrational and rotational degrees of freedom in ozone (Kryvohuz & Marcus, 2010); new calculations that include couplings between vibrational channels to investigate the role of Feshbach resonances and interaction of reaction pathways in which it is purported that Feshbach resonances explain the ΔZPE effect and some of η effect (Teplukhin et al., 2018c); and new calculations of vibrational states in singly- and doubly-isotopically substituted ozone isotopologs in which there is a deviation from the statistical factor of 2 for the ratio of the number of states in asymmetric and symmetric ozone that is different at different energies (near the dissociation threshold asymmetric ozone molecules may contain more than twice as many states as symmetric ozone which could lead to the η effect (Gayday et al., 2019)).

Relevant experimental work since 2005 includes crossed molecular beam experiments on the $^{18}O + {}^{32}O_2$ isotope exchange reaction which showed non-statistical behavior (by comparison with quantum statistical theory and QCT calculations) and its energy dependence (Van Wyngarden et al., 2007, 2014). Studies have also produced ozone in a high frequency RF discharge, and the reservoir O_2 isotopic composition was monitored during the distillation, determining the evolution

from a mass independent to a mass dependent fractionation as the pressure decreases (Robert et al., 2019). Cavity ring down spectroscopy was used to detect two very high energy vibrational bands that are combination and overtone bands around 7900 cm^{-1}, and confirmed the absence of an activation barrier towards dissociation threshold (Vasilchenko et al., 2020). Continued investigation into the potential energy surface (PES) of ozone includes calculations of ^{16}O-, ^{18}O- and ^{17}O-substituted ozone with a mass-dependent diagonal Born-Oppenheimer correction to the *ab initio* PES showing better alignments to experiment in the vibrational band calculations (Tajti et al., 2020). In addition, calculations of the high energy states of ^{16}O- and ^{18}O-substituted ozone found that levels are delocalized between the potential wells of ozone isomers and those below the potential barriers between the wells are split due to tunneling (Kokoouline et al., 2020).

Finally, we will note here that there remain no credible reports of mass-independent isotope effects in ozone photolysis. For example, Cole & Boering (2006) have shown that such claims usually result from interference from the huge MIF in ozone formation in experimental studies. Once modeled, they often can account for any MIF in ozone (or other species) measured, even when experimenters believe they have eliminated any contribution from ozone formation. Theoretical studies have corroborated this lack of MIF in ozone photolysis, including calculations of the branching ratios of electronic and isotopic photodissociation channels of ozone using quantum mechanical wave packet propagation (Ndengué et al., 2012), as well as a new model using full quantum theory to show the origin of the observed pattern of even-odd rotational state populations of O_3 after photodissociation to $O_2(^1\Delta)$ (Han et al., 2020); in this latter study the A1 Gamma doublet states are populated which can only occupy even rotational states due to symmetry conversion. Thus parity-selective curve-crossing cannot be a source of heavy isotope enrichment resulting from ozone photolysis.

In summary, the origin in chemical physics of the large mass-independent enrichment in the ozone formation reaction remains unknown and represents an intriguing chemical physics puzzle that deserves further study. It may in part stem from ozone's unusually small anharmonicity up to the dissociation limit and relatively shallow potential well. It may also be largely limited to ozone. Yet that should not relegate this isotope effect to be considered a difficult and esoteric chemical physics problem that has little impact. Rather, as we will highlight in the next section, the O-MIF in ozone is photochemically transferred to many oxygen-bearing species in the atmosphere, including atmospheric CO_2, O_2, nitrates and sulfates. These in turn provide tracers of atmospheric processes not only in the contemporary atmosphere but also back in time through incorporation of these atmospheric isotope signals in ice cores and even in ancient minerals including sulfates, carbonates and bioapatites (i.e., fossilized teeth and bones). The robustness of all of these many tracers of atmospheric processes and climate, particularly back in time, ultimately depend on a complete understanding of the chemical physics of O-MIF in ozone formation.

4.3.2 Species with O-MIF derived from ozone

4.3.2.1 Stratospheric CO_2

In the early 1990s, measurements of $\delta^{17}O$ and $\delta^{18}O$ of CO_2 from samples of stratospheric air collected by aircraft (Thiemens, Jackson, & Brenninkmeijer, 1995) and rocket (Thiemens,

Jackson, Zipf, et al., 1995) showed non-mass-dependent enrichments. Although smaller than those in ozone, they were still significant and exhibited a $\delta^{17}O/\delta^{18}O$ slope larger than 1, including a slope of 1.2 in the upper stratosphere. The stratospheric observations that followed these initial measurements (Alexander et al., 2001; Boering et al., 2004; Kawagucci et al., 2008; Lämmerzahl et al., 2002; Wiegel et al., 2013) showed even larger $\delta^{17}O/\ \delta^{18}O$ slopes, ranging from 1.7 (Lämmerzahl et al., 2002) to 2.3 (Wiegel et al., 2013). Yung *et al.* (1997) predicted that the O-MIF in ozone could be photochemically transferred to CO_2 via UV photolysis of O_3 in reactions R3 and R4:

$$O_3 + h\nu \rightarrow O(^1D) + O_2 \qquad \text{(R3)}$$

$$O(^1D) + CO_2 \rightarrow CO_3^* \rightarrow O(^3P) + CO_2 \qquad \text{(R4)}$$

Yung *et al.* based this idea on enriched isotope studies from the early 1960s that used the R3 and R4 reaction sequence to study the chemistry of electronically excited oxygen atoms (Katakis & Taube, 1962; Weissberger et al., 1967), which found that there was substantial transfer of ^{18}O from ozone to CO_2. In fact, similar experiments showed that there is a 2/3 chance that an incoming ^{18}O atom wound up in the product CO_2 (Baulch & Breckenridge, 1966), which is what would be expected for the statistical isotope exchange (Kaye, 1986). Yung and co-workers (Liang et al., 2007) later simulated a slope of ~1.6 from the abundance of CO_2 and O_3 isotopologs in their stratospheric model. (They also postulated that the lower slope of 1.2 observed in the upper stratosphere is likely due to another source of $O(^1D)$ in the mesosphere – O_2 photolysis by solar Lyman α radiation – that imparts a smaller isotopic enrichment to CO_2 than O_3, and which can influence the upper stratosphere where the rocket samples were collected due to transport of air down from the mesosphere.)

Early laboratory studies also showed MIF enrichments in ^{17}O and ^{18}O of CO_2 in experiments in which CO_2 was irradiated with UV light in an O_2/CO_2 gas mixture (Johnston et al., 2000; Wen & Thiemens, 1993), although the experimental slopes were very close to 1, so were thought not to represent the processes determining the isotope composition of stratospheric CO_2. (A set of experiments in 2003 produced a slope of ~1.6 (Chakraborty & Bhattacharya, 2003) but it is now believed (Shaheen et al., 2007; Wiegel et al., 2013) that their absolute results for $\delta^{17}O$ and $\delta^{18}O$ are highly unusual and that isotopic self-shielding likely played a role due to high O_3 concentrations.) Furthermore, non–mass-dependent isotope effects apart from those in O_3 formation – and often in R4 above – were invoked to account for a $\delta^{17}O/\delta^{18}O$ slope > 1 (Thiemens, Jackson, Zipf, et al., 1995; Wen & Thiemens, 1993), including a coincidental near-resonance for $^{17}O^{12}C^{16}O_2^*$ or a nuclear spin/spin-orbit coupling effect in R4. And yet, the reaction in R4 is very different from the 3-body ozone formation reaction in R1. Although spin-forbidden, R4 proceeds at the gas kinetic rate (Davidson et al., 1976), and experiments (Baulch & Breckenridge, 1966) had shown transfer of ^{18}O from ozone to CO_2 that was close to statistical (2/3). Thus, CO_3^* may likely be relatively long-lived and, hence, non-RRKM effects might be expected to be negligible for CO_3^* compared to O_3^*.

To investigate the likelihood of O-MIF in R4, Boering, Lin and co-workers studied the reaction dynamics of R4 in crossed atomic and molecular beams (Perri et al., 2004, 2003). They found,

unlike for R1a in their $O+O_2$ isotope exchange studies (Van Wyngarden et al., 2007), that R4 behaves entirely statistically: the reaction scattering was isotropic, indicating a lifetime for the CO_3* complex that is long-lived with respect to its rotational period and suggesting that intramolecular vibrational energy redistribution was complete before dissociation to products. Thus, there is likely no unusual MIF in R4 as there is in the ozone formation reaction R1. There may be small statistical KIEs in R4 (e.g., Mebel et al., 2004) but the reaction dynamics of R4 suggest nothing similar to the ozone formation reaction, with its non-statistical differences in lifetimes for symmetric versus asymmetric isotopologs of O_3*, is occurring in CO_3*.

To explain the $\delta^{17}O/\delta^{18}O$ slopes ranging from 1.7 to as high as 2.3 observed in their own stratospheric CO_2 observations, Wiegel *et al.* (2013) combined laboratory experiments on the UV photolysis of O_2/CO_2 mixtures and photochemical modeling to show that the laboratory-generated CO_2 isotopic compositions can be quantitatively explained solely by KIEs in ozone formation and $O+O_2$ isotope exchange (see their Figure 2) when the CO_2 mixing ratio in the experiment is close to that in the atmosphere and when the isotopic compositions of the laboratory CO_2 and O_2 reactants in the model were changed to those for tropospheric CO_2 and O_2. No additional MIF isotope effects must be invoked. Rather, they hypothesize that *mass-dependent* isotope effects in ozone photolysis or an unusual temperature dependence for the ^{17}O KIEs for ozone formation, which have not been measured directly before, may explain both the $\delta^{17}O/\delta^{18}O$ slope differences between the laboratory and the stratospheric data and between the stratospheric data in different regions of the stratosphere (e.g., tropical regions are both colder and have higher O_3 photolysis rates than the midlatitudes, neither of which are simulated under the laboratory conditions). While transfer of the MIF from O_3 to CO_2 can explain the CO_2 isotope observations, additional theory and experiments are needed to be truly quantitative throughout the stratosphere, including O_3 photolysis isotope effects under solar actinic flux conditions and the temperature dependence of the individual KIEs for the formation of $^{17}O^{16}O^{16}O$ and $^{16}O^{17}O^{16}O$; only the temperature dependence of the average of these two reactions has been measured (Janssen, 2005; Janssen et al., 2001).

A more quantitative understanding of the O-MIF in stratospheric CO_2 is also needed to put the many applications involving O-MIF in tropospheric CO_2 and in O_2 on sounder footing, as described in the following sections.

4.3.2.2 Tropospheric CO_2

Because the stratospheric circulation brings CO_2 with non-mass-dependent isotope compositions from isotope exchange with O_3 down to the troposphere, and we can quantify the global mean annual net flux of $\Delta^{17}O$ of CO_2 from the stratosphere to the troposphere (see Garofalo et al.), measurements of $\Delta^{17}O$ of tropospheric CO_2 can in principle provide a means to measure global gross primary productivity – the gross rate of uptake of carbon by the biosphere, which has been difficult to measure on a global scale. The idea to use $\Delta^{17}O$ of tropospheric CO_2 as such a tracer was first put forth by Hoag e*t al.*, (2005), based on similar efforts using $\delta^{18}O$ of CO_2 (Ciais et al., 1997; Francey & Tans, 1987). Conceptually, when the stomata of plants are open for photosynthesis, the CO_2 diffusing in is either photosynthetically fixed and thus removed from the atmosphere or it rapidly exchanges isotopes with liquid water (which has a mass-dependent

isotopic composition) so that $\Delta^{17}O$ is reset to zero before it diffuses back out into the atmosphere (Hoag et al., 2005). Knowing the rate at which $\Delta^{17}O$ of CO_2 returns from the straotsphere, measurements of $\Delta^{17}O$ of tropospheric CO_2 can be used to infer annual global gross primary productivity. Several studies have pursued this idea (Adnew et al., 2020; Hofmann et al., 2012, 2017; Koren et al., 2019; Thiemens et al., 2014), although the signal is small. Although these applications can be pursued empirically – i.e., because we know the flux of $\Delta^{17}O$ of CO_2 from the stratosphere to the troposphere empirically from stratospheric observations (e.g., Garofalo et al., gives a review of these fluxes for many different isotopic species) – when the tracers are applied back in time and the fluxes are not known, knowledge of the underlying physical chemistry of the origin of the MIF in ozone and its transfer to CO_2, is needed to more confidently extrapolate the O-MIF in ozone and CO2 to different climates and atmospheric compositions.

4.3.2.3 O_2

On short timescales, ozone is mass-independently enriched in ^{17}O and ^{18}O. On a timescale of several years (during the transit of air through the stratosphere), that O-MIF signal in ozone is transferred to CO_2 (which is then lost to photosynthesis, and a smaller amount by uptake by the oceans). Thus, ozone formation followed by transfer of ^{17}O and ^{18}O to CO_2 effectively sequesters these isotopes from the atmospheric O_2 reservoir, thus producing a negative MIF signal in O_2. This MIF signal in O_2 on the time scale of the stratospheric circulation is tiny, but still can be used to help quantify photosynthesis, respiration, and gross primary productivity of soils and oceans (Angert et al., 2003; Ash et al., 2020; Juranek & Quay, 2013; Jurikova et al., 2016; Kaiser, 2011; Luz & Barkan, 2000, 2005, 2011; Nicholson et al., 2012; Prokopenko et al., 2011). On even longer time scales – such as the lifetime of O_2 in the atmosphere – currently about 1200 years – a negative MIF signal in $\Delta^{17}O$ of O_2 can build up further, and the magnitude will depend on the competing rates of production of negative MIF in the stratosphere via ozone and CO_2 with dilution by O_2 produced by the biosphere, which has no MIF signal, and removed by respiration. This idea was first put forth by Luz *et al.* (1999) and used to propose that measurements of $\Delta^{17}O$ of O_2 in ice cores could be used to infer global gross primary productivity on glacial-interglacial time scales. Oxygen gas trapped in ice bubbles is analyzed for the triple oxygen isotope composition and used to determine the gross primary productivity (Blunier et al., 2012; Brandon et al., 2020; Landais, Lathiere, et al., 2007; Landais, Masson-Delmotte, et al., 2007; Luz et al., 1999), oxygen productivity (Blunier et al., 2002), and the temperature (Suwa et al., 2006; Yau et al., 2016), and relative humidity (Winkler et al., 2012) in paleoclimates. Some key findings include that, during the last interglacial, the Greenland ice sheet did not fully melt (Yau et al., 2016), that biosphere productivity was higher during Termination V than in the more recent terminations (Brandon et al., 2020), and that the last interglacial was warmer than the current period (Suwa et al., 2006).

4.3.2.4 Minerals

For minerals whose composition depends on interactions with the atmosphere, the O-MIF signals in CO_2 and O_2, derived from the ozone formation reaction and transferred to CO_2 (and hence sequestered from O_2), may be preserved, their isotopic compositions may thus serve as proxies for atmospheric composition and/or biosphere signals. $\Delta^{17}O$ of mineral sulfates, for example, can be measured and used to determine biosphere productivity and the partial pressure

of CO_2 in Earth's atmosphere in the distant past (Bao et al., 2009, 2008; Crockford et al., 2016, 2018, 2019). The O-MIF signal in spherules can be used to check whether the atmosphere was isotopically homogeneous and may be useful as paleo-CO_2 proxies (Pack et al., 2017). Bioapatite is formed from the fossilization of teeth and bones of, e.g., rodents, marine invertebrates, which can be measured for their O-MIF signals to determine paleo-CO_2 concentrations (Pack et al., 2013), evaporation rates in paleoclimates (Passey et al., 2014), and as a paleothermometer (Gehler et al., 2016).

4.3.2.5 Atmospheric nitrates

The O-MIF generated in the ozone formation reaction can also be transferred to nitrates by reactions in the atmosphere, and the O-MIF signal in nitrates in soils has thus been found to be a useful way to quantify atmospherically deposited nitrates (e.g., Alexander et al., 2009; Dejwakh et al., 2012; Durka et al., 1994; Nelson et al., 2018; Savard et al., 2018; Tsunogai et al., 2010). The oxidation of NO_x leads to the formation of HNO_3, and measurements of the $\Delta^{17}O$ isotopic composition can also be used to understand the nitrogen cycle and the oxidative capacity of the atmosphere (Michalski et al., 2003).

The three pathways producing nitrate in the atmosphere are the gas phase reactions:

$$OH + NO_2 + M \rightarrow HNO_3 + M \quad \text{(R5)}$$

$$NO_2 + O_3 \rightarrow NO_3 + O_2 \quad \text{(R6a)}$$

$$NO_3 + HC, DMS \rightarrow HNO_3 + products \quad \text{(R6b)}$$

$$NO_2 + NO_3 \leftrightarrow N_2O_5 \quad \text{(R7a)}$$

and the heterogeneous reaction:

$$N_2O_5 + H_2O_{(surface)} \rightarrow 2HNO_{3\,(aq)} \quad \text{(R7b)}$$

where the O-MIF is passed to nitrates from ozone, and it is distinct from other sources of nitrate such as that from fertilizer and soil nitrogen (e.g., Michalski et al., 2003)

4.3.2.6 Atmospheric sulfates

Sulfate aerosols in the modern atmosphere are a major component in particulate matter in urban regions and are also formed during volcanic eruptions. Most sulfate formation occurs through the oxidation of SO_2 in the aqueous phase by hydrogen peroxide, ozone, oxygen, and hypohalous acid (e.g., HOBr), while the rest is oxidized in the gas-phase by hydroxyl radicals. The reactions are described in detail in Faloona *et al.* (2009). The aqueous phase reactions first require the formation S(IV) in aerosols through the following forms

$$SO_{2(g)} + H_2O \leftrightarrow SO_2 \cdot H_2O_{(aq)} \quad \text{(R8a)}$$

$$SO_2 \cdot H_2O_{(aq)} \leftrightarrow HSO_3^- + H^+ \quad \text{(R8b)}$$

$$HSO_3^- \leftrightarrow SO_3^{2-} + H^+ \quad \text{(R8c)}$$

These species can go on to react through three processes

$$S(IV) + O_3 \rightarrow SO_4^{2-} + \text{products} \quad \text{(R9)}$$

$$S(IV) + H_2O_2 + H+ \rightarrow SO_4^{2-} + \text{products} \quad \text{(R10)}$$

$$SO_3^{2-} + HOBr \rightarrow HSO_4^{-} + Br^{-} \quad \text{(R11)}$$

The gas phase reactions that produce sulfate are

$$SO_2 + OH \rightarrow HOSO_2 \quad \text{(R12a)}$$

$$HOSO_2 + O_2 \rightarrow HO_2 + SO_3 \quad \text{(R12b)}$$

$$SO_3 + H_2O \rightarrow H_2SO_4 \quad \text{(R12c)}$$

The oxygen isotopic composition of sulfate is representative of the oxidation processes that were involved because each oxidant imparts a different $\Delta^{17}O$, with H_2O_2 and O_3 leading to non-zero $\Delta^{17}O$ values. This was first shown by (Savarino et al., 2000) and most recently applied by Hattori *et al.* (2021), which is an excellent up-to-date reference for this topic.

In addition to measurements in the current atmosphere, the O-MIF signal in the sulfate aerosols contained in snow and ice samples can also be measured and allow the reconstruction of past volcanic activity, with large eruptions leading to stratospheric intrusions and potential changes in the chemical pathways occurring in the atmosphere, as described by Gautier *et al.* (2019), and of the oxidative capacity of the atmosphere over time (e.g, Ishino et al., 2021; Walters et al., 2019). There is also a recent review of this topic by Zhao *et al.* (2021). As for the other species with O-MIF signals used as tracers discussed in the sections above, a robust understanding of the chemical physics of KIEs in the ozone formation reaction and transfer of the resulting O-MIF from ozone to other species, such as CO_2, nitrates, and sulfates, will lead to sounder interpretations of these O-MIF signals, especially as O-MIF is used to trace these signals back to previous climates and atmospheric compositions.

4.3.3 O-MIF in other species: CO and SiO

Several other species are worth highlighting: CO – which has small values of $\Delta^{17}O$ but which also appears to be one of the few species with interesting non-mass-dependent isotope effects that are not traced back to the unusual KIEs in the ozone formation reaction (either directly, as described above in Section 4.3.2, or through experimental artifacts, which are unfortunately very common in systems in which even small amounts of O atoms and O_2 molecules are present) – and SiO, which could potentially be the source of the O-MIF found in the 4.5 billion-year-old meteorites noted earlier.

Both Brenninkmeijer and co-workers (Röckmann et al., 1998a; Röckmann et al., 1998b) and Thiemens and co-workers (Huff & Thiemens, 1998) measured non-zero values of $\Delta^{17}O$ in atmospheric CO. The anti-correlation of $\Delta^{17}O$ of CO and CO concentrations observed by both groups indicated that it is the sink reaction, CO+OH, that is largely responsible for the O-MIF (Huff & Thiemens, 1998; Röckmann et al., 1998b), albeit with a small contribution from O-MIF from ozone due to ozonolysis of hydrocarbons (Röckmann et al., 1998b). Laboratory

investigations indeed found that the reaction CO + OH is the dominant source of the MIF for which the remaining CO is mass-independently enriched in ^{17}O and 18O (Röckmann et al., 1998b). This finding was supported by laboratory experiments to determine reaction rates and KIEs (Feilberg et al., 2005; Feilberg et al., 2002). Just as the CO+OH reaction is complex, proceeding on a complicated PES with formation of a HOCO complex that can react to form H+CO_2 via several transition states and complex geometries or be collisionally stabilized to form HOCO (see, e.g., Zhu et al., 2001), so too are the ^{13}C, ^{17}O, and ^{18}O KIEs complex: ^{18}O exhibits an inverse KIE with little pressure dependence, ^{17}O shows a positive KIE, and ^{13}C shows a normal KIE at atmospheric pressure but changing to an inverse KIE at pressures < 400 mbar. All 3 KIEs show a different pressure dependence, and they in turn are different than the pressure dependence of CO+OH rate coefficient. Given the importance of this reaction in combustion and atmospheric chemistry, it is interesting that more experimental and theoretical work has not been done to bring additional insights via these unusual KIEs.

Self-shielding and other photolysis isotope effects are another means by which CO – one of the most common molecules in the universe – may obtain an O-MIF signature in interstellar clouds or in low temperature regions of the solar nebula, which has been invoked as an additional mechanism by which the most primitive meteorites could obtain their O-MIF signature, for example. Self-shielding may occur when an atmosphere or gas cloud becomes optically thick for the wavelengths that photodissociate the common isotopolog of a species (e.g., $C^{16}O$) but the wavelengths that photodissociate the rare isotopologs (e.g., $C^{17}O$ and $C^{18}O$) remain optically thin, which can induce a mass-independent fractionation effect. Experiments photodissociating CO with VUV synchrotron radiation found mass-independent enrichments in the product CO_2 with respect to the reactant CO, with wavelength-dependent enrichments (Chakraborty et al., 2008). It remains controversial whether the experimental results represent some form of self- or mutual-shielding or some other type of isotope effects in the photodissociation of CO (Lyons & Young, 2005).

In addition, while not atmospherically relevant, the reaction SiO + O occurring in the solar nebula has been proposed as a possible source of O-MIF that could occur during particle formation as the solar nebula cooled. This reaction was suggested as a possible source of MIF in meteorites with calcium-aluminum rich inclusions (Marcus, 2004), and one experimental study has generated SiO_2 through this gas-phase reaction and found a $\delta^{17}O/\delta^{18}O$ slope of 1 (Chakraborty et al., 2013). Additional work is needed to understand the O-MIF in this reaction.

4.4 Normal and Inverse Kinetic Isotope Effects in Atmospheric Species

The following sections highlight less exotic but still interesting and important KIEs and photolysis isotope effects that are important in atmospheric studies and which could also benefit from additional experimental and theoretical inputs. Here, we also note that KIEs in some of these systems may be more reliable than the absolute value of the rate coefficient (Melissas & Truhlar, 1993), providing additional insights than experiments alone, which are often extremely difficult to measure.

4.4.1 Methane (CH_4)

As a potent greenhouse gas and a regulator of the oxidative capacity of the atmosphere, quantifying methane sources and sinks is important, and extensive modeling efforts have been undertaken to understand fluctuations in the atmospheric growth rate (e.g., Fung et al., 1991; Turner et al., 2019). Concentrations of methane showed a steady increase, briefly leveling off from 2000-2007, and then continuing to increase, but the cause of these changes is not yet fully understood (Turner et al., 2019). The isotopic composition of methane in the troposphere has been used to constrain sources, sinks, and the global distribution of methane (e.g., Quay et al., 1999; Tyler et al., 1999). Isotopic analysis has been performed on ice cores, archived samples, and monitoring stations to see trends in concentrations and isotopic compositions in the past and present and to perform source attribution (recent observations include: Kai et al., 2011; Rice et al., 2016; Schaefer et al., 2016; Schwietzke et al., 2016).

To use the isotopic composition as a constraint, an accurate understanding of the KIEs of the sink reactions with OH, $O(^1D)$, and Cl are needed. Laboratory studies have investigated and found that OH has a large KIE (Cantrell et al., 1990; Saueressig et al., 2001) such that small differences or uncertainties can impact the isotopic composition in the troposphere (McCarthy et al., 2001) and the KIE of the reaction with Cl (Crowley et al., 1999; Joelsson et al., 2014; Saueressig et al., 1995; Tyler et al., 2000) can impact stratospheric and tropospheric isotopic compositions (Gupta et al., 1996; McCarthy, 2003; McCarthy et al., 2001; Tyler et al., 1999; Wang et al., 2002). The reaction $O(^1D) + CH_4$ has also been studied and found to have a smaller, but still significant, KIE (Davidson et al., 1987; McCarthy, 2003; Saueressig et al., 2001). These laboratory determined KIEs can then be used to investigate the isotopic composition of atmospheric CH_4 through measurements and modeling. Analysis of the stratosphere isotopic compositions, and their correlations with other long-lived tracers, can serve as a "kinetics laboratory" where reactions can be understood through observations and laboratory experiments combined with theory and atmospheric modeling. The stratosphere is useful because there is a high photon flux, mixing and transport time scales are relatively slow, and, since it is far from most sources and sinks at the surface and short-lived gases have reacted away, the stratosphere is not as chemically complicated as the troposphere. Measurements of the isotopic composition of CH_4 in the stratosphere (Brenninkmeijer et al., 1995; McCarthy, 2003; Rice, 2003; Röckmann et al., 2011; Sugawara et al., 1997) show large enrichments in $\delta^{13}C\text{-}CH_4$ and $\delta D\text{-}CH_4$ as CH_4 is oxidized by OH, $O(^1D)$ and Cl, providing insights into how the isotopic composition varies throughout the stratosphere (McCarthy, 2003; Rice, 2003) and over time (Röckmann et al., 2011).

In addition, theoretical studies have investigated the underlying chemical physics these oxidation KIEs. Variational TST was used to calculate the $OH + CD_4$ and $OH + {}^{13}CH_4$ KIEs finding the importance of zero-point energy differences, of course, as well as tunneling effects for both the D and ^{13}C KIEs (Melissas & Truhlar, 1993). Theory has also sought to quantify and understand the KIE for reaction with Cl by calculating differential cross sections (Totenhofer et al., 2016), and using ab initio semiclassical transition state theory (Barker et al., 2012), and molecular dynamics methods (Liu & Li, 2020). Nevertheless, remaining discrepancies between CH_4

oxidation KIEs between laboratory and stratospheric measurements and theoretical calculations remain.

4.4.2 Molecular hydrogen (H_2)

Both concentration and isotope composition measurements have been used to quantify the sources and sinks of atmospheric H_2. The importance of understanding hydrogen emissions grew with the development and discussion of hydrogen fuel cell vehicles, since the immense H_2 leaks that might occur could potentially lead to ozone depletion through increased water in the stratosphere due to oxidation by OH there (Tromp, 2003), and this led to an even more urgent need to understand the global hydrogen budget. Seeking to understand the global sources and sinks of H_2, measurements were made of the isotope fractionation due to soil uptake, biomass burning and fossil fuel combustion and compared with tropospheric δD-H_2 measurements and concentration measurements (Gerst & Quay, 2001). Without invoking a heavy source of H_2, however, the concentration budgets and the isotope budgets for H_2 were greatly out of balance. Notably, the inferences from concentration versus isotope measurements of H_2 for the global budgets were in conflict.

In 2003, measurements of H_2 in the stratosphere were used to resolve the large discrepancy between the H_2 concentration and isotope budgets (Rahn et al., 2003). As air in the stratosphere photochemically aged, H_2 showed enormous enrichments in deuterium, while the concentration remained fairly, indicating that there must be a process that enriches H_2 in the stratosphere such as the source or sink of hydrogen. Hydrogen is produced in the stratosphere by the oxidation of CH_4 which proceeds through CH_2O, and H_2 is destroyed by the H_2+OH reaction The stratospheric measurements demonstrated that both of these reactions lead to the enormously high values of dD-H_2 in the stratosphere that grow in over time (Rahn et al., 2003). Hydrogen isotopes continued to be measured in the stratosphere at different altitudes and latitudes corresponding to different temperatures, photon fluxes, and wavelengths. The observations were also compared with laboratory experiments to understand isotope effects in the photolysis of CH_2O isotopologs; there are two channels and it was shown that it is the molecular channel that produces H_2 enriched in deuterium and that the H_2 becomes further enriched as the pressure increases (Nilsson et al., 2010; Röckmann et al., 2010), as predicted by modeling in 2007 (Mar et al., 2007). The normal KIE in the sink reaction $H_2 + OH \rightarrow H_2O + H$ leads to enrichments that are relatively well quantified experimentally (Ehhalt et al., 1989; Talukdar & Ravishankara, 1996).

These observational and experimental studies can be combined with atmospheric modeling such as a 2D atmospheric radiative transport model to understand the implications that the KIEs have on the enrichments in the troposphere (Mar et al., 2007) and theoretical chemistry methods such as RRKM calculations of the CH_2O photolysis that indicate that there is competition between unimolecular dissociation and collisional relaxation that leads to some of the observed fractionation (Nilsson et al., 2014). The KIEs of the sink reaction H_2+OH have been calculated theoretically for HD and D_2 using semiclassical transition state theory down to 200 K (Nguyen et al., 2011), instanton and canonical variational theory with microcanonical optimized multidimensional tunneling down to 10 K (Meisner & Kästner, 2016) and quantum dynamics simulations over 150 to 1000 K (Welsch, 2019). Still lacking, however, are remaining KIEs and

photolysis KIEs that are rigorously calculated and compared to experiments over a full temperature range and, for photolysis reactions, over the full wavelength range relevant to the troposphere and stratosphere.

4.4.3 Nitrous oxide (N_2O)

Nitrous oxide concentrations need to be constrained because it is an important greenhouse gas (Yung et al., 1976) and has implications for stratospheric ozone destruction (Crutzen, 1970). An imbalance in the global budget of N_2O prompted further investigations in the stratosphere. This imbalance came from the understanding that soils emit isotopically depleted N_2O, so an isotopically heavy source was thought to be needed to match the atmospheric isotopic composition (Kim & Craig, 1993). Then, it was suggested that a source is not needed, rather there were gaps in the understanding of N_2O in the stratosphere and isotope enrichments that may be occurring there due to photolysis and oxidation by $O(^1D)$ (Rahn & Wahlen, 1997).

Laboratory photolysis experiments to photodissociate N_2O at 185 nm – which happens to be the absorption cross section maximum – showed no nitrogen or oxygen isotope enrichments (Johnston et al., 1995). Theoretical studies using a simplified zero-point energy model (Yung & Miller, 1997) suggested that ^{15}N- and ^{18}O-substituted isotopologs of N_2O should indeed show differences in photolysis cross-sections and, hence, in photolysis rates relative to $^{14}N^{14}N^{16}O$, so in fact, photolysis should cause isotope fractionation and should enrich the remaining N_2O in ^{15}N and ^{18}O. They suggested performing experiments at wavelengths not at 185 nm, since almost no solar radiation at 185 nm makes it down to the stratosphere but rather is absorbed or scattered above those altitudes, but at wavelengths in the stratospheric 'solar window' near 205 nm where most stratospheric N_2O is photolyzed. Additional balloon and aircraft measurements of the isotopologs in the lower and mid stratosphere found that, as altitude and/or photochemical processing times increases, the heavy isotope enrichments in N_2O increase (Park, 2004; Röckmann et al., 2001; Toyoda et al., 2001).

When experiments in the laboratory were done at the wavelengths relevant for stratospheric photolysis N_2O was found to be enriched in ^{18}O and ^{15}N preferentially at the central nitrogen due to breaking of the N-O bond (Rahn et al., 1998; Röckmann et al., 2000; Turatti et al., 2000; Umemoto, 1999; Zhang et al., 2000), and this enrichment was wavelength and temperature dependent (Kaiser et al., 2002, 2003). Theoretical studies were able to elucidate the underlying physical chemistry of this process and show that photolysis cross sections for heavy isotopologues have a zero-point energy shift. Since the cross sections of light isotopologues overlap more with the solar window in the stratosphere there is more rapid photolysis when compared with the blue-shifted heavy isotopologues, leading to the enrichments observed. Theoretical studies on this include photo-induced isotopic fractionation effects (Miller & Yung, 2000), time-dependent Hermite propagation (Johnson et al., 2001), and the Born-Oppenheimer photolysis model (Blake et al., 2003). Measurements of the KIE for the reaction of $O(^1D)$ with N_2O find that the magnitude of the IE is smaller than for photolysis, and the nitrogen IE is different than that of photolysis (Kaiser, 2002).

With the global N_2O isotope budget largely balanced by the new understanding of the stratospheric enrichments in ^{15}N and ^{18}O (McLinden et al., 2003; Park, 2004), the focus of N_2O isotope studies returned to quantifying the largest remaining uncertainties in the global budget, N_2O emissions. Isotopic analysis performed on archived air samples and firn air samples have quantified variation over time to determine that the decreasing global trend in heavy isotopes is due to agricultural fertilizer use (Park et al., 2012; Röckmann & Levin, 2005; Toyoda et al., 2013). New techniques using a quantum cascade laser spectrometer to analyze N_2O isotopomers real-time *in situ* has allowed for numerous studies of sources, for example, agricultural fields and how the isotopic composition of emissions vary over time and with different management practices (Mohn et al., 2012).

And yet, new and interesting physical chemistry studies are needed now to understand small but interesting new sources of N_2O in the upper atmosphere and in the low temperature regions of lightning discharges. High energy particle events can lead to N_2O production in the upper stratosphere and lower mesosphere that has been detected by the MIPAS and ACE satellites (Funke et al., 2008; Semeniuk et al., 2008), and N_2O isotopolog distributions derived from satellite observations show that the N_2O is increasingly enriched in ^{15}N and ^{18}O with altitude and at the poles(Bernath et al., 2017). Plasma discharges have recently been studied in the lab and found to have large ^{15}N enrichments (Chapter 2 of this dissertation), which could be an additional atmospheric source in low temperature lightning. These systems could also be useful for understanding the IEs in reactions producing N_2O in the upper atmosphere, due to similarities in the likely reactions producing N_2O.

4.4.4 Reactive nitrogen species (NO_x, NH_3, HNO_3, HONO)

Recent developments in isotopic analysis have allowed for measurements of a greater number of reactive nitrogen species and include the development of a collection and processing method to measure the ^{15}N composition of NO_x ($NO + NO_2$), HONO, and HNO_3 in aerosols and acid rain (Dahal & Hastings, 2016; Fibiger et al., 2014; Hastings et al., 2003; Wojtal et al., 2016). These advances have created the opportunity to study the isotopic composition of NO_x emissions from agriculture (Miller et al., 2018), biomass burning (Chai et al., 2019), and vehicle emissions (Miller et al., 2017) which can be used for source attribution and emissions reduction targets. They also provide exciting new opportunities to understand the isotopic composition of reactive species in numerous systems, including the plasma discharges studied in Chapter 2 of this dissertation and in Smith *et al.* (2021), which will allow for even greater mechanistic insights.

4.5 Multiply-substituted isotopolog abundances ("clumped isotopes")

Clumped isotopes are novel tracers of biogeochemical processes and, in cases where average isotopic compositions are ambiguous or for sources or sinks that are similar, they can be used to determine the atmospheric impact of these processes (reviewed in Garofalo et al.). Kinetic, equilibrium, and photolysis isotope effects for reactions involving multiply substituted isotopologues need to be calculated now that instrumentation has been developed that can measure these at natural abundances (see Section 4.2.3 Instrumentation and Garofalo et al.). Indeed, theoretical studies over the past decades have often included calculations of clumped isotopes (e.g.,

Butler et al., 1986) but the new instrumentation and applications in atmospheric chemistry and climate provide new motivation for such studies, as well as an arguably more feasible means of testing the theoretical results (and vice versa) for some species.

The first studies of clumped isotopes included CO_2 from carbonates to understand early hominid evolution (Passey et al., 2010) and the body temperature of dinosaurs (Eagle et al., 2011), as well as subsurface CH_4 sources to differentiate microbial versus geochemical sources (Ono et al., 2014). These initial studies involved equilibrium isotope effects for which empirical studies in the lab can provide the 'degree of clumping' expected. KIEs, however, which are especially relevant for the atmosphere and climate since most processes are generally governed by kinetics not equilibrium, are much harder to isolate and measure in the lab in most cases, and a combination of theoretical and laboratory studies are needed to make progress in understanding the underlying KIEs resulting in the measured clumped isotope compositions.

4.5.1 CO_2 ($^{13}C^{18}O^{16}O$)

The first measurements of clumped isotopes of CO_2 for $^{13}C^{18}O^{16}O$ (with mass 47), were performed using a Finnigan MAT 253 IRMS on samples collected in the Los Angeles basin and found to vary based on the extent of plant photosynthesis, making it a new tracer of sources (Eiler & Schauble, 2004). Subsequent studies demonstrated that it can be a useful tracer for additional sources, including as a constraint for human breath emissions and fossil fuel combustion (Affek & Eiler, 2006), and diurnal and seasonal variation has also been measured (Affek et al., 2007). Clumped isotope measurements in CO_2 from stratospheric samples revealed a meridional gradient where the midlatitudes data show a stochastic distribution likely resulting from R4 above ($O(^1D)$ + CO_2 isotope exchange), but the polar vortex data show a different pattern (Yeung et al., 2016) and require further investigation (see Chapter 2, Section 2.3.4 for discussion). Thus, clumped isotopes of CO_2 have proven to be a useful tracer of tropospheric and stratospheric processes.

4.5.2 O_2 ($^{18}O^{18}O$ and $^{17}O^{18}O$)

Clumped isotopes in O_2 can be used for source analysis and for investigation of the temperature and atmospheric concentration of ozone in past climates. Atmospheric samples show enhancements in $^{17}O^{18}O$ and $^{18}O^{18}O$, and these are sensitive to the $O(^3P)$ + O_2 isotope exchange reaction (R1a above) which resets the isotopic signatures from O_2 sources, such as photosynthesis (Yeung et al., 2012). These clumped isotopes can serve as a marker of local sources such as photosynthesis which emits depleted O_2 (Yeung et al., 2015) or the transport, temperature, and photochemistry of a sample (Laskar et al., 2019; Yeung et al., 2016). For example, measurements up to 33 km in the stratosphere show higher enrichments at colder formation temperatures due to faster photochemical cycling (Yeung et al., 2016), and measurements of clumped isotopes from firn air samples quantify changes in tropospheric ozone since the 16th century, finding that $^{18}O^{18}O$ decreased in the 20th century, which indicates an increase in tropospheric ozone consistent with climate model predictions (Yeung, Murray, et al., 2019). This technique has been advanced further through analysis of samples from the ground level to 33 km and atmospheric modeling showing the need to consider the pressure dependence of $^{18}O^{18}O$ abundances and provides a more accurate proxy for past tropospheric ozone and temperatures (Yeung et al., 2021).

4.5.3 CH_4 ($^{13}CH_3D$, CH_2D_2)

As discussed in section 4.4.1, quantification of the sources of methane are important to address changing emissions of this greenhouse gas, and clumped isotopes add another dimension to the singly-substituted isotopologs abundances. From natural gas samples, $^{13}CH_3D$ was first studied using spectroscopic techniques (Ma et al., 2008; Ono et al., 2014), and the development of high resolution IRMS techniques expanded the analysis to CH_2D_2, which could now be differentiated from $^{13}CH_3D$, finding that natural gas samples could identified between production from microbes or deep underground sources (Stolper, Lawson, et al., 2014), and to understand the temperature at which the methane was formed (Stolper, Sessions, et al., 2014). Additional methane sources that can be differentiated using clumped isotopes include cattle production, and microbial production in different environments (Douglas et al., 2016; Gruen et al., 2018; Stolper et al., 2015; Taenzer et al., 2020; Wang et al., 2015).

In addition to the source analysis, which relies on equilibrium isotope effects for which empirical studies in the laboratory can yield the fractionation constants, KIEs are much harder in most cases to isolate and measure experimentally. Clumped isotope KIEs have been measured in the laboratory for the sink reactions of $^{13}CH_3D$ and CH_2D_2 with the oxidants OH and Cl (Haghnegahdar et al., 2017; Joelsson et al., 2014; Whitehill et al., 2017) and for the reactions of CD_2H_2, CD_3H, and CD_4 with OH (Frederickson et al., 2019). Transition state theory (TST) calculations were used to determine the KIE of $^{13}CH_3D$ with Cl (Joelsson et al., 2014). Despite this recent progress, additional theoretical and experimental studies are needed to further quantify and understand the clumped isotope KIEs for all the methane sink reactions, including reaction with $O(^1D)$ for atmospheric applications.

4.5.4 H_2 (D_2)

Techniques to measure the abundance of D_2 on a MAT 253-Ultra IRMS with 2-6‰ precision are a new advance that will soon provide a new dimension to be added in using isotopes to quantify the atmospheric budget of molecular hydrogen. Of particular interest are the clumped isotope compositions of microbiological sources of H_2 which may deviate from thermodynamic equilibrium (Popa et al., 2019).Theoretical calculations of the isotope effect and rate coefficients for D_2+OH using quantum dynamics will also aid in the study of this system (Welsch, 2019). More theoretical calculations are needed to determine KIE for these his reaction over a range of temperatures relevant for the atmosphere, especially when atmospheric measurements are made.

4.5.5 N_2O ($^{14}N^{15}N^{18}O$ and $^{15}N^{14}N^{18}O$)

The early measurements of doubly-substituted N_2O – i.e., $^{14}N^{15}N^{18}O$ and $^{15}N^{14}N^{18}O$ – were made at isotopic equilibrium over a catalyst and for N_2O produced by denitrifying bacteria (Magyar et al., 2016). Theoretical calculations of the photolysis of clumped isotopolog of N_2O have been performed using time-dependent quantum mechanical methods (Schmidt & Johnson, 2015; Schmidt et al., 2011). Clumped isotope fractionation due to photolysis at 200 and 210 nm has recently been measured (Kantnerová, Jespersen, et al., 2020), but there is some discrepancy with theory and no additional experiments with which these results can be compared.

4.5.6 N_2 ($^{15}N^{15}N$)

The PANDORA instrument (see Section 4.2.3) can measure the relative abundance of the $^{15}N^{15}N$ isotoplog of N_2 (Young et al., 2016) and has since been used to measure air samples from throughout the troposphere and into the stratosphere, showing little variation throughout these regions of the atmosphere. Enrichments, however, could occur in the thermosphere due to the unique chemistry occurring there (Yeung et al., 2017). Measurements of $^{15}N^{15}N$ may also be useful in providing a better understanding the sources of volcanic gases, such as hydrothermal or emanating from the mantle in different regions of the world (Labidi et al., 2020). These clumped measurements of N_2 also show promise in quantifying soil emissions and understanding denitrification processes (Yeung, Haslun, et al., 2019).

4.5.7 Ethane ($^{13}C_2H_6$)

Developments in measuring the clumped isotopologs of ethane and other C_2 species such as ethanol and ethene show promise for being used as tracers of the source of natural gas (Clog et al., 2018; Taguchi et al., 2020). Initial theoretical studies of these systems have used Monte Carlo methods to calculate the equilibrium ^{13}C enrichments in ethane (Webb et al., 2017).

4.6 Conclusions

There remain interesting and unresolved questions with isotope effects in atmospheric chemistry to which physical chemists could contribute which have been highlighted here. Briefly, these include theoretical study of the fundamental physical cause of the O-MIF anomaly in the ozone formation, at a range of temperatures, pressures, and bath gases, with importance for Earth Science because of the transfer many other species used to study current and past atmospheres. Fundamental investigation is also still needed for the under-studied KIEs outlined above that are important for trace gases CH_4, H_2, CH_4, N_2O, and nitrogen oxides, at all conditions (temperatures, pressures, and photolysis wavelengths) that exist in the atmosphere. New and exciting frontiers are emerging in the study of multiply isotopically substituted species, and, with these new discoveries in atmospheric measurements, there are new experimental studies needed investigate the laboratory kinetics and photochemical processes as well as theoretical studies to understand and predict the underlying isotope effects.

References

Adnew, G. A., Pons, T. L., Koren, G., Peters, W., & Röckmann, T. (2020). Leaf-scale quantification of the effect of photosynthetic gas exchange on $\Delta^{17}O$ of atmospheric CO_2. *Biogeosciences*, *17*(14), 3903-3922. https://doi.org/10.5194/bg-17-3903-2020

Affek, H. P., & Eiler, J. M. (2006). Abundance of mass 47 CO_2 in urban air, car exhaust, and human breath. *Geochimica et Cosmochimica Acta*, *70*(1), 1-12. https://doi.org/10.1016/j.gca.2005.08.021

Affek, H. P., Xu, X., & Eiler, J. M. (2007). Seasonal and diurnal variations of $^{13}C^{18}O^{16}O$ in air: Initial observations from Pasadena, CA. *Geochimica et Cosmochimica Acta*, *71*(21), 5033-5043. https://doi.org/10.1016/j.gca.2007.08.014

Akoka, S., & Remaud, G. S. (2020). NMR-based isotopic and isotopomic analysis. *Progress in Nuclear Magnetic Resonance Spectroscopy*, *120-121*, 1-24. https://doi.org/https://doi.org/10.1016/j.pnmrs.2020.07.001

Alexander, B., Hastings, M. G., Allman, D. J., Dachs, J., Thornton, J. A., & Kunasek, S. A. (2009). Quantifying atmospheric nitrate formation pathways based on a global model of the oxygen isotopic composition ($\Delta^{17}O$) of atmospheric nitrate. *Atmos. Chem. Phys.*, *9*(14), 5043-5056. https://doi.org/10.5194/acp-9-5043-2009

Alexander, B., Vollmer, M. K., Jackson, T., Weiss, R. F., & Thiemens, M. H. (2001). Stratospheric CO_2 isotopic anomalies and SF_6 and CFC Tracer Concentrations in the Arctic Polar Vortex. *Geophysical Research Letters*, *28*(21), 4103-4106. https://doi.org/https://doi.org/10.1029/2001GL013692

Anderson, S. M., Morton, J., & Mauersberger, K. (1989). Laboratory measurements of ozone isotopomers by tunable diode laser absorption spectroscopy. *Chemical Physics Letters*, *156*(2), 175-180. https://doi.org/https://doi.org/10.1016/S0009-2614(89)87115-5

Angert, A., Rachmilevitch, S., Barkan, E., & Luz, B. (2003). Effects of photorespiration, the cytochrome pathway, and the alternative pathway on the triple isotopic composition of atmospheric O_2 [https://doi.org/10.1029/2002GB001933]. *Global Biogeochemical Cycles*, *17*(1). https://doi.org/https://doi.org/10.1029/2002GB001933

Ash, J. L., Hu, H., & Yeung, L. Y. (2020). What Fractionates Oxygen Isotopes during Respiration? Insights from Multiple Isotopologue Measurements and Theory. *ACS Earth and Space Chemistry*, *4*(1), 50-66. https://doi.org/10.1021/acsearthspacechem.9b00230

Ayouz, M., & Babikov, D. (2013). Global permutationally invariant potential energy surface for ozone forming reaction. *The Journal of Chemical Physics*, *138*(16), 164311. https://doi.org/10.1063/1.4799915

Babikov, D. (2003). Entrance channel localized states in ozone: Possible application to helium nanodroplet isolation spectroscopy. *The Journal of Chemical Physics*, *119*(13), 6554-6559. https://doi.org/10.1063/1.1604771

Babikov, D., Kendrick, B. K., Walker, R. B., Pack, R. T., Fleurat-Lesard, P., & Schinke, R. (2003a). Metastable states of ozone calculated on an accurate potential energy surface. *The Journal of Chemical Physics*, *118*(14), 6298-6308. https://doi.org/10.1063/1.1557936

Babikov, D., Kendrick, B. K., Walker, R. B., Schinke, R., & Pack, R. T. (2003b). Quantum origin of an anomalous isotope effect in ozone formation. *Chemical Physics Letters*, *372*(5), 686-691. https://doi.org/https://doi.org/10.1016/S0009-2614(03)00479-2

Bao, H., Fairchild, I. J., Wynn, P. M., & Spötl, C. (2009). Stretching the Envelope of Past Surface Environments: Neoproterozoic Glacial Lakes from Svalbard. *Science*, *323*(5910), 119-122. https://doi.org/10.1126/science.1165373

Bao, H., Lyons, J. R., & Zhou, C. (2008). Triple oxygen isotope evidence for elevated CO_2 levels after a Neoproterozoic glaciation. *Nature*, *453*(7194), 504-506. https://doi.org/10.1038/nature06959

Barkan, E., & Luz, B. (2005). High precision measurements of $^{17}O/^{16}O$ and $^{18}O/^{16}O$ ratios in H_2O. *Rapid Communications in Mass Spectrometry*, *19*(24), 3737-3742. https://doi.org/https://doi.org/10.1002/rcm.2250

Barker, J. R., Nguyen, T. L., & Stanton, J. F. (2012). Kinetic Isotope Effects for Cl + CH_4 ⇌ HCl + CH_3 Calculated Using ab Initio Semiclassical Transition State Theory. *The Journal of Physical Chemistry A*, *116*(24), 6408-6419. https://doi.org/10.1021/jp212383u

Baulch, D. L., & Breckenridge, W. H. (1966). Isotopic exchange of O(^{1}D) with carbon dioxide [10.1039/TF9666202768]. *Transactions of the Faraday Society*, *62*(0), 2768-2773. https://doi.org/10.1039/TF9666202768

Bernath, P. F., Yousefi, M., Buzan, E., & Boone, C. D. (2017). A Near-Global Atmospheric Distribution of N_2O Isotopologues. *Geophysical Research Letters*, *44*(20), 10,735-710,743. https://doi.org/10.1002/2017gl075122

Bigeleisen, J., & Mayer, M. G. (1947). Calculation of Equilibrium Constants for Isotopic Exchange Reactions. *The Journal of Chemical Physics*, *15*(5), 261-267. https://doi.org/10.1063/1.1746492

Blake, G. A., Liang, M.-C., Morgan, C. G., & Yung, Y. L. (2003). A Born-Oppenheimer photolysis model of N_2O fractionation. *Geophysical Research Letters*, *30*(12). https://doi.org/10.1029/2003gl016932

Blunier, T., Barnett, B., Bender, M. L., & Hendricks, M. B. (2002). Biological oxygen productivity during the last 60,000 years from triple oxygen isotope measurements [https://doi.org/10.1029/2001GB001460]. *Global Biogeochemical Cycles*, *16*(3), 3-1-3-13. https://doi.org/https://doi.org/10.1029/2001GB001460

Blunier, T., Bender, M. L., Barnett, B., & von Fischer, J. C. (2012). Planetary fertility during the past 400 ka based on the triple isotope composition of O_2 in trapped gases from the Vostok ice core. *Clim. Past*, *8*(5), 1509-1526. https://doi.org/10.5194/cp-8-1509-2012

Boering, K. A., Jackson, T., Hoag, K. J., Cole, A. S., Perri, M. J., Thiemens, M., & Atlas, E. (2004). Observations of the anomalous oxygen isotopic composition of carbon dioxide in the lower stratosphere and the flux of the anomaly to the troposphere [https://doi.org/10.1029/2003GL018451]. *Geophysical Research Letters*, *31*(3). https://doi.org/https://doi.org/10.1029/2003GL018451

Brandon, M., Landais, A., Duchamp-Alphonse, S., Favre, V., Schmitz, L., Abrial, H., Prié, F., Extier, T., & Blunier, T. (2020). Exceptionally high biosphere productivity at the beginning of Marine Isotopic Stage 11. *Nature Communications*, *11*(1), 2112. https://doi.org/10.1038/s41467-020-15739-2

Brenninkmeijer, C. A. M., Janssen, C., Kaiser, J., Röckmann, T., Rhee, T. S., & Assonov, S. S. (2003). Isotope Effects in the Chemistry of Atmospheric Trace Compounds. *Chemical Reviews*, *103*(12), 5125-5162. https://doi.org/10.1021/cr020644k

Brenninkmeijer, C. A. M., Lowe, D. C., Manning, M. R., Sparks, R. J., & van Velthoven, P. F. J. (1995). The ^{13}C, ^{14}C, and ^{18}O isotopic composition of CO, CH_4, and CO_2 in the higher southern latitudes lower stratosphere [https://doi.org/10.1029/95JD02528]. *Journal of Geophysical Research: Atmospheres*, *100*(D12), 26163-26172. https://doi.org/https://doi.org/10.1029/95JD02528

Brinjikji, M., & Lyons, J. R. (2021). Mass-Independent Fractionation of Oxygen Isotopes in the Atmosphere. *Reviews in Mineralogy and Geochemistry*, *86*(1), 197-216. https://doi.org/10.2138/rmg.2021.86.06

Butler, J. E., Jursich, G. M., Watson, I. A., & Wiesenfeld, J. R. (1986). Reaction dynamics of $O(^1D_2)+H_2$, HD, D_2: OH, OD($X\ ^2\Pi_i$) product internal energy distributions. *The Journal of Chemical Physics*, *84*(10), 5365-5377. https://doi.org/10.1063/1.449947

Cantrell, C. A., Shetter, R. E., McDaniel, A. H., Calvert, J. G., Davidson, J. A., Lowe, D. C., Tyler, S. C., Cicerone, R. J., & Greenberg, J. P. (1990). Carbon kinetic isotope effect in the oxidation of methane by the hydroxyl radical [https://doi.org/10.1029/JD095iD13p22455]. *Journal of Geophysical Research: Atmospheres*, *95*(D13), 22455-22462. https://doi.org/https://doi.org/10.1029/JD095iD13p22455

Chai, J., Miller, D. J., Scheuer, E., Dibb, J., Selimovic, V., Yokelson, R., Zarzana, K. J., Brown, S. S., Koss, A. R., Warneke, C., & Hastings, M. (2019). Isotopic characterization of nitrogen oxides (NO), nitrous acid (HONO), and nitrate (p NO_3) from laboratory biomass burning during FIREX. *Atmospheric Measurement Techniques*, *12*(12), 6303-6317. https://doi.org/10.5194/amt-12-6303-2019

Chakraborty, S., Ahmed, M., Jackson, T. L., & Thiemens, M. H. (2008). Experimental Test of Self-Shielding in Vacuum Ultraviolet Photodissociation of CO. *Science*, *321*(5894), 1328-1331. https://doi.org/10.1126/science.1159178

Chakraborty, S., & Bhattacharya, S. K. (2003). Experimental investigation of oxygen isotope exchange between CO_2 and $O(^1D)$ and its relevance to the stratosphere [https://doi.org/10.1029/2002JD002915]. *Journal of Geophysical Research: Atmospheres*, *108*(D23). https://doi.org/https://doi.org/10.1029/2002JD002915

Chakraborty, S., Yanchulova, P., & Thiemens, M. H. (2013). Mass-Independent Oxygen Isotopic Partitioning During Gas-Phase SiO_2 Formation. *Science*, *342*(6157), 463-466. https://doi.org/10.1126/science.1242237

Ciais, P., Denning, A. S., Tans, P. P., Berry, J. A., Randall, D. A., Collatz, G. J., Sellers, P. J., White, J. W. C., Trolier, M., Meijer, H. A. J., Francey, R. J., Monfray, P., & Heimann, M. (1997). A three-dimensional synthesis study of $\delta^{18}O$ in atmospheric CO_2: 1. Surface fluxes. *Journal of Geophysical Research: Atmospheres*, *102*(D5), 5857-5872. https://doi.org/https://doi.org/10.1029/96JD02360

Cicerone, R. J., & McCrumb, J. L. (1980). Photodissociation of isotopically heavy O_2 as a source of atmospheric O_3. *Geophysical Research Letters*, *7*(4), 251-254. https://doi.org/https://doi.org/10.1029/GL007i004p00251

Clayton, R. N., Grossman, L., & Mayeda, T. K. (1973). A Component of Primitive Nuclear Composition in Carbonaceous Meteorites. *Science*, *182*(4111), 485-488. https://doi.org/10.1126/science.182.4111.485

Clog, M., Lawson, M., Peterson, B., Ferreira, A. A., Santos Neto, E. V., & Eiler, J. M. (2018). A reconnaissance study of ^{13}C–^{13}C clumping in ethane from natural gas. *Geochimica et Cosmochimica Acta*, *223*, 229-244. https://doi.org/10.1016/j.gca.2017.12.004

Cole, A. S., & Boering, K. A. (2006). Mass-dependent and non-mass-dependent isotope effects in ozone photolysis: Resolving theory and experiments. *The Journal of Chemical Physics*, *125*(18), 184301. https://doi.org/10.1063/1.2363984

Crockford, P. W., Cowie, B. R., Johnston, D. T., Hoffman, P. F., Sugiyama, I., Pellerin, A., Bui, T. H., Hayles, J., Halverson, G. P., Macdonald, F. A., & Wing, B. A. (2016). Triple

oxygen and multiple sulfur isotope constraints on the evolution of the post-Marinoan sulfur cycle. *Earth and Planetary Science Letters*, *435*, 74-83. https://doi.org/https://doi.org/10.1016/j.epsl.2015.12.017

Crockford, P. W., Hayles, J. A., Bao, H., Planavsky, N. J., Bekker, A., Fralick, P. W., Halverson, G. P., Bui, T. H., Peng, Y., & Wing, B. A. (2018). Triple oxygen isotope evidence for limited mid-Proterozoic primary productivity. *Nature*, *559*(7715), 613-616. https://doi.org/10.1038/s41586-018-0349-y

Crockford, P. W., Kunzmann, M., Bekker, A., Hayles, J., Bao, H., Halverson, G. P., Peng, Y., Bui, T. H., Cox, G. M., Gibson, T. M., Wörndle, S., Rainbird, R., Lepland, A., Swanson-Hysell, N. L., Master, S., Sreenivas, B., Kuznetsov, A., Krupenik, V., & Wing, B. A. (2019). Claypool continued: Extending the isotopic record of sedimentary sulfate. *Chemical Geology*, *513*, 200-225. https://doi.org/https://doi.org/10.1016/j.chemgeo.2019.02.030

Crowley, J. N., Saueressig, G., Bergamaschi, P., Fischer, H., & Harris, G. W. (1999). Carbon kinetic isotope effect in the reaction CH_4+Cl: a relative rate study using FTIR spectroscopy. *Chemical Physics Letters*, *303*(3), 268-274. https://doi.org/https://doi.org/10.1016/S0009-2614(99)00243-2

Crutzen, P. J. (1970). The influence of nitrogen oxides on the atmospheric ozone content. *Quarterly Journal of the Royal Meteorological Society*, *96*(408), 320-325. https://doi.org/10.1002/qj.49709640815

Dahal, B., & Hastings, M. G. (2016). Technical considerations for the use of passive samplers to quantify the isotopic composition of NO_x and NO_2 using the denitrifier method. *Atmospheric Environment*, *143*, 60-66. https://doi.org/10.1016/j.atmosenv.2016.08.006

Davidson, J., Sadowski, C., Schiff, H., Streit, G., Howard, C. J., Jennings, D., & Schmeltekopf, A. (1976). Absolute rate constant determinations for the deactivation of O (^{1}D) by time resolved decay of O (^{1}D)→ O (^{3}P) emission. *The Journal of Chemical Physics*, *64*(1), 57-62.

Davidson, J. A., Cantrell, C. A., Tyler, S. C., Shetter, R. E., Cicerone, R. J., & Calvert, J. G. (1987). Carbon kinetic isotope effect in the reaction of CH_4 with HO [https://doi.org/10.1029/JD092iD02p02195]. *Journal of Geophysical Research: Atmospheres*, *92*(D2), 2195-2199. https://doi.org/https://doi.org/10.1029/JD092iD02p02195

Dejwakh, N. R., Meixner, T., Michalski, G., & McIntosh, J. (2012). Using ^{17}O to Investigate Nitrate Sources and Sinks in a Semi-Arid Groundwater System. *Environmental Science & Technology*, *46*(2), 745-751. https://doi.org/10.1021/es203450z

Dominguez, G., Jackson, T., Brothers, L., Barnett, B., Nguyen, B., & Thiemens, M. H. (2008). Discovery and measurement of an isotopically distinct source of sulfate in Earth's atmosphere. *Proceedings of the National Academy of Sciences*, *105*(35), 12769-12773. https://doi.org/10.1073/pnas.0805255105

Douglas, P. M. J., Stolper, D. A., Smith, D. A., Walter Anthony, K. M., Paull, C. K., Dallimore, S., Wik, M., Crill, P. M., Winterdahl, M., Eiler, J. M., & Sessions, A. L. (2016). Diverse origins of Arctic and Subarctic methane point source emissions identified with multiply-substituted isotopologues. *Geochimica et Cosmochimica Acta*, *188*, 163-188. https://doi.org/https://doi.org/10.1016/j.gca.2016.05.031

Durka, W., Schulze, E.-D., Gebauer, G., & Voerkeliust, S. (1994). Effects of forest decline on uptake and leaching of deposited nitrate determined from 15N and 18O measurements. *Nature*, *372*(6508), 765-767. https://doi.org/10.1038/372765a0

Eagle, R. A., Tütken, T., Martin, T. S., Tripati, A. K., Fricke, H. C., Connely, M., Cifelli, R. L., & Eiler, J. M. (2011). Dinosaur Body Temperatures Determined from Isotopic (^{13}C-^{18}O) Ordering in Fossil Biominerals. *Science*, *333*(6041), 443-445. https://doi.org/10.1126/science.1206196

Ehhalt, D. H., Davidson, J. A., Cantrell, C. A., Friedman, I., & Tyler, S. (1989). The kinetic isotope effect in the reaction of H_2 with OH. *Journal of Geophysical Research*, *94*(D7), 9831. https://doi.org/10.1029/jd094id07p09831

Eiler, J. M., Clog, M., Magyar, P., Piasecki, A., Sessions, A., Stolper, D., Deerberg, M., Schlueter, H.-J., & Schwieters, J. (2013). A high-resolution gas-source isotope ratio mass spectrometer. *International Journal of Mass Spectrometry*, *335*, 45-56. https://doi.org/10.1016/j.ijms.2012.10.014

Eiler, J. M., & Schauble, E. (2004). $^{18}O^{13}C^{16}O$ in Earth's atmosphere. *Geochimica et Cosmochimica Acta*, *68*(23), 4767-4777. https://doi.org/10.1016/j.gca.2004.05.035

Faloona, I. (2009). Sulfur processing in the marine atmospheric boundary layer: A review and critical assessment of modeling uncertainties. *Atmospheric Environment*, *43*(18), 2841-2854. https://doi.org/https://doi.org/10.1016/j.atmosenv.2009.02.043

Feilberg, K. L., Johnson, M. S., & Nielsen, C. J. (2005). Relative rates of reaction of $^{13}C^{16}O$, $^{12}C^{18}O$, $^{12}C^{17}O$ and $^{13}C^{18}O$ with OH and OD radicals [10.1039/B503350K]. *Physical Chemistry Chemical Physics*, *7*(11), 2318-2323. https://doi.org/10.1039/B503350K

Feilberg, K. L., Sellevåg, S. R., Nielsen, C. J., Griffith, D. W. T., & Johnson, M. S. (2002). $CO + OH \rightarrow CO_2 + H$: The relative reaction rate of five CO isotopologues [10.1039/B204827M]. *Physical Chemistry Chemical Physics*, *4*(19), 4687-4693. https://doi.org/10.1039/B204827M

Fibiger, D. L., Hastings, M. G., Lew, A. F., & Peltier, R. E. (2014). Collection of NO and NO_2 for Isotopic Analysis of NO_x Emissions. *Analytical Chemistry*, *86*(24), 12115-12121. https://doi.org/10.1021/ac502968e

Francey, R. J., & Tans, P. P. (1987). Latitudinal variation in oxygen-18 of atmospheric CO_2. *Nature*, *327*(6122), 495-497. https://doi.org/10.1038/327495a0

Frederickson, L. B., Andersen, S. T., & Nielsen, O. J. (2019). Rate coefficients for reactions of OH radicals with CH_3D, CH_2D_2, CHD_3, and CD_4 [https://doi.org/10.1002/kin.21262]. *International Journal of Chemical Kinetics*, *51*(6), 390-394. https://doi.org/https://doi.org/10.1002/kin.21262

Fujii, T., Moynier, F., & Albarède, F. (2009). The nuclear field shift effect in chemical exchange reactions. *Chemical Geology*, *267*(3), 139-156. https://doi.org/https://doi.org/10.1016/j.chemgeo.2009.06.015

Fung, I., John, J., Lerner, J., Matthews, E., Prather, M., Steele, L. P., & Fraser, P. J. (1991). Three-dimensional model synthesis of the global methane cycle. *Journal of Geophysical Research*, *96*(D7), 13033. https://doi.org/10.1029/91jd01247

Funke, B., López-Puertas, M., Garcia-Comas, M., Stiller, G., Clarmann, T. v., & Glatthor, N. (2008). Mesospheric N_2O enhancements as observed by MIPAS on Envisat during the polar winters in 2002–2004. *Atmospheric Chemistry and Physics*, *8*(19), 5787-5800.

Gao, Y. Q., & Marcus, R. A. (2001). Strange and Unconventional Isotope Effects in Ozone Formation. *Science*, *293*(5528), 259-263. https://doi.org/10.1126/science.1058528

Gao, Y. Q., & Marcus, R. A. (2007). An approximate theory of the ozone isotopic effects: Rate constant ratios and pressure dependence. *The Journal of Chemical Physics*, *127*(24), 244316. https://doi.org/10.1063/1.2806189

Garofalo, L., Kanu, A., Hoag, K. J., & Boering, K. A. The Effects of Stratospheric Chemistry and Transport on the Isotopic Compositions of Long-Lived Gases Measured at Earth's Surface. In *Advances in Atmospheric Chemistry* (pp. 529-587). https://doi.org/10.1142/9789813271838_0007

Gautier, E., Savarino, J., Hoek, J., Erbland, J., Caillon, N., Hattori, S., Yoshida, N., Albalat, E., Albarede, F., & Farquhar, J. (2019). 2600-years of stratospheric volcanism through sulfate isotopes. *Nature Communications*, *10*(1), 466. https://doi.org/10.1038/s41467-019-08357-0

Gayday, I., Teplukhin, A., & Babikov, D. (2019). The ratio of the number of states in asymmetric and symmetric ozone molecules deviates from the statistical value of 2. *The Journal of Chemical Physics*, *150*(10), 101104. https://doi.org/10.1063/1.5082850

Gayday, I., Teplukhin, A., Kendrick, B. K., & Babikov, D. (2020). The role of rotation–vibration coupling in symmetric and asymmetric isotopomers of ozone. *The Journal of Chemical Physics*, *152*(14), 144104. https://doi.org/10.1063/1.5141365

Gehler, A., Gingerich, P. D., & Pack, A. (2016). Temperature and atmospheric CO_2 concentration estimates through the PETM using triple oxygen isotope analysis of mammalian bioapatite. *Proceedings of the National Academy of Sciences*, *113*(28), 7739-7744. https://doi.org/10.1073/pnas.1518116113

Geiser, J. D., Dylewski, S. M., Mueller, J. A., Wilson, R. J., Toumi, R., & Houston, P. L. (2000). The vibrational distribution of $O_2(X^3\Sigma_g^-)$ produced in the photodissociation of ozone between 226 and 240 and at 266 nm. *The Journal of Chemical Physics*, *112*(3), 1279-1286. https://doi.org/10.1063/1.480679

Gerst, S., & Quay, P. (2001). Deuterium component of the global molecular hydrogen cycle. *Journal of Geophysical Research: Atmospheres*, *106*(D5), 5021-5031. https://doi.org/10.1029/2000jd900593

Grebenshchikov, S. Y., Qu, Z. W., Zhu, H., & Schinke, R. (2007). New theoretical investigations of the photodissociation of ozone in the Hartley, Huggins, Chappuis, and Wulf bands [10.1039/B701020F]. *Physical Chemistry Chemical Physics*, *9*(17), 2044-2064. https://doi.org/10.1039/B701020F

Grebenshchikov, S. Y., & Schinke, R. (2009). Towards quantum mechanical description of the unconventional mass-dependent isotope effect in ozone: Resonance recombination in the strong collision approximation. *The Journal of Chemical Physics*, *131*(18), 181103. https://doi.org/10.1063/1.3253994

Gruen, D. S., Wang, D. T., Könneke, M., Topçuoğlu, B. D., Stewart, L. C., Goldhammer, T., Holden, J. F., Hinrichs, K.-U., & Ono, S. (2018). Experimental investigation on the controls of clumped isotopologue and hydrogen isotope ratios in microbial methane. *Geochimica et Cosmochimica Acta*, *237*, 339-356. https://doi.org/https://doi.org/10.1016/j.gca.2018.06.029

Gupta, M., Tyler, S., & Cicerone, R. (1996). Modeling atmospheric $\delta^{13}CH_4$ and the causes of recent changes in atmospheric CH_4 amounts [https://doi.org/10.1029/96JD02386]. *Journal of Geophysical Research: Atmospheres*, *101*(D17), 22923-22932. https://doi.org/https://doi.org/10.1029/96JD02386

Haghnegahdar, M. A., Schauble, E. A., & Young, E. D. (2017). A model for $^{12}CH_2D_2$ and $^{13}CH_3D$ as complementary tracers for the budget of atmospheric CH_4 [https://doi.org/10.1002/2017GB005655]. *Global Biogeochemical Cycles*, *31*(9), 1387-1407. https://doi.org/https://doi.org/10.1002/2017GB005655

Han, S., Gunthardt, C. E., Dawes, R., Xie, D., North, S. W., & Guo, H. (2020). Origin of the "odd" behavior in the ultraviolet photochemistry of ozone. *Proceedings of the National Academy of Sciences*, *117*(35), 21065-21069. https://doi.org/10.1073/pnas.2006070117

Hastings, M. G., Sigman, D. M., & Lipschultz, F. (2003). Isotopic evidence for source changes of nitrate in rain at Bermuda. *Journal of Geophysical Research: Atmospheres*, *108*(D24). https://doi.org/10.1029/2003jd003789

Hathorn, B. C., & Marcus, R. A. (1999). An intramolecular theory of the mass-independent isotope effect for ozone. I. *The Journal of Chemical Physics*, *111*(9), 4087-4100. https://doi.org/10.1063/1.480267

Hathorn, B. C., & Marcus, R. A. (2000). An intramolecular theory of the mass-independent isotope effect for ozone. II. Numerical implementation at low pressures using a loose transition state. *The Journal of Chemical Physics*, *113*(21), 9497-9509. https://doi.org/10.1063/1.1321045

Hattori, S., Iizuka, Y., Alexander, B., Ishino, S., Fujita, K., Zhai, S., Sherwen, T., Oshima, N., Uemura, R., Yamada, A., Suzuki, N., Matoba, S., Tsuruta, A., Savarino, J., & Yoshida, N. (2021). Isotopic evidence for acidity-driven enhancement of sulfate formation after SO_2 emission control. *Science Advances*, *7*(19), eabd4610. https://doi.org/10.1126/sciadv.abd4610

Heidenreich, J. E., & Thiemens, M. H. (1983). A non-mass-dependent isotope effect in the production of ozone from molecular oxygen. *The Journal of Chemical Physics*, *78*(2), 892-895. https://doi.org/10.1063/1.444791

Heidenreich, J. E., & Thiemens, M. H. (1986). A non-mass-dependent oxygen isotope effect in the production of ozone from molecular oxygen: The role of molecular symmetry in isotope chemistry. *The Journal of Chemical Physics*, *84*(4), 2129-2136. https://doi.org/10.1063/1.450373

Hoag, K. J., Still, C. J., Fung, I. Y., & Boering, K. A. (2005). Triple oxygen isotope composition of tropospheric carbon dioxide as a tracer of terrestrial gross carbon fluxes. *Geophysical Research Letters*, *32*(2). https://doi.org/https://doi.org/10.1029/2004GL021011

Hofmann, M., Horváth, B., & Pack, A. (2012). Global long-term mean triple oxygen isotope composition of tropospheric CO_2.

Hofmann, M. E. G., Horváth, B., Schneider, L., Peters, W., Schützenmeister, K., & Pack, A. (2017). Atmospheric measurements of $\Delta^{17}O$ in CO_2 in Göttingen, Germany reveal a seasonal cycle driven by biospheric uptake. *Geochimica et Cosmochimica Acta*, *199*, 143-163. https://doi.org/https://doi.org/10.1016/j.gca.2016.11.019

Huff, A. K., & Thiemens, M. H. (1998). $^{17}O/^{16}O$ and $^{18}O/^{16}O$ isotope measurements of atmospheric carbon monoxide and its sources. *Geophysical Research Letters*, *25*(18), 3509-3512. https://doi.org/https://doi.org/10.1029/98GL02603

Ishino, S., Hattori, S., Legrand, M., Chen, Q., Alexander, B., Shao, J., Huang, J., Jaeglé, L., Jourdain, B., Preunkert, S., Yamada, A., Yoshida, N., & Savarino, J. (2021). Regional Characteristics of Atmospheric Sulfate Formation in East Antarctica Imprinted on ^{17}O-Excess Signature. *Journal of Geophysical Research: Atmospheres*, *126*(6), e2020JD033583. https://doi.org/https://doi.org/10.1029/2020JD033583

Ivanov, M. V., & Babikov, D. (2013). On molecular origin of mass-independent fractionation of oxygen isotopes in the ozone forming recombination reaction. *Proceedings of the National Academy of Sciences*, *110*(44), 17708-17713. https://doi.org/10.1073/pnas.1215464110

Ivanov, M. V., Grebenshchikov, S. Y., & Schinke, R. (2009). Quantum mechanical study of vibrational energy transfer in Ar–O_3 collisions: Influence of symmetry. *The Journal of Chemical Physics*, *130*(17), 174311. https://doi.org/10.1063/1.3126247

Ivanov, M. V., & Schinke, R. (2005). Temperature dependent energy transfer in Ar–O_3 collisions. *The Journal of Chemical Physics*, *122*(23), 234318. https://doi.org/10.1063/1.1927526

Ivanov, M. V., & Schinke, R. (2010). Vibrational energy transfer in Ar–O_3 collisions: comparison of rotational sudden, breathing sphere, and classical calculations. *Molecular Physics*, *108*(3-4), 259-268. https://doi.org/10.1080/00268970903397256

Janssen, C. (2005). Intramolecular isotope distribution in heavy ozone ($^{16}O^{18}O^{16}O$ and $^{16}O^{16}O^{18}O$). *Journal of Geophysical Research: Atmospheres*, *110*(D8). https://doi.org/https://doi.org/10.1029/2004JD005479

Janssen, C., Guenther, J., Krankowsky, D., & Mauersberger, K. (2003). Temperature dependence of ozone rate coefficients and isotopologue fractionation in ^{16}O–^{18}O oxygen mixtures. *Chemical Physics Letters*, *367*(1), 34-38. https://doi.org/https://doi.org/10.1016/S0009-2614(02)01665-2

Janssen, C., Guenther, J., Mauersberger, K., & Krankowsky, D. (2001). Kinetic origin of the ozone isotope effect: a critical analysis of enrichments and rate coefficients [10.1039/B107171H]. *Physical Chemistry Chemical Physics*, *3*(21), 4718-4721. https://doi.org/10.1039/B107171H

Joelsson, L. M. T., Forecast, R., Schmidt, J. A., Meusinger, C., Nilsson, E. J. K., Ono, S., & Johnson, M. S. (2014). Relative rate study of the kinetic isotope effect in the $^{13}CH_3D$+Cl reaction. *Chemical Physics Letters*, *605-606*, 152-157. https://doi.org/https://doi.org/10.1016/j.cplett.2014.05.022

Johnson, M. S., Billing, G. D., Gruodis, A., & Janssen, M. H. M. (2001). Photolysis of Nitrous Oxide Isotopomers Studied by Time-Dependent Hermite Propagation. *The Journal of Physical Chemistry A*, *105*(38), 8672-8680. https://doi.org/10.1021/jp011449x

Johnson, M. S., Feilberg, K. L., Hessberg, P. V., & Nielsen, O. J. (2002). Isotopic processes in atmospheric chemistry. *Chemical Society Reviews*, *31*(6), 313-323. https://doi.org/10.1039/b108011n

Johnston, J. C., Cliff, S. S., & Thiemens, M. H. (1995). Measurement of multioxygen isotopic ($\delta^{18}O$ and $\delta^{17}O$) fractionation factors in the stratospheric sink reactions of nitrous oxide. *Journal of Geophysical Research: Atmospheres*, *100*(D8), 16801-16804. https://doi.org/https://doi.org/10.1029/95JD01646

Johnston, J. C., Röckmann, T., & Brenninkmeijer, C. A. M. (2000). CO_2+$O(^1D)$ isotopic exchange: Laboratory and modeling studies [https://doi.org/10.1029/2000JD900070]. *Journal of Geophysical Research: Atmospheres*, *105*(D12), 15213-15229. https://doi.org/https://doi.org/10.1029/2000JD900070

Juranek, L. W., & Quay, P. D. (2013). Using Triple Isotopes of Dissolved Oxygen to Evaluate Global Marine Productivity. *Annual Review of Marine Science*, *5*(1), 503-524. https://doi.org/10.1146/annurev-marine-121211-172430

Jurikova, H., Guha, T., Abe, O., Shiah, F. K., Wang, C. H., & Liang, M. C. (2016). Variations in triple isotope composition of dissolved oxygen and primary production in a subtropical reservoir. *Biogeosciences*, *13*(24), 6683-6698. https://doi.org/10.5194/bg-13-6683-2016

Kai, F. M., Tyler, S. C., Randerson, J. T., & Blake, D. R. (2011). Reduced methane growth rate explained by decreased Northern Hemisphere microbial sources. *Nature*, *476*(7359), 194-197. https://doi.org/10.1038/nature10259

Kaiser, J. (2002). Intramolecular^{15}N and ^{18}O fractionation in the reaction of N_2O with O(^{1}D) and its implications for the stratospheric N_2O isotope signature. *Journal of Geophysical Research*, *107*(D14). https://doi.org/10.1029/2001jd001506

Kaiser, J. (2011). Technical note: Consistent calculation of aquatic gross production from oxygen triple isotope measurements. *Biogeosciences*, *8*(7), 1793-1811. https://doi.org/10.5194/bg-8-1793-2011

Kaiser, J., Röckmann, T., & Brenninkmeijer, C. A. M. (2002). Temperature dependence of isotope fractionation in N_2O photolysis. *Phys. Chem. Chem. Phys.*, *4*(18), 4420-4430. https://doi.org/10.1039/b204837j

Kaiser, J., Röckmann, T., Brenninkmeijer, C. A. M., & Crutzen, P. J. (2003). Wavelength dependence of isotope fractionation in N_2O photolysis. *Atmospheric Chemistry and Physics*, *3*(2), 303-313. https://doi.org/10.5194/acp-3-303-2003

Kantnerová, K., Jespersen, M. F., Bernasconi, S. M., Emmenegger, L., Johnson, M. S., & Mohn, J. (2020). Photolytic fractionation of seven singly and doubly substituted nitrous oxide isotopocules measured by quantum cascade laser absorption spectroscopy. *Atmospheric Environment: X*, *8*, 100094. https://doi.org/https://doi.org/10.1016/j.aeaoa.2020.100094

Kantnerová, K., Yu, L., Zindel, D., Zahniser, M. S., Nelson, D. D., Tuzson, B., Nakagawa, M., Toyoda, S., Yoshida, N., Emmenegger, L., Bernasconi, S. M., & Mohn, J. (2020). First investigation and absolute calibration of clumped isotopes in N_2O by mid-infrared laser spectroscopy. *Rapid Communications in Mass Spectrometry*, *34*(15). https://doi.org/10.1002/rcm.8836

Katakis, D., & Taube, H. (1962). Some Photochemical Reactions of O_3 in the Gas Phase. *The Journal of Chemical Physics*, *36*(2), 416-422. https://doi.org/10.1063/1.1732521

Kawagucci, S., Tsunogai, U., Kudo, S., Nakagawa, F., Honda, H., Aoki, S., Nakazawa, T., Tsutsumi, M., & Gamo, T. (2008). Long-term observation of mass-independent oxygen isotope anomaly in stratospheric CO_2. *Atmos. Chem. Phys.*, *8*(20), 6189-6197. https://doi.org/10.5194/acp-8-6189-2008

Kaye, J. A. (1986). Theoretical analysis of isotope effects on ozone formation in oxygen photochemistry. *Journal of Geophysical Research: Atmospheres*, *91*(D7), 7865-7874. https://doi.org/https://doi.org/10.1029/JD091iD07p07865

Kaye, J. A. (1987). Mechanisms and observations for isotope fractionation of molecular species in planetary atmospheres. *Reviews of Geophysics*, *25*(8), 1609. https://doi.org/10.1029/rg025i008p01609

Kim, K.-R., & Craig, H. (1993). Nitrogen-15 and Oxygen-18 Characteristics of Nitrous Oxide: A Global Perspective. *Science*, *262*(5141), 1855-1857. https://doi.org/10.1126/science.262.5141.1855

Klais, O., Anderson, P. C., & Kurylo, M. J. (1980). A reinvestigation of the temperature dependence of the rate constant for the reaction $O + O_2 + M \rightarrow O_3 + M$ (for M = O_2, N_2, and Ar) by the flash photolysis resonance fluorescence technique. *International Journal*

of Chemical Kinetics, *12*(7), 469-490. https://doi.org/https://doi.org/10.1002/kin.550120704

Kokoouline, V., Lapierre, D., Alijah, A., & Tyuterev, V. (2020). Localized and delocalized bound states of the main isotopologue $^{48}O_3$ and of ^{18}O-enriched $^{50}O_3$ isotopomers of the ozone molecule near the dissociation threshold [10.1039/D0CP02177F]. *Physical Chemistry Chemical Physics*, *22*(28), 15885-15899. https://doi.org/10.1039/D0CP02177F

Koren, G., Schneider, L., van der Velde, I. R., van Schaik, E., Gromov, S. S., Adnew, G. A., Mrozek Martino, D. J., Hofmann, M. E. G., Liang, M.-C., Mahata, S., Bergamaschi, P., van der Laan-Luijkx, I. T., Krol, M. C., Röckmann, T., & Peters, W. (2019). Global 3-D Simulations of the Triple Oxygen Isotope Signature $\Delta^{17}O$ in Atmospheric CO_2 [https://doi.org/10.1029/2019JD030387]. *Journal of Geophysical Research: Atmospheres*, *124*(15), 8808-8836. https://doi.org/https://doi.org/10.1029/2019JD030387

Krankowsky, D., Lämmerzahl, P., Mauersberger, K., Janssen, C., Tuzson, B., & Röckmann, T. (2007). Stratospheric ozone isotope fractionations derived from collected samples. *Journal of Geophysical Research: Atmospheres*, *112*(D8). https://doi.org/https://doi.org/10.1029/2006JD007855

Kryvohuz, M., & Marcus, R. A. (2010). Coriolis coupling as a source of non-RRKM effects in ozone molecule: Lifetime statistics of vibrationally excited ozone molecules. *The Journal of Chemical Physics*, *132*(22), 224305. https://doi.org/10.1063/1.3430514

Labidi, J., Barry, P. H., Bekaert, D. V., Broadley, M. W., Marty, B., Giunta, T., Warr, O., Sherwood Lollar, B., Fischer, T. P., Avice, G., Caracausi, A., Ballentine, C. J., Halldórsson, S. A., Stefánsson, A., Kurz, M. D., Kohl, I. E., & Young, E. D. (2020). Hydrothermal $^{15}N^{15}N$ abundances constrain the origins of mantle nitrogen. *Nature*, *580*(7803), 367-371. https://doi.org/10.1038/s41586-020-2173-4

Lämmerzahl, P., Röckmann, T., Brenninkmeijer, C. A. M., Krankowsky, D., & Mauersberger, K. (2002). Oxygen isotope composition of stratospheric carbon dioxide. *Geophysical Research Letters*, *29*(12), 23-21-23-24. https://doi.org/https://doi.org/10.1029/2001GL014343

Landais, A., Lathiere, J., Barkan, E., & Luz, B. (2007). Reconsidering the change in global biosphere productivity between the Last Glacial Maximum and present day from the triple oxygen isotopic composition of air trapped in ice cores [https://doi.org/10.1029/2006GB002739]. *Global Biogeochemical Cycles*, *21*(1). https://doi.org/https://doi.org/10.1029/2006GB002739

Landais, A., Masson-Delmotte, V., Combourieu Nebout, N., Jouzel, J., Blunier, T., Leuenberger, M., Dahl-Jensen, D., & Johnsen, S. (2007). Millenial scale variations of the isotopic composition of atmospheric oxygen over Marine Isotopic Stage 4. *Earth and Planetary Science Letters*, *258*(1), 101-113. https://doi.org/https://doi.org/10.1016/j.epsl.2007.03.027

Laskar, A. H., Mahata, S., Bhattacharya, S. K., & Liang, M. C. (2019). Triple Oxygen and Clumped Isotope Compositions of CO_2 in the Middle Troposphere. *Earth and Space Science*, *6*(7), 1205-1219. https://doi.org/10.1029/2019ea000573

Lee, C. C.-W., & Thiemens, M. H. (2001). The $\delta^{17}O$ and $\delta^{18}O$ measurements of atmospheric sulfate from a coastal and high alpine region: A mass-independent isotopic anomaly. *Journal of Geophysical Research: Atmospheres*, *106*(D15), 17359-17373. https://doi.org/https://doi.org/10.1029/2000JD900805

Liang, M.-C., Blake, G. A., Lewis, B. R., & Yung, Y. L. (2007). Oxygen isotopic composition of carbon dioxide in the middle atmosphere. *Proceedings of the National Academy of Sciences*, *104*(1), 21-25. https://doi.org/10.1073/pnas.0610009104

Liu, Y., & Li, J. (2020). An accurate potential energy surface and ring polymer molecular dynamics study of the Cl + CH_4 → HCl + CH_3 reaction. *Physical Chemistry Chemical Physics*, *22*(1), 344-353. https://doi.org/10.1039/c9cp05693a

Luther, K., Oum, K., & Troe, J. (2005). The role of the radical-complex mechanism in the ozone recombination/dissociation reaction [10.1039/B504178C]. *Physical Chemistry Chemical Physics*, *7*(14), 2764-2770. https://doi.org/10.1039/B504178C

Luz, B., & Barkan, E. (2000). Assessment of Oceanic Productivity with the Triple-Isotope Composition of Dissolved Oxygen. *Science*, *288*(5473), 2028-2031. https://doi.org/10.1126/science.288.5473.2028

Luz, B., & Barkan, E. (2005). The isotopic ratios $^{17}O/^{16}O$ and $^{18}O/^{16}O$ in molecular oxygen and their significance in biogeochemistry. *Geochimica et Cosmochimica Acta*, *69*(5), 1099-1110. https://doi.org/https://doi.org/10.1016/j.gca.2004.09.001

Luz, B., & Barkan, E. (2011). The isotopic composition of atmospheric oxygen [https://doi.org/10.1029/2010GB003883]. *Global Biogeochemical Cycles*, *25*(3). https://doi.org/https://doi.org/10.1029/2010GB003883

Luz, B., Barkan, E., Bender, M. L., Thiemens, M. H., & Boering, K. A. (1999). Triple-isotope composition of atmospheric oxygen as a tracer of biosphere productivity. *Nature*, *400*(6744), 547-550. https://doi.org/10.1038/22987

Lyons, J. R., & Young, E. D. (2005). CO self-shielding as the origin of oxygen isotope anomalies in the early solar nebula. *Nature*, *435*(7040), 317-320. https://doi.org/10.1038/nature03557

Ma, Q., Wu, S., & Tang, Y. (2008). Formation and abundance of doubly-substituted methane isotopologues ($^{13}CH_3D$) in natural gas systems. *Geochimica et Cosmochimica Acta*, *72*(22), 5446-5456. https://doi.org/https://doi.org/10.1016/j.gca.2008.08.014

Magyar, P. M., Orphan, V. J., & Eiler, J. M. (2016). Measurement of rare isotopologues of nitrous oxide by high-resolution multi-collector mass spectrometry [https://doi.org/10.1002/rcm.7671]. *Rapid Communications in Mass Spectrometry*, *30*(17), 1923-1940. https://doi.org/https://doi.org/10.1002/rcm.7671

Mar, K. A., McCarthy, M. C., Connell, P., & Boering, K. A. (2007). Modeling the photochemical origins of the extreme deuterium enrichment in stratospheric H_2. *Journal of Geophysical Research*, *112*(D19). https://doi.org/10.1029/2006jd007403

Marcus, R. A. (2004). Mass-independent isotope effect in the earliest processed solids in the solar system: A possible chemical mechanism. *The Journal of Chemical Physics*, *121*(17), 8201-8211. https://doi.org/10.1063/1.1803507

Mauersberger, K. (1981). Measurement of heavy ozone in the stratosphere [https://doi.org/10.1029/GL008i008p00935]. *Geophysical Research Letters*, *8*(8), 935-937. https://doi.org/https://doi.org/10.1029/GL008i008p00935

Mauersberger, K., Erbacher, B., Krankowsky, D., Günther, J., & Nickel, R. (1999). Ozone Isotope Enrichment: Isotopomer-Specific Rate Coefficients. *Science*, *283*(5400), 370-372. https://doi.org/10.1126/science.283.5400.370

Mauersberger, K., Krankowsky, D., Janssen, C., & Schinke, R. (2005). Assessment of the ozone isotope effect. In *Advances in Atomic, Molecular, and Optical Physics* (Vol. 50, pp. 1-54). Elsevier. https://doi.org/10.1016/s1049-250x(05)80006-0

McCarthy, M. C. (2003). Carbon and hydrogen isotopic compositions of stratospheric methane: 2. Two-dimensional model results and implications for kinetic isotope effects. *Journal of Geophysical Research*, *108*(D15). https://doi.org/10.1029/2002jd003183

McCarthy, M. C., Connell, P., & Boering, K. A. (2001). Isotopic fractionation of methane in the stratosphere and its effect on free tropospheric isotopic compositions [https://doi.org/10.1029/2001GL013159]. *Geophysical Research Letters*, *28*(19), 3657-3660. https://doi.org/https://doi.org/10.1029/2001GL013159

McLinden, C. A., Prather, M. J., & Johnson, M. S. (2003). Global modeling of the isotopic analogues of N_2O: Stratospheric distributions, budgets, and the ^{17}O–^{18}O mass-independent anomaly. *Journal of Geophysical Research: Atmospheres*, *108*(D8). https://doi.org/https://doi.org/10.1029/2002JD002560

Mebel, A. M., Hayashi, M., Kislov, V. V., & Lin, S. H. (2004). Theoretical Study of Oxygen Isotope Exchange and Quenching in the $O(^1D) + CO_2$ Reaction. *The Journal of Physical Chemistry A*, *108*(39), 7983-7994. https://doi.org/10.1021/jp049315h

Meisner, J., & Kästner, J. (2016). Reaction rates and kinetic isotope effects of $H_2 + OH \rightarrow H_2O + H$. *The Journal of Chemical Physics*, *144*(17), 174303. https://doi.org/10.1063/1.4948319

Melissas, V. S., & Truhlar, D. G. (1993). Deuterium and carbon-13 kinetic isotope effects for the reaction of OH with CH_4. *The Journal of Chemical Physics*, *99*(5), 3542-3552. https://doi.org/10.1063/1.466230

Michalski, G., Meixner, T., Fenn, M., Hernandez, L., Sirulnik, A., Allen, E., & Thiemens, M. (2004). Tracing Atmospheric Nitrate Deposition in a Complex Semiarid Ecosystem Using $\Delta^{17}O$. *Environmental Science & Technology*, *38*(7), 2175-2181. https://doi.org/10.1021/es034980+

Michalski, G., Scott, Z., Kabiling, M., & Thiemens, M. H. (2003). First measurements and modeling of $\Delta^{17}O$ in atmospheric nitrate. *Geophysical Research Letters*, *30*(16). https://doi.org/https://doi.org/10.1029/2003GL017015

Miller, C. E., & Yung, Y. L. (2000). Photo-induced isotopic fractionation of stratospheric N_2O. *Chemosphere - Global Change Science*, *2*(3), 255-266. https://doi.org/https://doi.org/10.1016/S1465-9972(00)00011-8

Miller, D. J., Chai, J., Guo, F., Dell, C. J., Karsten, H., & Hastings, M. G. (2018). Isotopic Composition of In Situ Soil NO_x Emissions in Manure-Fertilized Cropland. *Geophysical Research Letters*, *45*(21). https://doi.org/10.1029/2018gl079619

Miller, D. J., Wojtal, P. K., Clark, S. C., & Hastings, M. G. (2017). Vehicle NO_x emission plume isotopic signatures: Spatial variability across the eastern United States. *Journal of Geophysical Research: Atmospheres*, *122*(8), 4698-4717. https://doi.org/10.1002/2016jd025877

Mohn, J., Tuzson, B., Manninen, A., Yoshida, N., Toyoda, S., Brand, W. A., & Emmenegger, L. (2012). Site selective real-time measurements of atmospheric N_2O isotopomers by laser spectroscopy. *Atmospheric Measurement Techniques*, *5*(7), 1601-1609. https://doi.org/10.5194/amt-5-1601-2012

Moyer, E. J., Irion, F. W., Yung, Y. L., & Gunson, M. R. (1996). ATMOS stratospheric deuterated water and implications for troposphere-stratosphere transport. *Geophysical Research Letters*, *23*(17), 2385-2388. https://doi.org/10.1029/96gl01489

Ndengué, S. A., Schinke, R., Gatti, F., Meyer, H.-D., & Jost, R. (2012). Ozone Photodissociation: Isotopic and Electronic Branching Ratios for Symmetric and

Asymmetric Isotopologues. *The Journal of Physical Chemistry A*, *116*(50), 12271-12279. https://doi.org/10.1021/jp307195v

Nelson, D. M., Tsunogai, U., Ding, D., Ohyama, T., Komatsu, D. D., Nakagawa, F., Noguchi, I., & Yamaguchi, T. (2018). Triple oxygen isotopes indicate urbanization affects sources of nitrate in wet and dry atmospheric deposition. *Atmos. Chem. Phys.*, *18*(9), 6381-6392. https://doi.org/10.5194/acp-18-6381-2018

Nguyen, T. L., Stanton, J. F., & Barker, J. R. (2011). Ab Initio Reaction Rate Constants Computed Using Semiclassical Transition-State Theory: HO + H_2→ H2O + H and Isotopologues. *The Journal of Physical Chemistry A*, *115*(20), 5118-5126. https://doi.org/10.1021/jp2022743

Nicholson, D. P., Stanley, R. H. R., Barkan, E., Karl, D. M., Luz, B., Quay, P. D., & Doney, S. C. (2012). Evaluating triple oxygen isotope estimates of gross primary production at the Hawaii Ocean Time-series and Bermuda Atlantic Time-series Study sites [https://doi.org/10.1029/2010JC006856]. *Journal of Geophysical Research: Oceans*, *117*(C5). https://doi.org/https://doi.org/10.1029/2010JC006856

Nilsson, E. J. K., Andersen, V. F., Skov, H., & Johnson, M. S. (2010). Pressure dependence of the deuterium isotope effect in the photolysis of formaldehyde by ultraviolet light. *Atmospheric Chemistry and Physics*, *10*(7), 3455-3462. https://doi.org/10.5194/acp-10-3455-2010

Nilsson, E. J. K., Schmidt, J. A., & Johnson, M. S. (2014). Pressure dependent isotopic fractionation in the photolysis of formaldehyde. *Atmospheric Chemistry and Physics*, *14*(2), 551-558. https://doi.org/10.5194/acp-14-551-2014

Ono, S., Wang, D. T., Gruen, D. S., Sherwood Lollar, B., Zahniser, M. S., McManus, B. J., & Nelson, D. D. (2014). Measurement of a Doubly Substituted Methane Isotopologue, $^{13}CH_3D$, by Tunable Infrared Laser Direct Absorption Spectroscopy. *Analytical Chemistry*, *86*(13), 6487-6494. https://doi.org/10.1021/ac5010579

Pack, A., Gehler, A., & Süssenberger, A. (2013). Exploring the usability of isotopically anomalous oxygen in bones and teeth as paleo-CO_2-barometer. *Geochimica et Cosmochimica Acta*, *102*, 306-317. https://doi.org/https://doi.org/10.1016/j.gca.2012.10.017

Pack, A., Höweling, A., Hezel, D. C., Stefanak, M. T., Beck, A.-K., Peters, S. T. M., Sengupta, S., Herwartz, D., & Folco, L. (2017). Tracing the oxygen isotope composition of the upper Earth's atmosphere using cosmic spherules. *Nature Communications*, *8*(1), 15702. https://doi.org/10.1038/ncomms15702

Park, S. (2004). Measurements of N_2O isotopologues in the stratosphere: Influence of transport on the apparent enrichment factors and the isotopologue fluxes to the troposphere. *Journal of Geophysical Research*, *109*(D1). https://doi.org/10.1029/2003jd003731

Park, S., Croteau, P., Boering, K. A., Etheridge, D. M., Ferretti, D., Fraser, P. J., Kim, K. R., Krummel, P. B., Langenfelds, R. L., Van Ommen, T. D., Steele, L. P., & Trudinger, C. M. (2012). Trends and seasonal cycles in the isotopic composition of nitrous oxide since 1940. *Nature Geoscience*, *5*(4), 261-265. https://doi.org/10.1038/ngeo1421

Passey, B. H., Hu, H., Ji, H., Montanari, S., Li, S., Henkes, G. A., & Levin, N. E. (2014). Triple oxygen isotopes in biogenic and sedimentary carbonates. *Geochimica et Cosmochimica Acta*, *141*, 1-25. https://doi.org/https://doi.org/10.1016/j.gca.2014.06.006

Passey, B. H., Levin, N. E., Cerling, T. E., Brown, F. H., & Eiler, J. M. (2010). High-temperature environments of human evolution in East Africa based on bond ordering in

paleosol carbonates. *Proceedings of the National Academy of Sciences*, *107*(25), 11245-11249. https://doi.org/10.1073/pnas.1001824107

Perri, M. J., Van Wyngarden, A. L., Lin, J. J., Lee, Y. T., & Boering, K. A. (2004). Energy Dependence of Oxygen Isotope Exchange and Quenching in the $O(^1D) + CO_2$ Reaction: A Crossed Molecular Beam Study. *The Journal of Physical Chemistry A*, *108*(39), 7995-8001. https://doi.org/10.1021/jp0485845

Perri, M. J., Wyngarden, A. L. V., Boering, K. A., Lin, J. J., & Lee, Y. T. (2003). Dynamics of the $O(^1D)+CO_2$ oxygen isotope exchange reaction. *The Journal of Chemical Physics*, *119*(16), 8213-8216. https://doi.org/10.1063/1.1618737

Popa, M. E., Paul, D., Janssen, C., & Röckmann, T. (2019). H_2 clumped isotope measurements at natural isotopic abundances [https://doi.org/10.1002/rcm.8323]. *Rapid Communications in Mass Spectrometry*, *33*(3), 239-251. https://doi.org/https://doi.org/10.1002/rcm.8323

Prokhorov, I., Kluge, T., & Janssen, C. (2019). Optical clumped isotope thermometry of carbon dioxide. *Scientific Reports*, *9*(1). https://doi.org/10.1038/s41598-019-40750-z

Prokopenko, M. G., Pauluis, O. M., Granger, J., & Yeung, L. Y. (2011). Exact evaluation of gross photosynthetic production from the oxygen triple-isotope composition of O_2: Implications for the net-to-gross primary production ratios [https://doi.org/10.1029/2011GL047652]. *Geophysical Research Letters*, *38*(14). https://doi.org/https://doi.org/10.1029/2011GL047652

Qu, Z.-W., Zhu, H., Grebenshchikov, S. Y., & Schinke, R. (2005a). The photodissociation of ozone in the Hartley band: A theoretical analysis. *The Journal of Chemical Physics*, *123*(7), 074305. https://doi.org/10.1063/1.2001650

Qu, Z.-W., Zhu, H., Grebenshchikov, S. Y., & Schinke, R. (2005b). The triplet channel in the photodissociation of ozone in the Hartley band: Classical trajectory surface hopping analysis. *The Journal of Chemical Physics*, *122*(19), 191102. https://doi.org/10.1063/1.1925608

Quay, P., Stutsman, J., Wilbur, D., Snover, A., Dlugokencky, E., & Brown, T. (1999). The isotopic composition of atmospheric methane [https://doi.org/10.1029/1998GB900006]. *Global Biogeochemical Cycles*, *13*(2), 445-461. https://doi.org/https://doi.org/10.1029/1998GB900006

Rahn, T., Eiler, J. M., Boering, K. A., Wennberg, P. O., McCarthy, M. C., Tyler, S., Schauffler, S., Donnelly, S., & Atlas, E. (2003). Extreme deuterium enrichment in stratospheric hydrogen and the global atmospheric budget of H_2. *Nature*, *424*(6951), 918-921. https://doi.org/10.1038/nature01917

Rahn, T., & Wahlen, M. (1997). Stable Isotope Enrichment in Stratospheric Nitrous Oxide. *Science*, *278*(5344), 1776-1778. https://doi.org/10.1126/science.278.5344.1776

Rahn, T., Zhang, H., Wahlen, M., & Blake, G. A. (1998). Stable isotope fractionation during ultraviolet photolysis of N_2O. *Geophysical Research Letters*, *25*(24), 4489-4492. https://doi.org/10.1029/1998gl900186

Rice, A. L. (2003). Carbon and hydrogen isotopic compositions of stratospheric methane: 1. High-precision observations from the NASA ER-2 aircraft. *Journal of Geophysical Research*, *108*(D15). https://doi.org/10.1029/2002jd003042

Rice, A. L., Butenhoff, C. L., Teama, D. G., Röger, F. H., Khalil, M. A. K., & Rasmussen, R. A. (2016). Atmospheric methane isotopic record favors fossil sources flat in 1980s and 1990s with recent increase. *Proceedings of the National Academy of Sciences*, *113*(39), 10791-10796. https://doi.org/10.1073/pnas.1522923113

Robert, F., Baraut-Guinet, L., Cartigny, P., & Reinhardt, P. (2019). An experimental test for the mass independent isotopic fractionation mechanism proposed for ozone. *Chemical Physics*, *523*, 191-197. https://doi.org/https://doi.org/10.1016/j.chemphys.2019.03.024

Röckmann, T., Brass, M., Borchers, R., & Engel, A. (2011). The isotopic composition of methane in the stratosphere: high-altitude balloon sample measurements. *Atmospheric Chemistry and Physics*, *11*(24), 13287-13304. https://doi.org/10.5194/acp-11-13287-2011

Röckmann, T., Brenninkmeijer, C. A. M., Neeb, P., & Crutzen, P. J. (1998a). Ozonolysis of nonmethane hydrocarbons as a source of the observed mass independent oxygen isotope enrichment in tropospheric CO [https://doi.org/10.1029/97JD02929]. *Journal of Geophysical Research: Atmospheres*, *103*(D1), 1463-1470. https://doi.org/https://doi.org/10.1029/97JD02929

Röckmann, T., Brenninkmeijer, C. A. M., Saueressig, G., Bergamaschi, P., Crowley, J. N., Fischer, H., & Crutzen, P. J. (1998b). Mass-Independent Oxygen Isotope Fractionation in Atmospheric CO as a Result of the Reaction CO + OH. *Science*, *281*(5376), 544-546. https://doi.org/10.1126/science.281.5376.544

Röckmann, T., Brenninkmeijer, C. A. M., Wollenhaupt, M., Crowley, J. N., & Crutzen, P. J. (2000). Measurement of the isotopic fractionation of $^{15}N^{14}N^{16}O$, $^{14}N^{15}N^{16}O$ and $^{14}N^{14}N^{18}O$ in the UV photolysis of nitrous oxide. *Geophysical Research Letters*, *27*(9), 1399-1402. https://doi.org/10.1029/1999gl011135

Röckmann, T., Kaiser, J., Brenninkmeijer, C. A. M., Crowley, J. N., Borchers, R., Brand, W. A., & Crutzen, P. J. (2001). Isotopic enrichment of nitrous oxide ($^{15}N^{14}NO$, $^{14}N^{15}NO$, $^{14}N^{14}N^{18}O$) in the stratosphere and in the laboratory. *Journal of Geophysical Research: Atmospheres*, *106*(D10), 10403-10410. https://doi.org/https://doi.org/10.1029/2000JD900822

Röckmann, T., & Levin, I. (2005). High-precision determination of the changing isotopic composition of atmospheric N_2O from 1990 to 2002. *Journal of Geophysical Research*, *110*(D21). https://doi.org/10.1029/2005jd006066

Röckmann, T., Walter, S., Bohn, B., Wegener, R., Spahn, H., Brauers, T., Tillmann, R., Schlosser, E., Koppmann, R., & Rohrer, F. (2010). Isotope effect in the formation of H_2; from H_2CO studied at the atmospheric simulation chamber SAPHIR. *Atmospheric Chemistry and Physics*, *10*(12), 5343-5357. https://doi.org/10.5194/acp-10-5343-2010

Saueressig, G., Bergamaschi, P., Crowley, J. N., Fischer, H., & Harris, G. W. (1995). Carbon kinetic isotope effect in the reaction of CH_4 with Cl atoms [https://doi.org/10.1029/95GL00881]. *Geophysical Research Letters*, *22*(10), 1225-1228. https://doi.org/https://doi.org/10.1029/95GL00881

Saueressig, G., Crowley, J. N., Bergamaschi, P., Brühl, C., Brenninkmeijer, C. A. M., & Fischer, H. (2001). Carbon 13 and D kinetic isotope effects in the reactions of CH_4 with $O(^1D)$ and OH: New laboratory measurements and their implications for the isotopic composition of stratospheric methane. *Journal of Geophysical Research: Atmospheres*, *106*(D19), 23127-23138. https://doi.org/10.1029/2000jd000120

Savard, M. M., Cole, A. S., Vet, R., & Smirnoff, A. (2018). The $\Delta^{17}O$ and $\delta^{18}O$ values of atmospheric nitrates simultaneously collected downwind of anthropogenic sources – implications for polluted air masses. *Atmos. Chem. Phys.*, *18*(14), 10373-10389. https://doi.org/10.5194/acp-18-10373-2018

Savarino, J., Lee, C. C. W., & Thiemens, M. H. (2000). Laboratory oxygen isotopic study of sulfur (IV) oxidation: Origin of the mass-independent oxygen isotopic anomaly in

atmospheric sulfates and sulfate mineral deposits on Earth [https://doi.org/10.1029/2000JD900456]. *Journal of Geophysical Research: Atmospheres*, *105*(D23), 29079-29088. https://doi.org/https://doi.org/10.1029/2000JD900456

Savarino, J., & Thiemens, M. H. (1999). Analytical procedure to determine both $\delta^{18}O$ and $\delta^{17}O$ of H_2O_2 in natural water and first measurements. *Atmospheric Environment*, *33*(22), 3683-3690. https://doi.org/https://doi.org/10.1016/S1352-2310(99)00122-3

Sayres, D. S., Moyer, E. J., Hanisco, T. F., St. Clair, J. M., Keutsch, F. N., O'Brien, A., Allen, N. T., Lapson, L., Demusz, J. N., Rivero, M., Martin, T., Greenberg, M., Tuozzolo, C., Engel, G. S., Kroll, J. H., Paul, J. B., & Anderson, J. G. (2009). A new cavity based absorption instrument for detection of water isotopologues in the upper troposphere and lower stratosphere. *Review of Scientific Instruments*, *80*(4), 044102. https://doi.org/10.1063/1.3117349

Schaefer, H., Fletcher, S. E. M., Veidt, C., Lassey, K. R., Brailsford, G. W., Bromley, T. M., Dlugokencky, E. J., Michel, S. E., Miller, J. B., Levin, I., Lowe, D. C., Martin, R. J., Vaughn, B. H., & White, J. W. C. (2016). A 21st-century shift from fossil-fuel to biogenic methane emissions indicated by $^{13}CH_4$. *Science*, *352*(6281), 80-84. https://doi.org/10.1126/science.aad2705

Schinke, R., & Fleurat-Lessard, P. (2005). The effect of zero-point energy differences on the isotope dependence of the formation of ozone: A classical trajectory study. *The Journal of Chemical Physics*, *122*(9), 094317. https://doi.org/10.1063/1.1860011

Schinke, R., & Grebenshchikov, S. Y. (2008). On the photodissociation of ozone in the range of 5–9eV. *Chemical Physics*, *347*(1), 279-287. https://doi.org/https://doi.org/10.1016/j.chemphys.2007.08.024

Schinke, R., Grebenshchikov, S. Y., Ivanov, M. V., & Fleurat-Lessard, P. (2006). Dynamical Studies of the Ozone Isotope Effect: A Status Report. *Annual Review of Physical Chemistry*, *57*(1), 625-661. https://doi.org/10.1146/annurev.physchem.57.032905.104542

Schinke, R., McBane, G. C., Shen, L., Singh, P. C., & Suits, A. G. (2009). Production of O_2 Herzberg states in the deep UV photodissociation of ozone. *The Journal of Chemical Physics*, *131*(1), 011101. https://doi.org/10.1063/1.3157236

Schmidt, J. A., & Johnson, M. S. (2015). Clumped isotope perturbation in tropospheric nitrous oxide from stratospheric photolysis. *Geophysical Research Letters*, *42*(9), 3546-3552. https://doi.org/https://doi.org/10.1002/2015GL063102

Schmidt, J. A., Johnson, M. S., & Schinke, R. (2011). Isotope effects in N_2O photolysis from first principles. *Atmos. Chem. Phys.*, *11*(17), 8965-8975. https://doi.org/10.5194/acp-11-8965-2011

Schwietzke, S., Sherwood, O. A., Bruhwiler, L. M. P., Miller, J. B., Etiope, G., Dlugokencky, E. J., Michel, S. E., Arling, V. A., Vaughn, B. H., White, J. W. C., & Tans, P. P. (2016). Upward revision of global fossil fuel methane emissions based on isotope database. *Nature*, *538*(7623), 88-91. https://doi.org/10.1038/nature19797

Semeniuk, K., McConnell, J. C., Jin, J. J., Jarosz, J. R., Boone, C. D., & Bernath, P. F. (2008). N_2O production by high energy auroral electron precipitation. *Journal of Geophysical Research*, *113*(D16). https://doi.org/10.1029/2007jd009690

Shaheen, R., Janssen, C., & Röckmann, T. (2007). Investigations of the photochemical isotope equilibrium between O_2, CO_2 and O_3. *Atmos. Chem. Phys.*, *7*(2), 495-509. https://doi.org/10.5194/acp-7-495-2007

Siebert, R., Schinke, R., & Bittererová, M. (2001). Spectroscopy of ozone at the dissociation threshold: Quantum calculations of bound and resonance states on a new global potential energy surface. *Physical Chemistry Chemical Physics*, *3*(10), 1795-1798. https://doi.org/10.1039/b102830h

Stolper, D. A., Lawson, M., Davis, C. L., Ferreira, A. A., Neto, E. V. S., Ellis, G. S., Lewan, M. D., Martini, A. M., Tang, Y., Schoell, M., Sessions, A. L., & Eiler, J. M. (2014). Formation temperatures of thermogenic and biogenic methane. *Science*, *344*(6191), 1500-1503. https://doi.org/10.1126/science.1254509

Stolper, D. A., Martini, A. M., Clog, M., Douglas, P. M., Shusta, S. S., Valentine, D. L., Sessions, A. L., & Eiler, J. M. (2015). Distinguishing and understanding thermogenic and biogenic sources of methane using multiply substituted isotopologues. *Geochimica et Cosmochimica Acta*, *161*, 219-247. https://doi.org/https://doi.org/10.1016/j.gca.2015.04.015

Stolper, D. A., Sessions, A. L., Ferreira, A. A., Santos Neto, E. V., Schimmelmann, A., Shusta, S. S., Valentine, D. L., & Eiler, J. M. (2014). Combined ^{13}C–D and D–D clumping in methane: Methods and preliminary results. *Geochimica et Cosmochimica Acta*, *126*, 169-191. https://doi.org/https://doi.org/10.1016/j.gca.2013.10.045

Sugawara, S., Nakazawa, T., Shirakawa, Y., Kawamura, K., Aoki, S., Machida, T., & Honda, H. (1997). Vertical profile of the carbon isotopic ratio of stratospheric methane over Japan. *Geophysical Research Letters*, *24*(23), 2989-2992. https://doi.org/10.1029/97gl03044

Sun, Z., Liu, L., Lin, S. Y., Schinke, R., Guo, H., & Zhang, D. H. (2010). State-to-state quantum dynamics of O + O_2 isotope exchange reactions reveals nonstatistical behavior at atmospheric conditions. *Proceedings of the National Academy of Sciences*, *107*(2), 555-558. https://doi.org/10.1073/pnas.0911356107

Suwa, M., von Fischer, J. C., Bender, M. L., Landais, A., & Brook, E. J. (2006). Chronology reconstruction for the disturbed bottom section of the GISP2 and the GRIP ice cores: Implications for Termination II in Greenland [https://doi.org/10.1029/2005JD006032]. *Journal of Geophysical Research: Atmospheres*, *111*(D2). https://doi.org/https://doi.org/10.1029/2005JD006032

Taenzer, L., Labidi, J., Masterson, A. L., Feng, X., Rumble, D., Young, E. D., & Leavitt, W. D. (2020). Low $\Delta^{12}CH_2D_2$ values in microbialgenic methane result from combinatorial isotope effects. *Geochimica et Cosmochimica Acta*, *285*, 225-236. https://doi.org/https://doi.org/10.1016/j.gca.2020.06.026

Taguchi, K., Yamamoto, T., Nakagawa, M., Gilbert, A., & Ueno, Y. (2020). A fluorination method for measuring the ^{13}C- ^{13}C isotopologue of C 2 molecules. *Rapid Communications in Mass Spectrometry*, *34*(11). https://doi.org/10.1002/rcm.8761

Tajti, A., Szalay, P. G., Kochanov, R., & Tyuterev, V. G. (2020). Diagonal Born–Oppenheimer corrections to the ground electronic state potential energy surfaces of ozone: improvement of ab initio vibrational band centers for the $^{16}O_3$, $^{17}O_3$ and $^{18}O_3$ isotopologues [10.1039/D0CP02457K]. *Physical Chemistry Chemical Physics*, *22*(42), 24257-24269. https://doi.org/10.1039/D0CP02457K

Talukdar, R. K., & Ravishankara, A. R. (1996). Rate coefficients for $O(^1D)$ + H_2, D_2, HD reactions and H atom yield in $O(^1D)$ + HD reaction. *Chemical Physics Letters*, *253*(1-2), 177-183. https://doi.org/10.1016/0009-2614(96)00203-5

Teplukhin, A., & Babikov, D. (2018a). Properties of Feshbach and "shape"-resonances in ozone and their role in recombination reactions and anomalous isotope effects

[10.1039/C8FD00089A]. *Faraday Discussions*, *212*(0), 259-280. https://doi.org/10.1039/C8FD00089A

Teplukhin, A., & Babikov, D. (2018b). Several Levels of Theory for Description of Isotope Effects in Ozone: Symmetry Effect and Mass Effect. *The Journal of Physical Chemistry A*, *122*(47), 9177-9190. https://doi.org/10.1021/acs.jpca.8b09025

Teplukhin, A., Gayday, I., & Babikov, D. (2018c). Several levels of theory for description of isotope effects in ozone: Effect of resonance lifetimes and channel couplings. *The Journal of Chemical Physics*, *149*(16), 164302. https://doi.org/10.1063/1.5042590

Thiemens, M. H. (2006). History and Applications of Mass-Independent Isotope Effects. *Annual Review of Earth and Planetary Sciences*, *34*(1), 217-262. https://doi.org/10.1146/annurev.earth.34.031405.125026

Thiemens, M. H., Chakraborty, S., & Dominguez, G. (2012). The Physical Chemistry of Mass-Independent Isotope Effects and Their Observation in Nature. *Annual Review of Physical Chemistry*, *63*(1), 155-177. https://doi.org/10.1146/annurev-physchem-032511-143657

Thiemens, M. H., Chakraborty, S., & Jackson, T. L. (2014). Decadal $\Delta^{17}O$ record of tropospheric CO_2: Verification of a stratospheric component in the troposphere [https://doi.org/10.1002/2013JD020317]. *Journal of Geophysical Research: Atmospheres*, *119*(10), 6221-6229. https://doi.org/https://doi.org/10.1002/2013JD020317

Thiemens, M. H., & Heidenreich, J. E. (1983). The Mass-Independent Fractionation of Oxygen: A Novel Isotope Effect and Its Possible Cosmochemical Implications. *Science*, *219*(4588), 1073-1075. https://doi.org/10.1126/science.219.4588.1073

Thiemens, M. H., & Jackson, T. (1988). New experimental evidence for the mechanism for production of isotopically heavy O_3 [https://doi.org/10.1029/GL015i007p00639]. *Geophysical Research Letters*, *15*(7), 639-642. https://doi.org/https://doi.org/10.1029/GL015i007p00639

Thiemens, M. H., & Jackson, T. (1990). Pressure dependency for heavy isotope enhancement in ozone formation [https://doi.org/10.1029/GL017i006p00717]. *Geophysical Research Letters*, *17*(6), 717-719. https://doi.org/https://doi.org/10.1029/GL017i006p00717

Thiemens, M. H., Jackson, T., Zipf, E. C., Erdman, P. W., & van Egmond, C. (1995). Carbon Dioxide and Oxygen Isotope Anomalies in the Mesosphere and Stratosphere. *Science*, *270*(5238), 969-972. https://doi.org/10.1126/science.270.5238.969

Thiemens, M. H., Jackson, T. L., & Brenninkmeijer, C. A. M. (1995). Observation of a mass independent oxygen isotopic composition in terrestrial stratospheric CO_2, the link to ozone chemistry, and the possible occurrence in the Martian atmosphere [https://doi.org/10.1029/94GL02996]. *Geophysical Research Letters*, *22*(3), 255-257. https://doi.org/https://doi.org/10.1029/94GL02996

Thiemens, M. H., & Lin, M. (2019). Use of Isotope Effects To Understand the Present and Past of the Atmosphere and Climate and Track the Origin of Life. *Angewandte Chemie International Edition*, *58*(21), 6826-6844. https://doi.org/https://doi.org/10.1002/anie.201812322

Totenhofer, A. J., Connor, J. N. L., & Nyman, G. (2016). Angular Scattering Dynamics of the $CH_4 + Cl \rightarrow CH_3 + HCl$ Reaction Using Nearside–Farside, Local Angular Momentum, and Resummation Theories. *The Journal of Physical Chemistry B*, *120*(8), 2020-2032. https://doi.org/10.1021/acs.jpcb.5b10189

Toyoda, S., Kuroki, N., Yoshida, N., Ishijima, K., Tohjima, Y., & Machida, T. (2013). Decadal time series of tropospheric abundance of N_2O isotopomers and isotopologues in the

Northern Hemisphere obtained by the long-term observation at Hateruma Island, Japan. *Journal of Geophysical Research: Atmospheres*, *118*(8), 3369-3381. https://doi.org/10.1002/jgrd.50221

Toyoda, S., Yoshida, N., Urabe, T., Aoki, S., Nakazawa, T., Sugawara, S., & Honda, H. (2001). Fractionation of N_2O isotopomers in the stratosphere. *Journal of Geophysical Research: Atmospheres*, *106*(D7), 7515-7522. https://doi.org/10.1029/2000jd900680

Tromp, T. K. (2003). Potential Environmental Impact of a Hydrogen Economy on the Stratosphere. *Science*, *300*(5626), 1740-1742. https://doi.org/10.1126/science.1085169

Tsunogai, U., Komatsu, D. D., Daita, S., Kazemi, G. A., Nakagawa, F., Noguchi, I., & Zhang, J. (2010). Tracing the fate of atmospheric nitrate deposited onto a forest ecosystem in Eastern Asia using $\Delta^{17}O$. *Atmos. Chem. Phys.*, *10*(4), 1809-1820. https://doi.org/10.5194/acp-10-1809-2010

Turatti, F., Griffith, D. W. T., Wilson, S. R., Esler, M. B., Rahn, T., Zhang, H., & Blake, G. A. (2000). Positionally dependent ^{15}N fractionation factors in the UV photolysis of N_2O determined by high resolution FTIR spectroscopy. *Geophysical Research Letters*, *27*(16), 2489-2492. https://doi.org/10.1029/2000gl011371

Turner, A. J., Frankenberg, C., & Kort, E. A. (2019). Interpreting contemporary trends in atmospheric methane. *Proceedings of the National Academy of Sciences*, *116*(8), 2805-2813. https://doi.org/10.1073/pnas.1814297116

Tyler, S. C., Ajie, H. O., Gupta, M. L., Cicerone, R. J., Blake, D. R., & Dlugokencky, E. J. (1999). Stable carbon isotopic composition of atmospheric methane: A comparison of surface level and free tropospheric air [https://doi.org/10.1029/1999JD900029]. *Journal of Geophysical Research: Atmospheres*, *104*(D11), 13895-13910. https://doi.org/https://doi.org/10.1029/1999JD900029

Tyler, S. C., Ajie, H. O., Rice, A. L., Cicerone, R. J., & Tuazon, E. C. (2000). Experimentally determined kinetic isotope effects in the reaction of CH_4 with Cl: Implications for atmospheric CH_4 [https://doi.org/10.1029/1999GL011168]. *Geophysical Research Letters*, *27*(12), 1715-1718. https://doi.org/https://doi.org/10.1029/1999GL011168

Umemoto, H. (1999). $^{14}N/^{15}N$ isotope effect in the UV photodissociation of N_2O. *Chemical Physics Letters*, *314*(3-4), 267-272. https://doi.org/10.1016/s0009-2614(99)01145-8

Urey, H. C. (1947). The thermodynamic properties of isotopic substances. *Journal of the Chemical Society (Resumed)*, 562. https://doi.org/10.1039/jr9470000562

Urey, H. C., & Greiff, L. J. (1935). Isotopic exchange equilibria. *Journal of the American Chemical Society*, *57*(2), 321-327.

Valentini, J. J. (1983). Anomalous rotational state distribution for the O_2 photofragment in the UV photodissociation of ozone. *Chemical Physics Letters*, *96*(4), 395-398. https://doi.org/https://doi.org/10.1016/0009-2614(83)80715-5

Van Wyngarden, A. L., Mar, K. A., Boering, K. A., Lin, J. J., Lee, Y. T., Lin, S.-Y., Guo, H., & Lendvay, G. (2007). Nonstatistical Behavior of Reactive Scattering in the $^{18}O+^{32}O_2$ Isotope Exchange Reaction. *Journal of the American Chemical Society*, *129*(10), 2866-2870. https://doi.org/10.1021/ja0668163

Vasilchenko, S., Barbe, A., Starikova, E., Kassi, S., Mondelain, D., Campargue, A., & Tyuterev, V. (2020). Detection and assignment of ozone bands near 95% of the dissociation threshold: Ultrasensitive experiments for probing potential energy function and vibrational dynamics. *Physical Review A*, *102*(5), 052804. https://doi.org/10.1103/PhysRevA.102.052804

Vicars, W. C., & Savarino, J. (2014). Quantitative constraints on the ^{17}O-excess ($\Delta^{17}O$) signature of surface ozone: Ambient measurements from 50°N to 50°S using the nitrite-coated filter technique. *Geochimica et Cosmochimica Acta*, *135*, 270-287. https://doi.org/https://doi.org/10.1016/j.gca.2014.03.023

Walters, W. W., Michalski, G., Böhlke, J. K., Alexander, B., Savarino, J., & Thiemens, M. H. (2019). Assessing the Seasonal Dynamics of Nitrate and Sulfate Aerosols at the South Pole Utilizing Stable Isotopes. *Journal of Geophysical Research: Atmospheres*, *124*(14), 8161-8177. https://doi.org/https://doi.org/10.1029/2019JD030517

Wang, D. T., Gruen, D. S., Lollar, B. S., Hinrichs, K.-U., Stewart, L. C., Holden, J. F., Hristov, A. N., Pohlman, J. W., Morrill, P. L., Könneke, M., Delwiche, K. B., Reeves, E. P., Sutcliffe, C. N., Ritter, D. J., Seewald, J. S., McIntosh, J. C., Hemond, H. F., Kubo, M. D., Cardace, D., Hoehler, T. M., & Ono, S. (2015). Nonequilibrium clumped isotope signals in microbial methane. *Science*, *348*(6233), 428-431. https://doi.org/10.1126/science.aaa4326

Wang, J. S., McElroy, M. B., Spivakovsky, C. M., & Jones, D. B. A. (2002). On the contribution of anthropogenic Cl to the increase in $\delta^{13}C$ of atmospheric methane [https://doi.org/10.1029/2001GB001572]. *Global Biogeochemical Cycles*, *16*(3), 20-21-20-11. https://doi.org/https://doi.org/10.1029/2001GB001572

Webb, M. A., Wang, Y., Braams, B. J., Bowman, J. M., & Miller, T. F. (2017). Equilibrium clumped-isotope effects in doubly substituted isotopologues of ethane. *Geochimica et Cosmochimica Acta*, *197*, 14-26. https://doi.org/10.1016/j.gca.2016.10.001

Wehr, R., Munger, J. W., McManus, J. B., Nelson, D. D., Zahniser, M. S., Davidson, E. A., Wofsy, S. C., & Saleska, S. R. (2016). Seasonality of temperate forest photosynthesis and daytime respiration. *Nature*, *534*(7609), 680-683. https://doi.org/10.1038/nature17966

Weissberger, E., Breckenridge, W. H., & Taube, H. (1967). Reaction of $O(^1D)$ with CO_2 at Low Temperatures. *The Journal of Chemical Physics*, *47*(5), 1764-1769. https://doi.org/10.1063/1.1712161

Welsch, R. (2019). Kinetic isotope effects in the water forming reaction H_2/D_2 + OH from rigorous close-coupling quantum dynamics simulations. *Physical Chemistry Chemical Physics*, *21*(31), 17054-17062. https://doi.org/10.1039/c9cp02323b

Wen, J., & Thiemens, M. H. (1993). Multi-isotope study of the $O(^1D)$ + CO_2 exchange and stratospheric consequences [https://doi.org/10.1029/93JD00565]. *Journal of Geophysical Research: Atmospheres*, *98*(D7), 12801-12808. https://doi.org/https://doi.org/10.1029/93JD00565

Weston, R. E. (2006). When Is an Isotope Effect Non-Mass Dependent? *Journal of Nuclear Science and Technology*, *43*(4), 295-299. https://doi.org/10.1080/18811248.2006.9711092

Whitehill, A. R., Joelsson, L. M. T., Schmidt, J. A., Wang, D. T., Johnson, M. S., & Ono, S. (2017). Clumped isotope effects during OH and Cl oxidation of methane. *Geochimica et Cosmochimica Acta*, *196*, 307-325. https://doi.org/https://doi.org/10.1016/j.gca.2016.09.012

Wiegel, A. A., Cole, A. S., Hoag, K. J., Atlas, E. L., Schauffler, S. M., & Boering, K. A. (2013). Unexpected variations in the triple oxygen isotope composition of stratospheric carbon dioxide. *Proceedings of the National Academy of Sciences*, *110*(44), 17680-17685. https://doi.org/10.1073/pnas.1213082110

Winkler, R., Landais, A., Sodemann, H., Dümbgen, L., Prié, F., Masson-Delmotte, V., Stenni, B., & Jouzel, J. (2012). Deglaciation records of ^{17}O-excess in East Antarctica: reliable reconstruction of oceanic normalized relative humidity from coastal sites. *Clim. Past*, *8*(1), 1-16. https://doi.org/10.5194/cp-8-1-2012

Wojtal, P. K., Miller, D. J., O'Conner, M., Clark, S. C., & Hastings, M. G. (2016). Automated, High-resolution Mobile Collection System for the Nitrogen Isotopic Analysis of NO_x. *Journal of Visualized Experiments*(118). https://doi.org/10.3791/54962

Wyngarden, A. L. V., Mar, K. A., Quach, J., Nguyen, A. P. Q., Wiegel, A. A., Lin, S.-Y., Lendvay, G., Guo, H., Lin, J. J., Lee, Y. T., & Boering, K. A. (2014). The non-statistical dynamics of the $^{18}O + {}^{32}O_2$ isotope exchange reaction at two energies. *The Journal of Chemical Physics*, *141*(6), 064311. https://doi.org/10.1063/1.4892346

Xueref-Remy, I., Zazzeri, G., Bréon, F. M., Vogel, F., Ciais, P., Lowry, D., & Nisbet, E. G. (2020). Anthropogenic methane plume detection from point sources in the Paris megacity area and characterization of their $\delta^{13}C$ signature. *Atmospheric Environment*, *222*, 117055. https://doi.org/https://doi.org/10.1016/j.atmosenv.2019.117055

Yau, A. M., Bender, M. L., Blunier, T., & Jouzel, J. (2016). Setting a chronology for the basal ice at Dye-3 and GRIP: Implications for the long-term stability of the Greenland Ice Sheet. *Earth and Planetary Science Letters*, *451*, 1-9. https://doi.org/https://doi.org/10.1016/j.epsl.2016.06.053

Yeung, L. Y., Ash, J. L., & Young, E. D. (2015). Biological signatures in clumped isotopes of O2. *Science*, *348*(6233), 431-434. https://doi.org/10.1126/science.aaa6284

Yeung, L. Y., Haslun, J. A., Ostrom, N. E., Sun, T., Young, E. D., Van Kessel, M. A. H. J., Lücker, S., & Jetten, M. S. M. (2019). In Situ Quantification of Biological N_2 Production Using Naturally Occurring $^{15}N^{15}N$. *Environmental Science & Technology*, *53*(9), 5168-5175. https://doi.org/10.1021/acs.est.9b00812

Yeung, L. Y., Li, S., Kohl, I. E., Haslun, J. A., Ostrom, N. E., Hu, H., Fischer, T. P., Schauble, E. A., & Young, E. D. (2017). Extreme enrichment in atmospheric $^{15}N^{15}N$. *Science Advances*, *3*(11), eaao6741. https://doi.org/10.1126/sciadv.aao6741

Yeung, L. Y., Murray, L. T., Ash, J. L., Young, E. D., Boering, K. A., Atlas, E. L., Schauffler, S. M., Lueb, R. A., Langenfelds, R. L., Krummel, P. B., Steele, L. P., & Eastham, S. D. (2016). Isotopic ordering in atmospheric O_2 as a tracer of ozone photochemistry and the tropical atmosphere. *Journal of Geophysical Research: Atmospheres*, *121*(20), 12,541-512,559. https://doi.org/10.1002/2016jd025455

Yeung, L. Y., Murray, L. T., Banerjee, A., Tie, X., Yan, Y., Atlas, E. L., Schauffler, S. M., & Boering, K. A. (2021). Effects of Ozone Isotopologue Formation on the Clumped-Isotope Composition of Atmospheric O_2. *Journal of Geophysical Research: Atmospheres*, *126*(14), e2021JD034770. https://doi.org/https://doi.org/10.1029/2021JD034770

Yeung, L. Y., Murray, L. T., Martinerie, P., Witrant, E., Hu, H., Banerjee, A., Orsi, A., & Chappellaz, J. (2019). Isotopic constraint on the twentieth-century increase in tropospheric ozone. *Nature*, *570*(7760), 224-227. https://doi.org/10.1038/s41586-019-1277-1

Yeung, L. Y., Young, E. D., & Schauble, E. A. (2012). Measurements of $^{18}O^{18}O$ and $^{17}O^{18}O$ in the atmosphere and the role of isotope-exchange reactions. *Journal of Geophysical Research: Atmospheres*, *117*(D18), n/a-n/a. https://doi.org/10.1029/2012jd017992

Young, E. D., Rumble, D., Freedman, P., & Mills, M. (2016). A large-radius high-mass-resolution multiple-collector isotope ratio mass spectrometer for analysis of rare

isotopologues of O_2, N_2, CH_4 and other gases. *International Journal of Mass Spectrometry*, *401*, 1-10. https://doi.org/10.1016/j.ijms.2016.01.006

Yu, L., Harris, E., Henne, S., Eggleston, S., Steinbacher, M., Emmenegger, L., Zellweger, C., & Mohn, J. (2020). The isotopic composition of atmospheric nitrous oxide observed at the high-altitude research station Jungfraujoch, Switzerland. *Atmos. Chem. Phys.*, *20*(11), 6495-6519. https://doi.org/10.5194/acp-20-6495-2020

Yung, Y. L., Lee, A. Y. T., Irion, F. W., DeMore, W. B., & Wen, J. (1997). Carbon dioxide in the atmosphere: Isotopic exchange with ozone and its use as a tracer in the middle atmosphere [https://doi.org/10.1029/97JD00528]. *Journal of Geophysical Research: Atmospheres*, *102*(D9), 10857-10866. https://doi.org/https://doi.org/10.1029/97JD00528

Yung, Y. L., & Miller, C. E. (1997). Isotopic Fractionation of Stratospheric Nitrous Oxide. *Science*, *278*(5344), 1778-1780. https://doi.org/10.1126/science.278.5344.1778

Yung, Y. L., Wang, W. C., & Lacis, A. A. (1976). Greenhouse effect due to atmospheric nitrous oxide. *Geophysical Research Letters*, *3*(10), 619-621. https://doi.org/10.1029/gl003i010p00619

Zhang, H., Wennberg, P. O., Wu, V. H., & Blake, G. A. (2000). Fractionation of $^{14}N^{15}N^{16}O$ and $^{15}N^{14}N^{16}O$ during photolysis at 213 nm. *Geophysical Research Letters*, *27*(16), 2481-2484. https://doi.org/10.1029/1999gl011236

Zhao, Y., Zhang, Y.-L., & Sun, R. (2021). The mass-independent oxygen isotopic composition in sulfate aerosol-a useful tool to identify sulfate formation: a review. *Atmospheric Research*, *253*, 105447. https://doi.org/https://doi.org/10.1016/j.atmosres.2020.105447

Zhu, R. S., Diau, E. G. W., Lin, M. C., & Mebel, A. M. (2001). A Computational Study of the OH(OD) + CO Reactions: Effects of Pressure, Temperature, and Quantum-Mechanical Tunneling on Product Formation. *The Journal of Physical Chemistry A*, *105*(50), 11249-11259. https://doi.org/10.1021/jp0104536